Titre: Title:	Thermodynamic Modeling of Complex Solid Solutions for Lithium Battery Applications
Auteur: Author:	Anh Thu Phan
Date:	2020
Type:	Mémoire ou thèse / Dissertation or Thesis
Référence: Citation:	Phan, A. T. (2020). Thermodynamic Modeling of Complex Solid Solutions for Lithium Battery Applications [Thèse de doctorat, Polytechnique Montréal]. PolyPublie. https://publications.polymtl.ca/5238/

URL de PolyPublie: PolyPublie URL:	https://publications.polymtl.ca/5238/
Directeurs de recherche: Advisors:	Patrice Chartrand, & Aïmen E. Gheribi
Programme: Program:	Génie des matériaux

POLYTECHNIQUE MONTRÉAL

affiliée à l'Université de Montréal

Thermodynamic modeling of complex solid solutions for lithium battery applications

ANH THU PHAN

Département de génie chimique

Thèse présentée en vue de l'obtention du diplôme de *Philosophiæ Doctor*

Génie des matériaux

Mai 2020

POLYTECHNIQUE MONTRÉAL

affiliée à l'Université de Montréal

Cette thèse intitulée :

Thermodynamic modeling of complex solid solutions for lithium battery applications

présentée par **Anh Thu PHAN**

en vue de l'obtention du diplôme de *Philosophiæ Doctor*

a été dûment acceptée par le jury d'examen constitué de :

Fabio CICOIRA, président
Patrice CHARTRAND, membre et directeur de recherche
Aïmen GHERIBI, membre et codirecteur de recherche
Arthur PELTON, membre
Axel VAN DE WALLE, membre externe

DEDICATION

For my family

ACKNOWLEDGEMENTS

I would like to express my gratitude to my director, Professor Patrice Chartrand, for giving me the chance working on this research project with all the necessary intellectual liberty. Thank you very much for letting me and encouraging me to discover the new thermodynamic models and thank you for your patience while working with me. Especially, I would like to thank you for giving me the opportunity to complete my doctoral degree at the CRCT (centre de recherche en calcul thermochimique), an excellent research environment.

In addition, I would highly appreciate the support of Natural Science, Engineering Research Council of Canada and the Canadian Foundation for Innovation through the Automotive Partnership Canada program and our industry partner Johnson-Matthey. Moreover, I would like to express my recognition to Calcul-Québec and Compute Canada. Also, I would like to send my thanks to my friends and colleagues in CRCT for all their help during my journey.

My doctoral study wouldn’t have been realized without the unconditional support and great encouragement of my family and friends.

Finally, my deepest appreciation goes to Dr. Aïmen E. Gheribi. Thank you, my colleague and my great friend, for everything.

RÉSUMÉ

$LiFePO_4$ est un matériau attrayant pour les batteries au lithium car il conserve sa structure cristalline de type olivine et ce, malgré le mouvement réversible des ions lithium. Lorsque les ions Li^+ sont tous extraits de la triphylite ($LiFePO_4$), l'heterosite ($FePO_4$) se forme et une coexistence entre les deux phases, $LiFePO_4$ et $FePO_4$, conduit à la formation d'un plateau de tension électrique stable. La compréhension des équilibres de phases au sein du système $FePO_4$ -$LiFePO_4$ est donc nécessaire pour caractériser et optimiser d'une part les performances des batteries à base de $LiFePO_4$. Lors de cette étude, nous avons tout d'abord modélisé via une approche de type CALPHAD (Calculation of PHAse Diagram) le comportement thermodynamique du système $FePO_4$ -$LiFePO_4$ afin d'établir une description fine des transformations de phase dans le matériau de cathode pendant le fonctionnement de la batterie. Pour représenter l'état thermodynamique du système, l'énergie libre de Gibbs de la solution solide Li_xFePO_4 a été décrite via le « Compound Energy Formalism (CEF) ». Les équilibres des phases sont ensuite déterminés par une technique de la minimisation de l'énergie libre de Gibbs idoine implémentée sur le logiciel Matlab. Un ordre à longue distance (« LRO ») sur les sous-réseaux du Li et du Fe au sein de la solution solide Li_xFePO_4 fut introduit afin de reproduire simultanément et de manière critique les données expérimentales, disponibles dans la littérature, relatives à (i) la réaction eutectoïde, (ii) les trois lacunes de miscibilité et (iii) l'enthalpie de mélange. Il est montré, qu'aux basses températures (300 K < T <500 K), la lacune de miscibilité du système $LiFePO_4$-$FePO_4$ se décompose de deux sous-lacunes de miscibilité. En se basant sur l'analyse de la décomposition de spinoïdale calculée, nous montrons qu'un transport rapide de charge est possible dans le matériau de cathode et peut comporter deux étapes dans le processus décomposition spinoïdale.

Le consensus actuel veut que la structure d'olivine que conserve la cathode donne à $LiFePO_4$ une capacité aux hauts débits. Cependant, le matériau massif $LiFePO_4$ n'est utilisé que pour les applications aux faibles débits. En fait, c'est la transformation cohérente du système de taille nanométrique qui confère à $LiFePO_4$ sa capacité aux hauts débits. Pour comprendre et représenter les phénomènes de charge /décharge rapides au sein des batteries à $LiFePO_4$, les équilibres de phases du système cohérent $LiFePO_4$-$FePO_4$ à l'échelle nanométrique sont établis dans cette recherche. Pour cela, dans la deuxième partie de cette thèse nous avons étudié les équilibres de phases du système cohérent $LiFePO_4$-$FePO_4$ en fonction de la taille de particule jusqu'à 15 nm.

L’énergie libre de Gibbs du système cohérent est formulée en tenant compte des contraintes élastiques qui maintiennent la cohérence entre les deux réseaux cristallins $LiFePO_4$ et $FePO_4$. L’effet de taille est quant à lui quantifié via une expression idoine de l’énergie de surface des grains. Les calculs d’équilibres de phases ainsi réalisés nous ont permis de quantifier l’influence de la réduction de la taille des particules sur l’améliorantion des performances électrochimiques du matériau de la cathode. D’un point de vue théorique, nous avons développé un formalisme original qui généralise l’approche développée par Cahn pour des matériaux isotropes pour de faibles incohérences de mailles. Nous avons notamment proposé une expression d’énergie élastique pour les systèmes orthorhombiques telle que l’olivine. Cette approche fut appliquée pour calculer les énergies élastiques mises en jeu aux joints de grains cathode formée de $LiFePO_4$-$FePO_4$. Les calculs ont montré que le plan cristallographique (100) est le plus énergétiquement favorable tandis que les plans (110) et (010) conduisent à des transformations de phases cohérentes qui peuvent être également possibles. De plus, la transformation cohérente du matériau de cathode pourrait expliquer l’apparition d’une phase métastable, le plan énergétiquement favorable au processus lithiation/délithiation, et la formation de dislocations ou de fissures par cyclage. Les effets couplées cohérence-taille sont une originalité de cette thèse. Nous montrons que les domaines d’immiscibilité diminuent avec la taille des particules et conduise à l’existence d’une région de phase intermédiaire entre les deux lacunes de miscibilité. Finalement nous montrons que la transformation phase cohérente du matériau de cathode durant les processus électrochimiques est plus probable avec des particules de petite taille.

Il est connu que le dopage, particulièrement le dopage de Mn, contribuerait à enrichir les propriétés des transports électronique et ionique, et par extension, les propriétés électrochimiques des matériaux de cathode. Cela les rendrait bien plus efficaces pour les aux hauts débits. Le comportement thermodynamique de la cathode à base du matériau dopé au manganèse $Li(Mn_yFe_{1-y})PO_4$ a été étudié sur le joint $Li(Mn_yFe_{1-y})PO_4$ - $(Mn_yFe_{1-y})PO_4$. L’énergie libre de Gibbs du système $Li(Mn_yFe_{1-y})PO_4$ - $(Mn_yFe_{1-y})PO_4$ est formulée selon la méthode CALPHAD à l’aide des nouveaux modèles de sous-réseaux secondaire afin de décrire avec le joint para-équilibré $Li(Mn_yFe_{1-y})PO_4$ - $(Mn_yFe_{1-y})PO_4$ et les lacune de miscibilité qui découlent de réactions d’oxydoréduction et de l’ordre à longue distance entre les espèces Fe^{2+}/Fe^{3+}. Étant donné qu’aucune information sur les enthalpies de formation et les constants élastiques des composés, les enthalpies de mélange des sous-systèmes binaires sont disponibles dans la littérature, celles-ci furent prédites à partir de calculs premiers principes à base de la densité fonctionnelle de la densité (électronique) ou « DFT » via le logiciel VASP. Les caractéristiques électrochimiques du $LiFePO_4$ dopé au Mn, telle que les équilibres de phase induits par des processus électrochimiques, la tension de circuit ouvert (OCV), de l'asymétrie du processus de charge et de décharge ainsi que les changements de potentiels sont alors décrits grâce à ces nouveaux modèles thermodynamiques.

Il est connu qu'$LiFePO_4$ dopé au Mn possède une structure d'olivine de même que la phase délithiée, $(Mn_yFe_{1-y})PO_4$. De ce fait, la transformation cohérente de phase dans laquelle le mouvement réversible de Li^+ au sein du matériau de cathode ne modifie pas sa structure cristalline, est étudiée en détail dans le but d'optimiser le taux de charge/décharge ainsi que la cyclabilité du processus. Étant donné que l'incohérence des réseaux cristallins dépasse les 5%, nous avons développé un modèle théorique pour représenter l'énergie libre de Gibbs élastique de systèmes orthorhombiques (et de symétrie inferieur) pour de grandes déformations en considérant le tenseur des déformations d'Euler et les seconds tenseurs des contraintes de Piola-Kirchoff. Ce modèle, généralise le modèle développé pour de faibles déformations en considérant les tenseurs des contraintes et des déformations de Cauchy. L'énergie libre de Gibbs élastique ainsi formulée fut appliquée afin de calculer les lacunes cohérentes de miscibilité du joint $(Mn_yFe_{1-y})PO_4$ - $(Mn_yFe_{1-y})PO_4$ à température ambiante selon le plan (100). Il est alors montré que lorsque $LiFePO_4$ est dopé au Mn il est susceptible de subir une transformation de phase cohérente selon le plan cristallographique (100).

ABSTRACT

$LiFePO_4$ cathode material is attractive since it can remain its olivine crystal structure despite the reversible movement of lithium ions. As all Li^+ ions are extracted from olivine-$LiFePO_4$ (triphylite), olivine-$FePO_4$ (heterosite) is formed and the two olivine phases, $LiFePO_4$ and $FePO_4$, coexisted leads to the formation of the stable voltage plateau. Therefore, the understanding of phase equilibria within the $LiFePO_4$ - $FePO_4$ system is necessary to characterize and optimize the performance of $LiFePO_4$ battery. The thermodynamic behavior of the $LiFePO_4$ - $FePO_4$ system is modeled via the CALPHAD (Calculation of PHAse Diagram) approach in order to describe sufficiently the phase transformation in the cathode material during the battery operation. For representing the thermodynamic state of the system, the Gibbs free energy of the Li_xFePO_4 solid solution is modeled by compound energy formalism (CEF). The phase equilibria consequently are determined by the Gibbs energy minimization technique implemented on Matlab software. An extra long-range-order of the Li_xFePO_4 solid solution is introduced to reproduce simultaneously the eutectoid reaction, the three miscibility gaps, and the enthalpy of mixing in accordance with the reported experimental data. The study shows that at low temperatures ($298\ K < T < 500\ K$), the miscibility gap of the $LiFePO_4$ - $FePO_4$ system should be stated as the fusion of two sub-miscibility gaps. According to the analysis of the spinodal decomposition, fast charge transport within the cathode material is possible and it includes up to two sub-spinodal decomposition steps.

The general belief of unchanged olivine structure of the cathode gives $LiFePO_4$ a high-rate capability. However, bulk $LiFePO_4$ is only used for low-rate applications. In fact, the coherent phase transformation within the nanometric size of $LiFePO_4$ makes the material stand out among battery materials for the high-rate applications. For understanding and representing the rapid charge/discharge phenomena within $LiFePO_4$ cathode, the coherent phase equilibria of the $LiFePO_4$ - $FePO_4$ system at nanometric scale are established in this study. Consequently, the second contribution of this thesis presents the coherent phase equilibria of the $LiFePO_4$ - $FePO_4$ system as a function of particle size (≥ 15nm). The coherent Gibbs energy of the system is formulated by taking into account the elastic constraints which maintain the coherence between the two crystals, $LiFePO_4$ and $FePO_4$. The effect of particle size is quantified by a suitable expression of the surface energy of the particles. The calculation of phase equilibria allows us to quantify the influence of the reduction of particle size on improving the electrochemical performance of the cathode

material. From a theoretical point of view, an original formalism, which generalizes the Cahn's approach for isotropic materials in the small deformation regime, was developed. Noticeably, an expression of elastic Gibbs energy was proposed for orthorhombic systems such as olivine $LiFePO_4$ - $FePO_4$ cathode join. This approach was applied for calculating the elastic energy involved in the coherent grain boundaries of $LiFePO_4$ and $FePO_4$. The calculation of coherent miscibility gaps shows that (100) is the most energetically favorable habit plane while (110) and (010) coherent phase transformations are possible. In addition, the occurrence of a metastable phase, preferred phase boundaries during lithiation/delithiation, and the creation of dislocations or cracks via cycling can be explained by the coherent phase transformation. It is the first time that the combined coherency-size type of calculation is ever performed. The miscibility gaps reduce with the reduction of the particle size and the intermediate phase region between the two miscibility gaps occurs. Moreover, at small particle sizes, the coherent phase transformation within the cathode material during electrochemical processes is more likely.

It is known that doping, especially Mn doping, can enrich the electric and ionic properties hence the electrochemical properties of battery materials and makes them suitable for high-rate applications. The thermodynamic behavior of the $Li(Mn_yFe_{1-y})PO_4$ cathode has been considered by examining the $Li(Mn_yFe_{1-y})PO_4$ - $(Mn_yFe_{1-y})PO_4$ olivine join. The Gibbs free energy of the $Li(Mn_yFe_{1-y})PO_4$ - $(Mn_yFe_{1-y})PO_4$ system is formulated based on CALPHAD method using the new sublattice models containing secondary sublattices in order to successfully describe the para-equilibrium $Li(Mn_yFe_{1-y})PO_4$ - $(Mn_yFe_{1-y})PO_4$ battery join with the separation of miscibility gaps by redox reactions and Fe^{2+}/Fe^{3+} long-range-order. Due to no available information of enthalpy of mixing of the binary sub-systems and the shortage of study on the enthalpy of formation and elastic constants of the compounds in the literature, they are predicted from first principles calculations based on the density functional theory (DFT) using the VASP software. The electrochemical characteristics of the Mn-doped-$LiFePO_4$ such as the electrochemically driven phase diagrams, open-circuit voltage (OCV), asymmetry of charge/discharge processes, and potential shifts can be described sufficiently by using my thermodynamic models.

As known, like $LiFePO_4$, the Mn doping cathode material, $Li(Mn_yFe_{1-y})PO_4$, possesses olivine structure and so does the delithiated phase, $(Mn_yFe_{1-y})PO_4$. Therefore, coherent phase transformation, in which Li^+ reversible movement within cathode material does not change its

crystal structure, is concerned in order to enhance the charge/discharge rate and cyclability. Since the maximum lattice mismatch goes beyond 5%, a theoretical model was developed in order to represent the elastic Gibbs free energy of orthorhombic systems (and systems with low symmetry) in the large deformation regime by considering the Euler's strain tensor and the second order Piola-Kirchoff stress tensor. This model is an extension of the model developed in the small deformation regime using the Cauchy's stress and strain tensors. The formulated elastic Gibbs energy is then applied for calculating the (100) coherent miscibility gaps of the $Li(Mn_yFe_{1-y})PO_4$ - $(Mn_yFe_{1-y})PO_4$ system at room temperature. The calculation reveals the favourability of the cathode to experience (100) coherent phase transformation.

TABLE OF CONTENTS

LIST OF TABLES

LIST OF FIGURES

LIST OF SYMBOLS AND ABBREVIATIONS

α	Thermal expansion coefficient
a_i, b_i, c_i	Lattice constants of crystal i
B	Bulk modulus
$[\boldsymbol{C}]$	Right Cauchy-Green deformation tensor
C	Correction factor considering the shape effect
C_{ij}	Elastic constant (i and j are Voigt notations)
C_{anhar}	Anharmonic heat capacity
C_{def}	Heat capacity contribution of defects
C_p	Isobaric heat capacity
C_p^{mag}	Magnetic heat capacity
$C_p^{pho-mag}$	Heat capacity contribution of phonon-magnon interaction
C_v	Isochoric heat capacity
D	Particle size
ε	Strain
e	Artificial strain
$[\boldsymbol{e}]$	Almansi-Lagrange strain tensor
ε_{ij}	Strain tensor (i and j are Voigt notations)

E	Young's modulus
E_{def}	Formation energy of defects
$E_{elastic}$	Density of strain energy stored in coherent boundaries
f_{el} , $f_{el}^{s,l}$	Elastic energy stored in the crystal formulated in the small (s) or large (l) deformation regime
F	Faraday's constant
$[\boldsymbol{F}]$	Deformation matrix
G	Shear modulus
G_i°	Molar Gibbs energy of the specie i
G_m	Molar Gibbs energy
G_m^E	Total molar excess Gibbs energy
ΔG^{EX}	Gibbs exchange energy of an exchange reaction
G_m^{chem}	Chemical free energy of mixing
G_m^{el}	Elastic Gibbs energy of a solid solution
G_i^{el}	Elastic Gibbs energy of compound i
G_m^{coh}	Coherent Gibbs energy of mixing
$G_m^{tot}(D)$	Total molar Gibbs free energy of the solid solution at a particle size D
$G_m^{ref}(\infty)$	Referent molar Gibbs energy for a bulk material
$G_m^s(D)$	Molar surface energy gained by reducing to the particle size D

$G_i^{f,T}$	Gibbs energy of formation of compound i at temperature T
h	Planck's constant
$H^{[lmn]}$	Stored strain energy $E_{elastic}$ for *[lmn]* habit plane per unit volume
$\Delta H_i^{f,T}$	Molar enthalpy of formation of compound i at temperature T
k_B	Boltzmann's constant
$\Delta\mu_{Li}$	Difference of the Li chemical potential in the crystallite cathode and anode
M	molecular weight of the compound
n	Number of moles of atoms per mole of chemical formulation
$n^{(s)}$	Stoichiometric coefficient relating the sublattice s
$\eta = \frac{1}{a}\frac{da}{dx}$	Linear change in lattice parameter a of the solid solution phase at the investigated overall composition x per unit composition change
η'	Effective change of the lattice parameter induced by other than the lattice mismatch effect
N_A	Avogadro's number
ρ	Density
P	Pressure
R	Gas constant
s	Number of sublattice
S_{ij}	Elastic compliance (i and j are Voigt notations)

S_i^T	Molar entropy of compound i at temperature T
S_i^{mag}	Magnetic entropy compound i
ΔS_{Mi}	Entropy of mixing of model Mi
S_{def}	Entropy of defects
σ_{ij}	Stress tensor
T	Temperature
T_N	Neel temperature
$[\widetilde{\boldsymbol{T}}]$	Second Piola-Kirchhoff stress tensor
$t(x,T)$	Temperature dependent term representing the effect of change of physical properties with temperature on the stored strain energy G_m^{el}
t^i	Temperature dependent term of compound i
θ_D°	Debye temperature
ν	Poisson's ratio
v_m	Average sound velocity in the polycrystalline material
V_m	Molar volume
V_m^i	Molar volume of compound i
ω, ω_{ij}	Excess coefficient of the surface energy
x_c	Critical concentration
x_0	Overall composition

x^b	Bulk composition
x^s	Surface composition
x_i^s	Surface composition of particle of compound i
$y_i^{(s)}$	Site fraction of the species i within the sublattice s
$\langle\gamma\rangle$	Average surface energy of the solid solution
$\langle\gamma\rangle_\mathrm{i}$	Average surface energies of the isotropic compound i
$\langle\gamma\rangle^{ex}$	Excess surface energy
Y	Elastic constant of the elastically soft direction
Y'	Fitted elastic constant of the elastically soft direction
$Y_{lmn}^{s,l,Cahn}$	Elastic constant of the elastically soft direction *[lmn]* formulated in the small (s) or large (l) deformation regimes or by Cahn's approach
γ	Elastic Grüneisen parameter
Z	Coordination number
$\Delta\phi$	Overpotential or underpotential
CALPHAD	Calculation of PHAse Diagram (Computer coupling of phase diagrams and thermochemistry)
CEF	Compound energy formalism
CV	Cyclic Voltammetry
DFT	Density functional theory

DSC	Differential Scanning Calorimetry
EVs	Electric vehicles
LIB	Lithium ion batteries
LRO	Long range order
OCV	Open-circuit voltage
SAED	Selected Area Electron Diffraction
SRO	Short range order
XRD	X-Ray Diffraction
XAS	X-ray absorption spectroscopy

LIST OF APPENDICES

CHAPTER 1 INTRODUCTION

Due to the increasing trend of oil prices in the last decades as a result of the exhaustion of natural resources and the dramatical increase of the emission of greenhouse gas causing negative impact on the climate change, several actions are undertaken worldwide, e.g. COP21 agreement of keeping global warming below 2ºC [1] or EU target of reducing CO_2 level [2]. In order to improve urban air quality and consequently reduce its impacts on climate change, reducing the consumption of fossil fuels per kilometre and replacing fossil fuels with renewable fuels are encouraged [3]. Therefore, the market for electric vehicles (EVs) which can substitute fossil-based vehicles is accelerating. In 2016, more than 773000 EVs were sold. 41 million EVs are expected on the road in 2040 which would displace 13 million barrels of crude oil per day [4]. In 2015, the automobile battery ratio was 28.26% of the worldwide lithium ion batteries (LIB) producing about 100.75GWh and growing with a rate of 39.45% year-on-year [5]. LIB are widely used today because of their high-energy density, good performance and no memory effect as found in the ancient Ni-Cd or Ni-MH batteries [6]. However, pure electric vehicles are still costly in comparison with gasoline cars mainly because of the battery cost [7]. Although the LIB cost is reducing and it is predicted to continue decreasing in future, it needs about ten more years for the cost to reach the point of commercialization of battery electric vehicles (Figure 1.1) [8]. The reduction of LIB can be driven by improving cell manufacturing, enhancing learning rates for pack integration or scaling of economies (Gigafactories) [7]. For cell manufacturing, the cost of the cathode material has a significant contribution on the total cost of common LIB (at least 1/3 of the total cost) [9]. It means that reducing cathode cost is necessary in commercializing battery electric vehicles. At first, the name of LIB was given for the high-powered rechargeable cells made by $LiCoO_2$ cathode active material and a tailor-made carbonaceous anode announced by SONY Corp. in 1990 [6]. Nowadays, $LiCoO_2$ still dominates the market for hand-held devices since its revolutionary occurrence with SONY Corp. due to its superior volume energy density. However, it has strong disadvantages for using as a cathode of an electronic vehicle's battery because of (1) the limited reversible extraction of Li from $Li_{1-x}CoO_2$ (with $0.5 \gtrsim x \geq 0$) resulting a relative low specific capacity of ~ 140mAh/g [10]; (2) the safety concerns due to the magnitude of the exothermic reaction between the oxygen decomposed from $LiCoO_2$ with the organic electrolyte of the cell [11-13]; (3) the low Co abundance in Earth's crust; and (4) its toxicity [14]. Beside the layered $Li_{1-x}MO_2$ (M=Co, Ni) providing 2D Li$^+$-ion transport, the other two useful oxide host structures are the cubic Li$_{1\pm x}$[Mn$_2$]O$_4$ spinels with 3D Li$^+$-ion transport and the ordered olivines Li$_{1-x}$MPO$_4$ supporting only 1D Li$^+$-ion transport [15]. The limited reversibility capacity due to the 1V-step obtained at Li[Mn$_2$]O$_4$ and the capacity fade with cycling because of the Mn^{2+} dissolution from the surface in the 4 V domain make the spinel Li$_x$[Mn$_2$]O$_4$ less attractive to battery industry for automobiles [15]. Meanwhile, olivine-LiFePO$_4$ appears as an inexpensive, safe cathode with high theoretical reversible capacity and a good cyclability [15]. Therefore, research on LiFePO$_4$ with the aim of reducing the commercial price of nano-LiFePO$_4$ as a cathode material for automobile industry to 10$/kg was performed in APC project. This project was invested by Natural Science, Engineering Research Council of Canada and the Canadian Foundation for Innovation through the Automotive Partnership Canada program and our industry partner Johnson-Matthey, who operates a LiFePO$_4$ plant near Montreal. This PhD research is a part of the thermodynamic model section of APC project in which the thermodynamic behavior of LiFePO$_4$ during charge/discharge processes is studied.

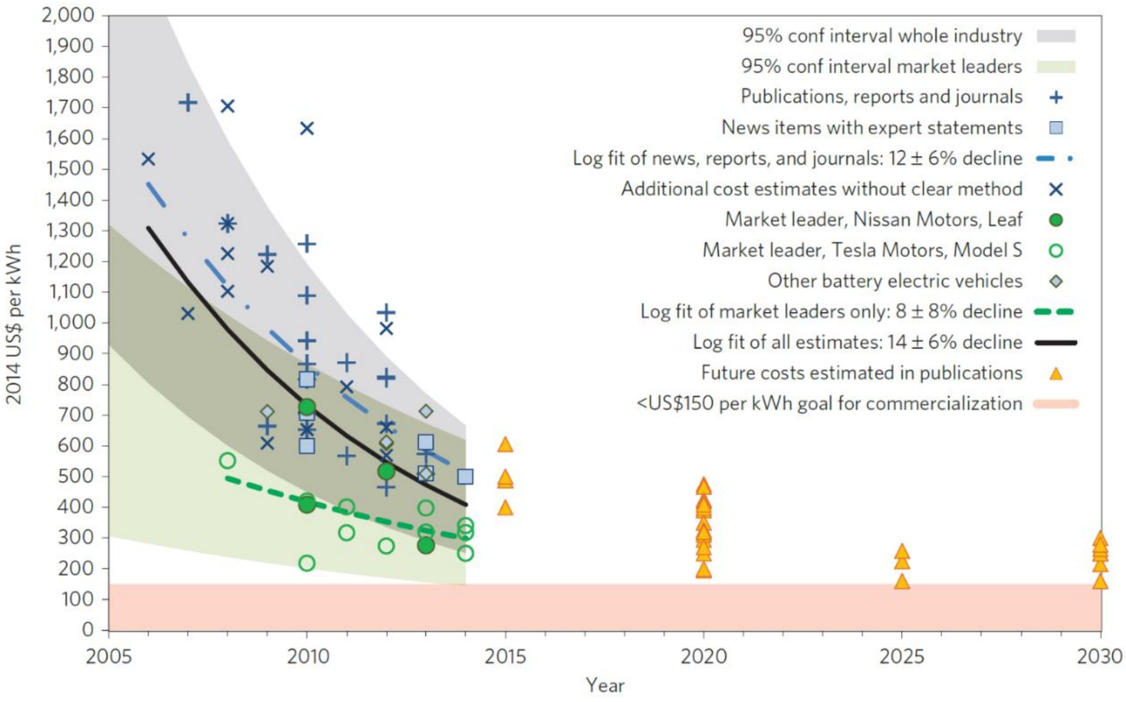

Figure 1.1: Cost of Li-ion battery packs in battery electric vehicles from multiple types of sources [8]. If costs reach US$150 per kWh this is commonly considered as the point of commercialization of battery electric vehicles [8].

After the study of Padhi et al. [16], olivine - $LiFePO_4$ draws a lot of attention as a promising cathode material. In iron lithium phosphate batteries, $LiFePO_4$ serves as the cathode material and the anode is graphite. The cathode and anode materials are placed in alternative layers and Li^+ is transferred through these layers. Even in reality carbon anode is utilized, in the literature and in this thesis, metallic Li anode is assumed when mentioning the properties of $LiFePO_4$ batteries such as redox potential, reversible capacity, etc. During charging, Li^+ is extracted from $LiFePO_4$ and as all Li^+ is removed, the cathode $LiFePO_4$ becomes olivine $FePO_4$. On the other hand, $FePO_4$ is lithiated to form $LiFePO_4$ via discharging. Both $LiFePO_4$ and $FePO_4$ have an olivine structure, orthorhombic space group *Pnma*. The framework of $LiFePO_4$ consists of FeO_6-octahedra and PO_4-tetrahedra and they contact each other by sharing oxygen vertices in *b*-*c* plane. Li atoms are situated in the interstitial voids of the framework (Figure 1.2). Besides the promising properties for electrochemical applications of $LiFePO_4$ such as safety, low toxicity, low cost, high chemical and structural stability, high theoretical reversible capacity, a flat charge-discharge profile of open circuit voltage (OCV) at ~ 3.5 V is observed [16-21] (Figure 1.3). The room temperature voltage plateau is considered as a result of the coexistence of triphylite ($LiFePO_4$) and heterosite ($FePO_4$) [18, 22-27] which is related to the miscibility gap of the $FePO_4$-$LiFePO_4$ phase diagram [26, 28, 29] (Figure 1.3, 2.1). Ichitsubo et al. [18] and Xie et al. [25] have shown the dependence of the OCV on the Gibbs energy of the cathode. It means that the knowledge of the phase transformation within the $LiFePO_4$ cathode during battery operation hence the Gibbs energy of the cathode would provide us information on the OCV and battery operation and vice versa.

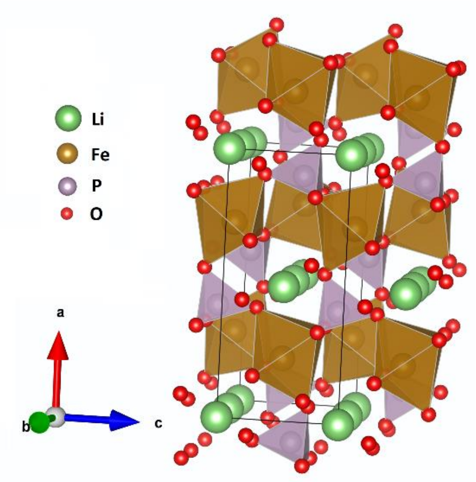

Figure 1.2: Visualization of crystal unit cell of olivine-$LiFePO_4$.

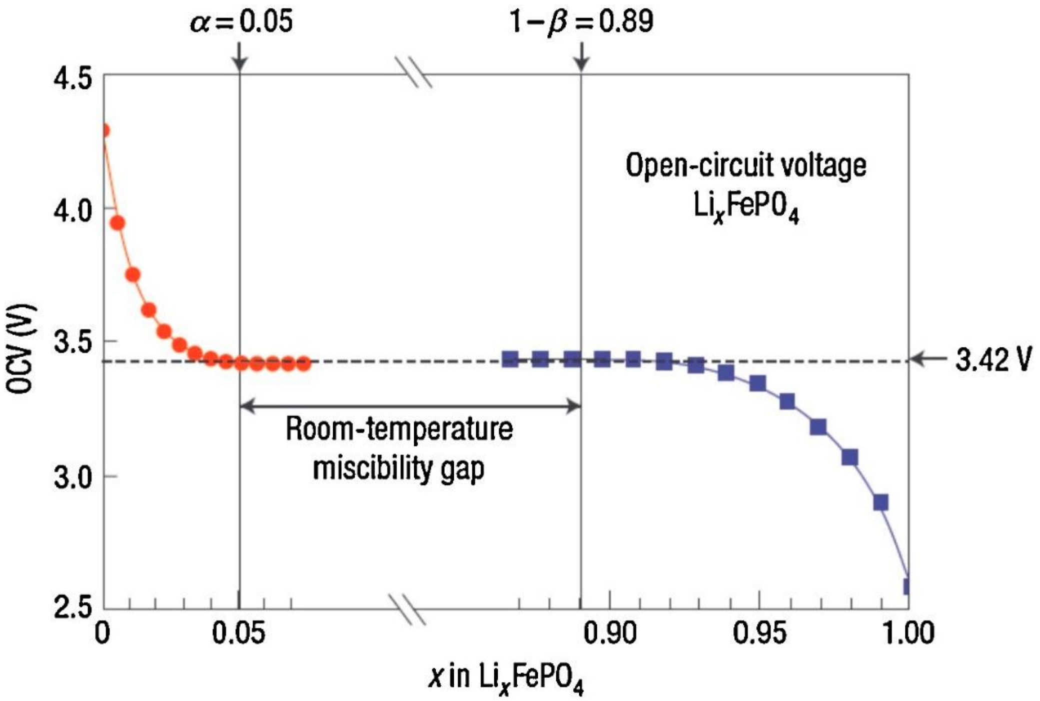

Figure 1.3: Reported open circuit voltage versus x in Li_xFePO_4 at 298 K showing the voltage plateau corresponding to the room-temperature miscibility gap [30].

Even though $LiFePO_4$ possesses some noticeable characteristics of a good cathode material, at room temperature, the electrical conductivity of $LiFePO_4$ is 10^{-10} S.cm^{-1} - extremely low for a cathode material [31]. In the olivine crystal structure of the $LiFePO_4$ cathode, the lightweight Li^+ ions, known as the charge carrier of the battery, are mobile only in the (010) channels [31-33] (Figure 1.2). It means that once the moving direction of Li^+ is blocked, it is very difficult to conduct electricity and the charging or discharging process stops. Hence, $LiFePO_4$ nanoparticles are utilized to reduce the length of Li^+ movement while elemental doping and carbon coating have been utilized for improving electronic conductivity and Li^+ movement in the cathode materials. Particle size of $LiFePO_4$ has significant effect on electrochemical (de)lithiation of the cells [23, 27, 34, 35]. Nevertheless, a high fraction of carbon coating can reduce the volumetric energy density of the cathode materials. While carbon coating enhances electric conductivity on the surface of $LiFePO_4$ particles, doping can efficiently improve the intrinsic electric and ionic conductivity. Doping on the Li-, Fe-, or even O-sites can enhance the electrochemical performance of $LiFePO_4$. Supervalent cations (such as Mg, Zr, Nb, Na, etc.) doping at Li-sites can dramatically increase the electronic conductivity of the battery materials up to eight orders of magnitude [36]. Anion such as F^-, Cl^-, etc. also can be doped at O-site to improve the electrochemical performance. Specifically, metal ion doping can improve effectively the redox potential of Fe^{2+}/Fe^{3+} [37] hence, increase the relatively low working voltage of $LiFePO_4$. The olivine lattice $LiFePO_4$ can accept aliovalent cations with 2+ to 5+ charges [38]. Bivalent cation doping such as Mn^{2+} [16], Ni^{2+} [39], Co^{2+} [40], Cu^{2+} [41] is promising as it is easy, low cost, and it is possible to increase the redox potentials, the electronic conductivity and discharge capacity of doped samples. Among the bivalent doping elements, Mn doping in Fe-sites has been the most attractive doping element since both $LiFePO_4$ and $LiMnPO_4$ belong to the olivine family and their operating voltages are suitable for ensuring the energy density without decomposing the organic electrolyte [42]. Mn-doping can significantly increase the electronic and ionic conductivity of the cathode materials [19, 43-51], consequently improve the rate capability and energy density of the batteries [52-55]. Moreover, in electrochemical experiments using $Li(Mn_yFe_{1-y})PO_4$ as the cathode material, two voltage plateaus were observed in numerous studies [16, 19, 37, 49, 51, 56-62]. The relative widths of the voltage plateaus are closely related to the Mn/Fe ratio [16, 19, 37, 49, 51, 56-62]. Like $LiFePO_4$, the OCV of the Mn-doped-$LiFePO_4$ should be related to the $Li(Mn_yFe_{1-y})PO_4$-$(Mn_yFe_{1-y})PO_4$ phase diagram. Therefore, the knowledge of the $FePO_4$-$LiFePO_4$ and $Li(Mn_yFe_{1-y})PO_4$-$(Mn_yFe_{1-y})PO_4$ phase diagrams is necessary for understanding the phase transformation within the cathode during battery operations and the electrochemical behavior of $LiFePO_4$ and Mn-doped $LiFePO_4$ cathode materials. This thesis presents a consistent thermodynamic model with the input of particle size, coherency from which the $FePO_4$-$LiFePO_4$ and $Li(Mn_yFe_{1-y})PO_4$-$(Mn_yFe_{1-y})PO_4$ phase diagrams can be computed by using CALPHAD (CALculation of PHAse diagrams) approach (details of CALPHAD can be found in Chapter 2).

CHAPTER 2 LITERATURE REVIEW

In this chapter, the important notions related to this work will be reviewed. This work is focusing on $LiFePO_4$ and $Li(Mn_yFe_{1-y})PO_4$ cathode materials for batteries which are considered as electrochemical cells that transform chemical energy into electricity. This review section starts with general concepts of batteries like open-circuit voltage (OCV), overpotential, etc. then the relation of thermodynamic behaviors of $LiFePO_4$ and $Li(Mn_yFe_{1-y})PO_4$ cathodes with battery operation is presented.

2.1 Open circuit voltage (OCV) of $LiFePO_4$||Li electrochemical cell

A battery is a device consisting of one or more electrochemical cells with external connections for powering electrical devices. An electrochemical cell can generate electrical energy from chemical reactions or vice versa, use electrical energy to cause chemical reactions. The chemical reaction related to an electrochemical cell is a redox reaction. The electromotive force of a cell, E_{cell}, is expressed by Nernst equation:

$$E_{cell} = E_{cell}^0 - \frac{RT}{nF}\ln Q \tag{2.1}$$

where R, T, F, Q and n are the gas constant, temperature in Kelvin, Faraday's constant, the reaction quotient ($Q = \frac{[C]^c[D]^d}{[A]^a[D]^d}$ for the reversible reaction aA+bB⇋cC+dD) and the number of moles of electrons transferred by the cell's reaction, respectively. The cell electromotive force at standard conditions, E_{cell}^0, is defined as:

$$E_{cell}^0 = -\frac{RT}{nF}\ln K = -\frac{\Delta G^0}{nF} \tag{2.2}$$

where K is equilibrium constant and ΔG^0 is standard Gibbs free energy of the redox reaction. The battery electromotive force or its full voltage as shown in Equation 2.1, 2.2 is represented as open circuit voltage when the battery is not connected to a circuit or load. When a circuit or load is connected to a battery, the electrode potential differs from the equilibrium potential and the difference of the two potentials is called overpotential. In electrochemistry, overpotential is the potential difference (voltage) between a half-reaction's thermodynamically determined reduction potential and the potential at which the redox event is experimentally observed. Overpotential is directly related to voltage efficiency of a battery. The fundamental relationship between the electrical current of an electrode and the applied electrode potential is shown by Butler-Volmer equation. Butler-Volmer equation is applicable for both anodic and cathodic half-cells.

Specifically, the $LiFePO_4||Li$ electrochemical cell is governed by the $LiFePO_4 \rightleftarrows FePO_4 + Li$ redox reaction. Considering the room temperature open circuit voltage (OCV) of $LiFePO_4||Li$ batteries, the voltage plateau at ~ 3.5 V appears as a noticeable feature of the OCV curves [16-21] (Figure 1.3). The OCV curve is obtained by considering the change of the cell voltage as a result of the change of the difference between the chemical potentials of lithium in lithium metallic anode (Li) and olivine-type lithium phosphate cathode (Li_xFePO_4) during (de)lithiation processes:

$$V(x) = -\frac{\mu_{Li}^{Li_xFePO_4}(x) - \mu_{Li}^{anode}}{nF} = -\frac{\mu_{Li}^{Li_xFePO_4}(x)}{F} \qquad (2.3)$$

In Equation 2.3, the chemical potential of Li in the Li_xFePO_4 cathode, $\mu_{Li}^{Li_xFePO_4}(x)$, is dependent on x while the chemical potential of the metallic Li anode, μ_{Li}^{anode} is zero (in this case, $n = 1$). The chemical potential of Li in the cathode can be calculated from the molar Gibbs energy, G, of the Li_xFePO_4 cathode:

$$\mu_{Li}^{Li_xFePO_4}(x) = -\frac{\partial G(x)}{\partial x} \qquad (2.4)$$

Depending on the phase transformation within the cathode during the lithiation (delithiation) processes and degree of (de)lithiation, $G(x)$ consequently, $V(x)$ and OCV change. The open-circuit voltage (OCV) at low rates of charging and discharging of $LiFePO_4||Li$ batteries depends on the chemical potential of the cathode via equilibrium phase transformation and consequently on the $FePO_4$-$LiFePO_4$ phase diagram [18, 22, 24-27]. The voltage plateau observed in Figure 1.3 occurs due to the coexistence of the $LiFePO_4$ lithiated phase and $FePO_4$ delithiated phases which appears as the room temperature miscibility gap in the $FePO_4$-$LiFePO_4$ phase diagram [26, 28, 29] (Figure 2.1). Therefore, investigation of $FePO_4$-$LiFePO_4$ phase diagram and $LiFePO_4$ thermodynamic behavior is helpful for considering battery charging or discharging processes.

2.2 $FePO_4$-$LiFePO_4$ phase diagram

As investigation of the $FePO_4$-$LiFePO_4$ phase diagram is necessary for understanding the battery operation, the phase equilibria of $FePO_4$-$LiFePO_4$ olivine join have been described by several authors. Both $FePO_4$ and $LiFePO_4$ show small solubility limits at room temperature [26, 28, 29]. Through the experimental data [28, 29] and computational simulation [63] of the binary phase diagram, a high temperature solid solution phase, a eutectoid transition (at ~150-250ºC, x_{Li}~0.4-0.6) separating two miscibility gaps were revealed (Figure 2.1). Although the eutectoid phase diagram of $FePO_4$-$LiFePO_4$ was exposed, there are still some discrepancies among experimental data [28, 29]. Differences in sample preparation and analysis explain these discrepancies. The samples in Dodd et al. [28] were heat treated over longer periods of time hence the equilibrium should be more likely to be obtained.

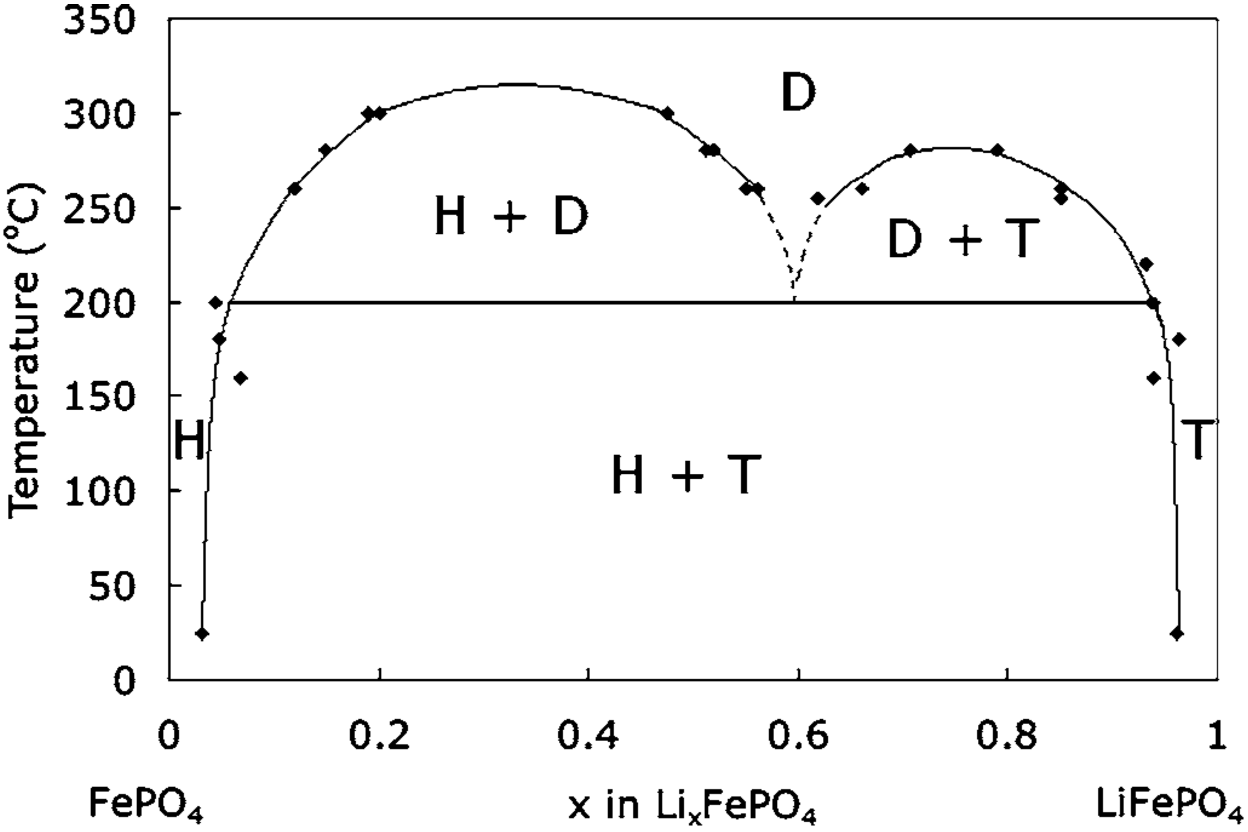

Figure 2.1: Reported experimental $FePO_4$-$LiFePO_4$ phase diagram (T, H, and D stand for triphylite, heterosite, and disordered phase correspondingly) [28].

The calculated phase diagram obtained from first principles simulations performed by Zhou et al. [63] does not represent well the experimental data [28]. Later, Lee [24] presented a thermodynamic model of the $LiFePO_4$-$FePO_4$ phase diagram using CALPHAD (CALculation of PHAse diagrams) approach that reproduced well Dodd et al. [28] experimental data. CALPHAD approach to phase diagram computation is based on: (i) development of Gibbs energy models to describe the thermodynamic properties for various phases which allows scientists to predict the thermodynamic properties of multicomponent phases and systems and calculation of phase equilibria using the Gibbs minimization technique for the system while respecting the elemental balance; (ii) critical evaluation of experimental data in order to optimize Gibbs energy model parameters and combine these parameters into self-consistent databases; (iii) software for optimizing thermodynamic parameters; and (iv) improvement of databases with the aim of enriching the understanding of various industrial and technological processes [64]. In Lee's work [24], the Gibbs energy of Li_xFePO_4 solid solution is effectively described by the Compound Energy Formalism (CEF), a method to treat the solid based on its crystal structure [65, 66]. In CEF, a solid phase is modelled by two or more sub-lattices on which different chemical species mix with variations in composition. The choice of sublattice stoichiometry and the mixing species on each sublattice for a solid phase defines a specific model within the formalism [65]. The structure of a solid phase is represented by a formula, for example $(A, B)_k(D, E, F)_l$ where A and B are mixing on the first sublattice and D, E and F mix on the second sublattice. Note that, the specie like A in a sublattice can represent an atom, a molecule, an ion or a vacancy. A sublattice can contains only one species. If a sublattice has more than one species, all the species belong to it must be different (e.g. $A \neq B$). However, a species can occur in several sublattices, for example $(A, B)_k(A, E, F)_l$. k and l are stoichiometric coefficients and these stoichiometric coefficients are generally noted as $n^{(s)}$ where the superscript defines the sublattice. The constitution of the phase is represented by the site fraction of every specie i in its own sublattice s, $y_i^{(s)}$, and in each sublattice, $\sum_i y_i^{(s)} = 1$. There are 6 end-members belong the $(A, B)_k(D, E, F)_l$ sublattice model, including A_kD_l, B_kD_l, A_kE_l, B_kE_l, A_kF_l, and B_kF_l. The mole fraction of an end-member in the phase is defined as the product of all the site fractions of every species forming the end-member in theirs corresponding sublattice. For instance, the mole fraction of A_kD_l is $y_A^{(1)} \cdot y_D^{(2)}$. The symbol for molar Gibbs energy of an end-member is given by showing the element on each sublattice in the subscripts, e.g. $G_{A:D}$. The molar Gibbs energy of the solid phase is then formulated as follow:

$$G_m^{(A,B)_k(D,E,F)_l} = \sum_i \sum_j y_i^{(1)} y_j^{(2)} G_{i:j} + RT \sum_s \sum_i n^{(s)} y_i^{(s)} \ln y_i^{(s)} + G_m^{ex} \qquad (2.5)$$

In Equation 2.5, and the excess term, G_m^{ex}, can be described with a Redlich-Kister polynomial [67]:

$$G_m^{ex} = \sum_i y_i^{(2)} y_A^{(1)} y_B^{(1)} \sum_m L_{A,B:i}^m \left(y_A^{(1)} - y_B^{(1)} \right)^m \qquad (2.6)$$

In Equation 2.6, all the L are the interaction parameters. CEF models have been used widely to describe thermodynamics of a solid phase. For example, the disordered trigonal-$LiCoO_2$ phase where vacancies and lithium atoms are mixing randomly in the Li planes was modelled as a substitutional solid solution with four sublattices: $(Li,Va)_{1/2}(Li, Va)_{1/2}(Co)_1(O)_2$ (Va denotes a vacancy) [68]. Similar to the $LiCoO_2$ phase, in Lee's work [24], the Li_xFePO_4 solid solutions is modeled by a 4-sublattice CEF model $(Li^+,Va^0)_1(Fe^{2+},Fe^{3+})_1(P^{5+})_1(O^{2-})_4$ which allows the Li^+ ions and Va^0 to mix on M1 sites and Fe^{2+} and Fe^{3+} to mix on M2 sites of the olivine crystal structure. Then, the $LiFePO_4$-$FePO_4$ phase diagram was obtained by minimizing the Gibbs energy of the solid solutions [24] as the global minimum of the Gibbs energy of a multiphase multicomponent system is the necessary and sufficient conditions to achieve equilibrium in the system at constant temperature and pressure [69]. According to the author, the short-range-order (SRO) of mixing ions on different sublattice is introduced in order to reproduce the eutectoid reaction and the split of the miscibility gap into two smaller gaps at the eutectoid temperature [24]. However, a year later, the XRD (X-Ray Diffraction) and SAED (Selected Area Electron Diffraction) examination of the eutectoid composition ($Li_{0.6}FePO_4$) sample annealed at 623.15K revealed the existence of a supercell microstructure which should be corresponding to at least an extra long-range-order (LRO) in the crystal [35] in comparison with what was proposed by Lee [24]. Hence, Lee's model describing only a simple unit cell of olivine-Li_xFePO_4 [24], is insufficient for describing simultaneously the $Li_{0.6}FePO_4$ solid solution with a supercell structure [35] and the $FePO_4$-$LiFePO_4$ phase diagram. Thermodynamic reassessment of the $FePO_4$-$LiFePO_4$ battery join is therefore necessary in order to provide a more accurate understanding of the thermodynamic behavior of the cathode during battery operations.

2.3 Li(Mn_yFe_{1-y})PO_4-(Mn_yFe_{1-y})PO_4 olivine joins

As mentioned in the previous section, the phase transformation within the Mn-doped-$LiFePO_4$ cathode is related to the Li(Mn_yFe_{1-y})PO_4-(Mn_yFe_{1-y})PO_4 phase diagram. It is necessary to first understand its binary sub-systems, $FePO_4$-$LiFePO_4$, $LiFePO_4$-$LiMnPO_4$, $FePO_4$-$MnPO_4$, and $LiMnPO_4$-$MnPO_4$. The $FePO_4$-$LiFePO_4$ system was studied more than the other three binary sub-systems. In the $LiFePO_4$-$LiMnPO_4$ system, the olivine Li(Mn_yFe_{1-y})PO_4 solid solution is very stable according to several studies [56, 70, 71] due to the small lattice distortion as a result of the small ionic radius difference between Fe^{2+} and Mn^{2+} [56]. Similarly, in the $FePO_4$-$MnPO_4$ system, the olivine (Mn_yFe_{1-y})PO_4 solid solution is quite stable in the thermal stability investigation of Kim et al. [72] and the first principles calculation of Snydacker & Wolverton [71]. The decomposition temperature of the (Mn_yFe_{1-y})PO_4 solid solution decreases generally as the manganese content increases [72]. ($Mn_{0.8}Fe_{0.2}$)PO_4 was reported to start decomposing at 523 K [73] while another study showed the thermal stability of (Mn_yFe_{1-y})PO_4 at up to 673 K with $y < 0.9$ [74]. Olivine $MnPO_4$ and (Mn_yFe_{1-y})PO_4 with high manganese contents were claimed to be unstable [56, 75, 76] due to the induced large anisotropic distortion caused by the electron $3d^4$ of the ion Mn^{3+}-lattice interaction [56]. Olivine-$MnPO_4$ can decompose into $Mn_2P_2O_7$ and O_2 gas at a temperature as low as 483 K [76]. The product of the decomposition of $MnPO_4$ can be $Mn_2P_2O_7$ or $Mn_3(PO_4)_2$ in the temperature range of 473 K to 523 K [77]. Choi et al. [78] reported that $MnPO_4$ undergoes amorphization above 453 K in agreement with the later reported existence of an amorphous phase above 473 K [72, 79]. Only Aurbach's group showed that $MnPO_4$ is as stable as $FePO_4$ [80]. Huang et al. [75] claimed that $MnPO_4$ can absorb water easily and change its crystal structure. Carbon coating plays an important role in the stability of $MnPO_4$ since only a small amount of carbon can prevent the amorphization of the olivine and keep it stable at up to 573 K [75]. So far, according to our knowledge, the only way to produce metastable olivine-$MnPO_4$ under ambient conditions is to delithiate olivine-$LiMnPO_4$ [81]. Like $LiFePO_4$, $LiMnPO_4$ is stable due to its strong P-O covalent bonding [16, 79, 82-84] and it can be used as a cathode material [81, 84-87]. $LiMnPO_4$||Li batteries have a similar theoretical capacity of 170 mAh/g, a energy density and a higher voltage plateau due to the higher Mn^{3+}/Mn^{2+} redox potential (~4.1 V versus Li/Li^{+}) [16, 84, 88-90] but a poorer rate capability [91] because of its low ionic and electrical conductivity [92, 93] in comparison with $LiFePO_4$ batteries. The poor Li^{+} intercalation/deintercalation kinetics within the olivine cathode is a result of the severe Jahn-Teller (JT) distortion caused by large Mn^{3+} ions [84, 88, 94] and the mismatched interface of $MnPO_4/LiMnPO_4$ [88, 89, 95, 96]. The two-phase coexistence resulting in a voltage plateau of ~4.1 V is commonly found in the OCV profiles of $LiMnPO_4$ batteries [19, 85, 86, 89, 97] (Figure 2.2). The voltage plateau exists even at high temperatures, e.g. 328 K [89]. Considering the $LiMnPO_4$-$MnPO_4$ phase diagram, similar to the case of $LiFePO_4$ batteries, the room temperature voltage plateau appearing in OCV should be corresponding to a miscibility gap at room temperature. In agreement with the electrochemical work [85, 86, 89, 97], Kim et al. [76] reported the two-phase stable regions at up to 473 K, the temperature at which $MnPO_4$ starts to decompose. Chen & Richardson [98] stated that after chemically removing lithium from olivine-$LiMnPO_4$, the two phases $LiMnPO_4$ and $Li_{\alpha}MnPO_4$ (α is small and $\alpha < 1$), not $MnPO_4$, coexist. The value of α is dependent on the extent of delithiation and on the crystalline domain size [98].

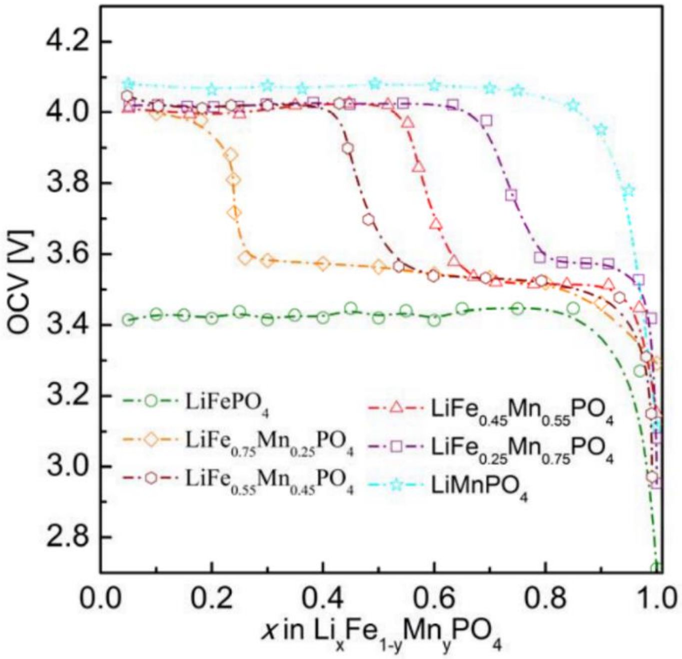

Figure 2.2: OCV for $Li(Mn_yFe_{1-y})PO_4||Li$ cells (y = 0, 0.25, 0.45, 0.55, and 1) [58].

Unlike $LiFePO_4$ and $LiMnPO_4$ batteries, not one but two voltage regions corresponding to the two redox reactions (Mn^{3+}/Mn^{2+}) and (Fe^{3+}/Fe^{2+}) were observed in the batteries with the olivine $Li(Mn_yFe_{1-y})PO_4$ cathodes (Figure 2.2) [16, 19, 37, 49, 51, 56-62]. Notice that the voltage regions are slightly change with Mn content (Figure 2.2). The shift of redox potentials is also noted in other studies [16, 37, 46, 62]. So far, papers are focusing on Li^+ mobility during the charging/discharging of the batteries without mentioning the mobility of iron or manganese ions. In practice, the small Li^+ ions are much more mobile than Mn^{2+} and Fe^{2+} ions in the olivine structure. Therefore, during the charge/discharge processes, the gradient concentration of lithium can be observed while the concentration ratio Mn/Fe apparently remains unchanged. Hence, the phase transformation within $Li(Mn_yFe_{1-y})PO_4$ cathodes can be considered as the phase transformation of a *para-equilibrium* system in which the ratio of Fe and Mn of all the existing phases remains constant. The phase para-equilibria of the $Li(Mn_yFe_{1-y})PO_4$-$(Mn_yFe_{1-y})PO_4$ system is actually reported in Yamada et al. [42] (Figure 2.3) even though the authors did not claim that their results are related to para-equilibrium. Yamada et al. [42] reported the phases present in the chemically prepared $Li_x(Mn_yFe_{1-y})PO_4$ samples through the results of XRD, Mossbauer spectroscopy, and X-ray absorption spectroscopy (XAS) analyses. By oxidizing the prepared olivine $Li(Mn_yFe_{1-y})PO_4$ ($y = 0.2;\ 0.4; 0.6;\ 0.8; 1.0$) samples, $(Mn_yFe_{1-y})PO_4$ formed and the reaction between $(Mn_yFe_{1-y})PO_4$ with various amounts of LiI in acetonitrile resulted in a lithiated phase $Li_x(Mn_yFe_{1-y})PO_4$ ($0 < x < 1$) [42]. It means that the lithiated phases were prepared without changing the Mn/Fe content ratio of the olivine phases during the synthesis. Therefore, the reported two-dimensional phase diagram at 298 K (Figure 2.3) [42] should be stated as the para-equilibrium $Li(Mn_yFe_{1-y})PO_4$-$(Mn_yFe_{1-y})PO_4$ phase diagram. The authors reported an unstable region of rich manganese-$(Mn_yFe_{1-y})PO_4$ ($y \geq 0.8$) [42]. In the lower manganese side of the para-equilibrium phase diagram (Figure 2.3), two distinguished regions are identified containing (i) the two-phase Mn^{3+}/Mn^{2+} redox region ($y \geq x$) and (ii) the Fe^{3+}/Fe^{2+} redox region ($y \leq x$) . The Fe^{3+}/Fe^{2+} redox region is formed by a single-phase and a two-phase regions [42]. In agreement with the experimental work of Yamada et al. [42], Malik et al. [62] showed the separation of the phase diagram into low-temperature miscibility gaps corresponding to two Fe^{2+}/Fe^{3+} and Mn^{2+}/Mn^{3+}redox reactions (Figure 2.4). The miscibility gaps were separated by a solid solution phase centered at $Li_{\sim y}(Mn_yFe_{1-y})PO_4$, at which most Fe ions were oxidized to Fe^{3+} and most Mn ions were still present as Mn^{2+}. The thermal stability of the partially delithiated

$Li_x(Mn_yFe_{1-y})PO_4$ ($0 \leq x, y \leq 1$) sample is dependent on its Fe/Mn content ratio. The higher the manganese content of the sample, the lower its thermal stability [72]. In summary, the two phase diagram regions associated with the two redox reactions and the two regions in OCV profiles of $Li(Mn_yFe_{1-y})PO_4$ batteries have been shown in a few available studies on the $Li(Mn_yFe_{1-y})PO_4$-$(Mn_yFe_{1-y})PO_4$ phase diagram.

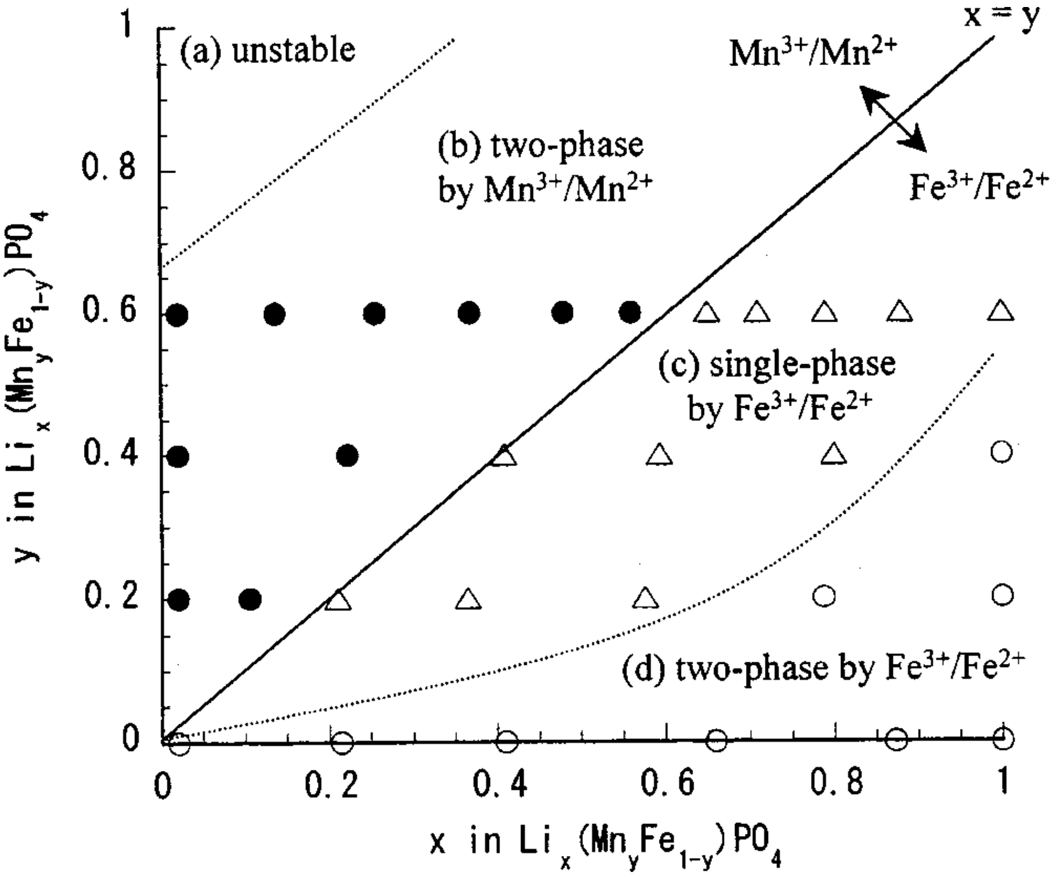

Figure 2.3: The (x, y) two-dimensional experimental phase diagram of the $Li_x(Mn_yFe_{1-y})PO_4$ ($0 \leq x, y \leq 1$) system obtained using XRD and Mössbauer spectroscopy. The map is divided into four areas: (a) the unstable region close to the point (x, y) = (0, 1); (b) the two-phase region by Mn^{3+}/Mn^{2+} (closed circles; $y \geq x$); (d) the two-phase region by Fe^{3+}/Fe^{2+} (open circles; a part of $y \geq x$); and (c) the single-phase region by Fe^{3+}/Fe^{2+} connecting (b) and (d) (open triangles) [42].

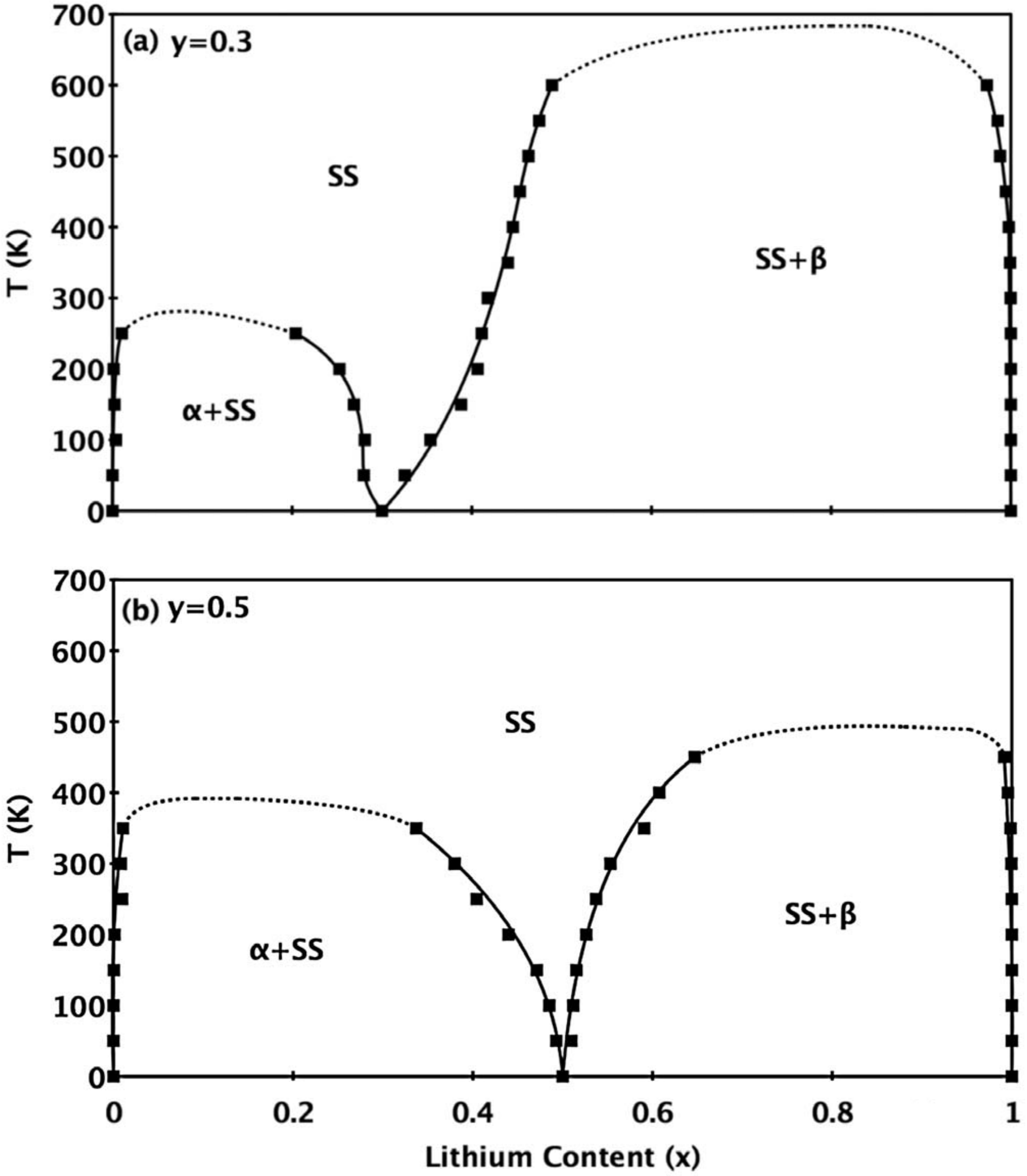

Figure 2.4: DFT based calculated isopleths of $Li_x(Mn_yFe_{1-y})PO_4$ for (a) y = 0.3, (b) y = 0.5. Dash line is speculative. Mn is substituted in Fe site only, Mn^{3+}/Mn^{2+} and Fe^{3+}/Fe^{2+} redox couples are corresponding to the voltage plateaus and only Li^+ is mobile [62].

A thermodynamic description of a system should not only describe well its phase diagram but also include its thermodynamic properties such as enthalpy of formation, Gibbs energy of formation, enthalpy of mixing, etc. Among the olivines utilized as cathodes, $LiFePO_4$ was studied the most. Its heat capacity was measured experimentally in the range of 2 to 773 K [99, 100]. The heat capacity of $LiFePO_4$ as a function of temperature was predicted in Seifitokaldani et al. [101] by combining Density functional theory (DFT) to a self-consistent method based on quasi-harmonic approximation (QHA) and a minimization procedure ensuring the respect of the Maxwell relations [102, 103]. Result of Seifitokaldani et al. [101] are consistent with reported experimental measurements [99, 100]. For $FePO_4$, only the measurement of isobaric heat capacity of $FePO_4$ from 2 to 300 K done by Shi et al. [104] has been found in the literature. Their experimental data reveals the transition from antiferromagnetic to paramagnetic at ~25 K [104]. In fact, they used α-$FePO_4$ or berlinite-$FePO_4$ with the Neel temperature of $T_N = 25\ K$ [104-107] in their experiments. The Neel temperature of the olivine-$FePO_4$ is higher ($T_N \cong 125\ K$) [108-110]. Like olivine-$FePO_4$, no study on the heat capacity of olivine $MnPO_4$ and $LiMnPO_4$ has been reported. On the other hand, the enthalpy and Gibbs energy of formation of all the olivine $LiFePO_4$, $FePO_4$, $MnPO_4$ and $LiMnPO_4$ compounds are summarized in the first principles simulations of Xie et al. [25]. The reported values of enthalpy of formation of $LiFePO_4$ and $FePO_4$ [25] are slightly more negative than the ones obtained by Iyer et al. [111] at room temperature through DSC measurements. The Gibbs energy of formation of $LiFePO_4$ at room temperature shown in He et al. [112] is slightly less negative than the one estimated in Xie et al. study [25]. Only Churikov et al. [113] showed the entropy of $LiFePO_4$ and $FePO_4$ at room temperature.

After considering the thermodynamic properties of olivine compounds, it is worth to review the current thermodynamic knowledge of sub binary systems. The binary $FePO_4$-$LiFePO_4$ system is studied the most among all the olivine battery joins. The enthalpy of mixing measured for a $Li_{0.47}FePO_4$ sample was estimated to be 0.50 kJ/mol with a peak temperature of 497 K upon heating and 0.70 kJ/mol with a peak at 409 K upon cooling for a Differential Scanning Calorimetry (DSC) scanning rate of 5 K/min [28]. According to the authors, the value of enthalpy of mixing should be higher with a lower scanning rate [28]. According to the DSC measurements of Stevens et al. [114], the enthalpy of disordering of $Li_{0.6}FePO_4$ is 1.40±0.30 kJ/mol. As stated by the authors [114], this value is too small as the transformation from the two-phase to disordered state is sluggish and incomplete by 593 K and only 55% of the sample was transformed. Assuming that the enthalpy needed to disorder 1% of the sample is unchanged, then the estimated enthalpy of transition is approximately 2.55±0.55 kJ/mol [114]. The measured enthalpy of mixing at the eutectoid point $Li_{0.6}FePO_4$ [114] is significantly higher than the one estimated by Zhou et al. [63] through DFT. This value [114] is much lower than the value that used by Lee in his study (~9.2 kJ/mol) [24]. Lee reported enthalpy of mixing data predicted by Monte Carlo simulations at 0 K with a maximum value of ~10 kJ/mol without giving any detailed information on his simulations [24]. Unlike the $FePO_4$-$LiFePO_4$ system, so far, there has not been any study reporting the enthalpy of mixing of the other binary systems, $MnPO_4$-$LiMnPO_4$, $FePO_4$-$MnPO_4$, and $LiFePO_4$-$LiMnPO_4$. The enthalpy of mixing of a binary solid phase can be calculated if the enthalpy of formation of the solid solution at various composition is known. The enthalpy of formation and then enthalpy of mixing of solid solution can be calculated by Density functional theory (DFT), a computational quantum mechanical modelling method. DFT simulations are performed under periodic boundary conditions based on plane-wave basis sets [115-118]. Unlike DFT simulations of metallic systems [119], in the $LiFePO_4$ olivine cathode, electrons involved in the ionization of lithium are the metallic valence electrons while electrons related to the oxidation change of Fe or Mn ions belong to the MO_6 octahedrons of the olivine crystal structure. Therefore, in order to improve the accuracy of the predicted electronic ground state properties of the Li_xFePO_4 solid solution in the DFT simulations, GGA+U should be considered [120].

In summary, even though the reported thermodynamic CEF model of Lee [24] represents well the experimental data [28, 29], it is insufficient to describe the supercell microstructure of the $Li_{0.6}FePO_4$ solid solution [35] and to reproduce the experimentally reported enthalpy of mixing [28, 114]. No thermodynamic model describing the stable olivine $(Mn_yFe_{1-y})PO_4$ and $Li(Mn_yFe_{1-y})PO_4$ solid solution and coexistence of two phases $LiMnPO_4$ and $MnPO_4$ was reported. Unstable olivine-$MnPO_4$ was noticed in the literature. The concerned para-equilibrium $Li(Mn_yFe_{1-y})PO_4$-$(Mn_yFe_{1-y})PO_4$ phase diagram reveals the separation of the phase diagram by the two Fe^{3+}/Fe^{2+} and Mn^{3+}/Mn^{2+} redox reactions [42, 62], corresponding to the two voltage regions observed in the OCV profiles [16, 19, 37, 49, 51, 56-62]. However, there is lack of knowledge on thermodynamic properties of olivine compounds and enthalpy of mixing of olivine binary sub-systems.

2.4 The importance of particle size of $LiFePO_4$ cathodes

Since both $LiFePO_4$ and $FePO_4$ possess an olivine structure, it seems that Li^+ can be transferred during charge/discharge operations without spending any energy on forming a new microstructure. Consequently, the cyclability and high-rate-performance can be improved. However, bulk $LiFePO_4$ is suitable for low-rate applications only. For high-rate applications, nano-$LiFePO_4$ is utilized. It means that the electrochemical properties of $LiFePO_4$ are dependent on particle size. Examining the $FePO_4$-$LiFePO_4$ phase diagram, some authors found a systematic shrinkage of the miscibility gaps with the decrease of particle size [23, 27, 34, 35]. The changes in solubility limits of the two olivine phases due to the particle size effect were noticed for both chemically and electrochemically delithiated experiments [23, 27, 34]. When the particle size is smaller than a critical size (~20 nm [23, 34] or ~10 nm [121]), the miscibility gaps disappear. According to Meethong et al. [23], the particle size effect can be explained by: (i) the increase caused by the relative contribution of particle-matrix surface energy and surface stress and (ii) the coherent stresses in two-phase particles with a coherent interface. Since micro-sized or nano-sized particles are commonly used for the electrochemical applications of olivine $LiFePO_4$, it is essential to investigate the particle size effect on the miscibility gap shrinkage. Since the role of particle size effect on $Li(Mn_yFe_{1-y})PO_4$ cathode has not been reported in the literature, it is out of concern of this study.

There has no thermodynamic model introducing particle size effect for $LiFePO_4$ - $FePO_4$ system has been ever reported. However, there exist studies which treat the particle size effect on metallic systems [122-126]. The change of miscibility gaps with particle size can be modeled by the dependence of the molar Gibbs free energy of the solid solution phase on the particle size. The thermodynamic assessment for the size-dependent phase diagram of a binary A-B system was approached and developed by Lee's group [122-124]. This model was later utilized in studies of Garzel et al. [125], Ghasemi et al. [126], etc. In order to examine the particle size effect, the surface energy contribution to Gibbs energy of the phases is considered in Lee's model [122-124]. The chemical potential of component *i* in a nanoparticle system is expressed by the following equation:

$$\mu_i^{NP} = \mu_i^{bulk} + \frac{2\sigma V_i}{r} \tag{2.7}$$

where μ_i^{NP} and μ_i^{bulk} are chemical potentials of i in nanoparticles and in bulk respectively; σ is the surface (or interface) tension; V_i is molar volume of i; and r is the radius of nanoparticles. Consequently, the total Gibbs free energy of a binary alloy A-B nanoparticle is given by:

$$\begin{aligned} G^{total} &= G^{bulk} + G^{surface} \\ &= \left[X_A G_A^{bulk} + X_B G_B^{bulk} + RT(X_A \ln X_A + X_B \ln X_B)\right] \\ &+ \left[X_A \frac{2\sigma_A V_A}{r} + X_B \frac{2\sigma_B V_B}{r} + G^{ex,nano}\right] \end{aligned} \quad (2.8)$$

where G^{total} is the molar Gibbs energy of the nanoparticle A-B solid solution; G^{bulk} and $G^{surface}$ are the molar Gibbs energies of the bulk and the surface phase of the system, respectively; $G^{ex,nano}$ is the excess surface energy. As shown in the Equation 2.7, 2.8, the surface energy contribution is only significant for small particles. In Lee's model [122-124], the surface energy is not only dependent on particle size but also a function of surface energy and particle shape. This model is formulated based on spherical particles (Equation 2.7, 2.8). However, it can be used for other particle shapes as a correction factor representing the shape effect is introduced in Equation 2.7, 2.8 [122-124]. It is possible to implement Lee's model in describing the particle size dependent $LiFePO_4$-$FePO_4$ phase diagram. Note that olivine Li_xFePO_4 is anisotropic, so the particles are likely non spherical.

2.5 Coherent phase transformation in $LiFePO_4$ and $Li(Mn_yFe_{1-y})PO_4$ cathodes

Although the reduction of particle size can reduce the Li^+ diffusion path, it is not enough to explain the high rate capability of $LiFePO_4$. Several mechanistic models of (de)lithiation describing the phase transformation in $LiFePO_4$ were proposed (Figure 2.5). As Li diffusion and $LiFePO_4$ are anisotropic [127], the isotropic core shell model [16, 26] (Figure 2.5a) and the mosaic model [128] (Figure 2.5b) are energetically and kinetically unfavorable. The domino-cascade model [129] (Figure 2.5c) can be used to explain the experimental observation of fully lithiated or delithiated phases at any (dis)charged states [129, 130]. In the domino-cascade model, the phase boundaries perpendicular to the (010) direction are claimed to move extremely fast in comparison with the nucleation rate, so the Li_xFePO_4 particle should be either fully lithiated or delithiated [129]. The spinodal decomposition process, which is an unmixing process, i.e. phase separation, taking place in a thermodynamically unstable solid solution, was also reported [18, 131-133] (Figure 2.5d). Later, the solid solution mechanistic model (Figure 2.5e) was suggested since it avoids nucleation and growth and allows a rapid (de)lithiation [20]. Both two-phase and a dual-phase solid solution mechanistic mechanisms were reported to simultaneously occur in the phase transformation of the $LiFePO_4$ cathode [21]. The reported mechanistic models are helpful in explaining the anisotropy of olivine structures, the movement of Li^+ ions in its preferred diffusion channels, and the rapid (discharge) capacity of batteries.

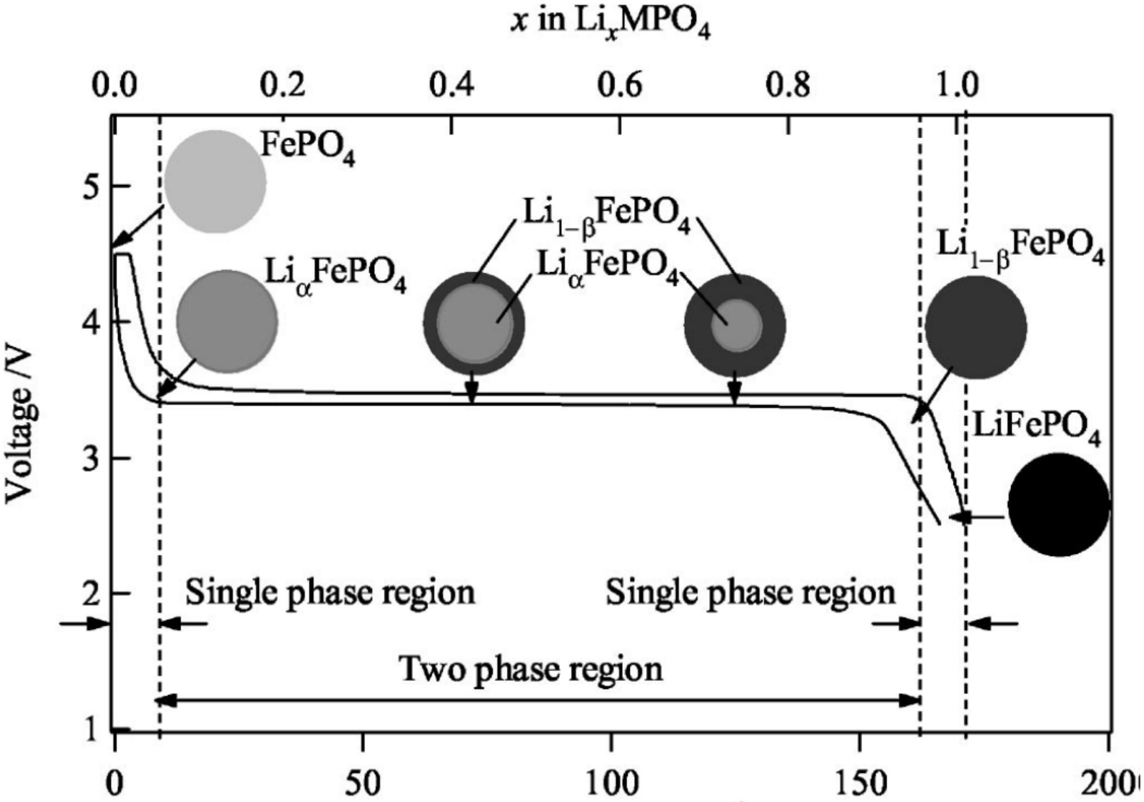

(a)

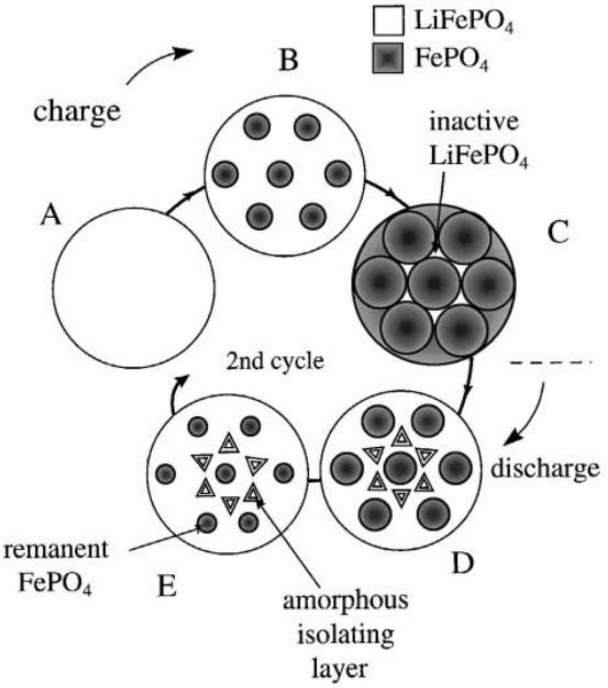
□ LiFePO4
▨ FePO4
charge
B
A
inactive
LiFePO4
C
2nd cycle
discharge
remanent
FePO4
E
D
amorphous
isolating
layer

(b)

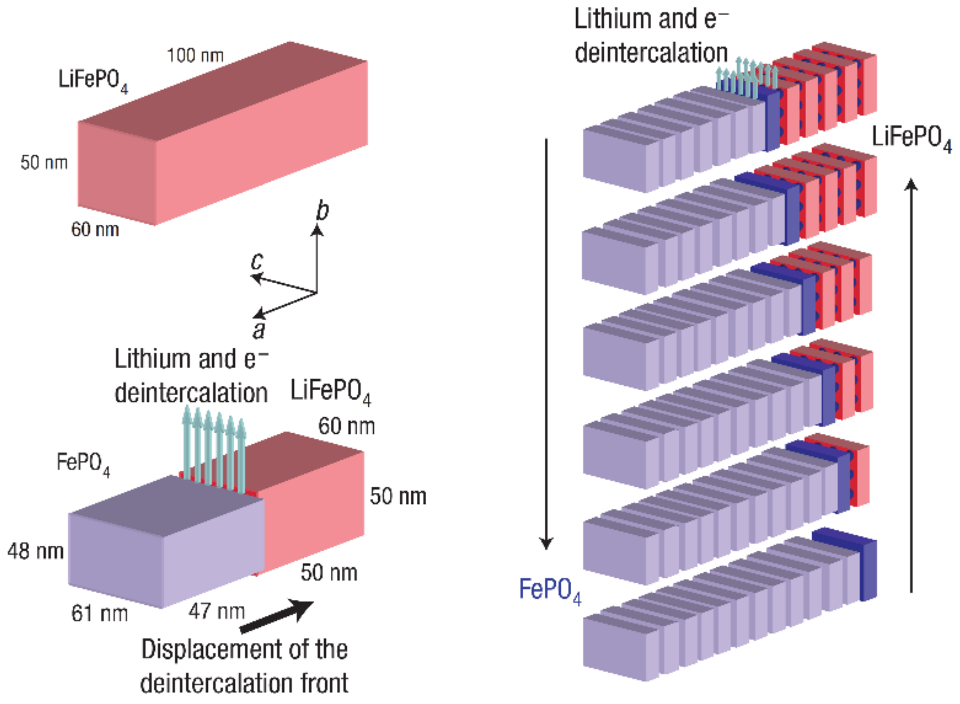
LiFePO4
100 nm
50 nm
60 nm
b
c
a
Lithium and e−
deintercalation
LiFePO4
60 nm
FePO4
50 nm
48 nm
50 nm
61 nm
47 nm
Displacement of the
deintercalation front
Lithium and e−
deintercalation
LiFePO4
FePO4

(c)

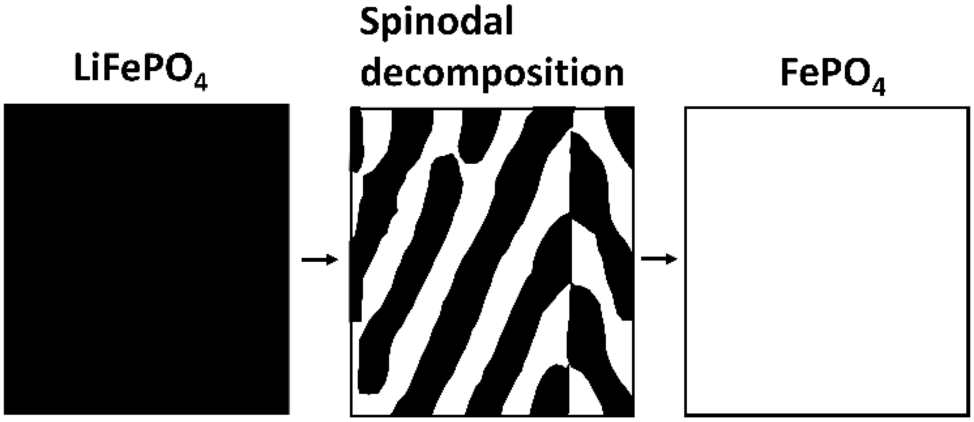

(d)

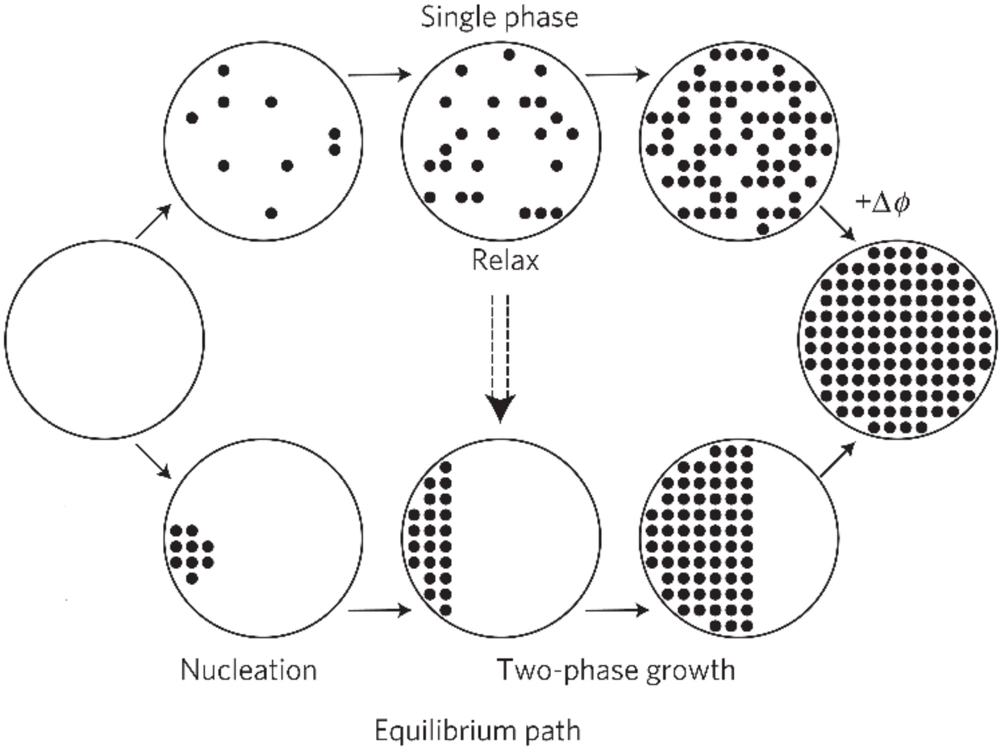

(e)

Figure 2.5: Several phase transformation mechanistic models for LiFePO$_4$ suggested in the literature: (a) core shell model [26]; (b) mosaic model [128]; (c) domino-cascade model [129]; (d) spinodal decomposition model (generated by using the simulated microstructure of Ichitsubo et al. [18]); (e) solid solution model [20].

However, these mechanistic models do not involve any elastic constraints which were observed experimentally [127, 134-136]. Meethong et al. [23, 127] claimed coherent strains in two-phase particles during the charge/discharge processes. Coherent strain occurs in the region of a coherent interface which is observed when the two crystals match perfectly at the interface and the two lattices are continuous across that interface (Figure 2.6). Coherent interface can only achieve if the interfacial plane has the same atomic configuration in both phases [137]. Therefore, it is important to consider the crystals are coherent at which specific crystallographic plane. When the lattice parameters of the two crystals in the coherent interface are not identical, coherency is maintained by straining one or both two lattices in the region near the interface (Figure 2.6) [138, 139]. As the differences of lattice parameters of the two crystals (known as lattice mismatch or lattice misfit) increase, the internal strain energy can become too large for the crystal to hold the coherency, energy relaxation in form of dislocations, cracks can be resulted consequently [134]. Meethong et al. [23, 127] were reasonable for suggesting coherent interface of $LiFePO_4/FePO_4$ during electrochemical (de)lithiation since both phases have the same olivine structure with similar lattice parameters which is the necessary condition for forming a coherent interface. In their electrochemical experiments, Meethong et al. [127] observed the largest strain in the sample with the smallest particle size. According to their investigation, this phenomenon is due to the smallest misfits between the lattice parameters and unit cell volume of $LiFePO_4$ and $FePO_4$ phases [127]. Coherent nucleation and growth within $LiFePO_4$ cathode are also supported by observing the cathode during battery operations [129, 140]. Coherent strains exist in the aligned phase boundaries and striped morphologies of Li_xFePO_4 [134-136]. The (100) phase boundaries were favorable [127, 134, 141] as they allow Li^+ ions to move in its preferred (010) direction [32, 33]. Wang et al. [142] showed that the $LiFePO_4/FePO_4$ interface moves only along certain preferential sites. As the coherent strains along the phase boundary becomes large, energy relaxation is resulted [134]. Cracks and dislocations are found during electrochemical Li insertion and deinsertion [143-147]. The coherent strains can be also reduced by reducing the lattice mismatches between the coherent phases. The observed metastable phase was claimed to reduce the lattice misfits between the lithiated and delithiated phases [148-151]. Therefore, the coherent phase transformation needs to be studied for explaining the existence of the elastic strains between $LiFePO_4$ and $FePO_4$ phases [127, 134-136], the preferential interfacial planes [127, 135, 136, 141, 144], the dislocations and cracks [142, 144-147] and the metastable phase [148-151] during charging or discharging processes. Cogswell and Bazant [144] reported that the coherent strain can make the solid solution stable above 423.15 K. However, their fully anisotropic analysis indicates (101) as the low-energy direction and they explained the observed (100) phase boundaries as a partial loss of coherency caused by dislocations or cracks [144]. The theoretical investigation of Cogswell and Bazant [144] was unsuccessful in describing the reported eutectoid reaction [28, 29, 63] and the existence of the metastable phase [148-151]. In addition, like for $LiFePO_4$, coherence should play an important role in the phase transformation of the Mn-doped-$LiFePO_4$ during charge/discharge. So far, only Ravnsbæk et al. [152] suggested the coherent phase transformation of $Li(Mn_{0.4}Fe_{0.6})PO_4$ cathode material via charging/discharging.

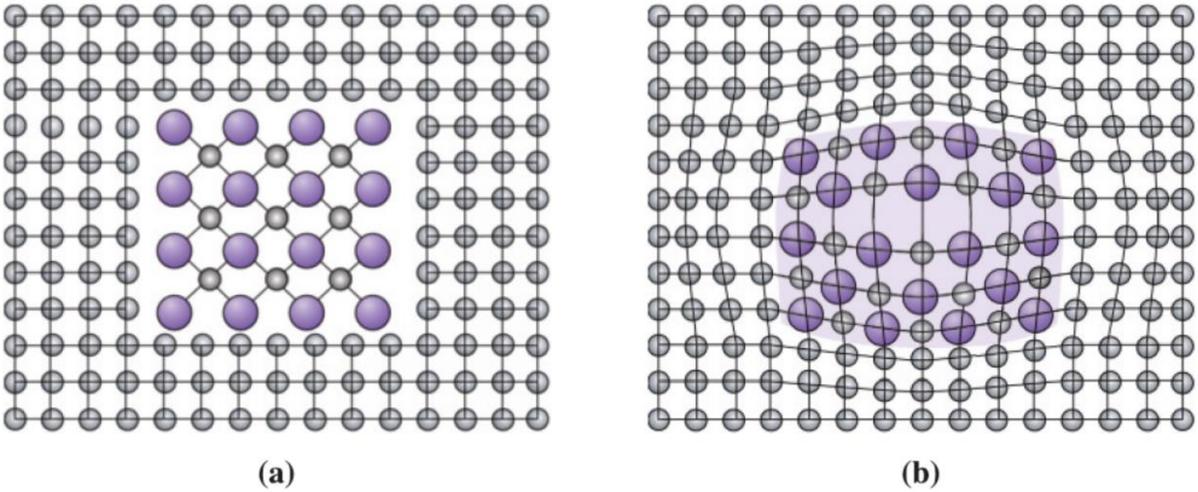

Figure 2.6: (a) A noncoherent precipitate and (b) a coherent precipitate [139].

2.6 Calculation of coherent spinodal decomposition and coherent miscibility gaps

As the importance of the coherent phase transformation in $LiFePO_4$ and $Li(Mn_yFe_{1-y})PO_4$ cathodes was revealed in the previous section, coherency should be taken into account while developing thermodynamic models for $FePO_4$-$LiFePO_4$ and $Li(Mn_yFe_{1-y})PO_4$-$(Mn_yFe_{1-y})PO_4$ olivine joins.

Coherent decomposition of a solid solution is obtained when a fully coherent interphase boundary between the two decomposed phases is achieved for most of or the entire interphase boundary area [138]. In an heterogeneous incoherent equilibrium miscibility gap, depending on the constitution of the system in combination with the lattice parameter relations between the two immiscible phases, coherent miscibility gaps can be distinguished [153] (Figure 2.7a). The storage strain energy exists near coherent interfaces of the two phases of the coherent miscibility gaps. The elastic strain energy contribution increases the Gibbs energy of the solid solution and narrows the equilibrium gaps in order to maintain the coherency relationship (Figure 2.7b). Hence, estimation of strain energy stored in the coherent interfaces is critical in developing thermodynamic models for coherent miscibility gaps.

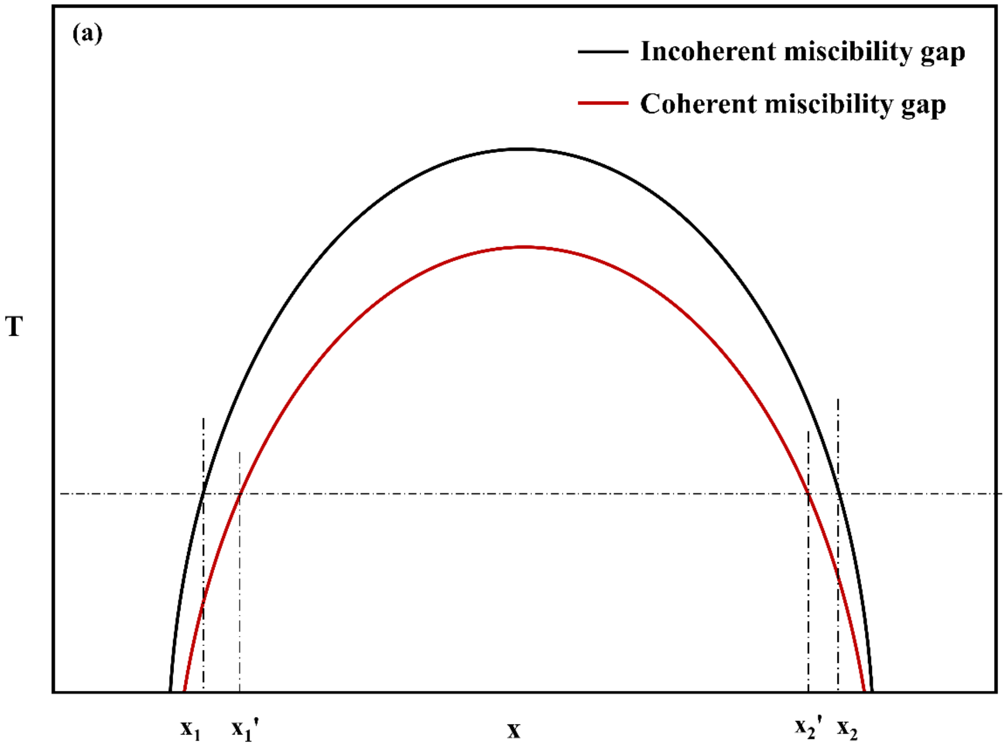

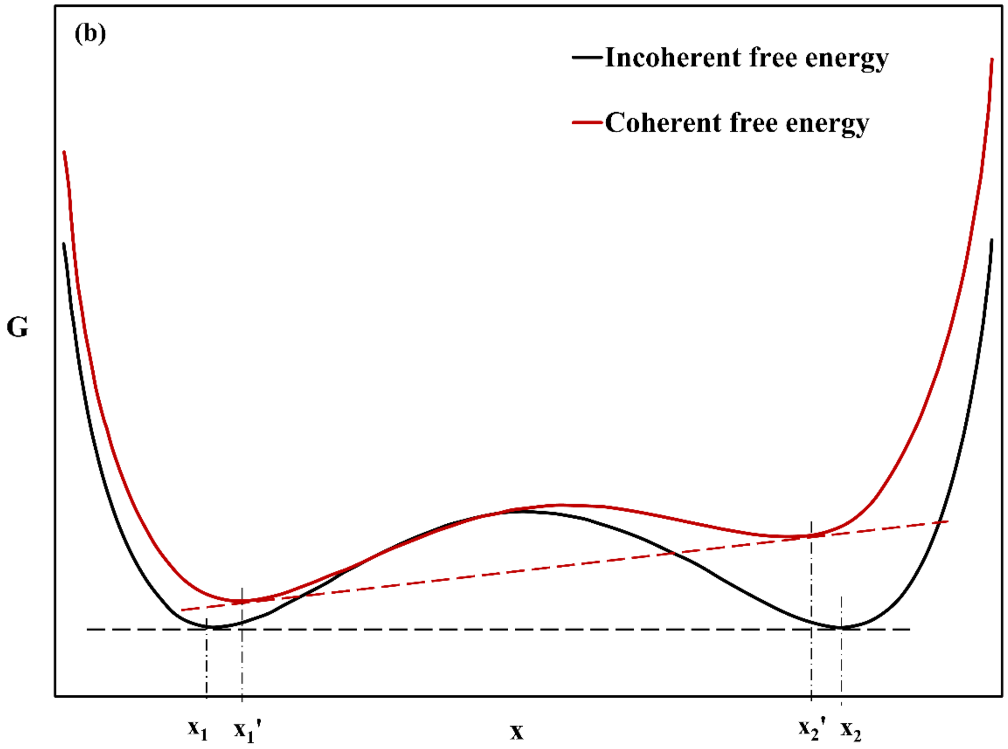

Figure 2.7: Schematic of (a) incoherent and coherent miscibility gaps and (b) the corresponding Gibbs free energy curve for incoherent and coherent miscibility gaps at a specific temperature T.

Coherent phase transformation draws attention mostly for metallic systems with cubic crystalline structures. Therefore, Cahn's group developed their method to calculate coherent miscibility gaps for isotropic systems [154-156]. In Cahn's approach, the coherent spinodal decomposition is treated, then the coherent miscibility gap can be estimated consequently. A sinusoidal plane wave fluctuation in an infinite defect-free cubic crystal was examined. The incoherent spinodal decomposition is stable when $\frac{\partial^2 G^{incoherent}}{\partial x^2} \geq 0$. Hence, the coherent spinodal decomposition is stable when $\frac{\partial^2 (G^{incoherent} + G^{elastic})}{\partial x^2} \geq 0$. The fluctuation of composition of the solid solution results the fluctuation of lattice parameters. The coordinate system was chosen in order to make the lattice changes stay along the z-axis. The only nonzero component of strain is ε_{zz}^{T}. The elastic energy is estimated based on the stress-strain relations and the coordinated system is then rotated to coincide with the cube axes of the crystalline. The elastic energy density is minimized with respect to the value of ε_{zz}^{T}. The limit of coherent spinodal decomposition determined by Cahn's approach is expressed as follow:

$$\frac{\partial^2 G^{incoherent}}{\partial x^2} + 2\eta^2 Y V_m = 0 \tag{2.9}$$

where $\eta = \frac{1}{a}\frac{da}{dx}$ is the linear change in lattice parameter a of the solid solution phase at the investigated overall composition x per unit composition change; V_m is the molar volume; Y is the elastic constant of the elastically soft direction. Cahn showed the expressions of Y for (100) and (111) soft direction:

$$\begin{gathered} Y_{100} = \frac{(C_{11} + 2C_{12})(C_{11} - C_{12})}{C_{11}} \\ Y_{111} = \frac{6(C_{11} + 2C_{12})C_{44}}{4C_{44} + C_{11} + 2C_{12}} \end{gathered} \tag{2.10}$$

where C_{11}, C_{12}, and C_{44} are elastic constants. Cahn's approach has shown the dependence of elastic energy stored in coherent boundaries on lattice mismatch, stiffness of materials, and habit planes [154-156].

Cahn's approach was extended to calculate the coherent miscibility gaps of TiO_2-SnO_2 tetragonal system [157-159]. Although coherent phase transformation of any orthorhombic systems has not been modelled in the literatures, it is possible to extend Cahn's approach for orthorhombic systems. It means that Cahn's model can possibly be used to calculate coherent miscibility gaps of $LiFePO_4$-$FePO_4$ and $Li(Mn_yFe_{1-y})PO_4$-$(Mn_yFe_{1-y})PO_4$ systems. It must be noticed that Cahn's approach is suitable for isotropic systems in which the linear dependence of Cauchy's strain on Cauchy's stress is ensured in every direction. The linear Cauchy's stress and strain relationship may still be valid in the $LiFePO_4$-$FePO_4$ system with ~5% lattice mismatch. However, it will be violated for large deformations like the one obtained in the coherent phase boundaries of $Li(Mn_yFe_{1-y})PO_4/(Mn_yFe_{1-y})PO_4$ where the lattice mismatch is relatively large ranging from ~5% on the $LiFePO_4$-$FePO_4$ side up to ~8% on the $LiMnPO_4$-$MnPO_4$ side. It means that even if Cahn's approach is successfully extended for calculating coherent miscibility gap of orthorhombic systems, it will not be suitable for $LiFePO_4$-$FePO_4$ system but not yet applicable for $Li(Mn_yFe_{1-y})PO_4$/$(Mn_yFe_{1-y})PO_4$ systems.

To sum up, developing thermodynamic models describing the equilibrium and coherent $FePO_4$-$LiFePO_4$ phase diagram is essential in understanding the phase transformation during electrochemical processes. Particle size effect in this system also captures my interest. Furthermore, investigating the phase para-equilibria and coherent phase transformation in the $Li(Mn_yFe_{1-y})PO_4$ cathode is important in order to justify the effect of the Mn-doping.

CHAPTER 3 ORGANIZATION OF THE THESIS

As the importance of understanding the thermodynamic behavior of both $LiFePO_4$ and Mn-doped-$LiFePO_4$ cathode materials was shown, thermodynamic models describing the equilibrium and coherent $LiFePO_4$-$FePO_4$ and $Li(Mn_yFe_{1-y})PO_4$-$(Mn_yFe_{1-y})PO_4$ phase diagrams are required. The objectives of the thesis will then be defined. The structure and organization of the thesis will be given in the following paragraphs in order to better visualize the research strategy which has been used to reach the objectives.

3.1 Objectives of the thesis

The outline of the doctoral research is as follows:

Research domain: Material Engineering

Research subject: Thermodynamic behavior of the cathode material $LiFePO_4$ and Mn-doped-$LiFePO_4$

Research question: Would the thermodynamic knowledge of the $LiFePO_4$-$FePO_4$ and $Li(Mn_yFe_{1-y})PO_4$-$(Mn_yFe_{1-y})PO_4$ olivine joins help us to understand the electrochemical behavior of the cathode material $LiFePO_4$ and Mn-doped-$LiFePO_4$?

Main objectives: To develop thermodynamic models describing coherent and particle size dependent phase equilibria of the $LiFePO_4$-$FePO_4$ olivine join and phase para-equilibria and coherent phase transformation in the $Li(Mn_yFe_{1-y})PO_4$-$(Mn_yFe_{1-y})PO_4$ system.

For achieving the main objectives of my doctoral research, secondary objectives are defined:

Secondary objectives:

1. Develop thermodynamic models of the $LiFePO_4$-$FePO_4$ olivine join.
2. Develop thermodynamic models of the para-equilibrium $Li(Mn_yFe_{1-y})PO_4$-$(Mn_yFe_{1-y})PO_4$ cathode join at room temperature.
3. Extend Cahn's approach for orthorhombic systems and apply it to calculate the coherent miscibility gaps of the $LiFePO_4$-$FePO_4$ olivine join.

4. Model the change of the miscibility gaps of the $LiFePO_4$-$FePO_4$ olivine join with the particle size.
5. Develop a new approach (elastic Gibbs energy approach) for calculating the coherent miscibility gap of cubic systems.
6. Extend the elastic Gibbs energy approach for calculating the coherent miscibility gap of orthorhombic systems and apply this approach for calculating coherent miscibility gaps of the $Li(Mn_yFe_{1-y})PO_4$-$(Mn_yFe_{1-y})PO_4$ cathode join.

3.2 Organization of the thesis

The following chapters of this thesis are built to achieve the objectives of the research. The present thesis is in the format of a thesis by articles (Figure 3.1). All secondary objectives defined in the previous section are achieved in different chapters. Each chapter corresponds to an article.

Chapter 4 presents the thermodynamic models of the equilibrium $LiFePO_4$-$FePO_4$ olivine join. In this chapter, several CEF sublattice models are proposed to reproduce the experimental data. An extra long-range-order of Fe^{2+} and Fe^{3+} or Li^+ and Va in the solid solution Li_xFePO_4 is considered to represent the unique feature of this phase diagram. Developing proper thermodynamic models of this system is critical since they will later be extended to thermodynamic models of the more complicated $Li(Mn_yFe_{1-y})PO_4$-$(Mn_yFe_{1-y})PO_4$ system.

Chapter 5 presents the thermodynamic models describing the coherent and particle size dependent $LiFePO_4$-$FePO_4$ phase diagram. For calculating the coherent miscibility gap, Cahn’s approach is extended for orthorhombic systems. In addition, the shrinkage of the miscibility gaps as a result of particle size reduction is modeled through molar surface Gibbs energy of the Li_xFePO_4 solid solution particles.

Note that Cahn’s approach is only valid for systems with small lattice mismatch while the maximum lattice mismatch of the $LiMnPO_4$-$MnPO_4$ system is up to ~8%. It means that the coherent miscibility gaps of the $Li(Mn_yFe_{1-y})PO_4$-$(Mn_yFe_{1-y})PO_4$ olivine join are only properly calculated if there is a valid approach for estimating the coherent miscibility gaps in a large deformation regime. Consequently, chapter 6 presents the coherent phase equilibria of cubic systems under large lattice mismatches (> 5%). The elastic Gibbs energy approach for calculating the coherent miscibility gap of cubic systems is developed. Several case studies are examined. This chapter is not directly related to the interested cathode materials, but it provides an effective tool for calculating the coherent miscibility gap under a large deformation regime where the elastic Gibbs energy is formulated from Euler's strain tensor and the second order Piola-Kirchoff stress tensor.

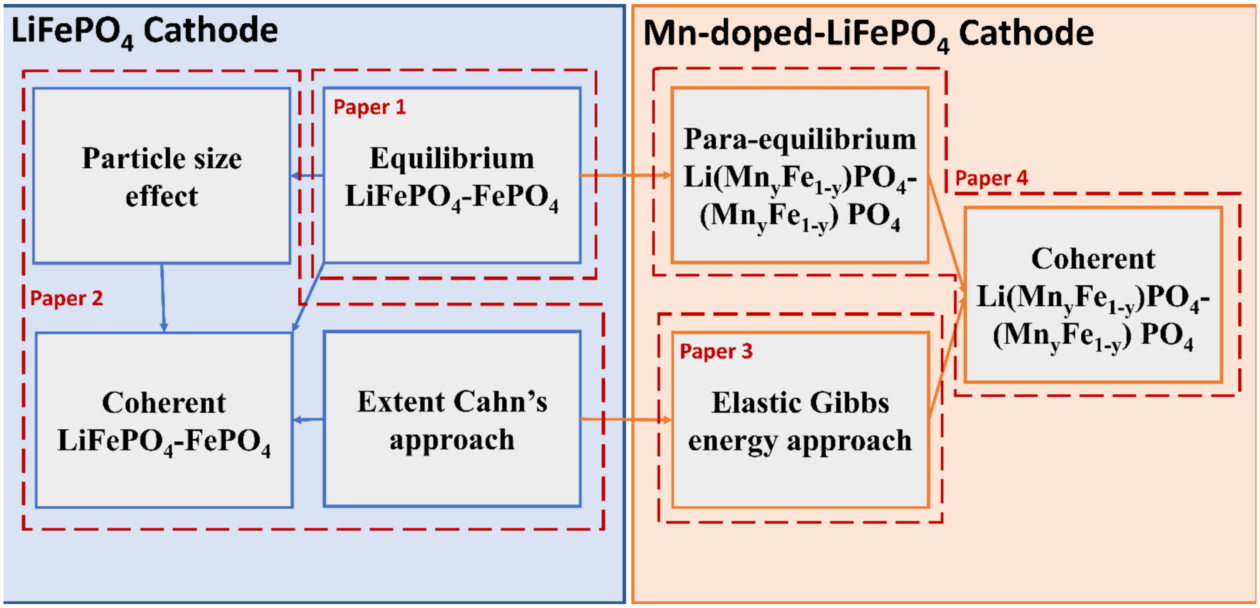

Figure 3.1: Scheme of the organization of the thesis.

Chapter 7 presents the thermodynamic models and the calculation of coherent miscibility gaps of $Li(Mn_yFe_{1-y})PO_4$-$(Mn_yFe_{1-y})PO_4$ olivine join at room temperature. First, the para-equilibrium $Li(Mn_yFe_{1-y})PO_4$-$(Mn_yFe_{1-y})PO_4$ join is described by considering newly developed thermodynamic models with secondary sublattices. Later, the elastic Gibbs energy approach is extended for orthorhombic systems and then applied to calculate the coherent miscibility of $Li(Mn_yFe_{1-y})PO_4$-$(Mn_yFe_{1-y})PO_4$ join at room temperature.

Finally, a general conclusion, limitation, and recommendation of my doctoral research are summarized in the last chapter of the thesis.

CHAPTER 4 ARTICLE 1: MODELLING OF PHASE EQUILIBRIA OF $LiFePO_4$-$FePO_4$ OLIVINE JOIN FOR CATHODE MATERIAL

Anh Thu Phan, Aïmen E. Gheribi and Patrice Chartrand

Published in The Canadian Journal of Chemical Engineering, volume 97, issue 8, pages 2224-2233, 2019

Abstract:

A thermodynamic model for the $FePO_4$-$LiFePO_4$ olivine join has been developed in order to provide support for the understanding of the charge transport behaviour within the cathode material during the battery operation. The Gibbs energy model for the olivine solution is based on the compound energy formalism with long-range-order and has been calibrated using the CALPHAD method, permitting the computation of phase equilibria by Gibbs energy minimization techniques. The model can simultaneously reproduce the reported eutectoid reaction, the 3 low-temperature miscibility gaps, the enthalpy of mixing, and the change of the voltage plateau with temperature during the delithiation process, in agreement with the available experimental data. The spinodal decomposition, which is possibly associated with fast charge transport within the cathode material, involves up to two sub-spinodal decompositions. Hence, the unique low-temperature miscibility gap of this system is considered as a blend of the two sub-miscibility gaps.

4.1 Introduction

The exhaustion of unrenewable energy sources is one of the biggest issues today. In recent years, there has been a considerable demand for a high-safety and high-performance large-scale energy storage system that permits energy obtained from less constant renewable sources to be stored. $LiFePO_4$ has opened the door for lithium ion batteries to play an important role in large-scale applications such as plug-in hybrid vehicles or electrical vehicles [18, 21, 27, 34]. This material provides several advantages over conventional cathodes: low cost, improved safety performance, high chemical stability, superior structural stability, low toxicity, high theoretical reversible capacity (170 mAh/g), and an extremely flat charge-discharge profile at a reasonably high potential versus Li/Li^+ [16-21]. $LiFePO_4$ is one of the safest, and can be the cheapest, battery material since it is based on available iron oxides. However, its poor intrinsic electronic conductivity and small tap density are addressed as major problems to be solved before it could be deployed commercially [18, 27, 34]. Since a report on $LiFePO_4$ published in 1997 by Padhi *et al.* [16], $LiFePO_4$ remains a hot topic in battery material research.

In Li-ion batteries, Li^+ is transferred through alternative layers of the $LiFePO_4$ cathode and the graphite anode. Reversible movement of lithium ions from one electrode to another is related to the charging and discharging of the battery. As Li^+ is extracted from triphylite ($LiFePO_4$), heterosite ($FePO_4$) is formed. Both triphylite and heterosite show the olivine structure (space group: *Pnma*) [160]. The coexistence of two phases $LiFePO_4$ and $FePO_4$ leads to the formation of a stable voltage plateau at ~3.5 V [21]. The open-circuit voltage (OCV) at a very low charging or discharging rate is dependent on the Gibbs energy of cathode, consequently on the equilibrium $FePO_4$-$LiFePO_4$ olivine join [18, 22-27]. In order to predict OCV or explain the observed OCV of the electrochemical cell, knowledge of the Gibbs energy change of the cathode due to the material phase transition during operation is necessary. Therefore, having a better understanding of the thermodynamic behavior of the cathode material during the battery operation is important.

4.2 Literature review

Important experimental phase diagram and thermodynamic data on the $LiFePO_4$-$FePO_4$ system are available in the literature. Also, density functional theory (DFT) calculations were published to estimate thermodynamic properties such as enthalpies of formation. In this section, this information will be reviewed. Firstly, few experimental data of the equilibrium $FePO_4$-$LiFePO_4$ join has been published. Solubility limits of $FePO_4$ and $LiFePO_4$ at 298 K have been estimated by Yamada *et al.* [26]. Later, the phase diagram of $FePO_4$-$LiFePO_4$ was determined experimentally up to 623 K [28, 29]. Both papers reported the existence of a miscibility gap at low temperatures, and this miscibility gap splits into two at higher temperatures. However, discrepancies between the two sets of experimental data is quite large (Figure 4.1a). While Delacourt *et al.* [29] showed the existence of $Li_{0.75}FePO_4$ and $Li_{0.5}FePO_4$ at the transition temperature of 423 K, Dodd *et al.* [28] revealed an eutectoid transition at $Li_{0.6}FePO_4$ at 473 K. The difference of the two set of experimental data comes from the difference in sample preparation and analysis. In a study by Delacourt *et al.* [29], two-phase mixtures were prepared and examined by a temperature-controlled XRD. The samples were kept at the investigated temperature for ~30 min [29]. In a different study, Dodd *et al.* [28] heat treated their samples under vacuum environment at various temperatures. After heat treated from 30 min–4 days, the samples were consequently quenched in cooled, blowing air or water [28]. Because their sample heat-treatments were performed over time, and the equilibrium was likely approached, the reported experimental data of Dodd *et al.* [28] is considered to be more reliable and should be utilized to verify any models of $FePO_4$-$LiFePO_4$ olivine join. Interestingly enough, the XRD (X-Ray diffraction) and SAED (selected area electron diffraction) patterns of the $Li_{0.6}FePO_4$ sample annealed at 623.15 K, confirming the existence of a supercell microstructure corresponding to long-range-order (LRO) [35]. Furutsuki *et al.* [35] then proposed short-range-order (SRO) distribution of Li^+ and Va^0 only within a supercell.

Zhou *et al.* [63] previously reported the olivine join by first-principle calculations, however, their calculated phase diagram does not represent the equilibrium experimental data well, and it needs improvement [28]. Later, the $LiFePO_4$-$FePO_4$ phase diagram calculated by Lee [24] showed a suitable agreement with the experimental data reported by Dodd *et al.* [28] For describing the $FePO_4$-$LiFePO_4$ join, Lee used the CALPHAD method [24]. The CALPHAD (CALculation of PHAse diagrams) method is an approach to phase diagram computation through the following: (i) development of Gibbs energy models to represent the thermodynamic properties for various phases that permit the prediction of the thermodynamic properties of multicomponent phases and systems (from binary and ternary subsystems) and the computation of phase equilibria by the minimization of the Gibbs energy of the system respecting the elemental balance; (ii) critical assessment of experimental data to obtain Gibbs energy model parameters by optimization and the incorporation of these parameters into self-consistent databases; (iii) optimization of thermodynamic parameters using software; and (iv) improvement of databanks for calculation to enhance understanding of various industrial and technological processes [64]. The compositional variation of the Gibbs energy of a solid phase can be described by compound energy formalism (CEF) [65, 66], a method to treat the solid based on its crystal structure. In CEF, thermodynamic properties of phases are described by two or more sub-lattices on which different chemical species mix with variations in composition. The choice of sublattice stoichiometry and the mixing species on each sublattice defines a specific model within the formalism, hence the name CEF.

During the charging and discharging processes, Li^+ ions move from one electrode to the other, and the oxidation state of iron in the Li_xFePO_4 cathode material changes among Fe^{2+} and Fe^{3+} [160]. Hence, for the olivine solid solution, a 4-sublattice model $(M_1)_1(M_2)_1(P^{5+})_1(O^{2-})_4$ was chosen by Lee [24] with the following ionic species on the sublattices $(Li^+,Va^0)_1(Fe^{2+},Fe^{3+})_1(P^{5+})_1(O^{2-})_4$. 2-phase immiscibility can be computed by Gibbs energy minimization at constant temperature (T), pressure (P), and moles of $LiFePO_4$ and $FePO_4$ using 2 independent sets of sublattice fractions ($y_{Li^+} = 1 - y_{Va^0}$ and $y_{Fe^{3+}} = 1 - y_{Fe^{2+}}$), one for each phase. A vector of 3 sublattice site fractions for 3-phase immiscibility at the eutectoid temperature can also be computed, and the thermodynamic properties of the phases and the system can be derived from their respective Gibbs energy and their derivatives in the $FePO_4$-$LiFePO_4$ join [24]. Using this approach, and with the sublattice species model implemented within the CEF, Lee calculated the Gibbs energy function of the solid solution [24]:

$$\begin{aligned} G_m(T,x) = {} & y_{Li^+} \cdot y_{Fe^{2+}} \cdot \overset{\circ}{G}_{LiFePO_4} + y_{Va^0} \cdot y_{Fe^{2+}} \cdot \overset{\circ}{G}_{FePO_4^-} + y_{Va^0} \cdot y_{Fe^{3+}} \cdot \overset{\circ}{G}_{FePO_4} \\ & + y_{Li^+} \cdot y_{Fe^{3+}} \cdot \overset{\circ}{G}_{LiFePO_4^+} + RT \\ & \cdot \left[y_{Li^+} \cdot \ln y_{Li^+} + y_{Va^0} \cdot \ln y_{Va^0} + y_{Fe^{2+}} \cdot \ln y_{Fe^{2+}} + y_{Fe^{3+}} \cdot \ln y_{Fe^{3+}} \right] \\ & + G_m^E(T,x) \end{aligned} \tag{4.1}$$

where $\overset{\circ}{G}_{LiFePO_4}$, $\overset{\circ}{G}_{LiFePO_4^+}$, $\overset{\circ}{G}_{FePO_4}, and\ \overset{\circ}{G}_{FePO_4^-}$ are the Gibbs energy of the corresponding end-members; G_m^E is the excess Gibbs energy gained from the mixing of ions and vacancies at the first and second sublattice; y_i is the site fraction of the species i in its sublattice (i can be Li^+, Va, Fe^{2+}, or Fe^{3+} and $y_{P^{5+}} = y_{O^{2-}} = 1$); R is the gas constant; and T is the absolute temperature. In Lee's model [24], the excess Gibbs energy was given by the Redlich-Kister polynomial [161], with an additional term:

$$\begin{aligned} G_m^E(T,x) = {} & y_{Li^+} \cdot y_{Va^0} \cdot \left[y_{Fe^{2+}} \cdot \textstyle\sum_{i=0}^{n} L_{Li^+,Va^0:Fe^{2+}}^{i} \cdot (y_{Li^+} - y_{Va^0})^i \right] + y_{Li^+} \cdot y_{Va^0} \cdot \\ & \left[y_{Fe^{3+}} \cdot \textstyle\sum_{i=0}^{n} L_{Li^+,Va^0:Fe^{3+}}^{i} \cdot (y_{Li^+} - y_{Va^0})^i \right] + y_{Fe^{2+}} \cdot y_{Fe^{3+}} \cdot \left[y_{Li^+} \cdot \right. \\ & \left. \textstyle\sum_{i=0}^{n} L_{Li^+:Fe^{2+},Fe^{3+}}^{i} \cdot (y_{Fe^{2+}} - y_{Fe^{3+}})^i \right] + y_{Fe^{2+}} \cdot y_{Fe^{3+}} \cdot \left[y_{Va^0} \cdot \textstyle\sum_{i=0}^{n} L_{Va^0:Fe^{2+},Fe^{3+}}^{i} \cdot \right. \\ & \left. (y_{Fe^{2+}} - y_{Fe^{3+}})^i \right] + y_{Li^+} \cdot y_{Va^0} \cdot y_{Fe^{2+}} \cdot y_{Fe^{3+}} \cdot I_{Li^+,Va^0:Fe^{2+},Fe^{3+}}^{ex} \end{aligned} \tag{4.2}$$

where L_j^i are adjustable coefficients; and n is the order of the polynomial expansion.

The last term $I^{ex}_{Li^+,Va^0:Fe^{2+},Fe^{3+}}$ of Equation (4.2) was claimed to imply an SRO interaction between Li^+ and Va^0 together with Fe^{2+} and Fe^{3+} via the following pair exchange reaction:

$$LiFePO_4 + FePO_4 \rightleftarrows LiFePO_4{}^+ + FePO_4{}^- \qquad \text{(i)}$$

The Gibbs exchange energy of the reaction (i) ΔG^{EX} is the difference between the Gibbs energy of reactants and that of products:

$$\Delta G^{EX} = \overset{\circ}{G}_{LiFePO_4{}^+} + \overset{\circ}{G}_{FePO_4{}^-} - \overset{\circ}{G}_{LiFePO_4} - \overset{\circ}{G}_{FePO_4} \qquad (4.3)$$

The contribution of SRO between mixing ions on different sublattices represented by $I^{ex}_{Li^+,Va^0:Fe^{2+},Fe^{3+}}$ in Equation (4.2) is known as the Blander's reciprocal term, although Lee did not mention it [24, 162, 163]. In fact, Blander's reciprocal term, which is valid for small deviations from the random mixing of species on their respective sublattice, should be solely dependent on the Gibbs exchange energy of pairs cited above [164]:

$$I^{ex}_{Li^+,Va^0:Fe^{2+},Fe^{3+}} = -(\Delta G^{EX})^2/2ZRT \qquad (4.4)$$

where Z is the coordination number usually taken as 6. As mentioned in Dessureault and Pelton's work [164], if the exchange energy is large enough, or if $I^{ex}_{Li^+,Va^0:Fe^{2+},Fe^{3+}}$ is negative enough, the model with the Blander's reciprocal term predicts that the miscibility gap wrongly splits into two smaller miscibility gaps. This is a problem for all sublattice models that are using a Temkin (Bragg-Williams) type of configurational entropy with the Blander reciprocal term. From the molar Gibbs energy of the end-members reported by Lee [24], at a temperature of 500 K (around the eutectoid temperature), the exchange Gibbs energy is computed to be -32 kJ/mol; therefore, if Equation (4.4) is respected, then the value of Blander's reciprocal should be $I^{ex}_{Li^+,Va^0:Fe^{2+},Fe^{3+}} \approx -20.5\ (\frac{kJ}{mol})$ (with $Z = 6$ and $T = 500\ K$). It is less negative than the actual value used in the model of Lee ($I^{ex}_{Li^+,Va^0:Fe^{2+},Fe^{3+}} \approx -33.9\ \left(\frac{kJ}{mol}\right)$ (with $Z = 6$)). This means that in order to recreate the two miscibility gaps in FePO$_4$-LiFePO$_4$ olivine join, Lee had to lower the value of Blander's reciprocal term to a much more negative value, implying the 2 miscibility gaps above the eutectoid temperature are due to SRO. Since the value of $I^{ex}_{Li^{+},Va^{0}:Fe^{2+},Fe^{3+}}$ from Lee's work [24] was not derived directly from the exchange energy, it is then merely a fitting parameter which does not describe the nature of the SRO if existing in the Li_xFePO_4 solid solution. Even if the two-miscibility-gap-diagram obtained by Lee is consistent with the experimental data [24], it is still an incorrect feature of the thermodynamic model.

Considering thermodynamic properties of the system, the values of enthalpy of the formation of pure $LiFePO_4$ and $FePO_4$ compounds have been measured from the oxides or from the elements [111]. The heat capacity functions of both $LiFePO_4$ and $FePO_4$ were predicted in our previous work [101] by combining DFT to a self-constant method based on quasi-harmonic approximation (QHA) and a minimization procedure to ensure that the Maxwell relations are respected [102, 103]. Our predictions [101] were found to be in very good agreement with the experimental data reported in the range from 2–773 K and from 2–300 K for $LiFePO_4$ [99, 100] and $FePO_4$ [104], respectively. Assuming the same agreement at higher temperature, the heat capacity was extrapolated via our theoretical prediction [101]. In addition, the entropy values of pure solid $LiFePO_4$ and pure solid $FePO_4$ at 298 K were calculated from the experimental value of heat capacity in Loos *et al.* [100] and Shi *et al.* [104], correspondingly.

Furthermore, according to Dodd *et al.* [28], for a DSC (differential scanning calorimetry) scanning rate of 5 K/min, the enthalpy of mixing measured for a $Li_{0.47}FePO_4$ sample was estimated to be 0.50 kJ/mol with a peak temperature of 497 K. Upon cooling, the enthalpy of unmixing was found to be 0.70 kJ/mol with a peak at 409 K [28]. As claimed by the author, the enthalpy of mixing is expected to be higher than their reported value if they could perform the experiments for a longer time [28] (Figure 4.2). Another direct DSC measurement of $Li_{0.6}FePO_4$ gave an enthalpy of disordering of 1.40 ±0.30 kJ/mol [114], a value, according to the authors, that is too small since the transformation from the two-phase to disordered state is sluggish and incomplete by 593 K. Since the sample was only transformed at 55 % in the temperature range where the enthalpy of mixing was measured, the total enthalpy of transition was estimated to be approximately 2.55 ±0.55 kJ/mol (Figure 4.2), assuming that the enthalpy needed to disorder 1 % of the sample is unchanged [114]. Because the reported thermodynamic data of this system is very limited, Lee had to adopt the enthalpy of mixing data predicted by Monte Carlo simulations at 0 K [24]. At the eutectoid point $Li_{0.6}FePO_4$, the enthalpy of mixing reported in his study is ~9.2 kJ/mol [24] (Figure 4.2), which is much higher than the predicted value of 0.83 kJ/mol reported by Zhou *et al.* [63] and is about three times higher than the experimentally reported value of 2.55 ±0.55 kJ/mol [114] (Figure 4.2). Since Lee did not provide any detailed information on his calculation of the enthalpy of mixing [24], it is impossible to evaluate his work. Nevertheless, the enthalpy of mixing calculated by Lee's model does not describe the measured value well [24, 114].

Up to now, Lee's work is the only reported thermodynamic model of the $FePO_4$-$LiFePO_4$ system [24]. However, his model failed to obtain the experimental enthalpy of mixing and the miscibility gap was wrongly split by using SRO Blander's term. Moreover, his intention of considering the SRO interaction between Li^+ and Va^0 together with Fe^{2+} and Fe^{3+} disagrees with the experimental evidence and the first principle calculation of supercell structures of the solid solution $Li_{0.6}FePO_4$ reported by Furutsuki *et al.* [35]. Additionally, Lee's model fails to obtain the experimental value of enthalpy of mixing. Hence, unlike Lee, in this work we would like to develop a thermodynamic model with an extra level of LRO that would reproduce at the same time the enthalpy of mixing, eutectoid reaction, and all the phase solubility of the $LiFePO_4$-$FePO_4$ phase diagram.

4.3 Thermodynamic models

In this section, we will describe the thermodynamic models that we tested for the olivine solid solution between the lithiated ($LiFePO_4$) and delithiated ($FePO_4$) end-member. 4 models based on different sublattice structures of the CEF were investigated. From a modelling point of view, in the CEF different levels of LRO can be imposed by dividing a given sublattice into 2 new sublattices. For example, in the olivine structure, the 2 M_1 sites can be divided into a M_1' and a M_1'' sites, with mixing of Li^+ and Va^0 on both sublattices providing different site fractions at equilibrium. In this study, we changed the sublattice description of the model within the CEF in order to introduce an extra level of LRO, as was hinted in Furutski *et al.*'s work [35], which opposes to the SRO suggested by Lee [24]. The aim is to obtain a better description of the phase diagram of the $FePO_4$-$LiFePO_4$ olivine join where the driving forces behind immiscibility are based on LRO rather than the SRO, which was wrongly induced by the Blander's term and reported by Lee [24]. The model and the Gibbs energy minimization technique are implemented in the FactSage [165, 166], and MATLAB software. Lee's ionic sublattice structure of the solid solution Li_xFePO_4 (model M4) will be re-evaluated without considering SRO effect (i.e., no Blander reciprocal term). Furthermore, unlike Lee [24] some ionic models taking into account LRO of M_1, or M_2 sites by splitting the 1st, 2nd, or both of the first two sublattices (model M5.L, M5.F, M6) will be tested. The Gibbs energy function of the solid solution corresponds to a sublattice model and is calculated as follows:

$$G_m(T,x) = \sum_i \sum_j \dots \sum_k y_i^{(1)} y_j^{(2)} \dots y_k^{(s)} G^{\circ}_{i:j:\dots:k} + \frac{1}{\sum_s n^{(s)}} RT \sum_s \sum_i n^{(s)} y_i^{(s)} \ln y_i^{(s)} + G_m^E(T,x) \tag{4.5}$$

$$G_m^E(T,x) = \sum_s \sum_i \sum_j y_i^{(s)} y_j^{(s)} \sum_{r \neq s} \sum_k y_k^{(r)} L^{(s)}_{i,j:\dots:k}(T) + \cdots$$

where $G^{\circ}_{i:j:\dots:k}$ is the Gibbs energy of the end-member $i:j:\dots:k$ formed by species i, j, …, k from different sublattices; s is the number of sublattice; $y_i^{(s)}$ is the site fraction of the species i within the sublattice s; $n^{(s)}$ are stoichiometric coefficient relating the sublattices; $G_m^E(T,x)$ is the excess Gibbs energy; and $L^{(s)}_{i,j:\dots:k}(T)$ is the binary parameters corresponding to the interaction between component i and j on the sublattice s while each other sublattice is occupied by a single specie. More excess terms can be added such as mixing of three species within a given sublattice or simultaneous mixing of two pairs of two species on two sublattices while the remaining sublattice are singly occupied. After finding suitable thermodynamic parameters, boundaries of the spinodal decomposition will be estimated. Spinodal decomposition is a mechanism where spontaneous fluctuations in the concentration of a solution of two or more components cause its separation into distinct regions (or phases) without it being necessary to cross the energy barrier corresponding to creation of an interface in order to form nuclei [167, 168]. The boundary of spinodal decomposition is predicted by taking the second derivative of the Gibbs energy of the solid solution versus its overall composition x [137]:

$$\left(\frac{\partial^2 G_m}{\partial x^2}\right)_{T,P} = 0 \tag{4.6}$$

In our models, we decided to take the values of the enthalpy of formation of pure compounds from the elements presented by Iyer *et al.* [111]. The entropy values of pure solid $LiFePO_4$ and pure solid $FePO_4$ at 298 K are taken from Loos *et al.* [100] and Shi *et al.* [104], respectively. The heat capacity functions of the pure compounds, which were fully accessed in our previous studies, have been used [101]. We have then supposed the Kopp-Neuman rule for the solid solution, i.e., a linear relationship between the heat capacity and the molar composition.

4.3.1 4-sublattice model M4: $(Li^{+}, Va^{0})_1(Fe^{2+}, Fe^{3+})_1(P^{5+})_1(O^{2-})_4$

M4 is the same sublattice structure with the same sublattice species as Lee's model [24]. In this study, instead of optimizing the Gibbs exchange energy ΔG^{EX} of the pair exchange reaction (i) for model M4, we optimized the Gibbs energy of the 4 end-members of the solution. While the Gibbs energy of pure compounds is calculated directly from their enthalpy of formation at 298 K, their entropy at 298 K, and their heat capacity functions, the energy of other non-neutral end-members must be formulated. The Gibbs energy of the two non-neutral end-members are set as follows:

$$\begin{gathered} \overset{\circ}{G}_{LiFePO_4{}^{+}} = \overset{\circ}{G}_{LiFePO_4} + \Delta\overset{\circ}{G}_{LiFePO_4{}^{+}} \\ \overset{\circ}{G}_{FePO_4{}^{-}} = \overset{\circ}{G}_{FePO_4} + \Delta\overset{\circ}{G}_{FePO_4{}^{-}} \end{gathered} \tag{4.7}$$

where $\overset{\circ}{G}_{LiFePO_4}$ and $\overset{\circ}{G}_{FePO_4}$ are the free energy function of pure compounds $LiFePO_4$ and $FePO_4$; and $\Delta\overset{\circ}{G}_{LiFePO_4{}^{+}}$ and $\Delta\overset{\circ}{G}_{FePO_4{}^{-}}$ are the corresponding molar energy gained by taking away electrons from $LiFePO_4$ and adding electrons to $FePO_4$ to form ionic end-member $LiFePO_4^{+}$ and $FePO_4^{-}$. Consequently, the Gibbs exchange energy of the reaction (i) is as follows:

$$\Delta G^{EX} = \Delta\overset{\circ}{G}_{LiFePO_4{}^{+}} + \Delta\overset{\circ}{G}_{FePO_4{}^{-}} \tag{4.8}$$

Therefore, rather than optimizing the Gibbs exchange energy ΔG^{EX} as normal, $\Delta\overset{\circ}{G}_{LiFePO_4{}^{+}}$ and $\Delta\overset{\circ}{G}_{FePO_4{}^{-}}$ are optimized. This approach, which is equivalent to the optimization of the Gibbs exchange energy, was developed for later use in our advanced models (M5.L, M5.F, and M6) with higher number of sublattices.

Without any addition of excess Gibbs energy (i.e., $G_m^E = 0$), a single-miscibility-gap phase diagram is obtained, and it describes the experimental data reasonably well but lacks the details of the diagram (Figure 4.1a). The Gibbs exchange energy of this model (22 kJ/mol at 298 K) is much lower than that of Lee's model (41.6kJ/mol at 298K) [24] and Blander's reciprocal is not used ($I^{ex}_{Li^+,Va^0:Fe^{2+},Fe^{3+}} = 0$), i.e., no SRO effect is taken into account in our optimization. This M.4 model must be improved in order to describe the reported experimental data of $LiFePO_4$-$FePO_4$ phase diagram [28] better.

Recently, a reported SAED pattern confirmed the existence of a supercell of the $Li_{0.6}FePO_4$ solid solution [35]. In addition, the authors showed their optimized structure of the solid solution revealing the long-range-order (LRO) of Li^+ and Va^0 [35]. The supercell pattern or LRO in the crystal structure of the $Li_{0.6}FePO_4$ sample inspired us to develop a more suitable thermodynamic model for $LiFePO_4$-$FePO_4$ olivine join taking into consideration an extra level of LRO of the solid solution. In order to form new sublattice models within the CEF for the olivine structure, we split each or both of the 1st and the 2nd sublattice (M_1, M_2 sites) of the model M4 by a ratio of 3:2 in order to recreate the eutectoid composition at $x \cong 0.6$ and we multiply the stoichiometric coefficients of the model M4 $(Li^+,Va^0)_1(Fe^{2+},Fe^{3+})_1(P^{5+})_1(O^{2-})_4$ by the multiples of 5 to obtain integer stoichiometric coefficients. From a modelling point of view, a 5-stoichiometry-model represents the array of 5 formula units of Li_xFePO_4 solid solution, or 1D LRO. The extra level of LRO could also be describes in 2D or 3D by using a 10-stoichiometry-model or a 20-stoichiometry-model, respectively. In reality, the orthorhombic unit cell of the olivine-type solid solution accommodates four formula units of Li_xFePO_4 [31]. As a result, a model consisting of 20 formula units is the most favourable since it could describe all kinds of the extra LRO, and the supercell of the model is a multiple of the olivine unit cell. However, from a calculation point of view, any models with a multiple of 5 formula units can be simplified to a corresponding 5-stoichiometry-model. Noticeably, the simplification of a thermodynamic model should not change the optimization, but it could change the interpretation of the model used. Merely 5-formula-unit-models are considered in this study for simplifying the calculation.

4.3.2 6-sublattice model M6: $(Li^{+}, Va^{0})_3(Li^{+}, Va^{0})_2(Fe^{2+}, Fe^{3+})_3(Fe^{2+}, Fe^{3+})_2(P^{5+})_5(O^{2-})_{20}$

As mentioned earlier, in this study for model M4, $\Delta G^{\circ}_{LiFePO_4^+}$, and $\Delta G^{\circ}_{FePO_4^-}$ are optimized to reproduce adequately the experimental data [28] instead of optimizing the Gibbs exchange energy ΔG^{EX} as usual. This approach shows its advantages especially for the model involving many end-members like our advanced models M5.L, M5.F, or M6. In a model consisting of many end-members, consequently, many pair exchange reactions and their corresponding values of Gibbs exchange energy need to be taken into account. The optimization of Gibbs exchange energy becomes more complicated not only because of the number of the Gibbs exchange energy but also the constraints among them. Alternatively, for our advanced models, we optimized three Gibbs energy parameters $\Delta G^{\circ}_{LiFePO_4^+}$, $\Delta G^{\circ}_{FePO_4^-}$, and $\Delta G^{\circ}_{adjust}$, which are used to determine the energy gained by forming the end-member from compounds. To make the model even more simple, the three terms are kept temperature independent.

This 6-sublattice model is obtained by splitting both the (Li^{+},Va^{0}) and the (Fe^{2+},Fe^{3+}) sublattices of the M4 model. With no excess Gibbs energy (i.e., $G_m^E = 0$), a phase diagram that contains 3 miscibility gaps is obtained, however, it does not describe both the experimental data and the eutectoid temperature well (Figure 4.1b). This model consists of 16 end-members, and, consequently, there are many independent parameters to handle in this optimization, resulting in a lower quality fit of the experimental phase diagram data. These problems inherent to the M6 model make it even more unattractive if coherent relationship, doping impurities, or anti-site defects are taken into account.

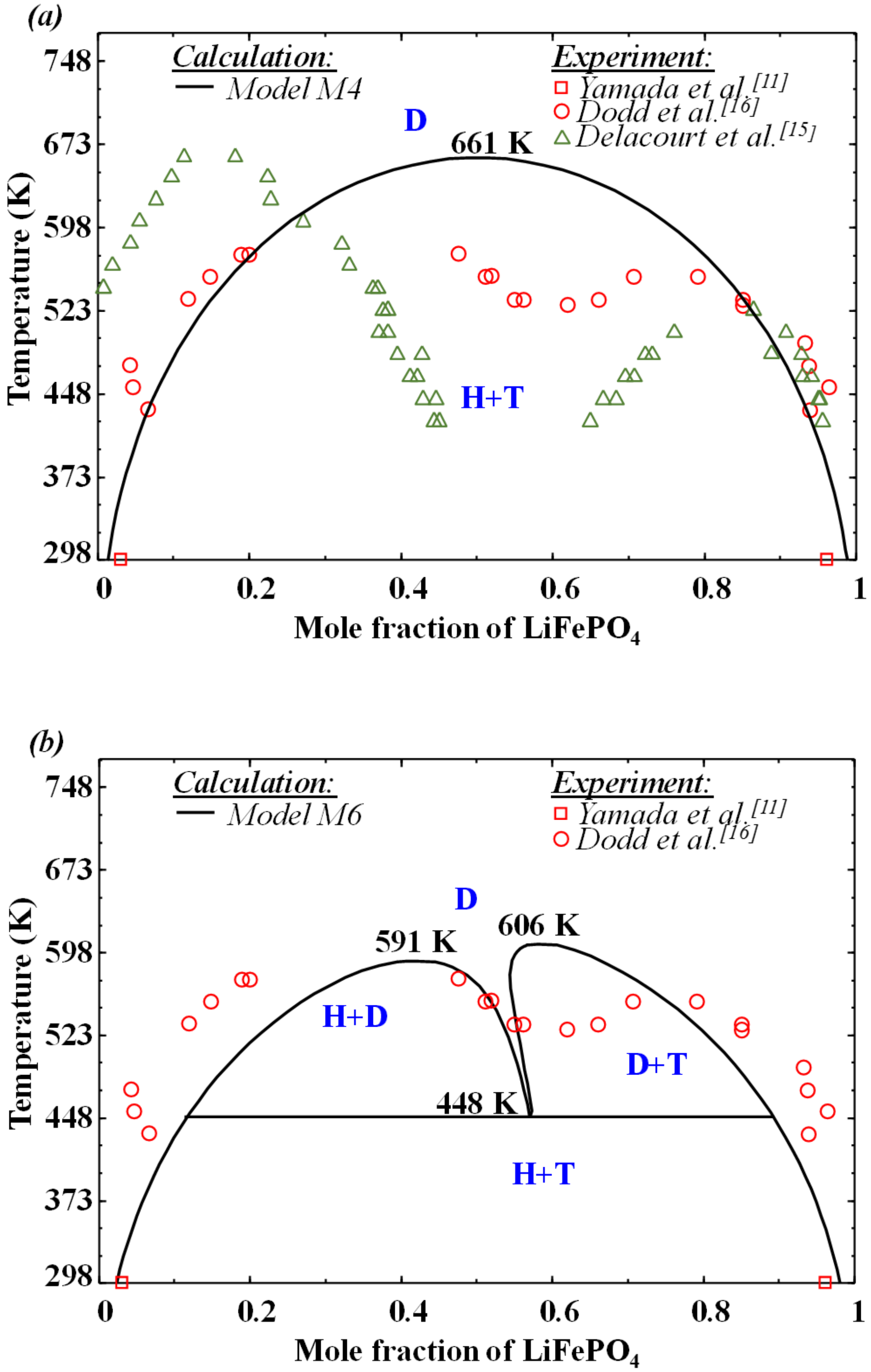
(a)
Calculation:
Model M4
Experiment:
Yamada et al.[11]
Dodd et al.[16]
Delacourt et al.[15]
D
661 K
H+T
748
673
598
523
448
373
298
Temperature (K)
0
0.2
0.4
0.6
0.8
1
Mole fraction of LiFePO$_4$
(b)
Calculation:
Model M6
Experiment:
Yamada et al.[11]
Dodd et al.[16]
D
591 K
606 K
H+D
D+T
448 K
H+T
748
673
598
523
448
373
298
Temperature (K)
0
0.2
0.4
0.6
0.8
1
Mole fraction of LiFePO$_4$

(c)

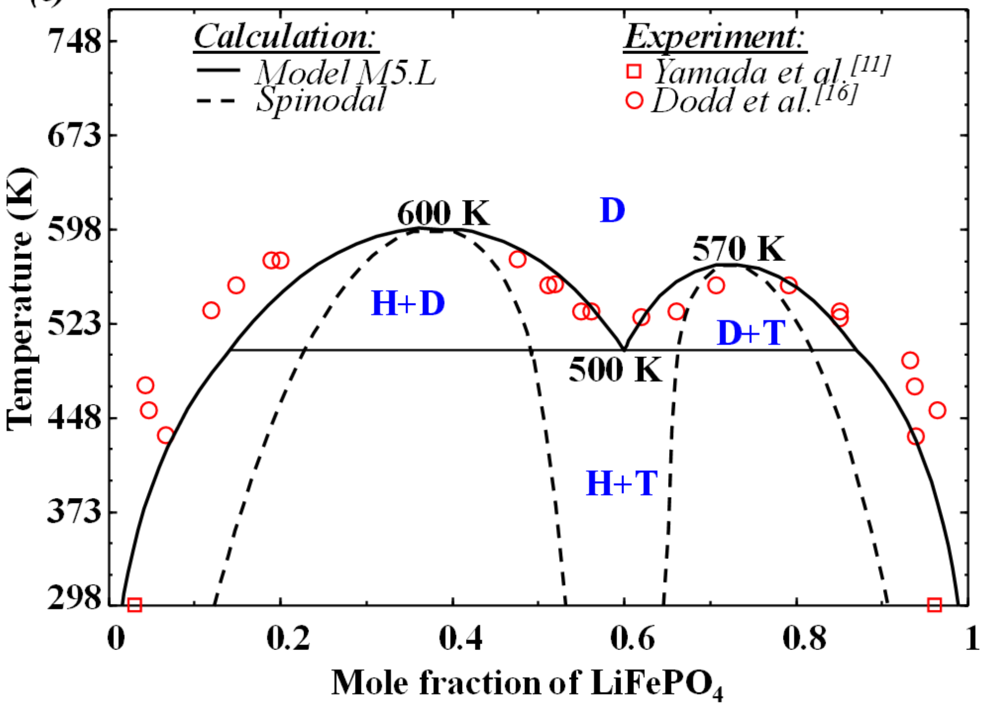
Calculation:
Model M5.L
Spinodal
Experiment:
Yamada et al.[11]
Dodd et al.[16]
748
673
598
523
448
373
298
Temperature (K)
600 K
D
570 K
H+D
D+T
500 K
H+T
0
0.2
0.4
0.6
0.8
1
Mole fraction of $LiFePO_4$

(d)

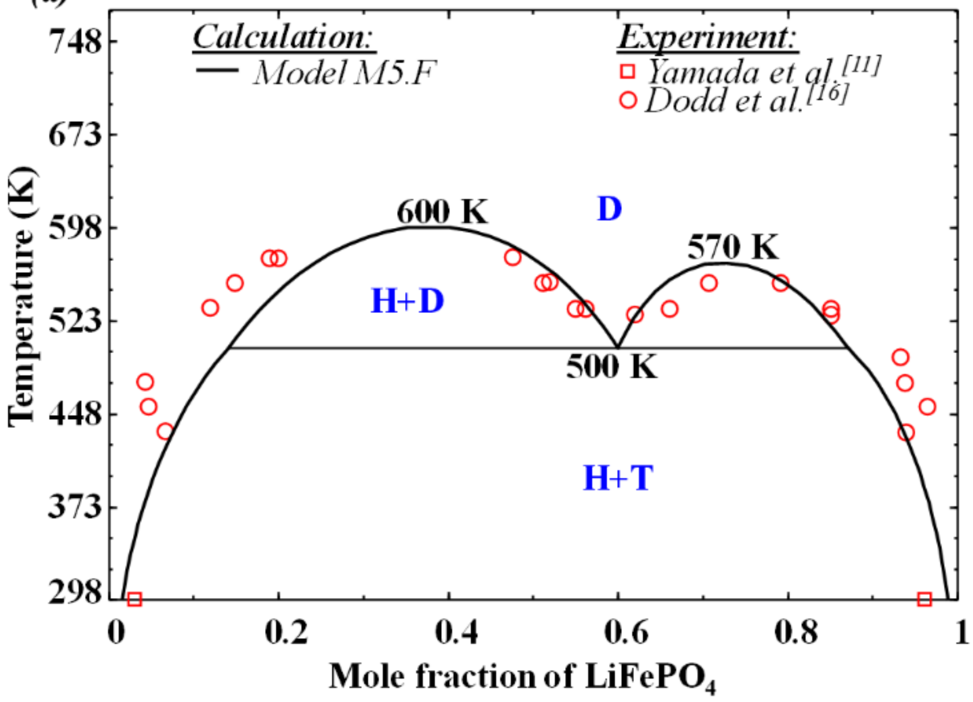
Calculation:
Model M5.F
Experiment:
Yamada et al.[11]
Dodd et al.[16]
748
673
598
523
448
373
298
Temperature (K)
600 K
D
570 K
H+D
500 K
H+T
0
0.2
0.4
0.6
0.8
1
Mole fraction of $LiFePO_4$

Figure 4.1: Phase equilibria of $LiFePO_4$-$FePO_4$ olivine join calculated by using: (a) model M4; (b) model M6; (c) model M5.L; (d) model M5.F in comparison with experimental data (□ Yamada et al. [26], ○ Dodd et al. [28] and Δ Delacourt et al. [29]). H, T, and D denote $FePO_4$ (heterosite), $LiFePO_4$ (triphylite) and Li_xFePO_4 (disordered) phase, respectively.

4.3.3 5-sublattice model M5.L: $(Li^+, Va^0)_3(Li^+, Va^0)_2(Fe^{2+}, Fe^{3+})_5(P^{5+})_5(O^{2-})_{20}$ and M5.F: $(Li^+, Va^0)_5(Fe^{2+}, Fe^{3+})_3(Fe^{2+}, Fe^{3+})_2(P^{5+})_5(O^{2-})_{20}$

Two 5-sublattice-models are obtained by splitting either the first (Li^+,Va^0) or the second (Fe^{2+},Fe^{3+}) sublattice of model M4 by a 3:2 ratio. The optimized thermodynamic parameters used for both M5.L and M5.F are given in Table 4.1. The value of each Gibbs energy parameter (Table 4.1) used in our models is the optimized value in order to fit the calculated phase diagram with the experimental point of $LiFePO_4$-$FePO_4$ olivine join [28]. In our models, the value of any Gibbs energy parameters is only around 1 % of the free energy of pure $LiFePO_4$ and pure $FePO_4$ (Table 4.1). Besides, no excess Gibbs energy term is utilized to keep the number of adjustable parameters in the model to the minimum.

Consequently, the obtained low-temperature phase diagram by using either model M5.L or model M5.F describes the experimental data satisfactorily, and the eutectoid composition is successfully obtained at $x = 0.6$ and $T = 500\ K$ (Figure 4.1c,d). Computation of the $FePO_4$-$LiFePO_4$ phase equilibria using either model M5.F or M5.L is reasonable with Blander's reciprocal $I^{ex}_{Li^+,Va^0:Fe^{2+},Fe^{3+}}$ set to 0 representing no SRO between mixing ions on different sublattices. The asymmetry of the obtained phase diagram is compatible with other authors [23, 27-29, 169]. The calculated cathode join shows greater solubility on the $FePO_4$ side at 298 K . A higher solid solution formation temperature on the low lithium composition side indicates a higher energy barrier to form a homogeneous solid solution with low $LiFePO_4$ composition. Therefore, it is more likely to form solid solution near $LiFePO_4$.

Below the eutectoid temperature, the 2-phase immiscibility is mainly driven by the enthalpy of mixing term as any negative excess entropy of reasonable value could only have a limited impact at the low temperatures. Our models M5.L and M5.F give an enthalpy of mixing of 3.5 kJ/mol at the eutectoid point ($x = 0.6$ and $T = 500\ K$) (Figure 4.2), which is in agreement with the reported experimental data [28, 114]. Even if it is possible to reproduce the enthalpy of mixing reported by Stevens *et al.* [114] using an excess entropy term, it would increase the number of parameters in our models. Therefore, because of the lack of experimental data on the enthalpy of mixing of this system, we did not use any excess entropy term to keep our model simple while still reproducing the reported experimental enthalpy of mixing properly. Additionally, the maximum solid solution free energy at 298 K was estimated to be ~1.5 kJ/mol by Malik *et al.* [170], which is in agreement with our maximum free energy of mixing of ~1.2 kJ/mol (Figure 4a). This value of the Gibbs energy of mixing is very different from what was estimated by Lee's model [24]. The Gibbs energy of mixing of the solid solution at 298 K according to the parameters provided by Lee is non-positive for any compositions and it reaches its minimum value of -14 kJ/mol at $x = 0.55$ [24]. Therefore, a solid solution phase with composition of $x = 0.55$ is always stable at 298 K according to Lee's model, proving that the thermodynamic model reported by Lee is unreliable.

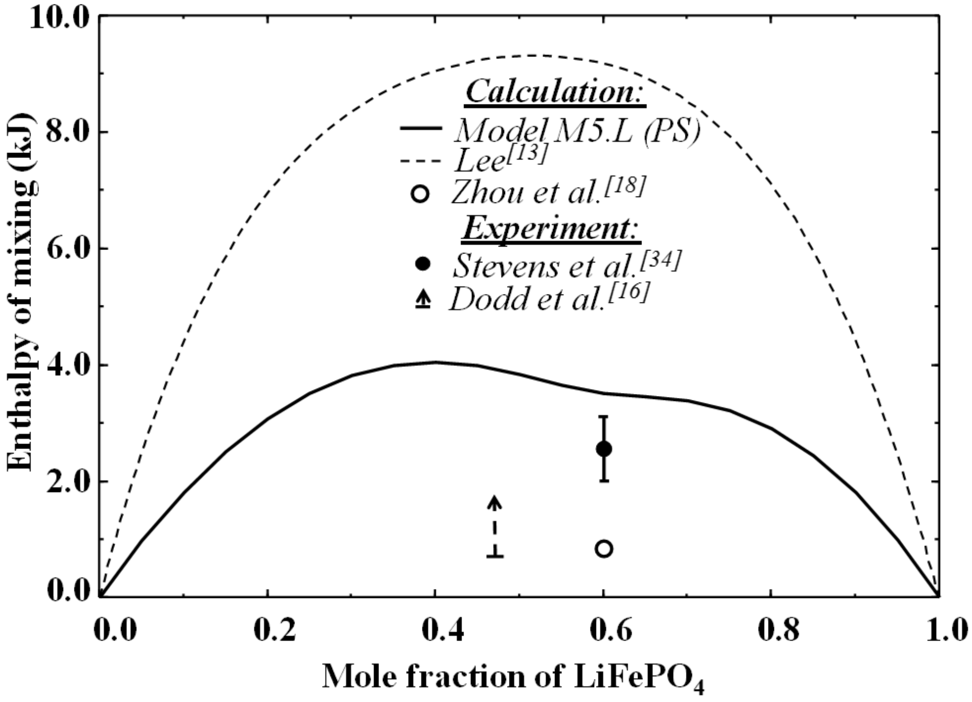

Figure 4.2: The calculated enthalpy of mixing at the eutectoid temperature of 500 K using our model M5.L in comparison with that estimated by Lee's model [24], Zhou et al. [63], the

experimental lower limit of the enthalpy of mixing suggested by Dodd et al. [28] and the experimental enthalpy of mixing with its error bar reported by Stevens et al. [114].

So far, we have mentioned the two models M5.L and M5.F together because, from an optimization point of view, they are equivalent. Model M5.F could produce exactly the same equilibrium phase diagram of $FePO_4$-$LiFePO_4$ as model M5.L. However, from a crystallographic point of view, they are different. Model M5.L describes the LRO of Li^+ and Va^0 while model M5.F describes the LRO of Fe^{2+} and Fe^{3+}. It is possible that the arrangement of oxidation states of iron (Fe^{2+} and Fe^{3+}) is more likely than the long-range arrangement of nuclei Li^+ and vacancy Va^0. Vice versa, the LRO of Li^+ and Va^0, as shown in the *ab initio* calculation of Furutski *et al.* [35], might be preferable. If the LRO of Li^+ and Va^0 exist, it could be detected through electron microscopy (e.g., TEM), whereas any long-range arrangement of different oxidation states of iron (Fe^{2+} and Fe^{3+}) could be uncovered through Mössbauer spectroscopy. In fact, the arrangement of Li^+ and Va^0 should involve the diffusion of the nuclei, while the LRO assembly of Fe^{2+} and Fe^{3+} ion should only require the adjustment of ionic charge via electron diffusion. In our opinion, since electrons are mobile, the electron movement is much easier than the nucleus jumps within the microstructure. Therefore, the LRO of Fe^{2+} and Fe^{3+} ion or model M.5F seems to be preferable than the long-range arrangement of nuclei Li^+ and vacancy Va^0 of model M.5L. Nevertheless, there has not been any experimental reports showing crystallographic evidence to prove which of our two models is more appropriate. Up to now, only Furutski *et al.* [35] has confirmed the existence of a supercell structure of the equilibrium solid solution $Li_{0.6}FePO_4$. Their DFT calculations, which provided their proposed supercell structure, appears to be the only evidence up to now. As a result, it is impossible to confirm which one among our proposed models is exact.

Briefly, our thermodynamic M5.L and M5.F models of Gibbs energy sufficiently reproduce the $LiFePO_4$-$FePO_4$ phase diagram consisting of three sub-miscibility gaps and a eutectoid reaction. Our two models that consider an extra level of LRO provide a better description of the solid solution than that reported by Lee since he used SRO represented by a bad Blander's term that wrongly split the miscibility gap [24]. Moreover, the models estimate the thermodynamic properties of the system quite well, such as the enthalpy of mixing and the maximum free energy of mixing.

Table 4.1 Parameters of the thermodynamic model M5.L and M5.F

Compounds	$\boldsymbol{G^{\circ}_{LiFePO_4}}(Jmol^{-1}) = \Delta H^{298}_{LiFePO_4} + \int_{298}^{T} C_p^{LiFePO_4} dT - T \cdot S^{298}_{LiFePO_4} - \int_{298}^{T} \frac{C_p^{LiFePO_4}}{T} dT$ $\Delta H^{298}_{LiFePO_4}(Jmol^{-1}) = -1616020$ [111] $S^{298}_{LiFePO_4}(Jmol^{-1}K^{-1}) = 130.95$ [100] $C_p^{LiFePO_4}(Jmol^{-1}K^{-1}) = -41.881336 + 0.78278483 \cdot T + 890694.39 \cdot T^{-2} - 0.0010255433 \cdot T^2 + 5.0862948 \cdot 10^{-7} \cdot T^3$ (with $250 \leq T \leq 773$ [99-101]) $= 247.915258 - 0.01771626 \cdot T - 28310678.63 \cdot T^{-2}$ (with $773 \leq T \leq 1473$ [99-101])
	$\boldsymbol{G^{\circ}_{FePO_4}}(Jmol^{-1}) = \Delta H^{298}_{FePO_4} + \int_{298}^{T} C_p^{FePO_4} dT - T \cdot S^{298}_{FePO_4} - \int_{298}^{T} \frac{C_p^{FePO_4}}{T} dT$ $\Delta H^{298}_{FePO_4}(Jmol^{-1}) = -1279230$ [111] $S^{298}_{FePO_4}(Jmol^{-1}K^{-1}) = 122.21$[104] $C_p^{FePO_4}(Jmol^{-1}K^{-1}) = 114.52232 + 0.05966384 \cdot T - 2690312 \cdot T^{-2}$ (with $298.15 \leq T \leq 2000$ [101, 104])
Gibbs energy parameter ($\boldsymbol{Jmol^{-1}}$)	$\Delta G^{\circ}_{FePO_4{}^{-}} = \Delta G^{\circ}_{LiFePO_4{}^{+}} = 15000$ $\Delta G^{\circ}_{adjust\_1} = 19500$ $\Delta G^{\circ}_{adjust\_2} = 29250$
End-member ($\boldsymbol{Jmol^{-1}}$)	***Model M5.L:*** $G^{\circ}_{Li^{+}:Li^{+}:Fe^{2+}} = 5 \cdot G^{\circ}_{LiFePO_4}$ $G^{\circ}_{Va^{0}:Va^{0}:Fe^{3+}} = 5 \cdot G^{\circ}_{FePO_4}$ $G^{\circ}_{Li^{+}:Li^{+}:Fe^{3+}} = 5 \cdot G^{\circ}_{LiFePO_4} + 5 \cdot \Delta G^{\circ}_{LiFePO_4{}^{+}}$ $G^{\circ}_{Va^{0}:Va^{0}:Fe^{2+}} = 5 \cdot G^{\circ}_{FePO_4} + 5 \cdot \Delta G^{\circ}_{FePO_4{}^{-}}$ $G^{\circ}_{Va^{0}:Li^{+}:Fe^{2+}} = 3 \cdot G^{\circ}_{FePO_4} + 3 \cdot \Delta G^{\circ}_{FePO_4{}^{-}} + 2 \cdot G^{\circ}_{LiFePO_4}$ $G^{\circ}_{Va^{0}:Li^{+}:Fe^{3+}} = 2 \cdot G^{\circ}_{LiFePO_4} + 2 \cdot \Delta G^{\circ}_{LiFePO_4{}^{+}} + 3 \cdot G^{\circ}_{LiFePO_4}$

	$G^{\circ}_{Li^{+}:Va^{0}:Fe^{2+}} = 3\cdot G^{\circ}_{LiFePO_4} + 2\cdot G^{\circ}_{FePO_4} + 2\cdot \Delta G^{\circ}_{FePO_4^{-}} - \Delta G^{\circ}_{adjust\_1}$ $G^{\circ}_{Li^{+}:Va^{0}:Fe^{3+}} = 2\cdot G^{\circ}_{FePO_4} + 3\cdot G^{\circ}_{LiFePO_4} + 3\cdot \Delta G^{\circ}_{LiFePO_4^{+}} - \Delta G^{\circ}_{adjust\_2}$ ***Model M5.F:*** $G^{\circ}_{Li^{+}:Fe^{2+}:Fe^{2+}} = 5\cdot G^{\circ}_{LiFePO_4}$ $G^{\circ}_{Va^{0}:Fe^{3+}:Fe^{3+}} = 5\cdot G^{\circ}_{FePO_4}$ $G^{\circ}_{Li^{+}:Fe^{3+}:Fe^{3+}} = 5\cdot G^{\circ}_{LiFePO_4} + 5\cdot \Delta G^{\circ}_{LiFePO_4^{+}}$ $G^{\circ}_{Va^{0}:Fe^{2+}:Fe^{2+}} = 5\cdot G^{\circ}_{FePO_4} + 5\cdot \Delta G^{\circ}_{FePO_4^{-}}$ $G^{\circ}_{Va^{0}:Fe^{3+}:Fe^{2+}} = 5\cdot G^{\circ}_{FePO_4} + 2\cdot \Delta G^{\circ}_{FePO_4^{-}}$ $G^{\circ}_{Li^{+}:Fe^{3+}:Fe^{2+}} = 5\cdot G^{\circ}_{LiFePO_4} + 3\cdot \Delta G^{\circ}_{LiFePO_4^{+}}$ $G^{\circ}_{Va^{0}:Fe^{2+}:Fe^{3+}} = 5\cdot G^{\circ}_{FePO_4} + 3\cdot \Delta G^{\circ}_{FePO_4^{-}} - \Delta G^{\circ}_{adjust\_2}$ $G^{\circ}_{Li^{+}:Fe^{2+}:Fe^{3+}} = 5\cdot G^{\circ}_{LiFePO_4} + 2\cdot \Delta G^{\circ}_{LiFePO_4^{+}} - \Delta G^{\circ}_{adjust\_1}$

4.4 Cell voltage prediction

The electromotive force and the open-circuit voltage (OCV) at low rates of charging and discharging of $LiFePO_4$||Li ion batteries are dependent on chemical potentials, and consequently on the $LiFePO_4$-$FePO_4$ phase diagram as shown in a number of studies [18, 22, 24-27]. The OCV depends on the chemical potential of lithium in both the lithium metallic anode and olivine-type lithium phosphate cathode:

$$V(x) = -\frac{\mu_{Li}^{cathode}(x) - \mu_{Li}^{anode}}{nF} \tag{4.9}$$

where $\mu_{Li}^{cathode}(x)$ is the chemical potential of Li in the intercalation compounds Li_xFePO_4; μ_{Li}^{anode} is the chemical potential of metallic Li ($\mu_{Li}^{anode} = 0$); F is Faraday's constant; and n is the charge (in electrons) transported by lithium through the electrolyte ($n = 1$ in this case). Therefore, the cell voltage is dependent on the chemical potential of Li in the solid solution Li_xFePO_4 only:

$$V(x) = -\frac{\mu_{Li}^{cathode}(x)}{F} = -\frac{\partial G(x)}{F \cdot \partial x} \tag{4.10}$$

where G is the molar Gibbs energy of the cathode Li_xFePO_4 calculating from the mixing Gibbs energy of the solid solution G_m. Considering the lithiation (delithiation) process during battery operation via equilibrium route, according to the optimized Gibbs energy of solid solution at 298 K, the coexistence of $FePO_4$ and $LiFePO_4$ should result in a stable voltage plateau at ~3.5 V (Figure 4.3a) as reported previously [21]. As the temperature increases, the voltage plateau increases and its width decreases. Raising the temperature above the eutectoid reaction should lead to the formation of the intermediate phase $Li_{\sim 0.6}FePO_4$ during equilibrium delithiation. Two voltage plateaus correspond to the coexistence of $LiFePO_4$-rich phase and the intermediate phase as well as the co-occurrence of the intermediate phase and $FePO_4$-rich phase (Figure 4.3a). According to our calculation, the voltage difference between the two plateaus is not very significant ($\Delta V = 8.6\ mV$ at $T = 563\ K$). Such a small voltage plateau separation due to the existence of the intermediate phase could be difficult to detect through experiments.

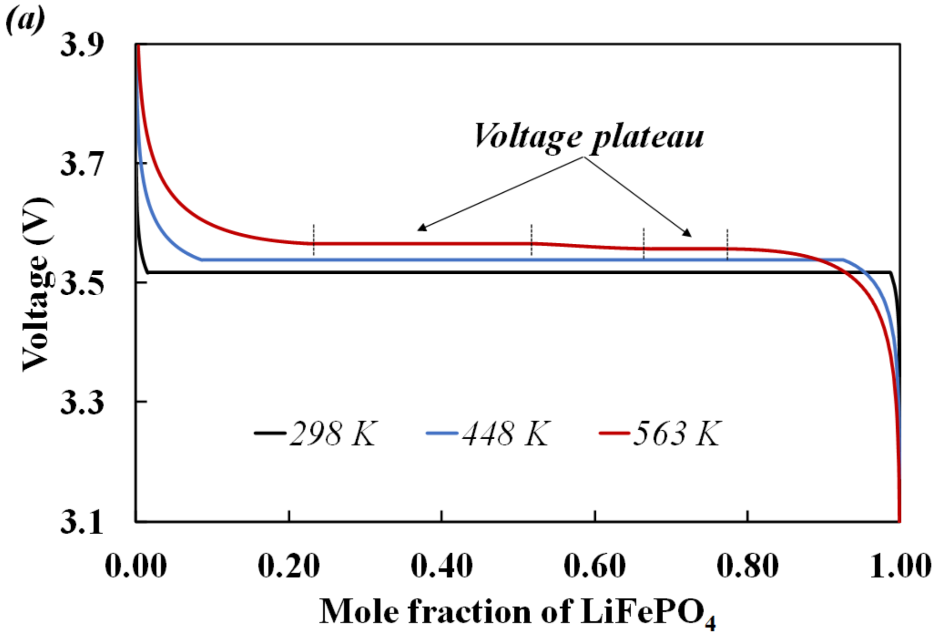

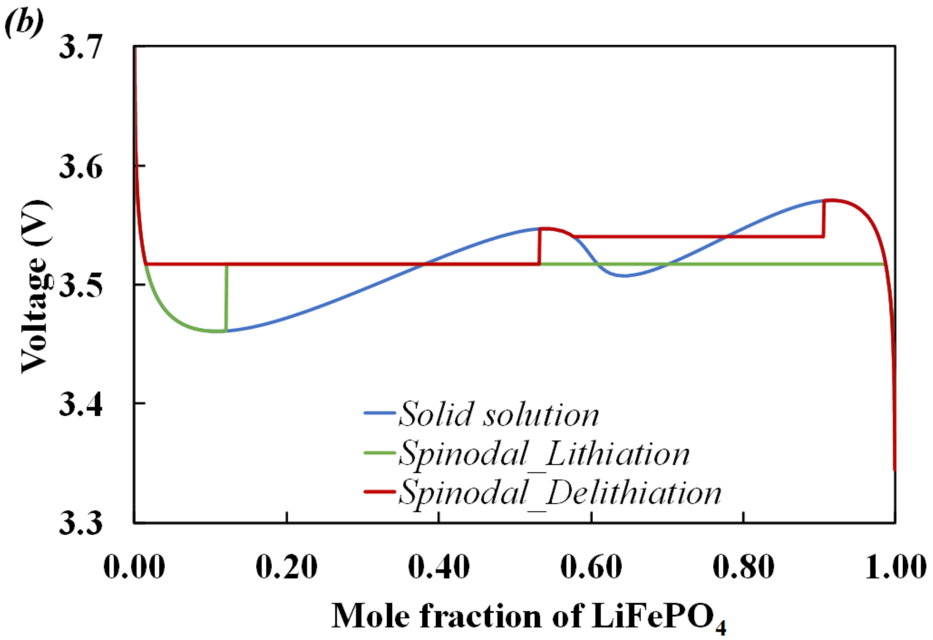

Figure 4.3: Calculated Open-Circuit Voltage (OCV) curves obtained by a/ delithiating a particle LiFePO4 via equilibrium phase transformation at various temperatures (298 K, 448 K, 563 K) where the two voltage plateaus at 563 K are marked and b/ delithiating a particle LiFePO4 and lithiating a particle FePO4 via spinodal decomposition and delithiating/lithiating a particle via solid solution route at 298 K.

A binary phase diagram with two miscibility gaps merging into one, like $FePO_4$-$LiFePO_4$ join, is rather rare. Therefore, spinodal decomposition of this system should be more complicated than the spinodal decomposition observed in other systems with only a single miscibility gap. In this study, model M5.L is picked as the basic model to calculate the boundary of spinodal decomposition (Figure 4.1c). The result of the spinodal decomposition calculation is exactly the same for model M5.F. The spinodal decomposition of the cathode join might be related to fast charge transport during the delithiation process [131, 132, 136, 171]. The change of the molar Gibbs energy of mixing of the solid solution via spinodal decomposition during the delithiation of a $LiFePO_4$ particles at 298 K follows the arrows illustrated in Figure 4.4. The delithiation of $LiFePO_4$ initially moves along the single-phase solid solution route where lithium ions diffuse conventionally. As the energy of charging is high enough, the $LiFePO_4$ particle can bypass the equilibrium $\mathbf{e_1}$/$\mathbf{e_2}$, and the Gibbs energy continues rising toward the point $\mathbf{s_2}$’. When the system reaches to any point $\mathbf{g_1}$ beyond the spinodal boundary $\mathbf{s_2}$’, any local composition fluctuation of the solid solution should result in a spinodal decomposition. The solid solution phase very quickly decomposes into a $LiFePO_4$-rich $\mathbf{a_1}$ phase and intermediate $\mathbf{a_2}$ phase, which are parts of a metastable common tangent. As the charging process continues, the Gibbs energy of the system moves along the $\mathbf{a_1a_2}$ line toward the $\mathbf{a_2}$ point by changing the mole fraction of the phases via lithium diffusion. The system continues to consume phase $\mathbf{a_1}$ until only phase $\mathbf{a_2}$ is left, and then it becomes a single solid solution phase. As lithium diffuses out of the solution, the Gibbs energy of the system arrives at $\mathbf{g_2}$, which is beyond the spinodal boundary $\mathbf{s_1}$”. At that point, any local composition fluctuation would make the solid solution decompose quickly via spinodal decomposition. Since there is no metastable common tangent line like $\mathbf{a_1a_2}$ existing in the $FePO_4$-rich region, the decomposition finally reaches to the equilibrium, i.e., the coexistence of the two equilibrium $\mathbf{e_1}$ and $\mathbf{e_2}$ phase. The phase fraction of $\mathbf{e_1}$ should increase, and the Gibbs energy moves along the $\mathbf{e_1e_2}$ line toward $\mathbf{e_1}$ as delithiation, which requires lithium diffusion, carries on. When only the $\mathbf{e_1}$ phase remains, the system finishes the delithiation process by driving lithium ions out of the solid solution (Figure 4.4a). It is noticeable that the delithiation of $LiFePO_4$ at 298 K via spinodal decomposition consists of a metastable and a stable spinodal decomposition. The metastable spinodal decomposition results the coexistence of the two metastable $\mathbf{a_1}$ and $\mathbf{a_2}$ phase, while the stable spinodal decomposition finally comes up with the co-occurrence of the two equilibrium $\mathbf{e_1}$ and $\mathbf{e_2}$ phase.

The lithiation of $FePO_4$ at 298 K via spinodal decomposition, however, is dissimilar to the delithiation process. The system has to follow the single-phase solid solution curve toward point $\mathbf{s_1}$’ as lithium ions diffuse and the lithiation progresses. Two possibilities can occur when the system reaches point $\mathbf{g_3}$ beyond the spinodal decomposition boundary $\mathbf{s_1}$’. If the driving force of lithiation is low, any local concentration variation then results in the coexistence of the equilibrium $\mathbf{e_1}$ and $\mathbf{e_2}$ phase. The system finally finishes the lithiation process via equilibrium route (Figure 4.4a). If the driving force is large enough to maintain the single-phase solid solution transformation, which requires lithium diffusion, the system could go over the first spinodal region (between $\mathbf{s_1}$’ and $\mathbf{s_1}$”) and reach $\mathbf{g_4}$, a point beyond the spinodal boundary $\mathbf{s_2}$”. At this point, any local variation of composition of the solid solution could cause the spinodal decomposition to decrease the energy of the system. Metastable $\mathbf{a_1}$ and $\mathbf{a_2}$ phase are formed. The system subsequently reaches $\mathbf{a_1}$ via lithiation and it follows the single-phase solid solution routes which involves conventional lithium ions diffusion to finish the lithiation process (Figure 4.4a). Obviously, the energy barrier for single-phase solid solution lithiation in an $FePO_4$-rich region is higher than that in a $LiFePO_4$-rich region (Figure 4.4a). If the system can overcome the first energy barrier in the $FePO_4$-rich region, it is likely to overcome the second barrier, and the system should follow the single-phase transformation rather than spinodal decomposition at any point $\mathbf{g_4}$ beyond $\mathbf{s_2''}$. Therefore, the second possibility is less preferable. Noticeably, lithiation via spinodal decomposition (either possibilities) requires the system to go over a higher energy barrier than that of delithiation, hence lithium insertion becomes more difficult than lithium extraction process. This agrees with the general knowledge that lithium insertion is harder to achieve and kinetically lower than lithium extraction [135, 172].

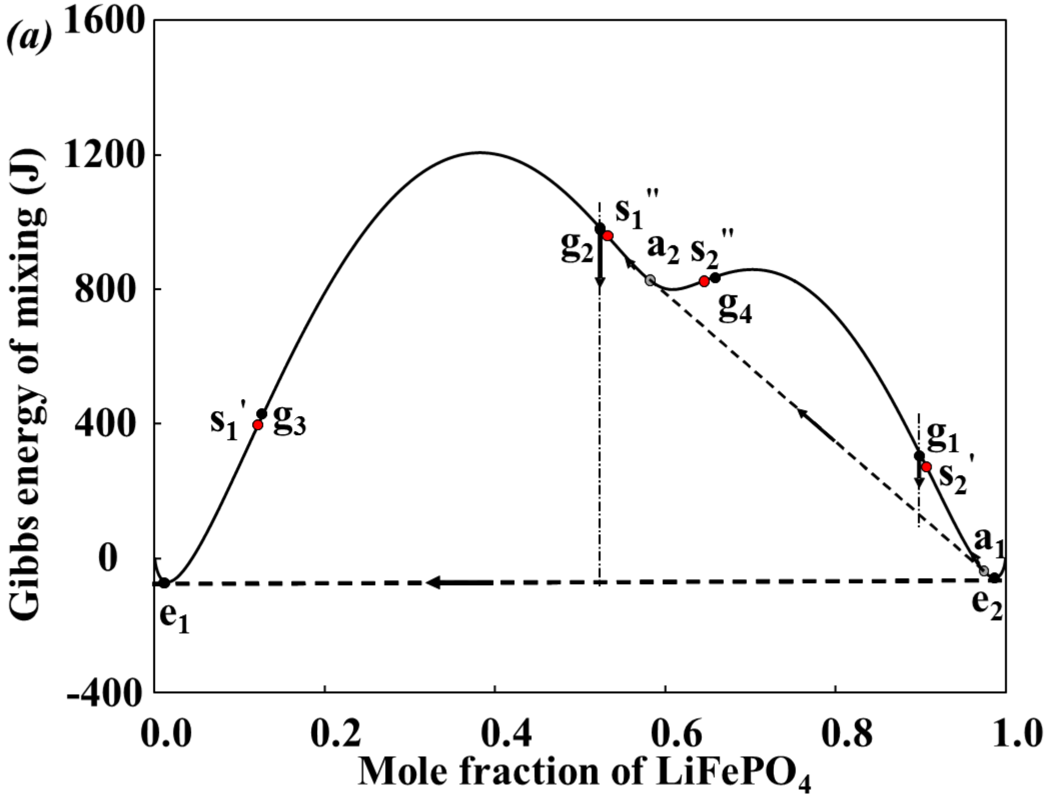

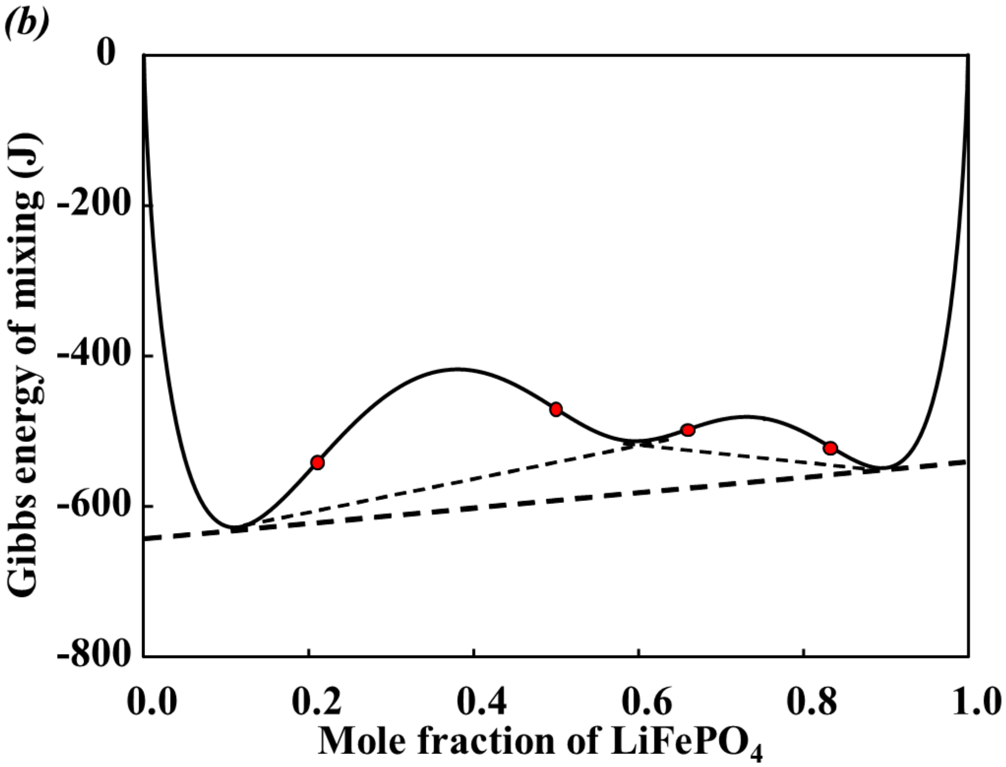

Figure 4.4: The Gibbs energy of mixing of the solid solution Li_xFePO_4 at a/ 298K and b/ 478K. e_1, e_2 are the two equilibrium compositions for the heterosite and the triphylite phase; s_1', s_1", s_2', and s_2" are the boundaries of spinodal decomposition; g_1, g_2, g_3, and g_4 are any solid solution within the corresponding spinodal decomposition region; a_1, and a_2 are the two compositions of the metastable common tangent corresponding to the $LiFePO_4$-rich region; the arrows illustrated the molar Gibbs energy of the system via spinodal decomposition during the delithiation of $LiFePO_4$.

By tracing the change of the molar Gibbs energy of the system, open circuit voltage (OCV) curves are calculated by lithiating a particle $FePO_4$ and delithiating a particle $LiFePO_4$ via spinodal decomposition in comparison with the OCV via a single-phase lithiation/delithiation process (Figure 4.3b). As the delithiation progressed to the first spinodal composition, the voltage suddenly drops to the equilibrium plateau, with an overpotential of 230 mV. The voltage drops even more to the equilibrium plateau according to the second spinodal decomposition as the lithium continues to extract from the solid solution (Figure 4.3b). In contrast, as lithium insert in $FePO_4$ via discharging, the voltage curve could fall abruptly to the equilibrium voltage as the overall solid solution composition goes beyond the spinodal point **s_1'**. Only one voltage plateau of lithiation via spinodal decomposition is observed (Figure 4.3b) rather than two voltage plateaus as reported by Bai *et al.* [132]. In brief, dissimilar lithiation and delithiation of the battery causes unalike OCV curves at 298K.

As the temperature increases, the intermediate phase becomes more stable. The metastable common tangent line of the $FePO_4$-rich region starts to occur at a temperature of 458 K. Thus, at any temperature higher than 458 K and lower than the eutectoid temperature, there exists two metastable common tangents and one stable common tangent (Figure 4.4b). Consequently, delithiation and lithiation become similar, and they both contain two metastable spinodal decompositions resulting in two voltage plateaus that are different from the equilibrium plateau in their OCV curves. As the temperature increases further to go over the eutectoid temperature, the miscibility gap split into two, the two metastable common tangents become stable ones, and, consequently, two stable spinodal decompositions should be evident.

In short, unlike spinodal decompositions in a conventional system, there exists up to two spinodal decomposition steps resulting in the two voltage plateaus through the charging/discharging process of the battery at a low temperature. Therefore, the low-temperature miscibility gap of $FePO_4$-$LiFePO_4$ join is considered as a combination of two miscibility gaps. Moreover, the different spinodal decomposition steps (metastable or stable spinodal decomposition), the unlike lithiation and delithiation processes, and consequently, the dissimilar OCV voltage plateaus via discharging or charging at low temperature reveal the asymmetric behavior of the system. Noticeably, the discussion of charging or discharging processes in this paper is suitable only at a very slow rate where atoms have enough time to move. Certainly, having only a thermodynamic description of the equilibrium transformation of the cathode materials is not enough to understand the behavior of materials during the battery operation. At last, it is important that we successfully developed an effective model to describe the $FePO_4$-$LiFePO_4$ olivine join. This model will be later extended in a future work to consider other factors affecting the cathode materials during charging or discharging.

4.5 Conclusion

A new formalism of the Gibbs energy of the solid solution Li_xFePO_4 bearing in mind an extra level of LRO is proposed for the thermodynamic description of the $LiFePO_4$-$FePO_4$ olivine join. The optimized phase diagram reproduces, with satisfactory accuracy, the available experimental data, including the eutectoid reaction, the asymmetry, and the enthalpy of mixing. The present thermodynamic model can also predict the increase of the voltage plateau with temperature during the lithiation or delithiation process. Further temperature rise could split the voltage plateau into two different plateaus. Besides, spinodal decomposition, which is possibly related to the fast charge of the battery, reveals the dissimilarity between delithiation and lithiation, hence the distinction of the corresponding OCV curves at 298 K. As the temperature increases, delithiation/lithiation via spinodal decomposition could change. Moreover, our thermodynamic model could be extended to a more advanced model to justify the roles of doping with impurities such as Ni, Co, Mn, Mg, Na, etc. or anti-site defects, which could affect the charge transport properties within the cathode material and, thus, the battery operation.

4.6 Acknowledgements

The authors recognize the support of Natural Science, Engineering Research Council of Canada and the Canadian Foundation for Innovation through the Automotive Partnership Canada program and our industry partner Johnson-Matthey.

CHAPTER 5 ARTICLE 2: MODELING OF COHERENT PHASE TRANSFORMATION AND PARTICLE SIZE EFFECT IN $LiFePO_4$ CATHODE MATERIAL AND APPLICATION TO THE CHARGING/DISCHARGING PROCESS

Anh Thu Phan, Aïmen E. Gheribi and Patrice Chartrand

Published in Electrochimica Acta volume 295, pages 632-644 February 01 2019

Abstract:

The effect of coherent strains which is involved during the fast charge/discharge processes and the influence of particle size reduction which improves the electrochemical performance of the cathode material are modelled in this study. An extension of the linear isotropic approximation for elastic energy stored in the coherent boundaries of an orthorhombic system is performed for the first time to calculate the coherent miscibility gaps of the $LiFePO_4$-$FePO_4$ cathode join. Noticeable, this approach is applicable for any thermodynamic models used for describing the equilibrium $LiFePO_4$-$FePO_4$ join. The coherent miscibility gaps corresponding to various crystallographic directions, which could explain the occurrence of a metastable phase, favorable phase boundaries during lithiation (delithiation), and the formation of dislocations or cracks via cycling, are presented. (100) is considered as the softest direction for coherence to form and the existence of (110) and (010) habit planes is also possible. Moreover, it is the first time that a model of particle size effect on both equilibrium and coherent olivine join is developed. Additionally, it is the first combined coherency-size type of calculation ever reported. The difference between the surface energies of the pure $LiFePO_4$ and $FePO_4$ and the excess surface energy of the olivine solid solution are the two important model parameters affecting the equilibrium and the coherent miscibility gaps. As the particle size decreases, the miscibility gaps shrink favoring the intermediate phase region between the two miscibility gaps. At nanoscale, coherent phase transformation seems to be more likely.

5.1 Introduction

The energy crisis is one of the greatest challenges in the 21st centuries, therefore, development of environmentally friendly, sustainable and renewable energy supplies becomes more and more vital for a sustainable modern society [173]. As excellent reversible energy storage devices, lithium-ion batteries (LIBs), which possess better features than the conventional batteries [174], play an important role not only in the area of consumer electronics but also in large-scale applications such as plug-in hybrid vehicles or electrical vehicles [10, 18, 21, 27, 34, 174]. $LiFePO_4$ is considered as a promising cathode material because of its low cost, improved safety performance, high chemical stability, low toxicity, high theoretical reversible capacity (170 mAh/g) and an extremely flat charge-discharge profile at a reasonably high potential of ~3.5 V versus Li/Li^+ [16-19, 175]. The flat charge-discharge profile is claimed as a consequence of the coexistence of two phases: heterosite ($FePO_4$) and triphylite ($LiFePO_4$) [18, 23-27]. Hence, reliable thermodynamic knowledge of $FePO_4$-$LiFePO_4$ phase equilibria, which is critical to understand the lithiation and delithiation of the cathode material during the battery operation, has been shown in our previous study [133].

Initially, the main drawbacks of the cheap and nontoxic $LiFePO_4$ cathode material are its poor electronic and ionic conductivity. Its electrical conductivity, which is ~10^{-10} $S.cm^{-1}$ at room temperature, is extremely low for a cathode material [31, 176]. Consequently, bulk $LiFePO_4$ is considered suitable for low-rate applications [20]. However, its rate performance has been improved significantly by: 1) reducing the active particle size to the nano-scale; and 2) coating active particles with carbon [21, 23, 27, 34]. The high capacity and rate capability related to the $LiFePO_4$/C cathode material was revealed recently [177]. Frequently, the specific capacity achieved by a $LiFePO_4$/C cell is close to the theoretical specific capacity of $LiFePO_4$ [175]. C-coated $LiFePO_4$ nanoparticles can remarkably provide high specifications for a power density of more than 5 kW/kg [18, 27, 34]. Its rate capability is comparable with or better than that of $LiCoO_2$ [175]. The reason why $LiFePO_4$ nanoparticles, unlike the bulk, can be considered as a high rate battery material has not yet been explained clearly. Therefore, the aim of this study is to provide our understandings of the phase transformation mechanism, thus the lithium intercalation pathway in $LiFePO_4$, and the importance of particle size since they directly determine the capacity, rate performance and columbic efficiency. The role of carbon coating will not be considered in the present study because carbon is said to improve physical properties of the battery material such as its electrical conductivity, its tap density, etc. [178] rather than its thermodynamic behavior. Nanoscale particles exhibited a very high stability during the carbon coating process without formation of any secondary phases [179].

5.1.1 Coherent phase transformation during charge/discharge

Several mechanistic models for describing (de)lithiation of $LiFePO_4$ during battery operation were proposed. The isotropic core shell model [16, 26] and the mosaic model [128] appear both energetically and kinetically unfavorable since both Li diffusion and coherent strain are anisotropic in $LiFePO_4$ [127], and the entire theoretical capacity (~170 mAh/g) becomes accessible even at high rate [180]. Delmas *et al.* [129] proposed the domino-cascade model, in which phase-boundary propagation perpendicular to the (010) direction is extremely rapid in comparison to the initial nucleation. It means that at any given snapshot of time, a Li_xFePO_4 particle is likely to be either fully lithiated or delithiated, as observed experimentally [129, 130]. Therefore, the driving force for domino-cascade phase transformation should be higher than the driving force for initial nucleation and it should take into account the formation of the coherent phase boundary. The phase separation could be also dominated by the spinodal decomposition process [18, 131-133]. In brief, the two-phase coexistence mechanism may change with particle size, morphology and electrochemical testing conditions [127, 134, 142-144, 181]. Although the knowledge of possible single-particle (de)lithiation mechanisms has progressed, the exceedingly rapid (dis)charging capability of $LiFePO_4$ had not been explained yet. One phase-phase solid solution mechanistic model, which might avoid crystalline nucleation and growth and deviate from the equilibrium phase diagram, was then suggested [20]. This solid solution transformation, especially in nano-particles, is energetically costlier but kinetically faster [20]. The $LiFePO_4$ cathode was claimed to even experience simultaneously both a two-phase reaction mechanism and a dual-phase solid solution reaction mechanism over the entire range of the flat voltage plateau [21]. Note that an implicit assumption of the single-particle behavior mirroring the electrodes-scale behavior was involved in the traditional analysis of experimentally obtained charging and discharging data. In an electrode assembly, it is experimentally observed that all $LiFePO_4$ particles are not (de)lithiated simultaneously but rather sequentially [142, 182-184]. Thus, any proposed mechanistic model for phase transformation of the cathode material should take into account the multi-particle behavior, rather than solely single-particle behavior.

Even though the anisotropy of the olivine crystal structure, the rapid charging and discharging capability are considered in the proposed mechanisms [16, 20, 26, 128, 129], none of them really puts concerns on the existing elastic constrains evidenced through experiments [127, 134-136]. It is highly possible to form a coherent interface between the two olivine phases ($LiFePO_4$ and $FePO_4$) during the battery charging or discharging processes. According to Novikov [185], the coherent interface is the "phase boundary wherein the atomic positions in adjoining planes of different crystal lattices coincide perfectly or almost perfectly". Any misfit between lattice parameters of the two phases at their coherent boundary should result in the formation of coherent strain. Undeniably, many existed similarities between $LiFePO_4$ and $FePO_4$ such as the same olivine crystal structure (space group: *Pnma*), equal to or less than 5% lattice parameter misfits [25, 29, 88, 160, 186-192]($a_{LiFePO_4} = 10.323$ Å [88], $b_{LiFePO_4} = 6.005$ Å [88], $c_{LiFePO_4} = 4.693$ Å [88] and $a_{FePO_4} = 9.8142$ Å [160], $b_{FePO_4} = 5.7893$ Å [160], $c_{FePO_4} = 4.782$ Å [160]) make them likely to be coherent. In a micrometer-sized all-solid-state battery cell, the growth pattern of both $LiFePO_4$ and $FePO_4$ was claimed to be clearly dominated by elastic effects rather than transport-controlled effects [193]. In addition, Meethoong *et al.* [127] noticed that the largest strain would occur in the sample with the smallest misfit in lattice parameters and unit cell volume between the triphylite and heterosite phase. Hence, the existence of coherent strain or compatibility stress in two-phase particles during charge/discharge was suggested [23]. The *in situ* observation of crystalline material during battery operation supports the prediction of coherent nucleation and growth [194].

Furthermore, the observation of a favorable interface, the existence the metastable phase during charge/discharge, and the presence cracks or dislocations via cycling should favor the coherent phase transformation hypothesis. Recently, Wang *et al.* [142] showed for the first time the coexistence of two phases in individual particles. The delithiation process and the $LiFePO_4/FePO_4$ interface were observed to move only along certain preferential sites [142]. The coherent strain is evidenced by the observation of aligned phase boundaries and striped morphologies in Li_xFePO_4 [134-136]. (100) is considered as the preferred direction [127, 134, 141], consistent with rapid Li diffusivity along the (010) direction [32, 33]. The origin of striped morphologies [134] was explained as a consequence of the characteristic wavelength of spinodal decomposition [136]. In addition, Malik *et al.* [20] claimed that a small and flat energetic difference between the phase separated state and the non-equilibrium solid solution would result in a weak thermodynamic driving force for solid solution phase to demix heterogeneously. However, as the eutectoid-like phase diagram of $LiFePO_4$-$FePO_4$ reveals three miscibility gaps [28], the free energy curve should not be totally flat all over the Li concentration range [141, 195]. A metastable phase, coherent strain and spinodal decomposition should exist and need to be considered. Besides, dislocations and cracks formed during electrochemical cycling should be related to lattice misfits in the two-phase coherent transformation mechanism rather than uniform change of lattice parameters via the one-phase solid solution mechanism. For nanosized particles, the structural mismatch inducing local constraints between the two phases makes the deintercalation easier [129]. Hence, a fully lithiated or delithiated single phase is formed in nano-size particles. In contrast, the lattice mismatch in micro scale particles generally results in energy relaxation [134]. Cracks and dislocations were found [142]. Energy relaxation by creating cracks and dislocations decreases the local constraints and weakens the driving force for boundary displacement. In fact, during electrochemical Li insertion and deinsertion, the occurrence of dislocations and cracks [143-147] increases the battery impedance and capacity fade over time. Less likely formation of dislocations and cracks in nano-$LiFePO_4$ results a long cycle life and reversibility at reasonable C-rates of the battery.

Even though there are many mechanistic models proposed, none of them is reliable to describe all of the phenomena occurring during battery operation. So far, no mechanistic model could explain the high kinetic rate of the Li_xFePO_4 olivine together with the existence of the strains between the two olivine phases during charging or discharging [127, 134-136], the presence of preferential interfacial planes [127, 135, 136, 141, 144], the observation of a metastable phase [148-151] and the occurrence of dislocations and cracks during cycling [142, 144-147].

In this study, the contribution of the stored strain energy during the coherent phase transformation within the cathode materials via delithiation or lithiation process will be studied to explain those phenomena. Cogswell and Bazant [144] showed only a single calculated coherent miscibility gap and suggested that the charge and discharge in batteries could follow either coherent transformation in each nanoparticle or mosaic scenarios where entire particles remain homogeneous with some particles existing at low concentration and others at high concentration. It appeared to possibly suppress coherent nucleation and growth of the second phase in particles at moderately elevated temperatures. Coherent strain was approximated to stabilize the solid solution at temperatures above 423.15 K - well below the disordering temperature [144]. Their fully anisotropic analysis [144] indicated that (101) should be the low-energy direction. They explained the observation of the phase boundaries along (100) as a partial loss of coherency caused by dislocations (or cracks) [144]. Although the authors showed the importance of coherent strains and spinodal decomposition during charge and discharge processes [144], the existence of the eutectoid reaction which could result the existence of a metastable phase and affect the coherent phase transformation, was totally omitted.

5.1.2 Effect of particle size during charge/discharge

Recently, a clear and systematic increase of solid solution nonstoichiometry with decreasing particle size and rising temperature was observed [23, 27, 34, 35]. The miscibility gap shrinkage was reported for both chemically [34], and electrochemically [23, 27] delithiated samples. According to the experimental report, miscibility gap reduction is noticeable when the particle size is smaller than ~100 nm. The two-phase region shrinks with decreasing particle size and for each particle size, and the miscibility gap boundaries shrink with increasing temperature [23, 27, 34, 35]. The solubility limits of both olivine phases, especially heterosite, obtained from the chemical analysis [34], are just slightly higher than that of electrochemical analysis [23, 27] (Figure 5.4). Moreover, there exists a critical particle size below which a complete olivine solid solution might be obtained at room temperature [23, 34, 121]. A certain appropriate particle size is required for the phase separation [121], and the miscibility gaps disappear below a critical size of ~20 nm [23, 34] or ~10 nm [121].

The reduction of the width of the miscibility gaps originates from particle-size-associated modifications to the molar free energy of mixing. Meethong *et al.* [23] suggested two different origins for the particle size effect: (i) increase due to the relative contribution of particle-matrix surface energy and surface stress, and (ii) coherency or compatibility stresses in two-phase particles with a coherent interface. The energy surface portion of the particle should be significant when the particle size is smaller than 100 nm [27]. On the other hand, the largest strain occurred in the sample with the smallest particle size, which gave the smallest misfits between the lattice parameters and unit cell volume of triphylite and heterosite phases [127]. It is possible that the coherent stress would rise when the misfits between two phases in a partially transformed particle are small enough to retain a coherent interface. As the lattice parameter misfits increase, incoherent interfaces and energy relaxation defects could form to relieve the strain. Chen *et al.* [134] revealed that phase boundaries in larger particles would consist of the boundary-dislocation network.

The objective of this study is to model the effect of coherent strains and particle size on the Gibbs energy of the olivine solid solution hence to report the modification of the $LiFePO_4$-$FePO_4$ olivine join. The appearance of coherent strains will be represented by the molar Gibbs elastic energy. The metastable phase, which could significantly reduce the internal elastic stress between the lithiated and delithiated phase, will be considered in our model of the Gibbs energy. Note that we do not consider the mechanistic model of the reaction within the cathode, i.e. no time parameter is involved. Moreover, since the $LiFePO_4$-$FePO_4$ olivine join changes by changing the particle size, the size constrained Gibbs energy which is possibly used to understand the thermodynamic behavior of the battery nanoparticles, is modeled.

5.2 Coherent miscibility gaps in the $FePO_4$-$LiFePO_4$ join

5.2.1 Deformation energy

In the measurement of phase compositions corresponding to any coherent miscibility gaps, a fully coherent interphase boundary between the two phases should be obtained for most of or the entire interphase boundary area [138]. The first condition for coherent decomposition to occur is the existence of an heterogeneous incoherent equilibrium miscibility gap. The second condition is an upper limit to the strain parameter δ of the second phase in complete analogy to the condition of coherent heterogeneous ordering reactions [153]. Depending on the constitution of a system in combination with its lattice parameter relations, coherent and non-coherent miscibility gaps can, therefore, be distinguished [153]. In an equilibrium miscibility gap, the solid solution demix heterogeneously to form two different phases which possess the same crystal structure, the same chemical potential of every end-member but have different lattice parameters, hence, no lattice deformation and therefore no elastic induced strain energy. Meanwhile, a coherent miscibility gap represents the demix of the solid solution into two phases which share the same lattice parameter at the coherent boundary by lattice deformation resulting in a stored elastic strain within the structure. This stored elastic energy compensates for the difference of the chemical potential of each end-member in the two coherent phases.

Coherent phase transformation draws attention in various thermodynamic systems such as alloys, oxides, alkalis, and lithium transition metal phosphate battery materials. Most of the thermodynamic systems whose coherent relationship is important, possess cubic crystalline structures, for example Au-Pt [196], Au-Ni [197], Al-Zn [198], Co-Cu [199], Ag-Cu [200], etc. Consequently, the most well-known method to calculate a coherent miscibility gap is the linear isotropic approximation developed by Cahn's group for cubic systems over 50 years ago [154-156]. It is applicable only in a linear medium where a strain is linearly dependent on the corresponding stress in every direction. In this approach, the coherent spinodal is calculated by considering the elastic energy resulting from the coherent misfit between the two cubic phases. The coherent spinodal boundary is computed by adding an elastic term which represents the elastic energy gained through coherent strain to the second derivatives of the chemical Gibbs energy of the solid solution:

$$\left(\frac{\partial^2 G_m^{chem}}{\partial \mathrm{x}^2}\right)_{T,P} + E_{elastic} = 0 \tag{5.1}$$

where G_m^{chem} is the chemical free energy of mixing of the solid solution $\mathrm{Li_xFePO_4}$ (x is the overall composition of $\mathrm{LiFePO_4}$); $E_{elastic}$ of a thermodynamic isotropic system which represents the density of strain energy stored is estimated as follow:

$$E_{elastic} = 2\eta^2 Y V_m = \frac{2\eta^2 E V_m}{1-\nu} \tag{5.2}$$

where $\eta = \frac{1}{a}\frac{da}{dx}$ is the linear change in lattice parameter a of the solid solution phase at the investigated overall composition x per unit composition change; V_m is the molar volume; Y is the elastic constant of the elastically soft direction (e.g. (111) direction in the fcc Al-Zn solid solution; (100) direction in the fcc NaCl-KCl solid solution); E stands for the Young's modulus; and ν is the

Poisson's ratio. The expression of Y is dependent on magnitude and temperature derivatives of elastic constants [154, 196]. Equation 5.2 is still valid even if the lattice parameter a does not obey Vegard's rule. As a result of Equation 5.2, the coherent spinodal temperature corresponding to any solid solution composition could be determined [201].

In order to take advantage of using the Gibbs energy minimization technique for calculating coherent miscibility gaps, in the present study, the molar elastic Gibbs energy which describe the energy contribution of the stored strain to the total Gibbs energy is expressed in terms of the overall composition rather than phase composition as shown previously [202-204]. Hence, the elastic Gibbs energy G_m^{el} of the olivine solid solution Li_xFePO_4 could be determined by double integrating the elastic term $E_{elastic}$ versus the overall composition x (with $0 \leq x \leq 1$):

$$G_m^{el} = \iint_0^x E_{elastic} dxdx + x \cdot G_{LiFePO_4}^{el} + (1 - x) \cdot G_{FePO_4}^{el} \qquad (5.3)$$

where $G_{LiFePO_4}^{el}$ and $G_{FePO_4}^{el}$ are the elastic energy of the two pure end-members of the olivine solid solution. In the isotropic approach, the $E_{elastic}$ term (Equation 5.2) or density of elastic energy is always positive when the reference states are the pure olivine-$FePO_4$ and olivine-$LiFePO_4$. Hence, the elastic Gibbs energy of the two pure compounds should be positive ($G_{LiFePO_4}^{el} > 0$ and $G_{FePO_4}^{el} > 0$). It is noticeable that physically, there should not be any coherent strain existed within a single phase like pure $LiFePO_4$, pure $FePO_4$ or solid solution Li_xFePO_4. A non-zero elastic energy is stored in and near the coherent boundary of the two coherent phases. It means that the elastic energy should exist only inside the miscibility gaps. In our model, the molar elastic energy does not describe the actual value of elastic energy stored in the coherent structure, but it is rather a representative of elastic effect on coherent phase transformation from a solid solution to the other two phases. This approach is selected for simplifying our calculations, even though physically speaking it is not exact. Our approach is better to use for modeling a wide miscibility gap (i.e. where the composition difference between the 2 phases is large) rather than a thin one. Utilizing the elastic Gibbs energy as a function of the overall composition helps us to not only employ Gibbs energy minimization techniques but also consider the available algorithm of thermodynamic softwares, e.g. Factsage.

Noticeably, according to Equation 5.3, the values of $G^{el}_{LiFePO_4}$ and $G^{el}_{FePO_4}$ should not change the value of the second derivative of G^{el}_m, hence the calculated coherent spinodal boundary does not alter. For convenience, $G^{el}_{LiFePO_4} = 0$ and $G^{el}_{FePO_4} = 0$ are chosen as boundary conditions of Equation 5.3 meaning that the elastic energy occurs only if two phases are co-existing. Nevertheless, the choice of the boundary conditions of G^{el}_m should affect the calculated value of the open circuit voltage (OCV) of the battery. With ~5% difference in molar volume and elastic constants of ~150-200 GPa [25], the total free energy of the system, according to Van der Ven *et al.* [141], increases by a maximum of nearly ~1000 J/mol when the coherent interface in the (100) plane forms between the two phases $LiFePO_4$ and $FePO_4$. It means that the energy gained by creating coherent interfaces does not significantly change the voltage profile (< ~10 mV) of the battery via charging or discharging. Therefore, our assumption of zero boundary conditions of G^{el}_m is reasonable. Moreover, the elastic Gibbs energy G^{el}_m is significantly dependent on the habit plane $[hlk]$. The most favorable habit plane should produce the least elastic Gibbs energy and the highest coherent consolute temperature. Our modification of Cahn's approach is successfully used for reproducing the coherent miscibility gap in the Au-Pt system, consistent with that reported by Xu *et al.* [196].

Since the solid solution Li_xFePO_4 possesses the olivine structure, for the first time, Cahn's approach is extended to an orthorhombic system (see appendix A). $E_{elastic}$ of an orthorhombic system is formulated based on Cahn's assumption [154-156] that the compositional fluctuation occurs along the direction of habit plane. It assumed that there is only one non-vanishing strain component occurring during the compositional fluctuation along the coherent direction. The corresponding stress and strain tensors based on different habit planes are then used to formulate the $E_{elastic}$ term (see appendix A). Estimation of $E_{elastic}$, then G^{el}_m require knowledge of physical properties of the solid solution. The physical properties such as lattice parameters, molar volume, elastic constants, etc. are composition and temperature dependent. Our calculations would consume a lot of time and resources if the composition and temperature dependence of every single physical properties are taken into account. In order to simplify the calculations, two cases are distinguished. In the first calculation, the coherent $LiFePO_4$-$FePO_4$ olivine join corresponding to various habit planes is estimated based on the physical properties which are only overall composition dependent. For the second calculation of coherent miscibility gaps, instead of adding the temperature effect to all the thermophysical properties of the olivine solid solution, a single temperature dependent term $t(x, T)$ (Equation B.4) which represents the influence of temperature on the calculated $\mathrm{E_{elastic}}$ value, hence the elastic Gibbs energy G_m^{el}, is used (see appendix B). Consequently, the change of the calculated coherent miscibility gaps by considering or not considering the temperature variation of all physical properties pertinent to the model will be revealed. In short, in the present study, the coherent miscibility gaps of $LiFePO_4$-$FePO_4$ join will be calculated by estimating the molar elastic energy for an orthorhombic system (see appendix A). All physical properties of the solid solution required for the model of the Gibbs elastic energy will be taken from literatures with suitable assumptions (see appendix B).

5.2.2 Calculated coherent miscibility gaps of $LiFePO_4$-$FePO_4$ olivine join

If the differences in lattice parameters are small enough (<~5%) to ensure a linear isotropic behavior [205], Cahn's approach is valid [154-156]. Fortunately, the $LiFePO_4$-$FePO_4$ system satisfies this condition in all three directions [25, 29, 88, 160, 186-192], therefore, Cahn's approach is applicable. It is the first time the coherent miscibility gaps are obtained by minimizing the coherent Gibbs energy of the olivine solid solution phase:

$$G_m^{coh} = G_m^{chem} + G_m^{el} = G_m^{chem} + \iint_0^x E_{elastic} dx dx \qquad (5.4)$$

In Equation 5.4, G_m^{coh} is the coherent Gibbs energy of mixing. In this study, the boundaries of coherent miscibility gaps at a specific temperature are estimated through minimization of the isothermal coherent energy. Substituting Equation 5.4 into Equation 5.1, the coherent spinodal decomposition can then be calculated as follow:

$$\left(\frac{\partial^2 G_m^{coh}}{\partial x^2}\right)_{T,P} = 0 \qquad (5.5)$$

Equation 5.1 and 5.5 are mathematically equivalent. However, as the temperature reaches the consolute temperatures, the total Gibbs free energy curve of the solid solution becomes less concave, consequently, the numerical approach reveals discrepancies when calculating coherent spinodal boundaries and coherent consolute temperature by considering either Equation 5.1 or 5.5. In order to avoid this inconsistency, the coherent miscibility gaps and coherent spinodals are calculated by minimizing the coherent Gibbs energy (Equation 5.4) and applying Equation 5.5, respectively.

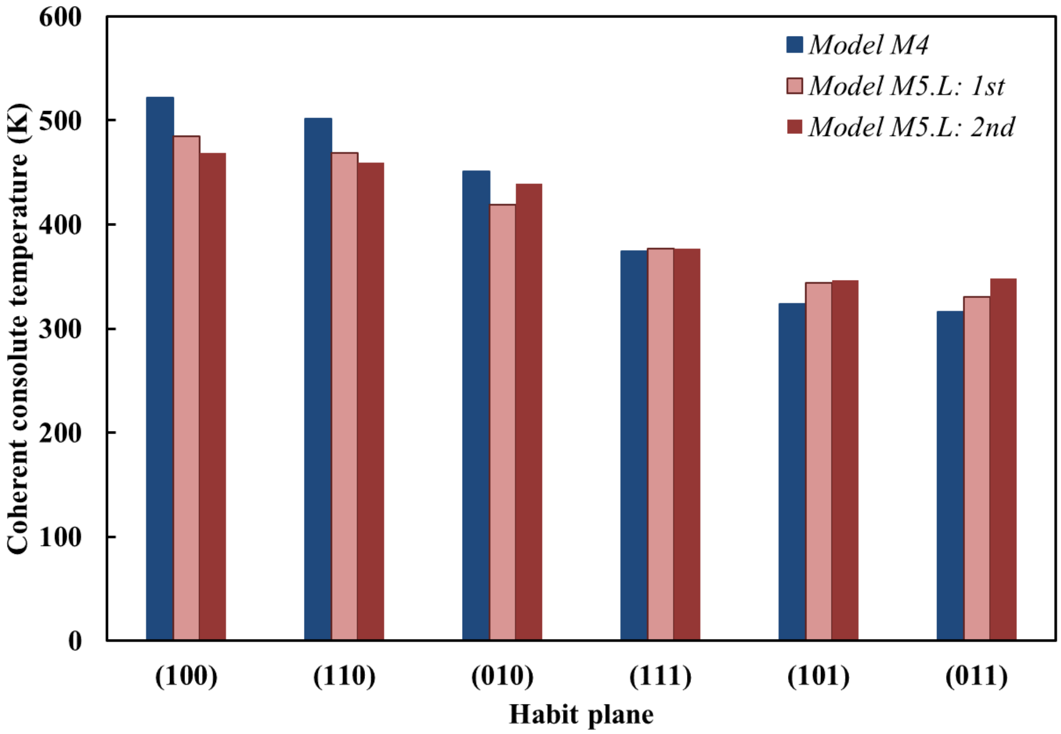

Figure 5.1: The consolute temperatures corresponding to various habit planes without considering temperature effect calculated by using model M4 $((Li^{+},Va)_{1}(Fe^{2+}, Fe^{3+})_{1}(P^{5+})_{1}(O^{2-})_{4})$ [133] and M5.L $((Li^{+},Va)_{3}(Li^{+},Va)_{2}(Fe^{2+}, Fe^{3+})_{5}(P^{5+})_{5}(O^{2-})_{20})$ [133] (1st and 2nd coherent consolute temperatures correspond to poor-Li and rich-Li coherent miscibility gaps).

The coherent miscibility gaps are calculated based on the incoherent equilibrium miscibility gaps of the $LiFePO_4$-$FePO_4$ phase diagram which was well considered in our previous study [133]. It means G_m^{chem} of Equation 5.4 is taken from our reported models of Gibbs energy of the olivine solid solution [133]. In our paper [133], the **M4** model $((Li^{+},Va)_{1}(Fe^{2+}, Fe^{3+})_{1}(P^{5+})_{1}(O^{2-})_{4})$ [133] is the simplest model for describing Gibbs free energy of the solid solution phase Li_xFePO_4. The

M4 model does not well represent the olivine join. Like Cogswell and Bazant [144], the incoherent equilibrium miscibility gap calculated by the **M4** model did not show the eutectoid reaction [133]. However, our calculated coherent consolute temperatures corresponding to various habit planes using the **M4** model [133] and Cahn's approach (without using the temperature dependent term $t(x,T)$) differs from that reported by Cogswell and Bazant [144] (Figure 5.1). Our calculation, which reveals (100) as the softest direction, disagrees with Cogswell and Bazant [144]. The expected consolute temperature of ~324 K of (101) coherent miscibility gap from our calculations is much lower than the consolute temperature of ~423.15 K calculated by Cogswell and Bazant [144].

In our previous report [133] on incoherent equilibrium phase diagram of $LiFePO_4$-$FePO_4$, both thermodynamic model **M5.L** and **M5.F** take into account an extra level of long-range-ordering of the solid solution. The thermodynamic model **M5.L** ($(Li^+,Va)_3(Li^+,Va)_2(Fe^{2+}, Fe^{3+})_5(P^{5+})_5(O^{2-})_{20}$) [133], one of our more advanced models, reproduces well the equilibrium miscibility gaps in the $LiFePO_4$-$FePO_4$ olivine join. The Gibbs energy $G_m^{chem}(x,T)$ function which possesses 4 inflexion points at a constant temperature, reveals the existence of the two incoherent equilibrium miscibility gaps [133]. Consequently, in the present study, the two coherent miscibility gaps and coherent spinodals are obtained by using Cahn's approach (without using the $t(x,T)$ term) based on the thermodynamic model **M5.L** [133] (Figure 5.1,2). Our calculated coherent miscibility gaps show that:

At a constant T, there exists 4 inflexion points in the coherent Gibbs energy $G_m^{coh}(x,T)$ curve of the olivine solid solution which are related to the four coherent spinodal compositions. As a result, there is a local minimum of the Gibbs free energy curve near the eutectoid composition $Li_{x\sim0.6}FePO_4$. This minimum is corresponding to the possible occurrence of the metastable phase (Figure 5.2). This metastable phase could play a role in reducing the lattice mismatch between the olivine-$LiFePO_4$ and olivine-$FePO_4$ phase.

As the coherent phase diagrams are calculated corresponding to various habit planes, a stable habit plane should be related to a large coherent miscibility gap in comparison with the others. It means that the coherent with a stable habit plane is more likely to occur. (100) is the most favorable coherent habit plane (Figure 5.2) and (110) is stable. The (010) habit plane might appear if the supplied energy is large enough to form coherent interface. According to our prediction, it is almost impossible to find coherent phases with habit planes (111), (001), (101) or (011) (Figure 5.1).

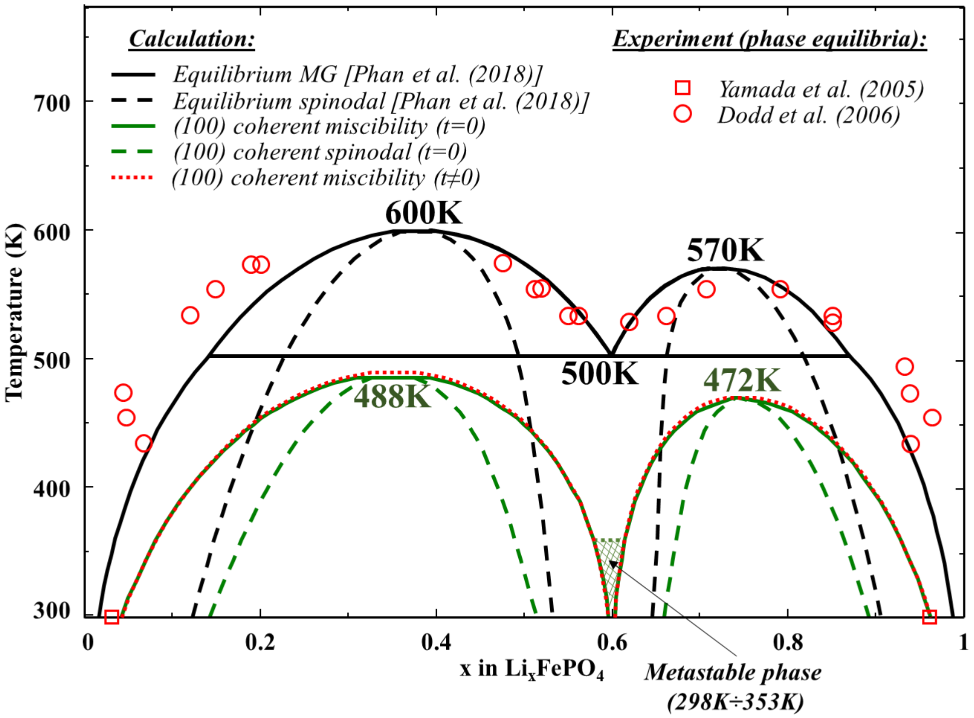

Figure 5.2: The calculated (100) habit plane coherent miscibility gaps of LiFePO$_4$-FePO$_4$ olivine join using model M5.L $((Li^+,Va)_3(Li^+,Va)_2(Fe^{2+}, Fe^{3+})_5(P^{5+})_5(O^{2-})_{20})$ [133] with and without considering temperature effect $t(x,T)$. Experimental data (□ Yamada et al. [26] and ○ Dodd et al. [28]) are related to the equilibrium phase diagram calculated by Phan et al. [133]. The shaded area is the metastable phase region in the 298 K - 353 K temperature range.

When the effect of change of physical properties with temperature on the stored strain energy G_m^{el} is investigated through the temperature dependent term $t(x,T)$, the calculated coherent miscibility gaps in the LiFePO$_4$-FePO$_4$ olivine join do not change significantly. Let the temperature dependent term vary within reasonable limits, the calculated consolute temperatures corresponding to different habit planes modify slightly (less than 5K) and the coherent miscibility gaps are almost unchanged (Figure 5.2). In fact, the thermal internal stress should be calculated from the elastic tensor (ΔC_{ij}) and the thermal expansion tensor ($\Delta\alpha_{ij}$). Since the olivine $LiFePO_4$ and $FePO_4$ possess similar physical properties, i.e. ΔC_{ij} and $\Delta\alpha_{ij}$ are small [25, 101], and since every physical property of the olivine solid solution is reasonably assumed to be linear with composition and temperature (see appendix B), the temperature effect on the stored elastic energy G_m^{el} should not be significant, as shown in our calculations. For that reason, the amount of entropy caused by the elastic effect, which is proportional to the change of elastic energy versus temperature, should be negligible.

5.2.3 Coherent phase transformation in $LiFePO_4$ battery

5.2.3.1 Coherent Gibbs free energy and overpotential

In this study, the mentioned overpotential is the part of overpotential or underpotential $\Delta\phi$, which is required to charge or discharge the battery via a specific phase transformation pathway of the Li_xFePO_4 cathode. This overpotential can be obtained from the instantaneous slope of the mixing free energy ΔG of the cathode material with its overall concentration x:

$$\Delta\phi = -\frac{1}{F}\Delta\mu_{Li} = -\frac{1}{F}\left(\frac{\partial \Delta G}{\partial x}\right)_T \tag{5.6}$$

where F is the Faraday's constant; $\Delta\mu_{Li}$ is the difference of the Li chemical potential in the crystallite cathode and anode [141]. Figure 5.3 illustrates the voltage curve for Li_xFePO_4 derived from the described free energy model of coherent transformation within the cathode while anode is pure Li. This voltage curve is strictly for a single crystallite when the bulk concentration of the crystallite is controlled externally (e.g. by controlling the electric charge). Upon discharging the particle, the voltage must be reduced to below the incoherent two-phase equilibrium voltage (dash-black line in Figure 5.3) to overcome the strain energy incurred by coherent two-phase equilibrium. As the two coherent phases ($FePO_4$-rich and intermediate) are formed, the first voltage plateau is reached. The second voltage plateau is created by the co-occurrence of the intermediate and $LiFePO_4$-rich phase after all the $FePO_4$- rich phase is consumed through lithiation. In a potential-controlled battery system consisting of an assembly of Li_xFePO_4 particles, the voltage vs composition profile exhibits a hysteresis, as illustrated in Figure 5.3. Similar to the explanation given by Malik *et al.* [20], the applied voltage must be reduced sufficiently below the equilibrium voltage plateau to create the coherent interfaces via discharging. Once that overpotential has reached and each particle achieves the critical concentration x_c, any fluctuation of Li out of an individual particle could start a coherent nucleation within that particle, as the driving force for charging increases abruptly. At this potential, the process repeats and the remaining lithiated particles charge sequentially, accounting for the voltage plateaus belonging to the hysteresis (dash-dot-red line in Figure 5.3).

Using our model of Gibbs free energy, no overpotential should be obtained for equilibrium phase transformation, a moderate overpotential (~70 mV) and a high overpotential (>100 mV) should be obtained for fully (100) coherent phase transformation and solid solution transformation, respectively (Figure 5.3). Different from our results, the single-particle solid solution transformation produces ~30 mV overpotential, estimated by Malik *et al.* [20]. According to the authors, their estimation could explain the experimentally observed voltage hysteresis of ~20 mV difference between charge and discharge of nanoparticles in the zero-current limit C/1000 [182]. From our perspective, overpotential measurements done by (dis)charging 17% or 28% of the theoretical capacity of the cell at various rates like in the experiments of Dreyer *et al.* [182] cannot represent the overpotential obtained by (dis)charging completely. Moreover, the overpotential obtained at a very low (dis)charge rate where Li^+ ions have enough time to diffuse should be related to the equilibrium phase diagram and therefore the ~20 mV overpotential obtained at C/1000 by Dreyer *et al.* [182] should not be considered as a typical overpotential for any non-equilibrium phase transformation mechanisms at a very low (dis)charge rate. Despite all the porous $LiFePO_4$ particle surfaces (outer and inner) was claimed to be covered with a 1÷2 nm-thick carbon film [182], the existence of close pores, the crystallographic defects within the porous material and the incomplete penetration of the electrolyte within the porous particles, which were not examined, could cause retardation or blockage of Li^+ ions movement. If a small amount of Li^+ ions is impeded, voltage hysteresis between charge and discharge should be visible. Therefore, from our perspectives, the observation of overpotential at a very low (dis)charge rate [182] is due to the blockage of Li^+ ions movement rather than a non-equilibrium phase transformation mechanism. Besides, phase-field modeling [206] reveals that the lowest overpotential for phase transformation upon fast Li diffusion kinetics in >150 nm-particles would be >70 mV, in agreement with our estimated overpotential for coherent phase transformation of a multi-particle system (Figure 5.3). In addition, the dissymmetry between charge and discharge electrochemical properties [132, 207], which was claimed to be due to the higher kinetics of delithiation than that of lithiation [135], is also detected through our calculations (Figure 5.3).

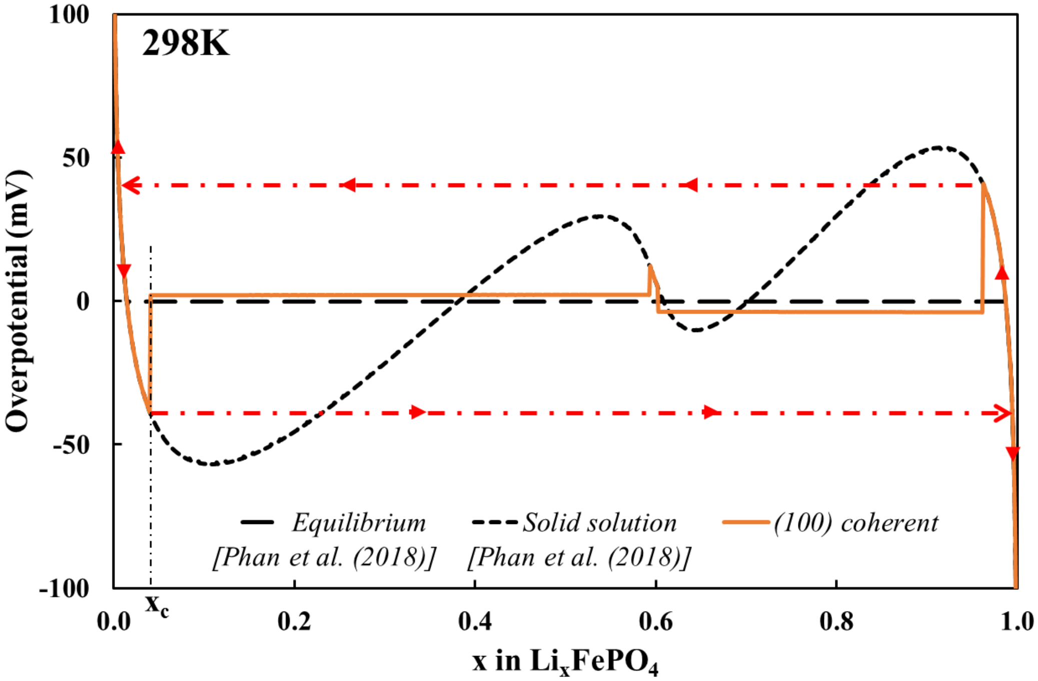

Figure 5.3: Calculated overpotentials of a single crystallite obtained via (100) habit plane coherent phase transformation in comparison with that obtained via equilibrium [133], solid solution transformation [133] at 298 K. Red dash-dot line represents the voltage hysteresis when a multi-particle system follows (100) coherent phase transformation via charging/discharging.

5.2.3.2 Existence of a metastable phase during phase transition

According to our calculations, the existence of the metastable phase $Li_{\sim 0.6}FePO_4$ is possible when there are coherent interfaces in the battery operating temperature range of 298÷353 K. This result is supported by a number of researches [149-151, 195, 208-211]. The electrochemically formed $Li_{0.61-0.66}FePO_4$ solid solution phase was observed during the charge-discharge reaction [150]. A preferred solid solution phase around the eutectoid concentration ($Li_{0.625}FePO_4$) was also detected at medium rates of 2-6 C [148]. The presence of the solid solution phase is transient. Its lifetime was estimated to be ~30 min [150] or ~ 10 min [151]. The metastable phase rapidly transforms into the stable $LiFePO_4$ and $FePO_4$ phase through relaxation process [150]. Hence, the amplitude of the overpotential $\Delta\phi$ decreases during the relaxation time [151]. According to Zhang *et al.*, intermediate (dis)charge rates lead to the formation of the $Li_{\sim 0.6}FePO_4$ metastable phase [149]. The intermediate solid solution zone with no dislocations was observed to be coherent with $LiFePO_4$ and $FePO_4$ phase [195, 208-210]. The existence of this intermediate phase allows the particles to initiate (de)lithiation at low overpotentials and increase rate capabilities for systems undergoing nucleation and growth. The presence of a thermodynamically favorable intermediate solid-solution region at the interface leads to a decrease in coherent strain energy. Therefore, it reduces mechanical damage upon cycling and improves cyclability [211]. If the (dis)charge rate becomes higher, metastable phase transition could be bypassed, a nonequilibrium solid solution phase Li_xFePO_4 with a composition covering the entire composition between two thermodynamic phases, $LiFePO_4$ and $FePO_4$, could be formed [149, 169].

5.2.3.3 Coherent habit planes

Although sometimes (101) or (311) are shown as the coherent interphases through calculations [144, 212] or electrochemical experiment [213], (010) and (100) are the most common habit planes reported in various studies. According to the reported values of lattice parameters of pure $LiFePO_4$ and $FePO_4$ [25, 29, 88, 160, 186-192], the misfit is largest along the (100) direction. Therefore, the (100) crystallographic plane appears to be the most preferable habit plane in order to minimize the lattice misfit and hence the elastic energy between the two olivine phases, $LiFePO_4$ and $FePO_4$ [18, 141], in agreement with our calculations and the observation in *ex-situ* chemically delithiated particles [134, 136]. For chemically delithiated particles, the observation of the largest strain [34] and the anisotropic strain broadening [192] in (100) plane indicate the existence of a coherent interface between the Li-poor and Li-rich phases. However, those results came from insights of chemical delithiation experiments and they cannot describe exactly the electrochemical lithiation mechanism [20]. In an electrochemical cell, Li^+ is incorporated from the electrolyte, and electrons come from the current collector. Meanwhile, there is no inherent separation of Li^+ from e^- in the chemical delithiation reaction [143]. For this reason, the habit plane between the lithiated and delithiated phase during battery operations should also be affected by the (010) favorable lithium migration path [32, 33], which typically gives prominent (010) surface facet in Li_xFePO_4 particles [214, 215]. However, these diffusion channels can be impeded by antisite defects [216].

Based on the common knowledge of the favored diffusion direction of Li^+ ion in olivine structures, many authors claimed that (010) would be the favorable phase transition direction during (dis)charge process. From first principle calculation, the (010) interface was claimed to be favorable under the thermodynamic two-phase mechanism, since it has a remarkably low chemical interfacial energy with respect to that of the (100) and (001) interfaces [217]. As stated by the authors, since the interface orientation with minimum chemical interfacial energy would be different from that with minimum coherent strain energy, the preferred interface orientation in a $LiFePO_4$ single particle should depend on the particle size and particle morphology. Similarly, molecular dynamic simulation done by Park *et al.* [218] demonstrated that (010) direction would be the most favorable migration path. The delithiated $FePO_4$ were observed aligned along this direction in the chemical delithiated $LiFePO_4$ samples [218]. Atomic-scale observations of the boundary migration mechanism and the anisotropic lithiation in $FePO_4$ microparticles at a discharge rate of ~0.1C presented a phase boundary, which appeared on (010) plane and moved toward (010) direction [219]. Analogously, the phase boundary propagation along (010) orientation during electrochemical lithiation (delithiation) was revealed through *in situ* X-ray measurements [193]. From another work, electrochemical cycling of $LiFePO_4$ particles included the fracture surfaces predominantly parallel to (100) and (010) planes [220]. The occurrence of the fracture surfaces could result from the movement of both (100) and (010) coherent habit planes via cycling process.

Interestingly, Amin *et al.* [221] showed that in a single crystalline $LiFePO_4$, Li diffusivity values presented for (010) and (001) direction would be comparable and distinctly greater than that for (100) direction. This result indicates a preferential chemical diffusion of Li in (100) plane and consequently, (100) becomes the favorable habit plane not only with the lowest mismatch but also with favorable Li^+ ion movement directions. The fast lithium ion movement would explain the impressive rate capability along with the excellent cycling stability of the synthesized (100)-oriented $LiFePO_4$ nanoflakes [222, 223] during the reversible electrochemical reaction. After observing the electrochemical deintercalated ~100nm nanoparticle $LiFePO_4$, Delmas *et al.* [129]

proposed the domino-cascade model. According to the authors, it is easier to remove lithium ions from the (010) tunnels rather than start a new nucleation of the deintercalated phase elsewhere in the crystal. In the domino-cascade model, the forming boundary plane would move in (100) direction through the crystal on lithium deintercalation. This displacement could be considered as a wave going through the crystal without any energy barriers, allowing a high rate of lithium intercalation/deintercalation. The domino-cascade model could be explained using our (100) habit plane coherent phase diagram (Figure 5.2). In a single-particle system, charge/discharge could occur rapidly via (100) coherent phase transformation where the metastable phase could serve as a coherent boundary region between fully lithiated and fully delithiated phase in order to reduce the coherent strain. If the (dis)charge rate is not too fast, Li^+ diffusion is relatively low, then the domain of coherent boundary could be small enough to be neglected and our model becomes the domino-cascade model. Experimental observation reported by Brunetti *et al.* [130], in which mostly fully lithiated or fully delithiated particles were found, strongly supports the domino-cascade model. Careful observation of the two-phase particles showed that they would be monocrystalline with a coherent interface boundary between the Li-rich and Li-poor parts [130]. Hence, Brunetti *et al.* [130] observation could be explained as a fast movement of the (100) coherent interface with or without the occurrence of the metastable phase under the effect of elastic energy.

Since the electric field is unidirectional, in a thick electrode assembly, all Li_xFePO_4 particles should lithiate (delithiate) sequentially [142, 182-184]. The electrode material could be divided into three regions: the reacted region, the active region and the unreacted region. The reacted region contained all the particles which finish their (de)lithiation, in contrast, all the particles which has not given or accepted any lithium ions stay in the unreacted region. The most concern one is the reacted region where diffusion of lithium ions is taking place. It is possible that there are particles with coherent coexistence of the intermediate phase and either the $FePO_4$-rich or $LiFePO_4$-rich phase as in the *in situ* TEM observation of electrochemically cycled $LiFePO_4/FePO_4$ nanowire given by Niu *et al.* [195] It is also possible that three phase co-occur within a particle of the active region. An ordered solid solution interface region between the delithiated and lithiated phase was found in a number of studies [208-210]. A dual-interphase model where three phase $LiFePO_4/Li_{0.5}FePO_4/FePO_4$ coexist was used to describe the delithiation mechanism of $LiFePO_4$ upon charging [209]. The lithium extraction was claimed to favor an alternated layer way rather than sequentially (layer-by-layer) [224].

In summary, the comparable overpotential between calculations and experiments, the existence of the metastable phase, and the occurrence of the preferential habit planes make our calculations of coherent $LiFePO_4$-$FePO_4$ phase diagram reliable.

5.3 Size-dependent phase diagram of $LiFePO_4$-$FePO_4$

5.3.1 Model of Gibbs energy with size constraint

Our thermodynamic model of the Gibbs energy, which has been already used to represent the equilibrium and coherent miscibility gaps, is then extended for isotropic spherical nanoparticles of the solid solution Li_xFePO_4. The two main causes of miscibility gap shrinkage are considered in our study to reproduce the experimental data. The equilibrium $LiFePO_4$ – $FePO_4$ olivine join was previously described through the molar Gibbs free energy of the solid solution Li_xFePO_4 ($0 \leq x \leq 1$) [133]. In order to describe this olivine join at nanoscale, the total molar Gibbs free energy of the solid solution is calculated as a function of a particle size:

$$G_m^{tot}(D) = G_m^{ref}(\infty) + G_m^s(D) \tag{5.7}$$

where $G_m^{tot}(D)$ is the total molar Gibbs free energy of the solid solution at a particle size D; $G_m^s(D)$ is the molar surface energy gained by reducing the particle size to D and $G_m^{ref}(\infty)$ is the referent molar Gibbs energy which is independent on particle size. Two cases corresponding to our proposed scenarios are considered:

If only the surface energy causes the miscibility gap shrinkage, the referent Gibbs energy is purely chemical Gibbs energy: $G_m^{ref} = G_m^{chem}$;

If both the surface energy and coherent strain cause the miscibility gap shrinkage, the referent Gibbs energy is the coherent Gibbs energy: $G_m^{ref} = G_m^{coh} = G_m^{chem} + G_m^{el}$.

The molar chemical Gibbs energy G_m^{chem} is taken from our **M5.L** model [133] and the molar elastic Gibbs energy G_m^{el} is taken from the coherent Gibbs energy of the most favorable (100) habit plane as discussed above. The molar surface energy G_m^s is considered to be dependent on the surface energies of the particle only. No interfacial energy between different phases is considered since the interfacial area is smaller than the surface area, and the interfacial energy is about an order smaller than the surface energy [121, 187, 214, 215, 217]. Moreover, coherency, if it exists, does not change the surface energy of a particle and reduces the interfacial energy [225]. Therefore, when considering the molar surface energy G_m^s, the coherent effect is ignored. The molar surface energy G_m^s of one mole Li_xFePO_4 nanoparticles is estimated using Lee's model [122-126]:

$$G_m^s = \frac{4C\langle\gamma\rangle V_m}{D} \tag{5.8}$$

where C is a correction factor considering the shape effect; $\langle\gamma\rangle$ is the average surface energy of the solid solution; and D is the particle size. Since olivine is an anisotropic structure, the Li_xFePO_4 particle is more likely not spherical. However, there is no detailed information about the particle shape provided in experimental studies [23, 27, 34]. Kobayashi *et al.* [27] reported the mean particle size confirmed by two independent evaluations: the coherent length and SEM images. The study of Wagemaker *et al.* [34] shows a particle size corresponding to the crystallite size and Meethong *et al.* [23] utilized the equivalent spherical particle diameters. Since there are not enough specific details about the powder used in studies [23, 27, 34], we consider the powder to be formed of single crystallite spherical particles in our calculation ($C = 1$). Our assumption is acceptable since no significant difference between the reported sets of experimental points [23, 27, 34] is shown (Figure 5.4). Moreover, any other particle shapes (plate-like particle, rod-like particle, etc.) could easily be also considered by changing the value of the correction factor C in Equation 5.8. The molar volume V_m of the solid solution is linearly dependent on composition as shown in a number of studies [29, 189, 191], and the average surface energy of the isotropic solid solution $\langle\gamma\rangle$ is a function of the surface composition:

$$\langle\gamma\rangle = \langle\gamma\rangle_{\mathrm{FePO_4}} \cdot (1 - x^s) + \langle\gamma\rangle_{\mathrm{LiFePO_4}} \cdot x^s + \langle\gamma\rangle^{ex} \tag{5.9}$$

where $\langle\gamma\rangle_{\mathrm{FePO_4}}$ and $\langle\gamma\rangle_{\mathrm{LiFePO_4}}$ are the average surface energies of the isotropic pure compounds, $FePO_4$ and $LiFePO_4$; x^s is the surface composition of component $LiFePO_4$; and $\langle\gamma\rangle^{ex}$ is the excess surface energy of the solid solution. Since any olivine structure material is anisotropic, so are $LiFePO_4$, $FePO_4$, and the solid solution Li_xFePO_4. Therefore, different crystallographic surface planes should possess different surface energies [214, 215]. Consequently, crystallographic planes do not distribute arbitrarily at the particle surfaces and the particles are not strictly spherical. For simplifying our calculations, the average surface energy or so-called isotropic surface energy $\langle\gamma\rangle$ is chosen to represent the increase of surface energy via Li_xFePO_4 particle size reduction and it is dependent on the surface composition x^s (Equation 5.9). The surface composition x^s is equal to the surface composition taken from the ideal solution model [226] and it is independent on value of the excess surface energy $\langle\gamma\rangle^{ex}$ (Equation C.2). Furthermore, $\langle\gamma\rangle^{ex}$ is considered as a function of surface composition but not temperature:

$$\langle\gamma\rangle^{ex} = \omega \cdot x^s \cdot (1 - x^s) \tag{5.10}$$

The excess coefficient ω can be a scalar or surface composition dependent (Equation C.4). Note that, the surface energy of a solid behaves differently from the surface tension of a liquid. Therefore, the isotropic surface energy $\langle\gamma\rangle$ of the solid solution Li_xFePO_4 does not need to follow Butler's equation [227].

5.3.2 Size constrained equilibrium and coherent miscibility gaps

5.3.2.1 Scenario (i): Miscibility gap shrinkage due to solely particle surface energy

According to Meethong et al. [23], at a small particles size, the surface energy could be a significant contribution to the molar free energy of heterosite and triphylite phases. Noticeably, the absolute increase of the total free energy of the two end-member $LiFePO_4$ and $FePO_4$ is not important. The driving force of demixing a solid solution inside a miscibility gap is chemical potential difference. As the chemical potentials of a species in different phases are the same, decomposition stops, and the two phases are at equilibrium. If small particles are used, the reference states now become nanoparticle $LiFePO_4$ and nanoparticle $FePO_4$, i.e. the reference states translated into higher energies. This translation of reference states should not affect the chemical potential equality hence, it does not affect the change of miscibility gaps. It should be the deviation from linearity of the surface energy of the solid solution versus its composition responsible to the shrinkage of the miscibility gaps of the $LiFePO_4$-$FePO_4$ olivine join. Keeping that in mind, we examine the behavior of the surface energy of the solid solution Li_xFePO_4 in order to reproduce the experimental data [23, 27, 34].

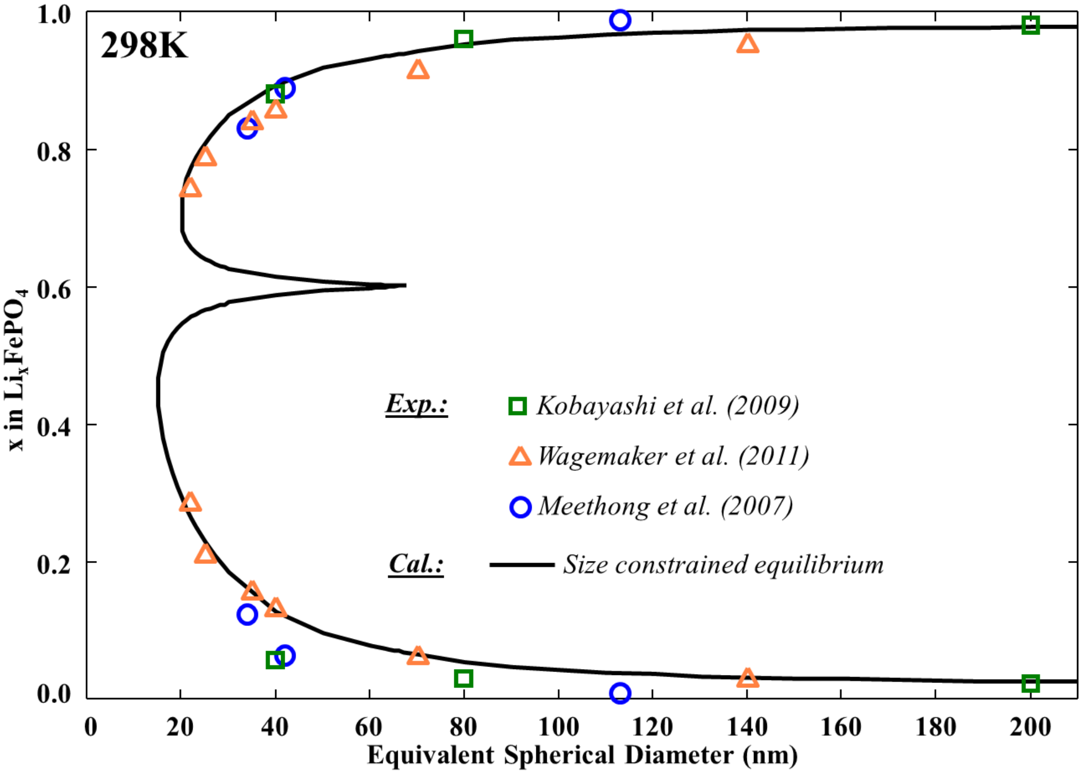

Figure 5.4: The calculated particle size constrained equilibrium miscibility gaps at 298 K as a function of particle size according to the scenario (i) in comparison with experimental data taken from Kobayashi et al. [27], Wagemaker et al. [34], and Meethong et al. [23].

If ω is composition-independent, it is possible to reproduce the experiment data [23, 27, 34] of the miscibility gaps. When the particles are very small (~20 nm), the calculated miscibility gaps are in good agreement with experimental data. However, the calculated shrinkage rate of the miscibility gaps via particle size reduction is higher than the reported experimental shrinkage rate [23, 27, 34]. In order to improve our model, more parameters are introduced: the excess term ω is then considered as a function of the surface composition x^s (Equation C.4). The additional parameters are optimized parameters revealing the asymmetricity of $\langle\gamma\rangle^{ex}$. The excess surface energy produces reasonable miscibility gaps, fitting well with experimental data [23, 27, 34] (Figure 5.4, 5.5). A metastable phase of Li$_{0.6}$FePO$_4$ could occur as the particle size is smaller than 67 nm. The molar surface contribution could narrow the miscibility gaps from the two ends simultaneously only when the optimized excess surface energy of the solid solution is roughly symmetrical and deviates significantly from ideality (Figure 5.6).

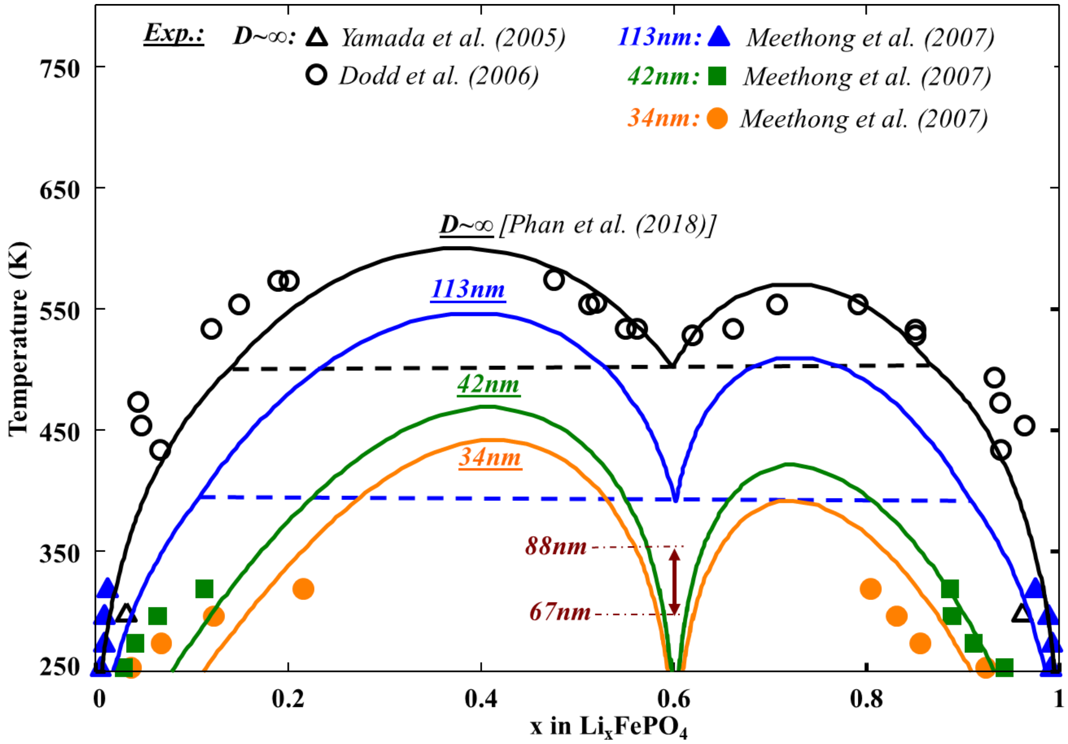

Figure 5.5: The calculated equilibrium miscibility gaps as a function of particle size in comparison with experimental data taken from and Meethong et al. [23], Yamada et al. [26] and Dodd et al. [28] The arrow shows the 298 K÷353 K temperature range with the corresponding range of the maximum particle size at which the equilibrium metastable phase starts to occur.

Based on the calculated surface energies of LiFePO$_4$ and FePO$_4$ on different orientations [214, 215], the surface energies of the pure compounds are chosen in the range of 0.5-1.2 J/m^2. The selected values of the surface energies of the two pure compounds are not important in our model for the purpose of calculating the miscibility gaps. However, it is worth noticing that the spinodal decomposition is very sensitive to the rate of change of the surface energy via the bulk concentration (Equation D.6). Therefore, $\frac{\partial\langle\gamma\rangle}{\partial x}$ or $\Delta\langle\gamma\rangle$ is very important in optimizing the size dependent phase equilibria of the $LiFePO_4$ - $FePO_4$ olivine join. Moreover, $\Delta\langle\gamma\rangle$ is also used to determine the surface composition (Equation C.2). The larger the magnitude of $\Delta\langle\gamma\rangle$ is, the higher the possibility of mostly one species occupying the particle surface is. It means that the minimum surface energy is obtained at either rich or poor-Li composition. As a result, the miscibility gaps will be significantly narrower from one side only. It is likely to obtain the minimum surface energy at the bulk composition of ~$Li_{0.5}FePO_4$ to shrink the miscibility gaps from both sides at nanoscale. Since the surface energy curve should be nearly symmetric, if high magnitude of $\Delta\langle\gamma\rangle$ is utilized, composition-dependent excess term ω will be used to compensate the asymmetry caused by $\Delta\langle\gamma\rangle$ and reproduce the miscibility gaps. However, this scenario does not allow any strains in nanoparticles as reported experimentally [127]. Therefore, coherent Gibbs energy must be taken into account.

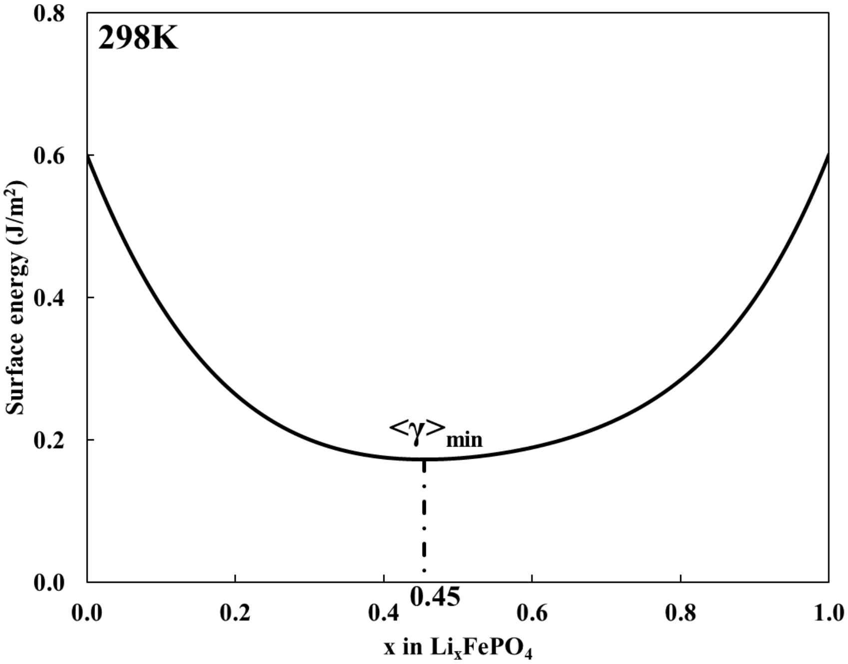

Figure 5.6: The calculated surface energy of 40 nm-nanoparticles of Li_xFePO_4 solid solution used in the present study in order to reproduce the experimental data of particle size-dependent phase equilibria according to scenario (i).

5.3.2.2 Scenario (ii): Miscibility gap shrinkage due to particle surface energy and coherent relationship

Since the stiffness of the interatomic bonds represent the elasticity of the system, the moduli of the crystal seem to be independent from the size of the crystal. Unlike the bulk, the existence of an effective surface tension on the surface of nanoparticles implies that the atoms within the particles are under an effective force. Hence, they should have a different equilibrium spacing than the atoms within the bulk, consequently, the moduli of the crystal of a nano system should be different from that of a bulk [228]. It means that as the particle size decreases, the elastic constants of Li_xFePO_4 change. The surface effect on the value of elastic constants is not pronounced for nanoparticles larger than 10 nm [229], and the elastic constants have a small influence on G_m^{el} (see appendix A). Therefore, the change in the elastic constants has a negligible contribution on the molar elastic Gibbs energy G_m^{el} as particle size reduces. In addition, almost no change in lattice parameters of the two pure compounds, $LiFePO_4$ and $FePO_4$, was observed [27, 34], and Vegard's rule was obeyed even at a small particle size of 40 nm [23, 27, 189]. As a result, no change in Vegard's coefficient is considered and consequently considering G_m^{el} independent on the particle size is a good approximation. If coherency is counted, less excess surface energy is required to reproduce the phase diagram. We use the (100) habit plane coherent Gibbs energy for our calculations in this study since it is the lowest energy habit plane.

Similar to *scenario (i)*, in order to best model the particle size effect on the coherent miscibility gaps, both composition-independent and composition-dependent ω are considered (Table S.1). The selected excess surface energy of the solid solution in this case is lower than that in the *scenario (i)* because of the coherent Gibbs energy contribution. Composition-independent ω, as in the previous case, is not enough to describe the reduction rate of the miscibility gaps. Composition-dependent ω could describe the miscibility gaps better but more parameters are required (Figure 5.7). Coherent phase transformation becomes dominant as the particle size decreases, especially when the size is lower than 50 nm. The metastable phase should always exist via the coherent phase transformation.

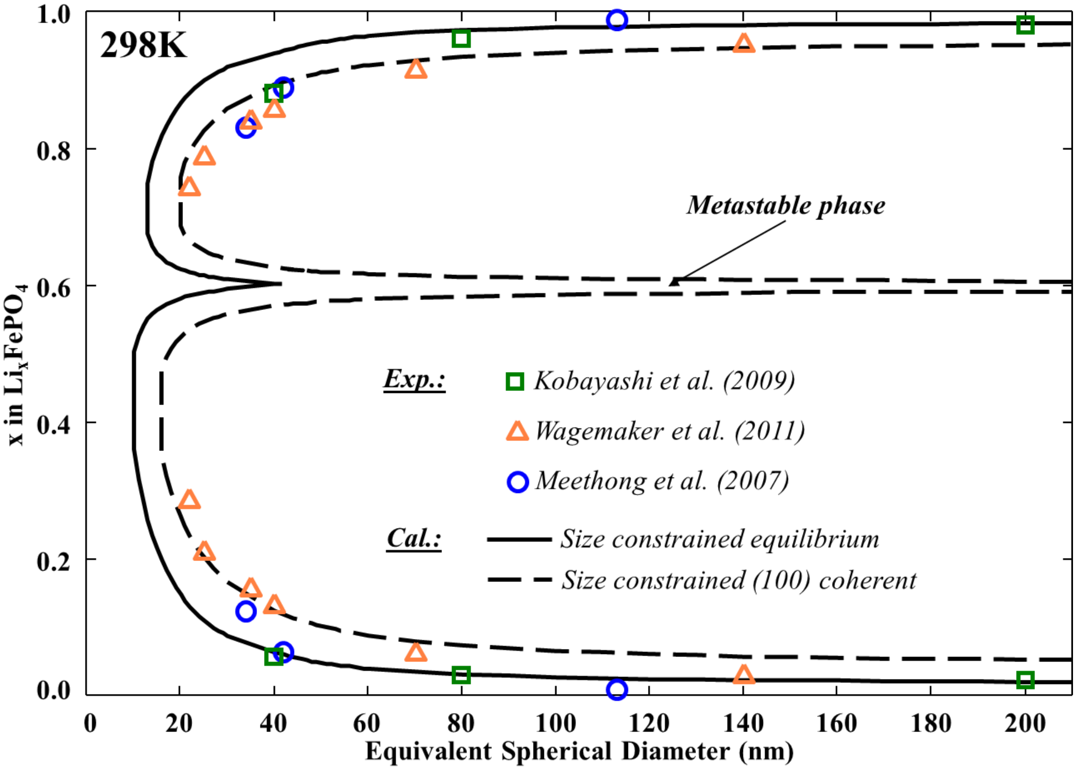

Figure 5.7: The calculated particle size constrained equilibrium miscibility gaps and coherent miscibility gaps of (100) habit plane as a function of particle size according to the scenario (ii) in comparison with experimental data taken from Kobayashi et al. [27], Wagemaker et al. [34], and Meethong et al. [23] The metastable phase always exists in coherent phase transformation.

5.3.2.3 Discussion

In our model, the surface energy of the solid solution deviates significantly from ideality. Even the significant excess surface energy could help us to reproduce the phase diagram, no experiment or calculation has shown any significant amount of excess surface energy of the solid solution to support our assumption. Our calculations are based on the assumption that all crystallographic faces are randomly distributed at the isotropic unrelaxed surface of a solid solution Li$_x$FePO$_4$ particle. However, the surface behavior of the solid solution Li$_x$FePO$_4$ is far from ideal. Its strong anisotropic crystal structure leads to non-random distribution of the crystallographic faces. Size distribution, anti-site defects, etc. are minor factors which could affect the surface energy of the solid solution. In addition, there could be surface stresses related to its electronic structure. Hence, the surface energy of the solid solution considered in this study is the effective surface energy, taking into account its physical surface energy, anisotropy, electronic structure effect, size distribution, anti-site disorder, etc.

As the particle size decreases, the intermediate phase becomes more stable. It has been observed that the solid solution phase of the 26 nm-particle $Li_{0.65}FePO_4$ is less favorable to decompose into nano-particle $LiFePO_4$ and $FePO_4$ than the bulk $Li_{0.65}FePO_4$ is toward decomposition [230]. The nanoparticle $Li_{0.65}FePO_4$ does not unmix in the range of 298 – 643 K [230]. When the particles are very small (<20 nm), the surface energy and coherent energy reduce the energy barrier for the solid solution transformation and cause the disappearance of the miscibility gaps. It is noticeable that the contraction of the miscibility gaps is observed in both chemical and electrochemical samples [23, 27, 34]. Similar solubilities observed through experiments show that the shrinkage of the miscibility gaps is related to the particle size rather than the delithiation method. According to our best knowledge, two possible scenarios corresponding to our calculations above can be interpreted as follow:

Scenario (i) No coherency occurs, the miscibility gap shrinkage is only due to the increase of the surface energy when two equilibrium phases coexist within each particle, or when Li^+ ions are allowed to transfer between particles through the surrounding to reach equilibrium (particles exist with either rich- or poor-Li concentration). The intermediate phase becomes stable when the particle size is smaller than 60 nm, and consequently, two voltage plateaus occur. One plateau is higher, and the other is lower than the voltage plateau obtained by charging or discharging a single crystal Li_xFePO_4 particle (Figure 5.8a). The voltage difference between the two plateaus increases as the particle size decreases ($\Delta V = 19.76\ mV$ for $D = 42\ nm$ and $\Delta V = 30.12\ mV$ for $D = 34\ nm$).

Scenario (ii) Only when two phases coexist within each particle, coherent phase diagram becomes meaningful. According to Ichitsubo et al. [121], the solubility of lithium could change due to the coherent elastic effect caused by the lattice mismatch. In general, for a large particle size, misfit dislocations are easily introduced for energy relaxation. However, for smaller particles, fewer misfit dislocations occur in the crystals. Hence, it is reasonable that Li solubility of heterosite increases and that of triphylite decreases as the particle size decreases. For small particles, elastic strains due to lattice mismatch could be easily released near the surface. Consequently, elastic effects are expected to weaken. Therefore, the miscibility gaps shrink at nanoscale. If the particle size is smaller than the spinodal wavelength, no miscibility gap can be observed. Since the spinodal wavelength was estimated to be of 10→30 nm [121], a certain appropriate particle size (>10-30 nm) is required for the phase separation [121]. On the other hand, a metastable phase should occur at any particle size via coherent phase transformation. Electrochemical experiments done by Pongha et al. [151] revealed the existence of a metastable phase without showing specific composition for 50nm-particles. An intermediate phase being coherent with both $LiFePO_4$ and $FePO_4$ was found in delithiated particles of 70 nm [210]. According to our calculations, as the charge/discharge process follows the coherent transformation, the intermediate phase should exist, hence two voltage plateaus should form (Figure 5.8b). However, the difference between the two plateaus is significant only at nanoscale ($\Delta V = 40.37\ mV$ for $D = 42\ nm$ and $\Delta V = 47.12\ mV$ for $D = 34\ nm$). Nevertheless, the voltage plateau separation due to the existence of the intermediate phase has not been observed or reported in any papers yet.

From our perspective, the *scenario (ii)* is more proper since it could explain the observed boundary-dislocation network in large particles [134], and the internal strain within nanoparticles during battery operation [127].

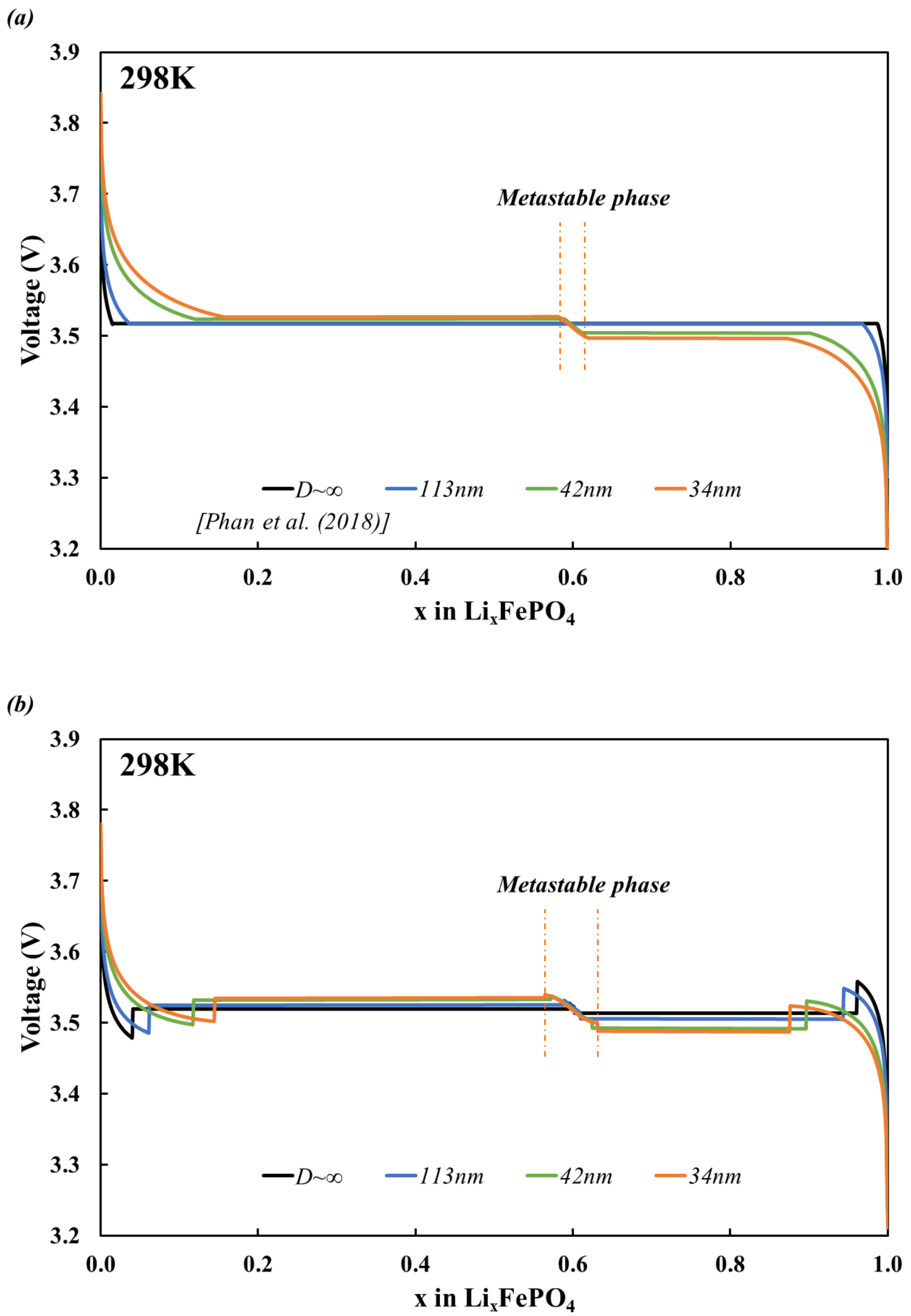

Figure 5.8: The calculated open-circuit voltage (OCV) curves a/ via particle size constrained equilibrium phase transformation and b/ particle size constrained (100) coherent phase

transformation of a single crystallite as a function of particle size. Metastable phase region by charging/discharging of a particle of 34 mn via a/ equilibrium and b/ (100) coherent phase transformation are shown.

5.4 Conclusion

In conclusion, coherent and size dependent phase diagram of $LiFePO_4$-$FePO_4$ has been described in this study. The coherent elastic energy is estimated by extending the linear isotropic approximation for an orthorhombic system for the first time. The coherent miscibility gaps of $LiFePO_4$-$FePO_4$ system are calculated by using the equilibrium Gibbs energy models (**M4** and **M5.L**) [133] and evaluating the coherent elastic energy. More noticeably, this approach of calculating the coherent elastic energy is still applicable if another thermodynamic model is used for the $LiFePO_4$-$FePO_4$ system. The description of the coherent olivine join with respect to various habit planes brings us some notable ideas. First, the calculation of coherent spinodal gives us a better understanding of the kinetics of demixing process under elastic stress. If the battery material goes through the coherent spinodal transformation, it improves its rate and cyclability. Second, the occurrence of the metastable phase reduces the internal stress, consequently, reduces the occurrence of dislocations and defects, and improves the cycling properties of the battery. Third, from our results, if one can control the grain orientation, the coherent phase transformation is more likely to be obtained. Hence, the rate and cyclability of the battery should be improved significantly. Furthermore, having a better understating of the coherent behavior of this system should help people develop a better model of phase transformation during battery operations.

In addition, knowledge of phase equilibria of $LiFePO_4$-$FePO_4$ as a function of particle size is very important to control the lithiation (delithiation) process. In this work, we have provided both size-dependent phase equilibria and size-dependent coherent phase diagram and their implication on the open-circuit voltage (OCV). Our calculation of size-dependent coherent phase diagram is the first ever reported calculation considering the combination of coherent relationship and size effect. The discussion of the two different scenarios is useful in understanding and designing the lithium iron phosphate battery. The effect of particle shape such as nanoplates, nanowires, etc. in compare with the spherical one could be considered in the future. Combination of understandings in coherent phase transformation and particle size effect on the $LiFePO_4$-$FePO_4$ olivine joins could help people to design a better cathode material. For example, according to our calculations, [100]-oriented nanoplates or nanowires along [100] direction are predicted to provide good electrochemical behavior during charge (discharge).

5.5 Acknowledgements

The authors recognize the support of Natural Science, Engineering Research Council of Canada and the Canadian Foundation for Innovation through the Automotive Partnership Canada program and our industry partner Johnson-Matthey.

CHAPTER 6 ARTICLE 3: COHERENT PHASE EQUILIBRIA OF SYSTEMS WITH LARGE LATTICE MISMATCH

Anh Thu Phan, Aïmen E. Gheribi and Patrice Chartrand

Published in Physical Chemistry Chemical Physics, volume 21, issue 20, pages 10808-10822, 2019

Abstract:

In many metallurgical applications, an accurate knowledge of miscibility gaps and spinodal decompositions is highly desirable. Some binary systems where the main constituents of the same crystal structures have similar lattice parameters (less than 15 % difference) reveal a composition, temperature shift of the miscibility gap due to lattice coherency. So far, the well-known Cahn's approach is the only available calculation method to estimate the coherent solid state phase equilibria. Nevertheless, this approach shows some limitations, in particular it fails to predict accurately the evolution of phase equilibria for large deformation, i.e. the large lattice parameter difference (more than 5%). The aim of this study is to propose an alternative approach to overcome the limits of Cahn's method. The elastic contribution to the Gibbs energy, representing the elastic energy stored in the coherent boundary, is formulated based on the linear elasticity theory. The expression of the molar elastic energy corresponding to the coherency along both directions (100) and (111) has been formulated in the small and large deformation regimes. Several case studies have been examined in cubic systems, and the proposed formalism is showing an appropriate predictive capability, making it a serious alternative to the Cahn's method. The present formulation is applied to predict phase equilibria evolution of systems under other stresses rather than only those induced by the lattice mismatch.

6.1 Introduction

Coherence exists in many processes including phase changes in solids. If two phases are coherent, they should have the same lattice parameters at the coherent boundary. In order to determine the phase compositions corresponding to a coherent miscibility gap, a fully coherent interphase boundary between the two phases should be observed for most of or the entire interphase boundary area [138]. Coherent decomposition occurs if there exists a heterogeneous incoherent equilibrium miscibility gap and an upper limit to the strain parameter δ of the second phase is in complete analogy to the condition of coherent heterogeneous ordering reactions [153]. Depending on the constitution of a system in combination with its lattice parameter relations, coherent and non-coherent miscibility gaps can, therefore, be distinguished [153]. In an equilibrium miscibility gap, the phases coexist when each phase is subjected to the same hydrostatic pressure and temperature and when the chemical potentials of each component of the coexisting phases are the same. Meanwhile, a coherent miscibility gap represents the demix of the solid solution into two phases sharing the same lattice parameters at the coherent boundary by lattice deformation resulting in a stored elastic strain within the structure of both phases. This stored elastic energy compensates the chemical potential difference of each end-member in the two coherent phases. Coherent phase transformation is interesting in various thermodynamic systems such as alloys, oxides, alkali salts, and lithium transition metal phosphate battery materials. In fact, most thermodynamic systems in which coherent relationships are important are alloys with cubic crystalline structures, for example, Au-Pt, Au-Ni, Al-Zn, etc. Consequently, the most well-known method to calculate a coherent miscibility gap and coherent spinodal decomposition is the linear isotropic approximation developed by Cahn for cubic systems over 50 years ago [154-156, 231]. This method was later used for calculating the coherent phase equilibria of tetragonal systems [157-159]. Recently, our group has extended this approach for calculating the coherent miscibility gap of orthorhombic systems [232].

In summary, Cahn developed the continuum model through the spinodal concept. In a binary system possessing a miscibility gap, the spinodal decomposition boundary marks the limit of the metastability of the homogeneous phase. The so-called chemical spinodal boundary is defined as the set of locus points where the second derivative of the free energy of the homogeneous phase versus composition is zero [137]. The coherent spinodal decomposition involves continuous composition fluctuations around an average composition and reaches a final state consisting of a two-phase mixture in which the two phases with similar crystal structures remain coherent with one another. Cahn was the first one to consider the elastic energy corresponding to the coherent composition fluctuations [154-156, 231]. Cahn's approach is easy because the elastic Gibbs energy can be estimated directly from physical properties of the solid solution. However, there is no controllable parameter in Cahn's approach. The stresses are only generated from the lattice mismatch, but no exact stress-strain relation has been revealed. Note that the mentioned lattice mismatch (δ) or lattice misfit in this paper is defined as the difference between the lattice parameters of the two constituents forming the binary system. Moreover, this isotropic approach is only suitable for linear isotropic systems consisting in weak deformations ($\delta < \sim 5\%$) resulting from small lattice mismatch between the two constituents [205, 233]. Cahn's approach [154-156, 231] is valid in a linear medium where a strain is linearly dependent on the corresponding stress in each direction. If the lattice misfit between two pure compounds forming the binary system is large ($\delta > 5\%$), a higher order term of the elastic energy needs to be introduced. This work aims to develop another approach in order to overcome the limitations of Cahn's approach. We propose the elastic Gibbs energy approach based on the stress tensor variable. We want to employ a stress-strain relationship to formulate the elastic Gibbs energy in the small deformation regime, then extend it to use in the large deformation regime ($\delta > 5\%$). Note that the small and large deformation regimes mentioned in this paper are associated with the lattice mismatch and are distinguished by a 5% lattice mismatch. Our approach is subsequently tested on several cubic binary systems.

6.2 Elastic energy associated with coherent deformation

From the thermodynamic point of view, phase equilibria of a fully relaxed system at constant temperature and pressure is defined by the equality of the chemical potentials of the system's constituents in every phase. The Gibbs energy minimization technique [234-237] can be employed to compute the phase equilibria. Similarly, the compositions of the two phases forming a coherent miscibility gap are calculated by minimizing the molar Gibbs energy of the deformed/strained solid solution, where an elastic Gibbs energy contribution is now added to the chemical contribution of the relaxed state:

$$G = G_m^{chem} + G_m^{el} \tag{6.1}$$

where G and G_m^{chem} are the molar Gibbs energy of the deformed and undeformed crystal respectively; G_m^{el} is the molar elastic Gibbs energy describing the energy contribution of the stored coherent strain to the total Gibbs energy G. As stated in our previous study [232], the elastic Gibbs energy G_m^{el} is expressed in terms of the overall composition x of the solid solution rather than phase composition as shown earlier [202-204]:

$$G_m^{el} = \iint_0^x E_{elastic} dx dx \tag{6.2}$$

with the boundary conditions:

$$G_m^{el}{}_{x=0;1} = 0 \tag{6.3}$$

In Equation 6.2, $E_{elastic}$ represents the density of strain energy stored due to coherency. The elastic energy occurs only if two phases are co-existing with a coherent interface [232]. The molar elastic energy in Equation 6.2 describes the maximum elastic energy that the crystal can store to allow a stable composition fluctuation. Clearly, $E_{elastic}$ is dependent on lattice mismatch of the lattice parameters of the two pure compounds forming the binary system, elastic constants and habit plane. In Cahn's approach [154-156, 231], no exact stress-strain relation has been revealed in order to formulate $E_{elastic}$. In the present paper, our formalism is developed based on the Gibbs energy expression of elastic energy as a function of stress since it is the variable describing the Gibbs energy ($V_0(\lambda_i + \varepsilon_i) = \partial G/\partial \sigma_i$ with $\sum_i \lambda_i = 1$) [238]. The detailed formalism of elastic energy stored in the crystal is demonstrated in appendix F. Hence, the boundary of the coherent spinodal decomposition for a molar volume of an isotropic material is calculated as follow:

$$\frac{\partial^2 G}{\partial x^2} + 2V_m Y \eta^2 = 0 \tag{6.4}$$

i.e.

$$E_{elastic} = 2V_m Y \eta^2 \tag{6.5}$$

where V_m is the molar volume of the solid solution; $\eta = 1/a \cdot \partial a/\partial x$ is the rate of change of the lattice constant a of the solid solution with its global composition x; and Y is the elastic constant of the elastically soft direction. Substituting Equation 6.5 into Equation 6.2, the molar elastic energy is estimated through a double integration:

$$G_m^{el} = \iint_0^x [2V_m Y \eta^2] dx dx \qquad (6.6)$$

with the boundary conditions stated in Equation 6.3. The expression of Y is dependent on the elastic constants and strain:

$$\begin{cases} \text{For the (100) habit plane:} & \\ Y = Y_{100}^{l} = \dfrac{1}{(S_{11}+S_{12})} \cdot \left[\dfrac{S_{12}}{(S_{11}+S_{12})} + \dfrac{S_{11}}{(S_{11}+S_{12})(\varepsilon+1)^2} + \dfrac{\varepsilon}{2(\varepsilon+1)^2} \right] & (6.7\text{a}) \\ \text{For the (111) habit plane:} & \\ Y = Y_{111}^{l} = \dfrac{1}{4S_{11}} \dfrac{(\varepsilon+2)[(\varepsilon_2+1)^2 - \varepsilon^2/4]}{(\varepsilon+1)^3} & (6.7\text{b}) \\ \qquad + \dfrac{1}{2S_{44}} \dfrac{(\varepsilon+1)(\varepsilon_2+1)}{[(\varepsilon_2+1)^2 - \varepsilon^2/4]} \left[\dfrac{2(\varepsilon_2+1)^2 + \varepsilon^2/2}{[(\varepsilon_2+1)^2 - \varepsilon^2/4]^2} - 1 \right] & \end{cases}$$

Please note that ε occurred as the elastic Gibbs energy G_m^{el} is formulated based on the stable fluctuation of the composition via coherent phase transformations (Appendix F), here the elastic strain, ε, is defined as the difference between the lattice parameter of the solid solution with the fluctuated composition and that of the solid solution with the overall composition. It means that, for a specific binary system, $\varepsilon \leq \delta$. Even if in theory, the elastic strain ε could take the maximum value of δ – the lattice mismatch, the real value of ε should be smaller since the coherent phases are normally not the pure constituents of the binary. Noticeably, when the value of ε is small (i.e. small deformation associated with the small lattice mismatch), Equation 6.7a,b become:

$$\begin{cases} \text{For the (100) habit plane:} & \\ Y = Y_{100}^{s} = \dfrac{1}{(S_{11}+S_{12})} = Y_{100}^{Cahn} & (6.8\text{a}) \\ \text{For the (111) habit plane:} & \\ Y = Y_{111}^{s} = \dfrac{1}{2} \left[\dfrac{1}{S_{11}} + \dfrac{1}{S_{44}} \right] \neq Y_{111}^{Cahn} & (6.8\text{b}) \end{cases}$$

In this study, Y is formulated in the large deformation regime only for the (100) and (111) habit planes since they are the two most common habit planes occurring in cubic binary systems. In developing the formalism, the coherent stress-strain relations corresponding to the (100) and the (111) habit planes are first considered in order to calculate the elastic Gibbs energy in the small deformation regime. Using the assumption stated by Cahn [154-156, 231], we have developed a stress-strain relation reproducing exactly Cahn's expression of Y for the (100) habit plane (Equation 6.8a and Appendix F). According to Cahn [154-156, 231], in a binary system the habit plane (100) is stable when $2C_{44} - C_{11} + C_{12} > 0$. For a material with elastic constants satisfying the condition $2C_{44} - C_{11} + C_{12} < 0$, the habit plane (111) is stable. As in the case of the (100) habit plane, we would like to find a stress-strain relation to reproduce the elastic Gibbs energy of the (111) habit plane as reported in Cahn's approach [154-156, 231]. However, it is impossible to find such a proper stress tensor which is linearly dependent on the strain tensor corresponding to the (111) habit plane to reproduce the elastic Gibbs energy reported by Cahn [154-156, 231] (Appendix F). Since no stress-strain relation could be found, Cahn's approach is inconsistent with the basic idea of elasticity. The issue is less severe as systems where the habit plane is (111) are much less frequent than systems where the habit plane is (100). In order to estimate the elastic Gibbs energy stored in the (111) habit plane, in this study, we propose another stress-strain relation for calculating the coherent miscibility gap (Equation 6.8b and Appendix F). Our proposed relation is applied to estimate the coherent Gibbs energy corresponding to (111) habit plane in the chosen case studies.

As stated, when ε is small, Equation 6.7a,b becomes Equation 6.8a,b, respectively, consequently $f_{el}^{s} = f_{el}^{l}$ where f_{el}^{s} and f_{el}^{l} are the elastic energy stored in the crystal in the small and large deformation regimes respectively. For a large deformation, we cannot ignore the effect of ε on the value of the polynomial inside the square bracket of Equation 6.7a,b. For investigating the difference between f_{el}^{s} and f_{el}^{l}, an artificial strain e is applied. As observed from our calculations, when e increases, f_{el}^{l} becomes smaller than f_{el}^{s}. For example, for the $Au_{0.5}Pt_{0.5}$ solid solution, at $e = 0.15$, f_{el}^{l} is only about 61% of f_{el}^{s} (Figure 6.1). A similar relation is found for other cubic materials. Therefore, using the formula of elastic Gibbs energy developed in the small deformation regime for a system with large deformation could overestimate the elastic Gibbs energy, hence lower the coherent miscibility gap and coherent spinodal of the isotropic system. Notably, it is very difficult to find an exact analytical expression of the elastic Gibbs energy G_m^{el} when either Equation 6.7a or 6.7b is substituted into Equation 6.6. In order to simplify the problem, in the large deformation regime, a suitable constant Y' which is independent from ε but still represents properly the elastic Gibbs energy is found. For a certain composition x_0 of the solid solution, the scalar value of Y' is the best fitted coefficient of the calculated values of f_{el}^l (Equation F.25 and F.32) as a function of e^2 in the range of $0 \leq e \leq 0.15$ (Figure 6.1):

$$f_{el}^l = Y'e^2 \tag{6.9}$$

The value of Y' is then substituted into Equation 6.6 to calculate the elastic Gibbs energy at the composition x_0. It is important to note that the e used to calculate f_{el}^s and f_{el}^l in Figure 6.1 and that used to estimate the value of Y' is an artificial strain e rather than the elastic strain ε with a physical meaning used for calculating the Gibbs elastic energy G_m^{el}. For the Au-Pt system, the maximum value of the elastic strain ε should be 3.86% (lattice mismatch). A large value for the artificial e (up to 15%) is used in order to better show the difference between the calculations of f_{el} in the small and the large deformation regimes. The artificial range of e chosen for estimating Y' is well covered the range of lattice misfits of the case studies that will be discussed later.

Moreover, it is worth mentioning that the values of f_{el}^s and f_{el}^l calculated in this study represent the elastic energy caused by coherent relationship only. Our assumption of coherent relationship is kept even in large deformation regimes despite the likeliness of dislocations, reducing the coherent energy and encouraging semi-coherent or incoherent phase boundaries. Irreversible plastic deformation related to the movement of dislocations is out of scope of this study. Both the small and large deformation regimes are elastic, i.e. reversible from the thermodynamic point of view. The comparison between the value of elastic energy f_{el} calculated in the small and the large deformation regimes shows a difference of the two calculations by using two formulae rather than representing different elastic energies. f_{el}^s and f_{el}^l are compared to find which one is better at representing the real elastic energy f_{el} related to the complete coherent phase boundaries.

In short, in the small deformation regime, our Gibbs energy approach gives us the same expression for the elastic energy of the (100) habit plane reported by Cahn [154-156, 231], and a stress-strain relation is proposed for the (111) habit plane. Our approach is extended to be valid in the large deformation regime. In the limiting case, where the deformation is small, the formulae of the elastic Gibbs energy in the large deformation regime becomes the corresponding formulae in the small deformation regime. The expression of elastic Gibbs energy in the large deformation regime is more precise but more complicated than that in the small deformation regime. Our approach is more advantageous than Cahn's approach since stress is considered as a variable. Normally, the stress counted in the calculation of the coherent spinodal is induced by the lattice mismatch.

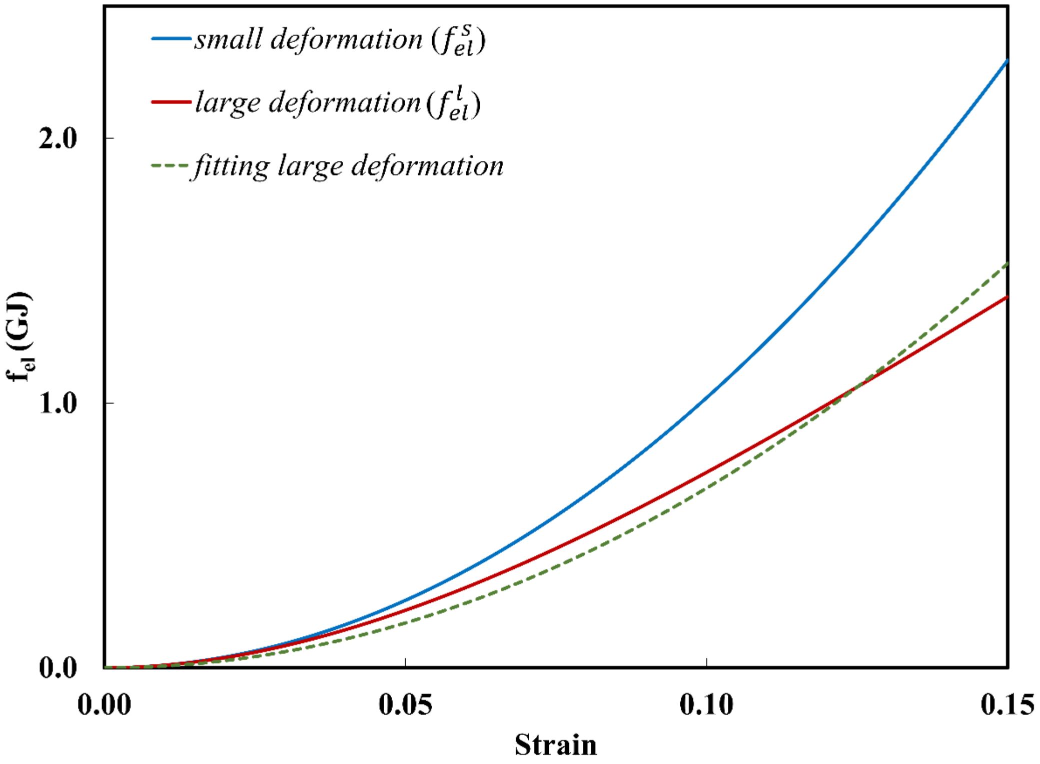

Figure 6.1: Calculated maximum stress causing the formation of coherent miscibility gap according to our approach for various systems.

6.3 Case study

After developing the formalism of the elastic Gibbs energy in both the small and the large deformation regimes and for both the (100) and (111) habit planes, in this section, our Gibbs energy approach is used to calculate the coherent spinodal and coherent miscibility gap of some cubic systems. Our literature review identified the Au-Pt, MgO-CaO, Cu-Ag, Al-Zn, NaCl-KCl, Au-Ni and Cu-Co systems as good candidates for applying our model. For every system, we applied our calculation in both the small and large deformation regimes. Moreover, the influence of the change of physical properties upon temperature and the impact of η on the calculation of the coherent miscibility gap is clarified. We will discuss case by case in details before presenting a general discussion on the elastic Gibbs energy approach. Note that the calculation of coherent miscibility gap and coherent spinodal in the large deformation regime is shown for every binary system since it is more exact. It is later compared with the calculation in the small deformation regime. It is worth mentioning that our calculation preferences and the values of the relevant physical properties of the materials used in this study are listed in the appendices. The chemical component of the Gibbs energy expression (Equation 6.1) was taken from published CALPHAD [239] evaluations. We used the previously reported thermodynamic models to describe the equilibrium miscibility gap appearing in every binary system of interest. Noticeably, in the following figures, we show only the equilibrium miscibility gap rather than the equilibrium phase diagram and the extrapolation part of the equilibrium miscibility gap which does not appear in the equilibrium phase diagram is shown as a dashed line.

6.3.1 Au-Pt

Even if the Au-Pt system has always been considered as an example for the calculation of the coherent miscibility gap of an isotropic system, there are not many available experimental data on Au-Pt coherent miscibility gap. Van der Toorn [240] showed that unlike 31.7 and 89.6 at% Pt polycrystalline samples, 41.8 and 81.2 at% Pt alloys aging at 873 K exhibits sidebands and hence are inside the coherent miscibility gap [240]. In the same work, sidebands were observed after 2 and 4 min of aging 86.6% Pt single crystals at 973 K while they are absent in 90.1% single crystals under the same condition [240]. The modulated structures were also detected in a temperature range by x-ray technique [241]. The author pointed out that the stability of a periodically modulated lattice appears to be dependent on the difference in lattice constants, i.e. the elastic strain energy [241].

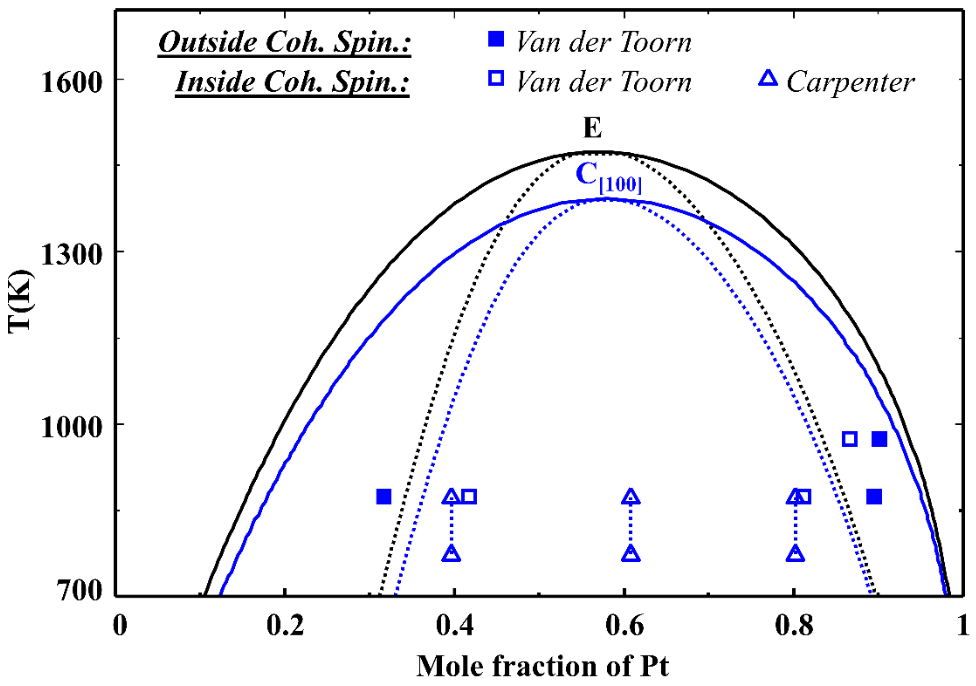

Figure 6.2: Calculated coherent miscibility gap and coherent spinodal decomposition of the Au-Pt system for the (100) habit plane in the large deformation regime without considering the temperature effect in comparison with experimental data [240, 241]. **E** and **C**$_{\mathbf{(100)}}$ are the incoherent equilibrium and coherence of the (100) habit plane, respectively.

The Au-Pt equilibrium phase diagram, which describes well the equilibrium experimental data [196], is modelled using thermodynamic parameters reported by Xu et al. [242]. Physical properties of Au and Pt, including lattice parameters, thermal expansion coefficients, elastic constants are well investigated [196, 243-250]. Since the lattice parameter of the solid solution is linearly dependent on its composition [250], only constant η is considered. Elastic constants of the solid solution in this work are considered to be linearly dependent on composition as in Xu et al. [196]. Our calculations of the coherent miscibility gap using formulae for the large deformation regime ($\eta \cong 0.0386$) show that the (100) habit plane is more stable than (111). It is consistent with the declaration that the Au-Pt system appears to be approximate to the ideal (100) coherent structure [251]. Our calculation shows a similar result to the calculations done by Jantzen & Herman [252] which revealed the coherent critical point for (100) modulations at approximately 1373K. Our calculated coherent spinodal agrees well with the experimental data [240, 241] (Figure 6.2). The reported occurrence of modulated structure in the 86.6% Pt single crystals [240], which is out of our predicted coherent spinodal, does not make our model bad since our model is aimed at polycrystalline material.

6.3.2 MgO-CaO

It is difficult to find any experimental work on coherent miscibility gap of this system due to high liquidus temperatures, vaporization of MgO and chemical reactivity of CaO. Most of the experiments related to the MgO-CaO system are based on the epitaxial growth of oxides or solid solution films. In this case, the $Mg_xCa_{1-x}O$ solid solution is a metastable phase which can exist at a temperature up to 973K [253, 254]. Spinolo and Anselmi-Tamburini [255] reported the decomposition of a $Mg_xCa_{1-x}O$ solid solution into a couple Mg-rich and Ca-rich oxide phases. The compositions of the two oxide phases are considered in

between the chemical and coherent spinodal decomposition rather than thermodynamic equilibrium. Later, Li et al. [256] investigated the nonequilibrium epitaxial growth process of $Mg_xCa_{1-x}O$ solid solution films at 873 K. In the MgO-CaO solid solution region growing on CaO [001] surface, lattice spinodal lines were observed indicating uprising diffusion causing the unmixing of the solid solutions after annealing at 1073 K. The lattice structure could be

maintained after spinodal decomposition since the annealing process was very short. $Mg_{0.53}Ca_{0.47}O$ and $Mg_{0.12}Ca_{0.88}O$ were estimated as the minimal and maximal compositions corresponding to the coherent spinodal decomposition after annealing at 1073 K [256]. However, the phases obtained through coherent spinodal decomposition in the interface of CaO-$Mg_{0.7}Ca_{0.3}O$ could not represent the coherent spinodal decomposition of the solid solution $Mg_{0.7}Ca_{0.3}O$.

The MgO-CaO equilibrium miscibility gap was reproduced using thermodynamic data for the solid phase taken from Wu et al. [257] Lattice constants of MgO and CaO are taken from Fiquet et al. [258]. Vegard's law is applicable as shown previously [259, 260] and the estimated value of η is 0.1332 showing a large difference between the lattice parameters. When considering the temperature effect, instead of taking the reported thermal expansion coefficients of both oxides [261], the lattice parameters are obtained by fitting the experimental data from Fiquet et al. [258] linearly with temperature. Moreover, experimental data of the elastic constants of the oxides are well reported [255, 262-268]. We assume a linear dependence of the elastic constants of the solid solution on its composition. Our assumption is acceptable in comparison to the relation of the calculated elastic constants and composition reported by Fan et al. [260].

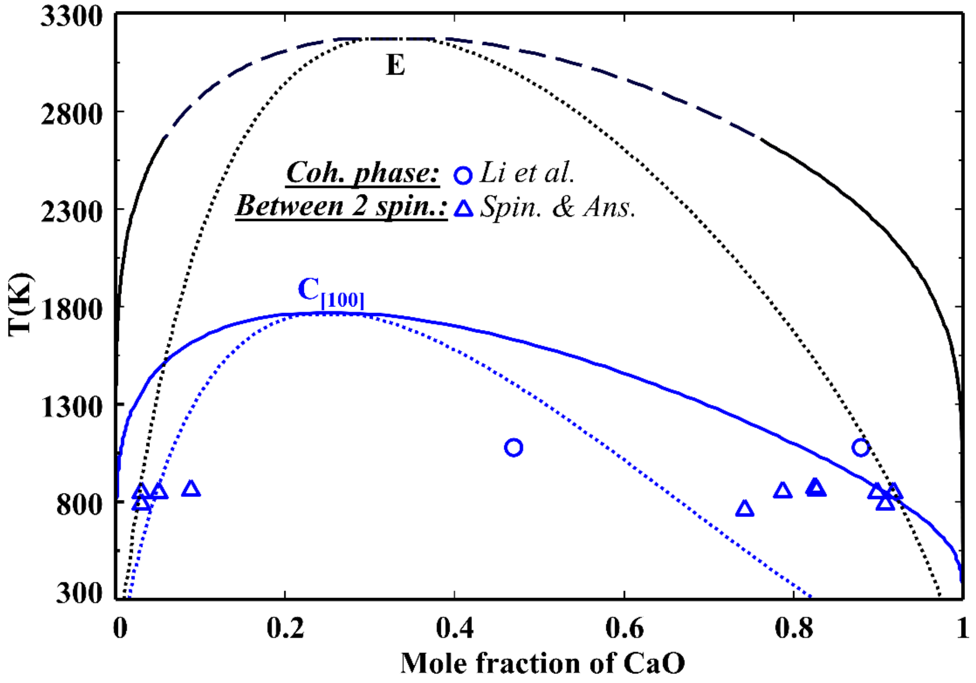

Figure 6.3: Calculated coherent miscibility gaps and coherent spinodal of the MgO-CaO system for the (100) habit plane in the large deformation regime without considering the temperature effect in comparison with experimental data [255, 256]. **E** and $\mathbf{C}_{(100)}$ are the incoherent equilibrium and coherence of the (100) habit plane, respectively.

As mentioned previously, in the MgO-CaO coherent system, (111) should be the minimal elastic plane using Cahn's approach [269]. However, our calculations using Cahn's approach show that (100) is preferable. Our calculations of the coherent spinodal decomposition boundary using formulae in the large deformation regime ($\eta \cong 0.1332$) are consistent with the reported data of Spinolo and Anselmi-Tamburini [255] (Figure 6.3). However, despite their claim that these experimental points were lying in between the coherent and equilibrium spinodal [255], no clear evidence was shown. Therefore, the calculation of spinodal decomposition in our study is a prediction more than a description of experimental data.

6.3.3 Cu-Ag

Not many experiments report the existence of coherency in the Cu-Ag system. A cube-on-cube orientation relationship between the Ag-rich precipitates and the Cu-rich matrix has been reported in several studies [200, 270-275]. However, the habit plane is not clearly mentioned in those studies. Repeated misfit dislocations in the binary Cu-Ag (111) interface was observed approximately every 9 atomic spacings of Cu apart. This agrees with the theoretical calculation based on the lattice constants of the two metals [270]. Similar observation of semi-coherent habit planes revealing periodic interfacial dislocations in 9 plane spacing of either (100)Cu or (111)Cu has been reported by Liu et al. [200, 274]. In another study, the disc-shaped aggregates were produced in the (100) planes of the single crystal matrix Cu-5.7 wt% Ag in the temperature range from 673 K to 913 K [273]. Briefly, there is no experimental evidence defining the most favourable coherent habit plane of the Cu-Ag system.

In this study, the miscibility gap formed by the FCC phase is described using thermodynamic parameters taken from Moon et al. [276]. The physical properties of pure metals have been well investigated [245, 247, 249, 277-279]. The lattice parameter of the solid solution is assumed to obey Vegard's rule because it does not deviate significantly from linearity as shown in Subramania and Perepezko [277]. Since no evidence from experiments or calculations has been found, a linear dependence of the elastic constants on composition is expected for the solid solution.

Calculating the coherent miscibility gap using Cahn's approach shows that the (100) habit plane is preferable, contrary to the reported experimental data. However, our calculations of coherent miscibility gap and coherent spinodal show no considerable difference between the (100) and (111) habit planes (Figure 6.4). The coherent miscibility calculated in the large deformation regime ($\eta \cong$

0.1224) is a good description of the available experimental points [200, 270-273] (Figure 6.4). Because of the lack of the experimental data, it is very difficult to justify our calculation of coherent miscibility gap for this system. The calculated coherent miscibility gap is considered as a prediction rather than a description.

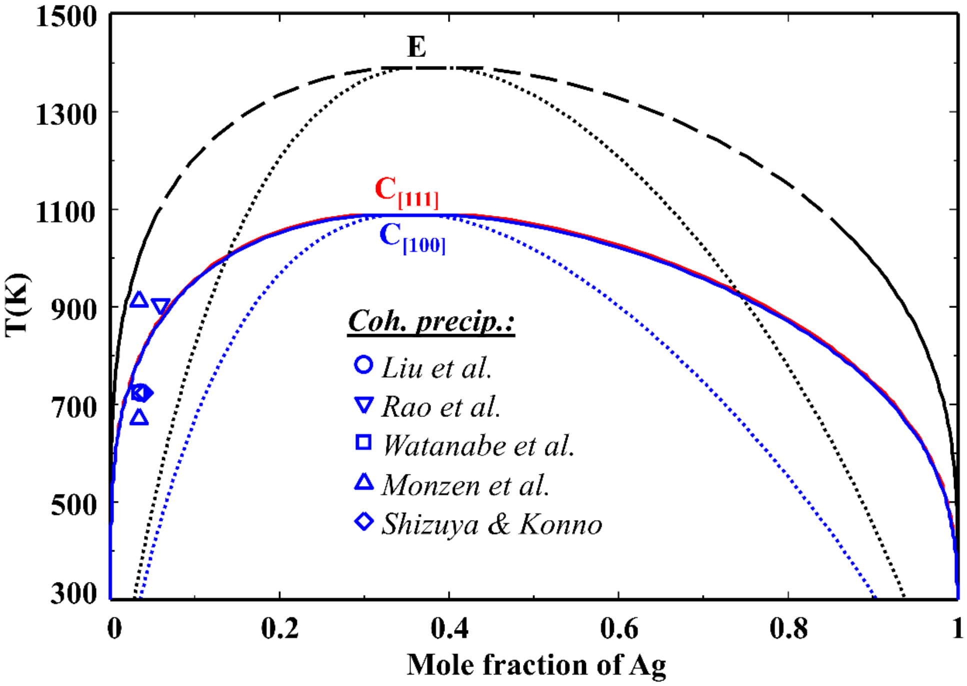

Figure 6.4: Calculated coherent miscibility gaps and coherent spinodal of the Ag-Cu system corresponding to the (100) and (111) habit planes in the large deformation regime without considering the temperature effect, in comparison with experimental data [200, 270-273]. **E, $\mathbf{C_{(100)}}$** and **$\mathbf{C_{(111)}}$** are the incoherent equilibrium, the coherence of the (100) and the coherence of the (111) habit plane, respectively.

6.3.4 Al-Zn

The coherent miscibility gap and coherent spinodal of the Al-Zn system have been investigated in numerous studies [280-297]. Experimental work related to the coherent phase diagram has been reviewed by Murray et al. [280]. According to Simerska et al. [292], the precipitation processes in Al-Zn alloys can be characterized by the following sequence: spherical GP zones → ellipsoidal GP zone → rhombohedral αR’-phase → cubic α’-phase → stable β-phase (HCP-Zn). The GP zone is considered as a coherent metastable phase while the αR’-phase is a partially coherent metastable phase. For their part, Murray et al. [280] did not distinguish the GP zones and the rhombohedrally distorted platelets as two phases. According to them, the formation of rhombohedral platelets was governed by the coherent solvus which is independent of particle size. The metastable phase is then thermodynamically a single phase [280]. The coherent miscibility gap is depressed below the equilibrium incoherent gap because of the additional elastic energy required to maintain coherence within the matrix. As stated by Schwahn and Schmatz [290], the temperature depression is about 28 K. For this system, the elastic energy is dependent on the shape of the coherent particle according to Murray et al. [280]. A small spherical particle is undistorted by the matrix and maintain the FCC structure even in the stress environment. At a critical size, the precipitation becomes ellipsoidal since the stress applied by the matrix distorts the FCC lattice to a rhombohedral structure. Thermodynamically, the ellipsoidal precipitation has an FCC structure if it relaxes in a stress-free environment [280]. In the ellipsoidal zones, coherency is maintained with the matrix on the (111) planes. (111) relationship has been found experimentally [284, 288, 292, 297, 298]. As it can be seen from the reported experimental data in Figure 6.5, the boundary of GP zones and that of rhombohedral αR’-phase are indistinguishable.

The equilibrium incoherent FCC phase was reproduced using thermodynamic parameters of Sabine an Mey [299]. Later, Kogo and Hirosawa [198] re-assessed this binary system and slightly changed the thermodynamic parameters. They claimed that the new set of parameters describes the FCC miscibility gap better, however, the calculated phase diagram is not significantly different from that reported by Sabine an Mey [299]. Hence, for this study, we decided to keep using the thermodynamic parameters of the FCC phase by Sabine an Mey [299]. The lattice constants of FCC-Al and FCC-Zn are taken from Kittel [300] and Muller et al. [301]. The lattice parameter and molar volume of the solid solution are also assumed to be linearly dependent on its overall composition. It is reasonable to assume Vegard’s rule for the FCC solid solution since the experimental data on lattice parameters of the solid solution as a function of composition listed by Murray [280] does not deviate considerably from the linear relationship. Thermal expansion coefficients of Al are taken from Cohen et al. [245] while there has been no thermal expansion coefficient found for FCC-Zn. For convenience, we assume that the thermal expansion coefficient of FCC-Zn is similar to that of HCP-Zn reported in Cohen et al. [245]. In addition, elastic constants of FCC-Al were examined experimentally by a number of authors [302-306]. When comparing with DTF calculations of Pham et al. [307], experimental data reported by Kamm and Alers [304] and Gerlich and Fisher [305] are considered to describe well the physical properties of Al. Elastic constants of the metastable FCC-Zn is calculated (Appendix H) since no experimental data available. Even if our estimation of C_{12} is similar to Magyari-Köpe's calculations [308], the significant difference between our estimations and their values for C_{11} and C_{44} needs to be verified in another study. Elastic constants of the FCC solid solution are assumed to be linearly dependent on composition. However, since there has not been any calculation or evidence for the linearity of the elastic constants dependance on composition, this assumption might not be correct. Elastic anomalies could possibly exist similarly to what was observed in Ag-Zn alloys [308].

The calculated coherent miscibility gap and coherent spinodal using Cahn's approach do not describe well the experimental data [281-297]. Previously, Kogo and Hirosawa [198] claimed that the coherent miscibility gap was reproduced well using Cahn's approach. Why are there differences between our calculation and Kogo and Hirosawa [198], even if the same principle was adopted? First of all, for calculating the elastic Gibbs energy, Kogo and Hirosawa [198] used a value of η taken from Cahn [155], which is about 2.5 times less than what is estimated by us ($\eta \cong 0.0614$) (Appendix G). Cahn [155] did not explain how the value was obtained. However, a similar value of η could be obtained under the assumption of similar molar volume between FCC-Zn and HCP-Zn. Considering an equal molar volume of HCP-Zn and FCC-Zn could raise a significant error in the calculation of η since, in HCP-Zn, the ratio of a/c is more than 1.85 at a temperature higher than the room temperature [309], which is very different from the theoretical value of 1.633 [310]. Moreover, from our perspective, the lattice parameter of FCC-Zn, calculated from first-principles calculations done by Muller et al. [301], is more reliable. Secondly, the authors used different Young's modulus of metals [198]. Calculated from our selected elastic constants, Young's modulus of FCC-Al is 1.5 times higher than the reported values used in the coherent calculation of Kogo and Hirosawa [198] and our Young's modulus of FCC-Zn is only about half of theirs [198]. It is impossible to access the reference in which Kogo and Hirosawa took the value of Young's modulus of FCC-Zn while our value is close to what was obtained by EMTO-CPA calculation done by Magyari-Köpe [308]. In short, using an incorrect value of η and an unreliable value of Young's modulus of metals lead Kogo and Hirosawa [198] to an inaccurate calculation of the coherent miscibility gap.

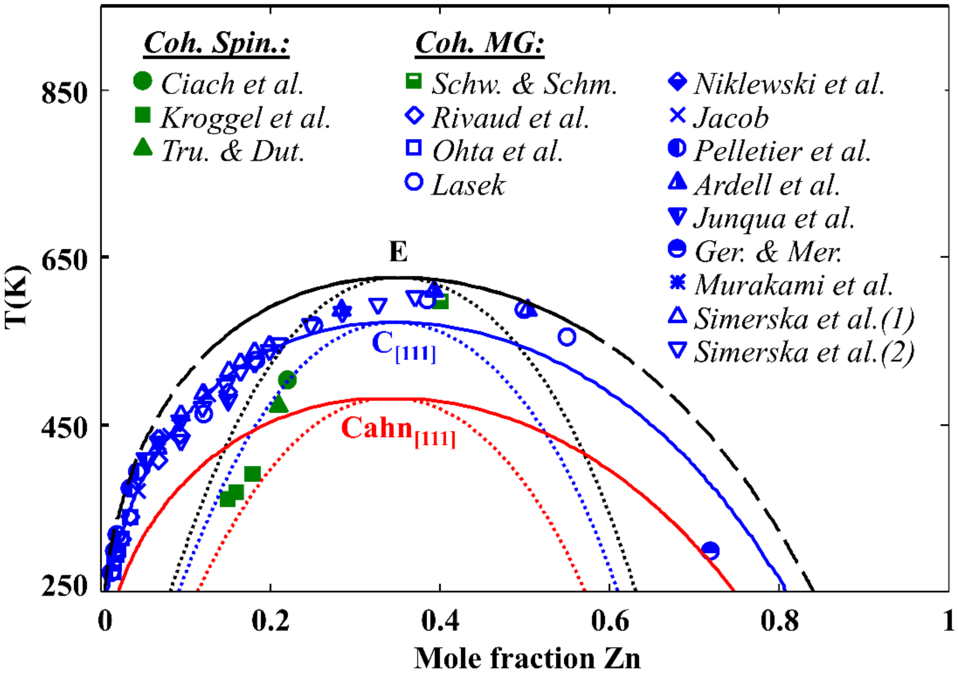

Figure 6.5: Calculated coherent miscibility gap and coherent spinodal of the Al-Zn system for the (111) habit planes using Cahn's approach or our approach in the large deformation regime without considering the temperature effect, in comparison with experimental data of coherent miscibility gap [281-293] and experimental data of coherent spinodal [294-297]. **E**, **C**$_{\mathbf{(111)}}$ and **Cahn**$_{\mathbf{(111)}}$ are the incoherent equilibrium, the coherence of the (111) habit plane calculated by using our approach and Cahn's approach, respectively.

Using Cahn's approach, the calculated (111) coherent miscibility gap is slightly less stable than the calculated (100) coherent miscibility gap. The stability of (100) was also reported in Lasek [311].

However, Muller et al. [301] showed that the (111) superlattices are the lowest energy coherent structures in Al-Zn. The coherent plane (111) has been observed experimentally in a number of studies [284, 288, 292, 297, 298]. Using our proposed formulation for the (111) habit plane, the calculated (111) coherent miscibility gap describes experimental data sufficiently (Figure 6.5). Our calculations could be improved by using a better estimation of elastic constants of FCC-Zn taking into account their changes upon temperature, or using a better description of elastic constants of the solid solution versus its composition. Results shown in Figure 6.5 are still in very good agreement with the experimental points reported in the literature.

6.3.5 NaCl-KCl

It is very hard to find any experimental data on the coherent diagram of NaCl-KCl. According to Andreev & Buritskova [312], for an equimolar mixed crystal, the coherent spinodal decomposition took place below 100ºC [312] while for the decomposition at 130ºC and above, it was by nucleation and growth mechanism [313]. The temperature difference between incoherent and coherent nucleation and growth of an equimolar crystal is reported to be 400 K [312]. Noticeably, the author was actually examining the crystal bulk density versus the temperature and time [312], hence, the results regarding coherent phase transformation did not come directly from any microstructure observation or elastic strain detection.

Both solid NaCl and KCl possess a simple cubic B1 structure. The incoherent phase equilibria of this system were described by Pelton et al. [314]. This study used their reported thermodynamic parameters to reproduce the equilibrium incoherent miscibility gap of the NaCl-KCl system. Lattice parameters of NaCl and KCl are taken from Barrett & Wallace [315]. Besides, according to their examination, the lattice constant of the solid solution does not obey Vegard's rule [315]. By fitting their experimental data [315], the lattice parameter of the solid solution can be satisfactorily expressed as a polynomial function of the second order of the composition. However, since the deviation from linearity is not significant, we assume that Vegard's rule is still applicable in this study. Thermal expansion coefficients of the two compounds are taken from Pathak & Vasavada [316]. Elastic constants are well reported, both experimentally [266, 317-327] and theoritically [328-331]. According to the collected experimental data, the elastic constants C_{11}^{NaCl}

and C_{44}^{NaCl} or C_{11}^{KCl} and C_{44}^{KCl} are consistent among studies and they behave almost as a linear function of temperature. C_{12}^{NaCl} or C_{12}^{KCl}experimental data vary slightly among studies. Since our temperature range of interest is 273K-800K (from near room temperature to slightly above the critical temperature of the miscibility gap) and the excellent agreement in reported measurement of elastic constants of NaCl [266, 317, 323] and KCl [266, 317, 324] in this temperature range, elastic constants within this range of temperature are chosen to calculate the coherent miscibility gap of this system. Specifically, elastic constants at room temperature and elastic constants as functions of temperature are taken from Slage & McKinstry [317]. In addition, Botaki et al. [319] measured the elastic constants of the solid solution at various temperatures. Unlike other systems, the solid solution $Na_{1-x}K_xCl$ does not show linearity between its elastic constants and its composition [319]. The elastic constants of solid solution at 300 K repoted by Botaki et al. [319] were fitted as a function of both temperature and composition.

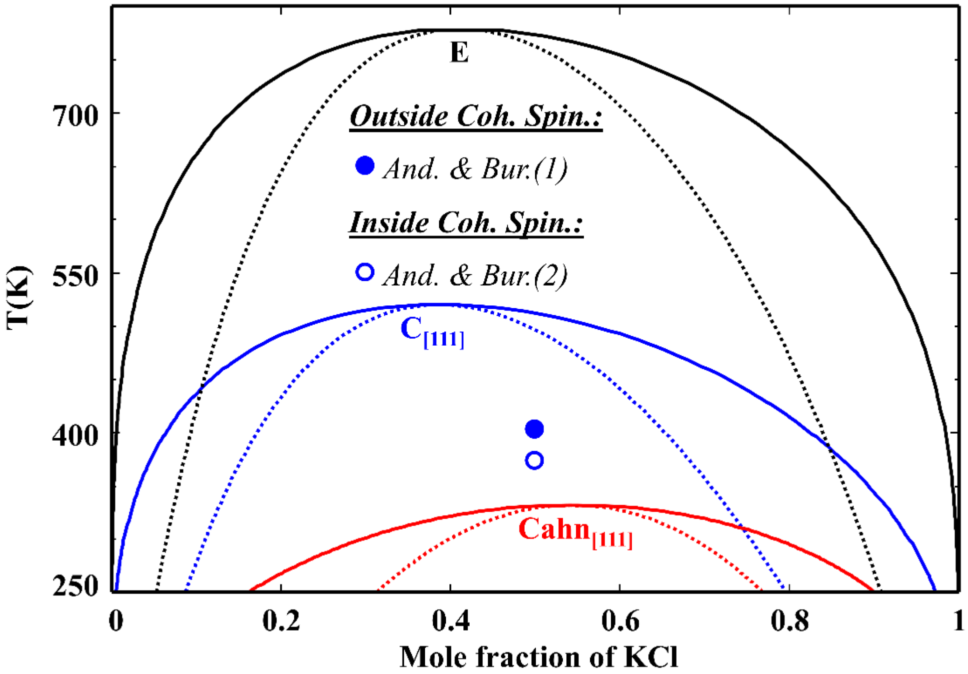

Figure 6.6: Calculated maximum stress causing the formation of coherent miscibility gap according to our approach for various systems.

According to Cahn's approach, the favorable habit plane is (111) and the (111) coherent consolute temperature $T_{coh} \cong 342\ K$, which is lower than the experimental values (Figure 6.6). Calculation of coherent miscibility gap with the (100) habit plane using any approach shows a coherent consolute temperature lower than room temperature. As mentioned by Wolfson et al. [332], "spinodal decomposition is highly unlikely in this system" because "the lattice parameter of KCl is ~10% larger than that of NaCl, the disparity in the sizes of the cations is much larger, 36%". The calculated (111) coherent miscibility gap using our approach in the large deformation regime ($\eta \cong 0.1092$), is higher than the experimental data [312, 313]. However, it is very difficult to justify any approach using only two experimental points.

6.3.6 Au-Ni

The coherent spinodal decomposition in Au-Ni alloys has been studied quite extensively [197, 333-339]. The modulated structure of Au-Ni alloys has also been observed in various studies [197, 333-338]. (100) was shown to be the preferable habit plane for these studies [197, 334, 338]. Available experimental datasets are in good agreement with each other in the Au-rich region. However, there is a discrepancy in the expected coherent spinodal boundaries among authors (Figure 6.7a). Some observed a modulated structure only for alloys with a composition between 20 and 60 at.% Ni [334]. However, Gronsky's group [335-337] and Wu [338] have found a modulated structure for the Au-77 at.% Ni sample at 423 K.

Golding & Moss [340] calculated the coherent spinodal using Cahn's approach. However, their calculations were performed at a much lower temperature than that of Hofer & Warbichler [197]. More importantly, the calculated coherent spinodal [197, 340] is different from the reported experimental results. According to Abadias et al. [233], the discrepancy between the coherent consolute temperature reported in the calculations of Golding and Moss [340] and Hofer and Warbichler [197] originates from the difference in the experimental value of entropy and the linear expansion coefficient used to calculate the coherent spinodal. Abadias et al. [233] claimed that their calculated coherent spinodal is in reasonable agreement with the region where modulated structures have been observed experimentally. However, according to our observation, their calculations also failed to predict the coherent spinodal decomposition in the Au-rich region.

For calculating the coherent miscibility gap, first, the Au-Ni thermodynamic behaviour was modelled using thermodynamic parameters reported by Wang et al. [341] The magnetic Gibbs energy of mixing which is shown in Gheribi et al. [342] is dependent on composition and temperature. For simplicity, the magnetic energy is fitted with an exponential function before taking the second derivative of the molar Gibbs energy to estimate the spinodal decomposition curve. Like in previous case studies, the elastic constants of Au are taken from Cagin et al. [247] assuming a linear temperature dependence. The reported experimental elastic constants of Ni are in good agreement among studies [343-345] but they are not well described by calculations [247, 346, 347]. Therefore, in this case study, elastic constants are taken from Alers et al. [345]. The elastic constants of the solid solution are assumed to be linearly dependent on composition as expected from experimental data of alloys reported by Golding et al. [348]. Lattice parameters and molar volumes of pure metals are taken from Lubarda [243]. The physical properties of the solid solution are assumed to be linearly dependent on composition. Thermal expansion coefficients are taken from Cohen et al. [245], which are in excellent agreement with the reported values of Cverna [246].

According to our calculations, (100) appears to be the most favourable direction, consistent with experimental evidence [197, 334, 338]. However, the calculated coherent spinodal decomposition in the large deformation regime ($\eta \cong 0.1458$) cannot reproduce the experimental points (Figure 6.7a). The critical temperature and composition are different from those expected through experimental data. Even worse, the composition range of the coherent spinodal is not well predicted.

In order to reproduce the experimental data of the coherent miscibility gap, we considered some possibilities. Considering nonlinear elastic constants could not shift the coherent miscibility gap to match the experimental data. Neither considering third-order elastic constants would help to improve our calculations since it would make the calculation of the elastic Gibbs energy too complicated. Even if the lattice parameter of a solid solution is treated to obey the reported nonlinear relationship [349, 350], the calculated coherent miscibility gap and coherent spinodal do not change significantly. Later, the magnetism of this system is put into concern. It is well known that the Curie temperature of metals and alloys is affected by pressure [351]. Also the magnetic moment could be modified according to the pressure [352]. Therefore, the existence of coherent stress could change the magnetic properties of the solid solution of the Au-Ni system. However, the changes of magnetic properties due to the coherent stress has no significant impact on the calculation of the coherent miscibility gap. Even not taking into account the magnetic Gibbs energy does not change the calculated coherent miscibility gap and the coherent spinodal considerably (Figure 6.7a). So far, no simple explanation could help us to understand the cause of the abnormal coherent miscibility appearing in this system.

When reproducing the coherent miscibility gap of the Au-Ni system, we believe that there is an additional unknown effect contributing to the coherent relationship in this system. This effect should cause a similar stress tensor σ'_{ij} on the crystal. This stress can be treated similarly as the stress caused by lattice mistmatch in Equation 6.4. We suppose that σ'_{ij} would cause an effective strain tensor, ε'_{ij} and the corresponding effective change of the lattice parameter versus the solid solution composition η'. Hence, the coherent spinodal boundary should obey:

$$\frac{\partial^2 G}{\partial x^2} + 2V_m Y(\eta + \eta')^2 = 0 \qquad (6.10)$$

It means that both lattice mismatch and an unknown effect cause the displacement of the coherent miscibility gap and coherent spinodal. Then, experimental data of coherent spinodal of the Au-Ni system [197, 333-335, 353] are well described (Figure 6.7b) by using the optimized effective η':

$$\eta' = -0.2226\, x_{Ni} - 0.14734 \qquad (6.11)$$

Here, η' is an adjustable parameter. It is an empirically linear function of composition. The physical origin of η' is unclear since no experimental data, first principle analysis or modelling related to this phenomenon has been found. η' could arise from the kinetic residual stresses or from the change of magnetic susceptibility under mechanical stresses (known as magnetoelastic effect or Villari effect) [354] or from the modification of magnetic properties of Ni under tensile strain on or near coherent boundaries [355, 356].

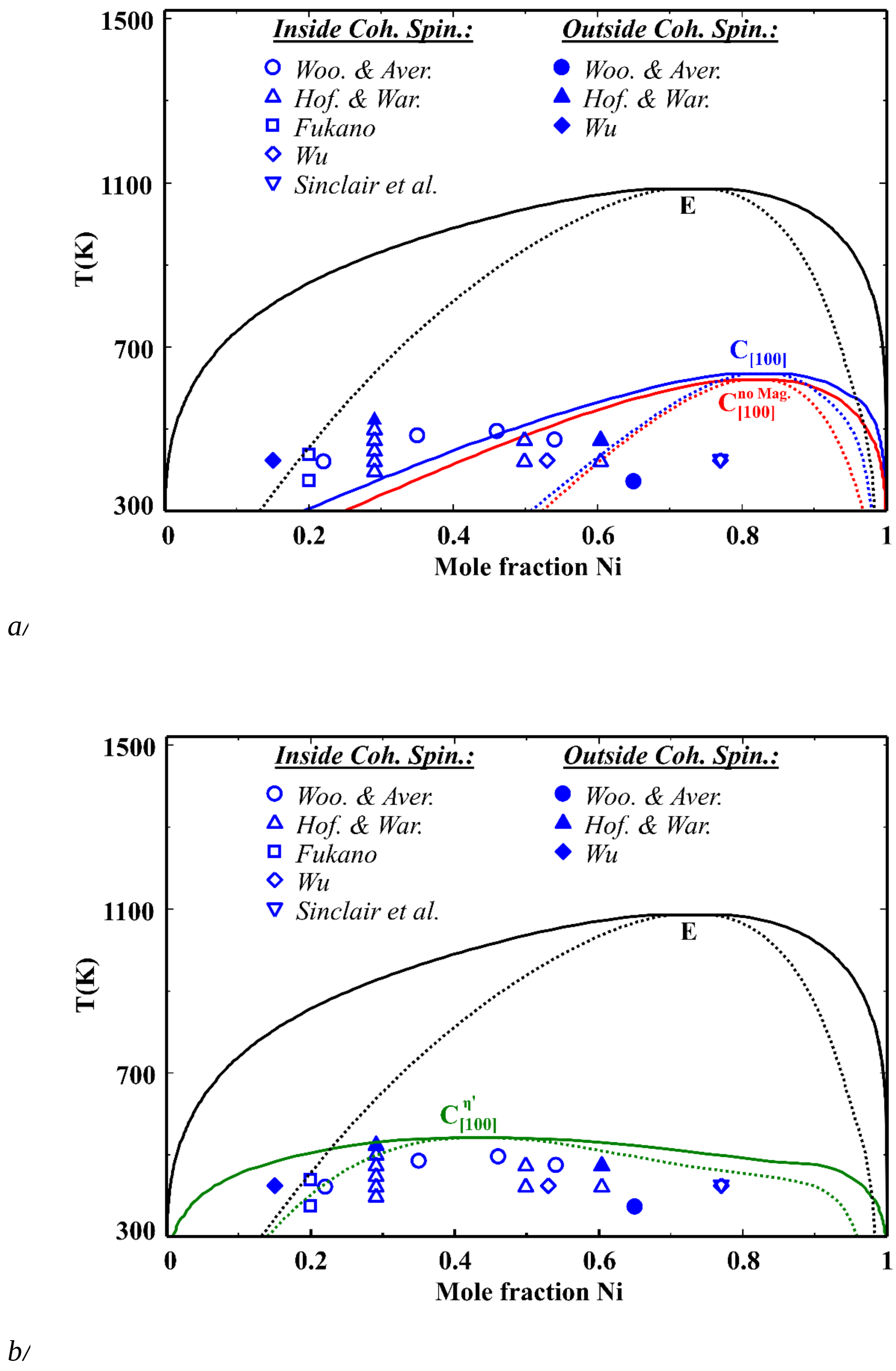

Figure 6.7: Calculated coherent miscibility gap and coherent spinodal of the Au-Ni system for the (100) habit plane: a/ in the large deformation regime without the temperature effect and with and

without considering the magnetic properties, in comparison with experimental data [197, 333-335, 353]; b/ in the large deformation regime without temperature effect using our optimized η' to reproduce the experimental data [197, 333-335, 353]. $\mathbf{E}$, $\mathbf{C}_{(100)}$, $\mathbf{C}^{\text{no Mag.}}_{(100)}$ and $\mathbf{C}^{\eta'}_{(100)}$ are incoherent equilibrium, the coherence of the (100) habit plane with and without magnetism and coherence of the (100) habit plane using η', respectively.

6.3.7 Cu-Co

According to Shim et al. [357], because Co has a limited solubility in Cu and a relatively small lattice mismatch, Co precipitates can form and maintain a coherent FCC transition phase until losing coherency at larger sizes. Coherent precipitation of Co in the Cu matrix has been observed in numerous studies [358-365]. Small coherent spherical precipitates were observed early after aging [358, 360, 363-365]. The coherent spherical precipitates were considered to increase in volume while changing shape to form cubes [358, 364]. Octahedral FCC-Co-rich precipitates were also observed by Takeda et al. [361, 362]. The observed habit planes are different among studies [358, 359, 361, 362, 364, 365]. However, (100) is the most frequently observed habit plane [358, 361, 364, 365] which is in agreement with the observation of typical (100) modulated structures in the alloys decomposing spinodally during aging [199]. Kozakai et al. [199] determined the coherent spinodal temperature, T_s, based on the theoretical analysis of their experimental results. Their calculated coherent spinodal shifts toward the Cu side and it has a broad extension along the magnetic transformation line [199].

The equilibrium incoherent Co-Cu system is approached by using parameters reported in Nishizawa & Ishida [366], and magnetic properties are taken from Wang et al. [367] The lattice parameter of Cu is taken from Subramania & Perepezko [277]. When calculating the coherent miscibility gap, the FCC-Co phase is considered. The lattice parameter of FCC-Co is taken from Cerda et al. [368]. Since there is no data for thermal coefficient of FCC-Co, we assume that the thermal coefficient of HCP-Co is analogous to that of FCC-Co. The thermal expansion coefficients of both metals are then taken from Cohen et al. [245]. The elastic constants of Cu are taken from Chang & Himmel. [249]. and the elastic constants of FCC-Co are taken from Strausse et al. [369]

Even if the values of elastic constants of FCC-Co are consistent among studies [369-371], they are not yet temperature dependent.

According to our calculations, (100) should be the most stable habit plane in agreement with experiments [199, 358, 361, 364, 365]. However, the estimated miscibility gap is much larger than what is observed experimentally. Since the value of η of this system is so small ($\eta \cong 0.0186$), the difference ΔT^c between the equilibrium and coherent consolute temperature is also very small. It means that there is almost no difference between the coherent miscibility gap and incoherent equilibrium miscibility gap. In fact, our calculations could describe the observed coherent precipitation in various studies [358-365]. However, it does not describe well the experimental data of the coherent spinodal boundary reported by Kozakai et al. [199] in which the temperature difference ΔT^c is expected to be around 400 K (Figure 6.8).

Our calculation of the coherent miscibility gap can be improved by using the temperature dependence of elastic constants and temperature dependent lattice parameter of FCC-Co. The calculation can be improved further if the change of lattice parameters and elastic constants of the solid solution versus composition are involved. Introducing the 3rd order elastic constants to the calculation of the elastic energy density would make it too complicated and time-consuming. Even if all the mentioned factors are taken into account, it is impossible to lower the coherent miscibility gap to ~400 K below equilibrium because of the very small lattice mismatch between the two crystals. Considering magnetism involved in the Cu-Co system, unsurprisingly, the change of the Curie temperature and the magnetic moment via pressure [351, 352] could not help us to reproduce successfully the experimental coherent spinodal curve [199]. Even worse, the calculated coherent miscibility gap changes insignificantly even when no magnetism is involved. Hence, like the Au-Ni system, we optimized an additional η' (Equation 6.10) in order to reproduce the reported experimental data of coherent miscibility gap [358-365] and coherent spinodal [199] (Figure 6.8):

$$\eta' = 0.15 \tag{6.12}$$

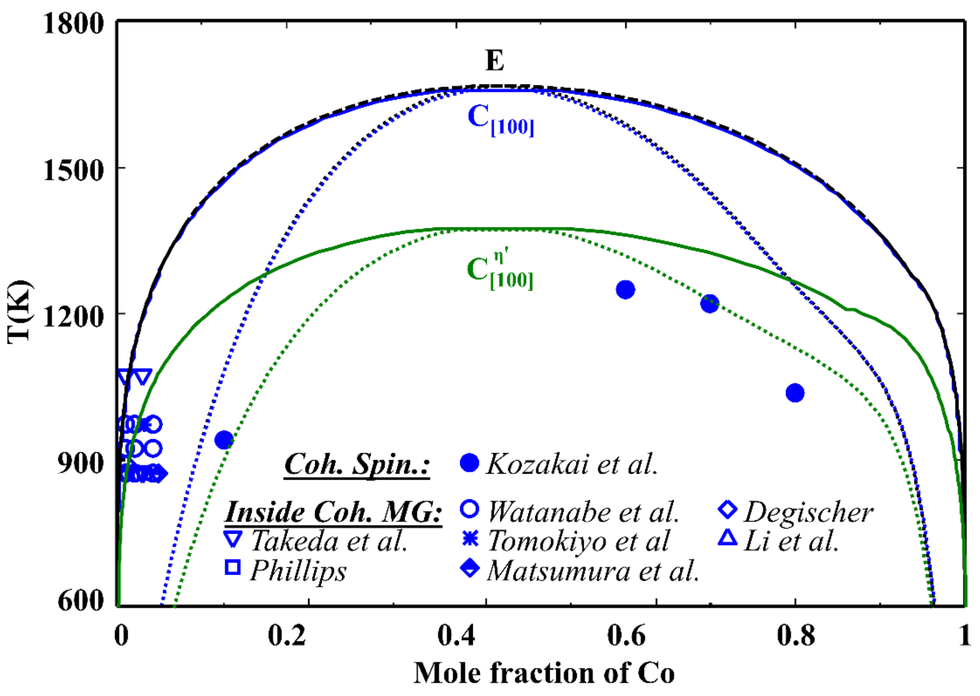

Figure 6.8: Calculated coherent miscibility gaps and coherent spinodal of the Cu-Co system for the (100) habit plane in the large deformation regime without temperature effect and with or without considering our optimized η_k, in comparison with experimental data [199, 358-365]. **E**, $\mathbf{C_{(100)}}$ and $\mathbf{C^{\eta'}_{(100)}}$ are the incoherent equilibrium, the coherence of (100) habit plane without and with our optimized η_k, respectively.

It is possible that η' results from the interaction between coherency and magnetism similarly to our proposed scenario in the Au-Ni system. However, η' could be caused by another effect. It is observed that the experimental coherent consolute temperature is in the vicinity of the melting point of copper. Therefore, thermal vacancies should contribute to the depletion of the consolute temperature due to coherency. If the molar volume of thermal vacancies is assumed to be 50% of that of Cu, using the known concentration of thermal vacancies of Cu metals at the fusion temperature [372], our calculated molar volume of Cu with thermal vacancies increase by less than 0.04%. A slight change of molar volume of Cu makes almost no difference in our calculations of the coherent miscibility gap. Hence, thermal vacancies should not be the main cause of η'. Interestingly, deep undercooling of the Cu-Co alloys into the miscibility gap was allowed [373]. Cao et al. [374, 375] had measured the metastable liquid miscibility gap. The measured critical temperature of phase separation at a Co concentration of 47 at.% is about 108 K below the corresponding liquidus temperature [375]. The metastable liquid miscibility gap occurred due to the influence of both bulk supercooling and cooling rate on the microstructure and phase selection during solidification of Cu-Co alloys [376]. Lowering the liquidus temperature could consequently reduce the stability of the solid solution and hence lower the coherent miscibility gap. This kinetics effect could possibly be the main origin of η'. To sum up, η' could be a result of the interaction between magnetism and coherency like in the Au-Ni system or it could be caused by the kinetic effect. We suggested two scenarios for η', however, another not-yet-found-effect could be the answer.

6.3.8 Discussion

In general, our approach shows elastic energy in both the small and large deformation regimes while Cahn's approach is only applied in the small deformation regime. To compare our Gibbs energy approach with Cahn's approach, the ratio m has been defined and investigated:

$$m = \frac{E_{elastic}^{Gibbs\,energy}}{E_{elastic}^{Cahn}} \tag{3.4}$$

For examining the value of m in this study, $E_{elastic}^{Gibbs\,energy}$ in Equation 3.4 is calculated using the formulae in the large deformation regime without considering the temperature effect. The maximum value of m for different systems at room temperature is shown in Figure 6.9. It is easy to notice that for systems where no magnetism is involved, the value of m is almost unchanged versus the overall composition of the solid solution and $m < 1$, meaning that our estimated elastic energy density is smaller than that of Cahn's (Figure 6.9). It is consistent with the idea of developing the formulae in the large deformation regime. Consequently, our estimated coherent consolute temperature is lower than the one given by Cahn's approach. For systems involving magnetism like Au-Ni and Cu-Co, the occurrence of η' is causing the value of m to differ significantly from these of the other systems. Because of the employment of the composition dependent η' in the Au-Ni system, the value of m changes with the overall composition and its maximum value is higher than 1. The large value of η' in the Cu-Co system make the value of m significantly larger than these for other systems.

Considering our Gibbs energy approach, in general, the elastic energy calculated in the large deformation regime is smaller than the corresponding energy calculated in the small deformation regime, since a higher order of elastic energy is considered. As a result, the coherent miscibility gap and coherent spinodal calculated in the large deformation regime are larger than the corresponding curves in the small deformation regime. The calculated coherent consolute temperatures using formulae in the large deformation regime is higher than that in the small deformation regime (Figure 6.10).

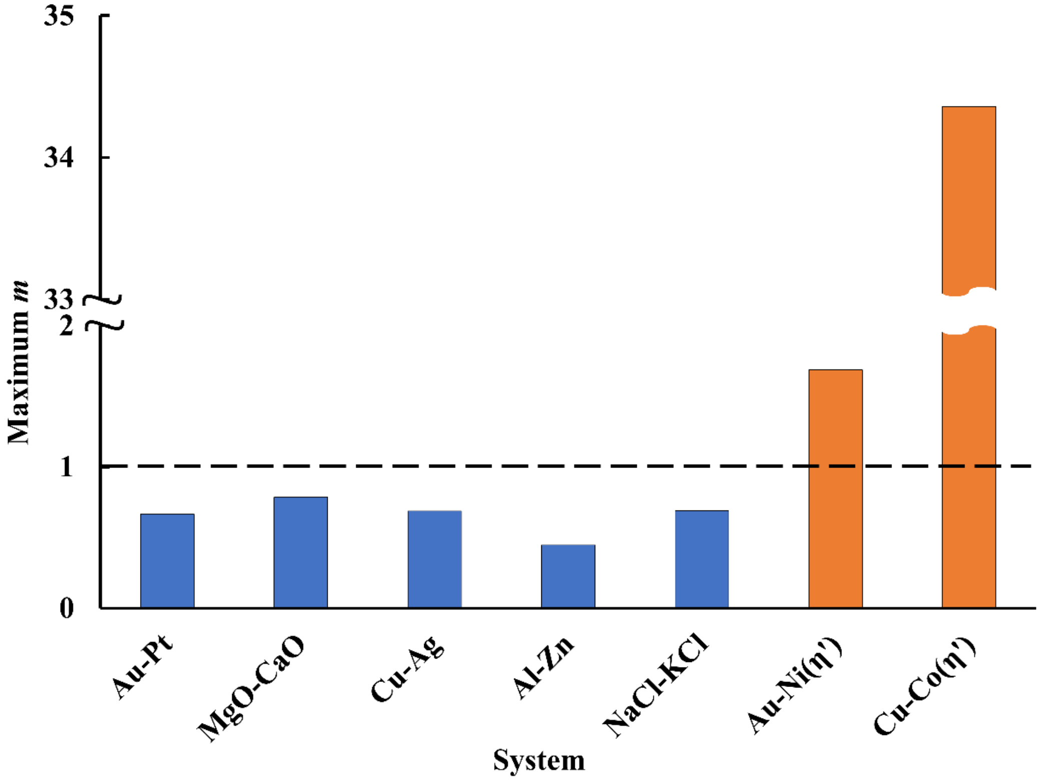

Figure 6.9: Calculated maximum ratio m of elastic energy density estimated by our Gibbs energy approach and by Cahn's approach for various systems at 298 K.

The differences between the coherent miscibility gaps and coherent temperatures calculated in the small and large deformation regimes are very small for systems with small values of η (like Au-Pt and Al-Zn) but they become significant for systems with large lattice parameter mismatch. The MgO-CaO system shows the largest difference (Figure 6.10) since the bulk moduli of oxides are significantly higher than those of metals. To sum up, the formulae of elastic Gibbs energy in the large deformation regime should provide us more exact coherent miscibility gap, however, it is simpler to calculate the coherent phase equlibria using elastic energy in the small deformation regime.

Moreover, the change of physical properties upon temperature and the change of η versus the overall composition should affect our calculations. Considering the temperature effect of physical properties in the calculation of the coherent miscibility gap and coherent spinodal does not change the results significantly (Figure 6.10). Depending on the case study, taking into account the temperature effect could increase the calculated coherent consolute temperature of a few Kelvin, up to ~120 K. However, the calculated consolute temperature shift is less than 13% of the magnitude of the coherent consolute temperature calculated without a temperature dependent term (Figure 6.10). In addition, it is worth mentioning that the magnitude of η could change the calculation of elastic energy significantly. That is why a clear and consistent method for calculating η is provided in appendix G. For every system considered in this paper, since the lattice constant of the solid solution does not deviate significantly from Vegard's rule, using either constant η or composition dependent $\eta(x)$ does not significantly change the calculation of coherent miscibility gap and spinodal.

Besides, the isostatic pressure and non-cubic precipitation due to the coherent stress should not affect the validity of our Gibbs energy approach. For geological systems like MgO-CaO or NaCl-KCl, under an isostatic pressure, even the physical properties of the solid solution (such as elastic constants, lattice parameters, thermal expansion coefficients, etc.) should change, our approach is still valid for calculating the coherent miscibility gap. Additionally, in our case studies, the non-cubic coherent precipitation occurring in the Al-Zn alloy is considered as a deformed form of an equilibrium cubic solid solution phase. Like the Al-Zn system, the coherent miscibility gap of other systems containing the observed non-cubic coherent precipitation could be calculated similarly.

Table 6.1 The group of habit plane for each endmember based on Cahn’s criteria at 298 K

Habit plane	**End-member**
(100)	Al, Ag, Au, Co(FCC), Cu, Ni, Pt, MgO
(111)	Zn(FCC), CaO, KCl, NaCl

Criteria for predicting the (100) or (111) habit plane also need to be discussed. According to Cahn [154-156, 231], the habit plane (100) is stable when $2C_{44} - C_{11} + C_{12} > 0$ and for a material with elastic constants satisfying the condition $2C_{44} - C_{11} + C_{12} < 0$, the habit plane (111) is stable. Let us consider the criteria reported by Cahn [154-156, 231] for all the end-members of our studied systems at 298 K and categorize them into 2 groups: (100) and (111) which stand for their favorable habit plane according to Cahn’s criteria (Table 6.1). As we can see from table 6.1, both end-members of the Au-Pt, Ag-Cu, Au-Ni, and Cu-Co systems belong to the (100) group and both end-members of the NaCl-KCl belong to the (111) group. The predicted group of habit plane using Cahn’s criteria for those systems are satisfactory. However, in Al-Zn or MgO-CaO systems, the two end-members belong to different habit plane group. Therefore, Cahn’s criteria is not good for determining the favorable habit plane for the systems like Al-Zn or MgO-CaO. In our previous study [232], Cahn’s approach is extended for an orthorhombic system, and Cahn’s criteria are no longer valid. We considered that the elastic energy reproducing the highest coherent miscibility corresponds to the most stable habit plane. In general, for cubic systems, Cahn’s criteria are consistent with our criteria [232] using Cahn’s approach. However, our criteria [232] are no longer valid if our proposed stress-strain relationship for the (111) habit plane is used to estimate the elastic Gibbs energy. Therefore, our stress-strain relation is used only when criteria of the (111) habit plane of Cahn is applied or if there are available experimental evidence for the (111) coherent miscibility gap. In fact, for any cubic system, it is easier to form the (100) habit plane as it is observed in most cases. Therefore, the calculation of elastic energy for the (111) habit plane becomes less important. Eventhough, our proposed stress-strain relation of the (111) habit plane is not based on Cahn’s stress-strain assumption. Our (111) stress-strain relation is a suggestion for calculating the (111) coherent miscibility gap for cubic systems and it could be improved further in the future.

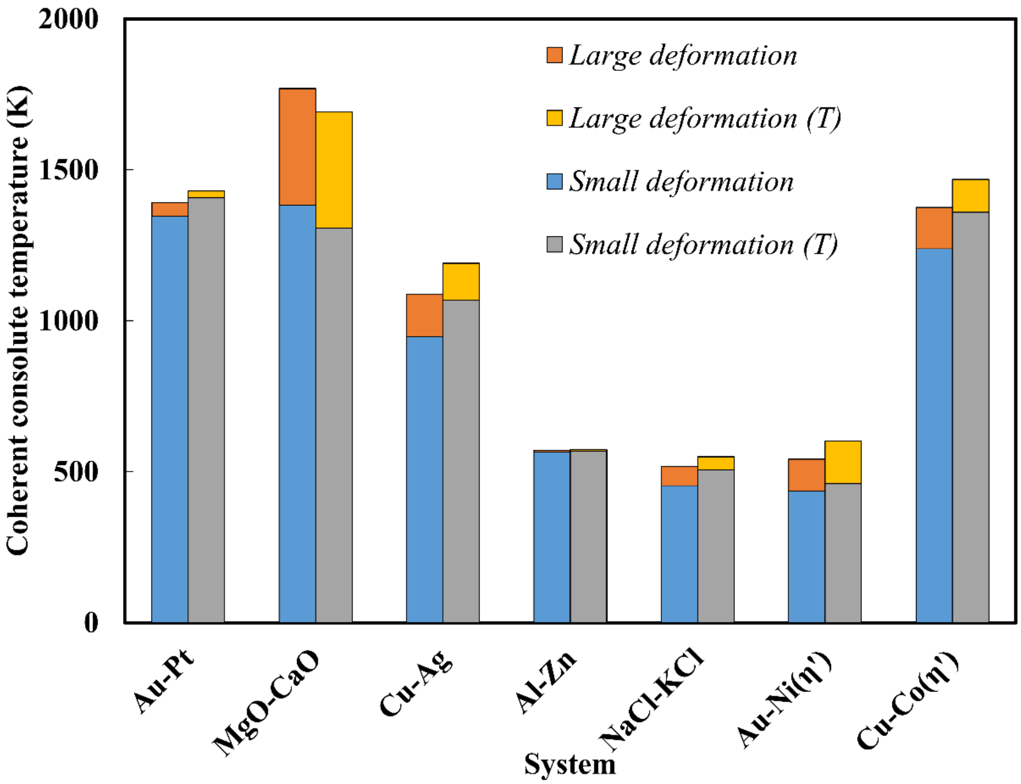

Figure 6.10: The calculated coherent consolute temperatures using our Gibbs energy approach in the small and large deformation with and without considering the temperature effect for various systems.

From our case studies, we have found that Cahn's approach cannot be applied directly to a system including magnetism like Au-Ni or Co-Cu. For such systems, an effective η' representing the additional effect causing the shift of the miscibility gap by coherency, must be optimized. We have proposed scenarios causing η' without finding any firm evidences. It is noticeable that the coherent consolute temperature in both systems are in the neighborhood of the Curie temperature of the magnetic elements. However, it is possible that η' has no relation with magnetism. As stated, η' is the effective change of lattice mismatch versus the overall composition due to the contribution of additional stresses to the coherency. Therefore, the total maximum stress occurring during the compositional fluctuation used to calculated the coherent miscibility gaps for the Au-Ni and Co-Cu systems should change. The calculated maximum stresses due to the composition fluctuation for the Au-Ni and Co-Cu systems with or without an additional effect have been compared with the maximum stresses occurring in other systems (Figure 6.11). Our calculations reveal that the maximum stresses of various systems are comparable (Figure 6.11). Note that the calculation of stress does not take into account the temperature effect on physical properties and the stresses do not change whether the calculation is in the small or large deformation regime. The small and large deformation regimes define the formulae of elastic energy only. The outstanding maximum stress of the MgO-CaO system is due to the ionic nature of the compounds, causing their enormous bulk moduli. The employment of the effective η' in the Au-Ni system does not significantly change the value of maximum stress, but it does change the composition where maximum stress occurs hence shifting the composition of the consolute point. On the other hand, the use of the effective η' in the Cu-Co system increases the stress, hence decreases the consolute temperature signifcantly. Therefore, our method for considering additional stresses to the contribution of cohernet miscibility gap is valid. Consequently, including an effective η' means that our approach is no longer restricted to calculating the coherent miscibility gap purely by lattice mismatch. Other kinds of effects due to kinetics, magnetism, electronic structure, etc. could also be considered.

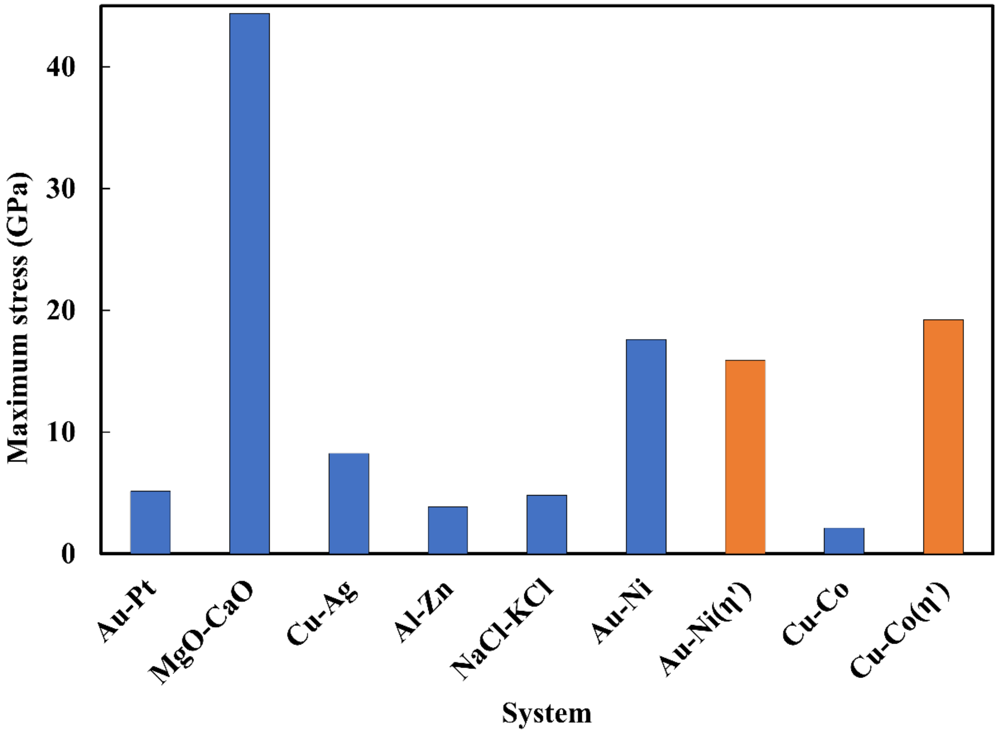

Figure 6.11: Calculated maximum stress causing the formation of coherent miscibility gap according to our approach for various systems.

6.4 Conclusions

In conclusion, we have introduced the elastic Gibbs energy approach to calculate the coherent miscibility gap and coherent spinodal decomposition and our proposed approach has been used to examine a number of case studies. In this paper:

- ✓ Stress-strain relationships corresponding to the (100) and (111) habit plane have been revealed.
- ✓ Elastic energy has been formulated both in the small deformation regime and in the large deformation regime.
- ✓ In general, the coherent miscibility gap and coherent spinodal calculated using formulae in the large deformation regime is larger than those calculated in the small deformation regime since high orders of elasticity is considered.
- ✓ The calculation of coherent miscibility gap in the large deformation regime is more precise but the calculation in the small deformation regime is simpler.
- ✓ We must acknowledge that the original elastic Gibbs energy approach is insufficient to describe the coherent phase diagram of a system where magnetism is involved (e.g. Au-Ni and Cu-Co system). The adjustable parameter η' is used to reproduce the experimental data on the Au-Ni and Cu-Co systems. It is the self-consistent way to describe the coherent phase diagram of the two systems. It means that the elastic Gibbs energy caused only by lattice mismatch is not enough to describe all coherent phase diagrams. Other additional stresses which contribute to the coherency could be considered. Therefore, the calculation of the coherent phase diagram becomes more flexible.
- ✓ Our approach gives a smaller value of elastic energy density than Cahn's approach and for systems where magnetism is involved, the employment of η' contributes to the significant difference between the elastic energy density estimated by our Gibbs energy approach and that of Cahn's approach.
- ✓ Our proposed stress-strain relation for calculating the elastic energy corresponding to the (111) coherent plane is suitable only if Cahn's criteria are applied or experimental evidence is shown.

- ✓ Temperature dependence of physical properties and compositional dependence of η does not significantly change the calculation of coherent miscibility gap and coherent spinodal.

6.5 Acknowledgements

The authors recognize the support of Natural Science, Engineering Research Council of Canada and the Canadian Foundation for Innovation through the Automotive Partnership Canada program and our industry partner Johnson-Matthey. Computations were made on the supercomputer Briaré at the Université de Montréal, managed by Calcul-Québec and Compute Canada.

CHAPTER 7 ARTICLE 4: COHERENT AND PARA-EQUILIBRIUM PHASE TRANSFORMATIONS IN Mn-DOPED-$LiFePO_4$ CATHODE MATERIALS: IMPLICATIONS FOR LITHIUM ION BATTERY PERFORMANCES

Anh Thu Phan, Aïmen E. Gheribi and Patrice Chartrand

Submitted to Journal of Alloys and Compounds on March 9th, 2020.

Abstract:

Due to the important similarities between olivine-$LiFePO_4$ and olivine-$LiMnPO_4$, manganese doping has drawn a lot of attention since it can improve the electronic and ionic conductivity of $LiFePO_4$, hence enhance the electrochemical properties. The thermodynamic behavior of Mn-doped-$LiFePO_4$ cathodes has been examined through the thermodynamic investigation of $Li(Mn_yFe_{1-y})PO_4$-$(Mn_yFe_{1-y})PO_4$ olivine joins. New sublattice thermodynamic models are proposed to describe the para-equilibrium in $Li(Mn_yFe_{1-y})PO_4$-$(Mn_yFe_{1-y})PO_4$ joins. Moreover, the elastic Gibbs energy approach extended in the large deformation regime is used to calculate the coherent miscibility gaps corresponding to (100) habit plane. The para-equilibrium and coherent miscibility gaps are calculated providing our prior estimated enthalpy of formation and the elastic constants of olivine compounds and enthalpy of mixing of binary sub-systems from first principles simulations based on Density Functional Theory (DFT). The experimental data on the para-equilibrium join is successfully reproduced, and the system is likely to experience the (100) coherent phase transformation. Our thermodynamic models of the $Li(Mn_yFe_{1-y})PO_4$-$(Mn_yFe_{1-y})PO_4$ join are able to describe most of the features of the electrochemical behavior of $Li(Mn_yFe_{1-y})PO_4$ cathodes including the electrochemically driven phase diagram, open circuit voltage (OCV), asymmetry of charging/discharging processes, potential shift and favorable coherent phase transformation.

7.1 Introduction

7.1.1 Mn-doped-$LiFePO_4$ cathode material

$LiFePO_4$, with its safety, low cost, environmentally friendliness, long-term cycle life, and relatively high theoretical capacity (170mAh/g) [56, 76], serves as a cathode material in Li-ion batteries [16, 25, 42, 56, 57, 377, 378]. However, $LiFePO_4$ has not replaced $LiCoO_2$, who suffers from its toxic disadvantage, because of its low electric and ionic conductivity values, and limiting high-rate charge/discharge. The performance of $LiFePO_4$-batteries at high-rates can be improved by carbon coating, particle size minimization, and doping [19, 49]. In contrast with carbon coating which improves the electric conductivity on the surface of $LiFePO_4$ particles, doping is another efficient way to enhance the intrinsic conductivity and Li-ion diffusion rate. Bivalent cation doping (for example Mn^{2+}, Ni^{2+}, Co^{2+}, Cu^{2+}) [16, 39-41] is an easy, low cost method to increase the redox potentials, the electronic conductivity and the discharge capacity. Among the cations, Mn doping on Fe-sites has been investigated in the olivine family as the operating voltage of ~3.5 V and ~4.1V of $LiFePO_4$ and $LiMnPO_4$, respectively, are not too high to make the organic electrolyte decomposed but also not too low to scarify energy density [42]. Substitution of iron by larger manganese cations can substantially increase the lattice parameter c, then enhance the electrical and ionic conductivity values [19, 379]. The electrical conductivity of the lightly doped compound is claimed to increase up to 5 orders of magnitude higher than that of the un-doped $LiFePO_4$ [51]. Substitution of 25% of Fe^{2+} by Mn^{2+} causes a slight increase of the electrical conductivity [19]. However, further increase of the Mn content deteriorates the electrical conductivity [19, 379, 380]. In general, enhancement of the electrical and ionic conductivity and improvement of the battery performance due to the introduction of Mn in the $LiFePO_4$ cathode material has been revealed [19, 43-51].

The promising $Li(Mn_yFe_{1-y})PO_4$ cathode material has shown higher energy densities compared to pure $LiFePO_4$ [52-54]. According to the study of Li et al. [381] and Wang et al. [55], substitution of Fe in $LiMnPO_4$ or Mn in $LiFePO_4$ improves the rate capability of the cathode material. In electrochemical experiments using $Li(Mn_yFe_{1-y})PO_4$ as the cathode material, two voltage regions corresponding to the two redox reactions (Mn^{3+}/Mn^{2+}) and (Fe^{3+}/Fe^{2+}) were observed in many studies [16, 19, 37, 49, 51, 56-62]. The relative width of the ~4.1 V voltage region (Mn^{3+}/Mn^{2+})

increases relative to the ~3.5 V voltage region (Fe^{3+}/Fe^{2+}) as the manganese content increases [16]. As shown in our previous papers [133, 232], having an accurate phase diagram of the studied cathode join is important when considering the change of the cathode material during charging/discharging processes and calculating the open circuit voltage (OCV) of the battery. Therefore, the objective of this paper is to develop thermodynamic models of the $Li(Mn_yFe_{1-y})PO_4$-$(Mn_yFe_{1-y})PO_4$ system usable in electrochemical charging/discharging conditions.

Note that replacing of Fe-sites by Mn up to 100% changes the lattice parameters but it does not change the olivine crystal structure [16, 42, 56, 57, 70, 97, 382-388]. Mn^{2+} which can coexist with Fe^{2+} in the tetrahedral *4c* site of the olivine structure, is commonly found in the solid solution phase $Li_x(Mn_yFe_{1-y})PO_4$ [384]. Mn^{2+} can substitute Fe^{2+} in $LiFePO_4$ easily [33] and Mn^{2+} doping is mainly reported in Mn-doped $LiFePO_4$ for battery applications [16, 19, 42, 44, 49, 51, 56, 58, 62, 379, 389]. The Fe^{2+} and Mn^{2+} cations are reported to distribute randomly in $Li(Mn_yFe_{1-y})PO_4$ [51, 390]. In Mn-doped-$LiFePO_4$, manganese is mainly located on the Fe^{2+} sites, the remaining is found on the Li^+-sites or impurities [51, 391]. Mn anti-site cations on the Li^+-sites impede the bulk Li^+ mobility [392]. Impurity phases containing manganese are less likely to form [51]. In this study, only the most important and common manganese doping position, Mn^{2+} doping in the Fe^{2+} tetrahedral sites, is taken into account. Hence, the concerned olivine with the coexistence of Mn^{2+} and Fe^{2+} ions in the tetrahedral *4c* site is represented as $Li(Mn_yFe_{1-y})PO_4$.

7.1.2 Importance of para-equilibrium $Li(Mn_yFe_{1-y})PO_4$-$(Mn_yFe_{1-y})PO_4$ phase diagram

The knowledge of the full equilibrium state of the $Li(Mn_yFe_{1-y})PO_4$-$(Mn_yFe_{1-y})PO_4$ join is not much relevant in the present situation as kinetics play an important role during the charge/discharge of the cathode material. Indeed, within the Mn-doped-$LiFePO_4$ system, the mobility values of both Mn^{2+} and Fe^{2+} are negligible compared to the one of Li^+. Therefore, during the charge/discharge processes, only the concentration gradient of lithium varies while the concentration ratio Mn/Fe remains in appearance unchanged. It means that at any moments during the charge/discharge processes, the system can be considered as a kinetically constrained equilibrium [393, 394]. In terms of thermodynamic modelling, it is considered a para-equilibrium state, in which the ratio of

Fe and Mn remains constant in all phases existing in para-equilibrium, especially if an olivine-olivine immiscibility is occurring. The present research situation is similar to the para-equilibrium state obtained from a rapidly cooled homogeneous single-phase Fe-Cr-C system, in which the mobilities of the interstitial element, C, is much higher than those of Cr and Fe [395]. Distinction of equilibrium and para-equilibrium is important since in austenitic stainless steel, the para-equilibrium carbon solubility can be orders of magnitude higher than the equilibrium solubility [396]. Therefore, the thermodynamic behavior of Mn-doped-$LiFePO_4$ served as a cathode material should be considered under the para-equilibrium modelling framework.

We found only a few papers containing data on the phase diagram of the $Li(Mn_yFe_{1-y})PO_4$-$(Mn_yFe_{1-y})PO_4$ olivine join. The most important and systematic work on this phase diagram was performed by Yamada et al. [42]. The olivine $Li(Mn_yFe_{1-y})PO_4$ ($y = 0.2;\ 0.4;\ 0.6;\ 0.8;\ 1.0$) samples were prepared and $(Mn_yFe_{1-y})PO_4$ formed by oxidizing chemically the $Li(Mn_yFe_{1-y})PO_4$ samples. Other lithiated samples of $Li_x(Mn_yFe_{1-y})PO_4$ ($0 < x < 1$) were prepared by reacting $(Mn_yFe_{1-y})PO_4$ with various amounts of LiI in acetonitrile. A two-dimensional phase diagram at 298 K corresponding to different lithium and manganese compositions was described based on the X-ray powder diffraction (XRD), Mossbauer spectroscopy, and X-ray absorption spectroscopy (XAS) analysis [42]. Noticeably, the reported phase diagram [42] should be stated as the *para-equilibrium* phase diagram because the manganese contents of the samples were fixed before the lithiation. Several features of the para-equilibrium phase diagram were identified [42]. First, the local lattice distortion induced by a large amount of Mn^{2+} ($y \geq 0.8$) makes olivine $(Mn_yFe_{1-y})PO_4$ unstable [42]. The reversible delithiation-lithiation reactions of $Li_x(Mn_yFe_{1-y})PO_4$ ($y \geq 0.8$) occurred within the limited lithium composition x but had very slow kinetics [42]. It is in agreement with other studies stating that $(Mn_{0.8}Fe_{0.2})PO_4$ is not able to maintain the olivine framework [56] and the olivine $MnPO_4$ phase is unstable [56, 72, 73, 75, 76, 78, 79, 81, 98]. Second, in the low manganese content side of the para-equilibrium phase diagram ($y \leq 0.6$), two distinguished regions are identified including *i)* the two-phase Mn^{3+}/Mn^{2+} redox region ($y \geq x$) with a potential of ~4.1 V vs Li/Li^+; *ii)* a partial conversion of reaction from two-phase to single-phase with a potential of ~3.5 V vs Li/Li^+ in the Fe^{3+}/Fe^{2+} redox region ($y \leq x$) [42].

The reported para-equilibrium of the $Li(Mn_yFe_{1-y})PO_4$-$(Mn_yFe_{1-y})PO_4$ system by Yamada et al. [42] is comparable to the results of first principles calculations reported by Malik et al. [62]. The phase diagram of $Li_x(Mn_yFe_{1-y})PO_4$ showed two low-temperature miscibility gaps separated by a solid solution phase centered at $x \approx y$ lithium composition, at which most Fe ions were oxidized and most Mn ions were not [62]. As stated, in the single-phase region, the unfavorable Li^+ coordination causes the Fe^{3+} and Mn^{2+} states to have higher energy than that in their pure $FePO_4$ or $LiMnPO_4$ phases leading to the formation of two voltage plateaus [62]. The two voltage plateaus are corresponding to the two miscibility gaps occurring in various equilibrium sections of $Li_x(Mn_yFe_{1-y})PO_4$. By substituting Mn on the Fe sublattices, the solid solution phase is stable at low temperatures, and the isoplethal section consists of two miscibility gaps at low temperatures. The first miscibility gap is between $(Mn_yFe_{1-y})PO_4$ and the solid solution $Li_y(Mn_yFe_{1-y})PO_4$ and the second one is between the solid solution $Li_y(Mn_yFe_{1-y})PO_4$ and $Li(Mn_yFe_{1-y})PO_4$ $(0 \leq y \leq 1)$ [62]. In another study, Kim et al. [72] examined the thermal stability of Fe-Mn binary olivine cathodes for lithium rechargeable batteries with temperature-controlled *in situ* XRD for various Fe/Mn ratios and state of charges (SOCs). Fully lithiated $Li(Mn_yFe_{1-y})PO_4$ $(0 \leq y \leq 1)$ remained stable up to high temperatures (>700ºC) while the delithiated phases were vulnerable to partial phase transformation upon heating, in agreement with the reported unstable $(Mn_yFe_{1-y})PO_4$ $(y \geq 0.8)$ phase [42]. Thermal stability of partially delithiated $Li_x(Mn_yFe_{1-y})PO_4$ $(0 \leq x, y \leq 1)$ was influenced sensitively by the Fe/Mn content in the structure. Moreover, the delithiation mechanism (one-phase vs. two-phase reaction) was dependent on the Fe/Mn ratio. Generally, the olivines with a high manganese content exhibited lower thermal stability in charged states and a stronger preference for the two-phase behavior [72].

In brief, there are very few studies on the phase para-equilibria of the $Li(Mn_yFe_{1-y})PO_4$-$(Mn_yFe_{1-y})PO_4$ battery joins. Among those, Yamada et al. [42] provided the most systematic and consistent study. However, their reported para-equilibrium phase diagram was derived from their investigation of chemically synthesized samples. The chemical (de)lithiation in which electrons swap directly within the material might be different from the electrochemical (de)lithiation of the electrode material in which electrons are indirectly exchanged through the electrolyte. In fact, the reported electrochemical-driven phase diagrams of $Li(Mn_yFe_{1-y})PO_4$-$(Mn_yFe_{1-y})PO_4$ [397] are different from the chemical one [42]. However, since there are differences between the charge and discharge phase diagrams [397], they are not suitable for describing para-equilibrium. Due to the lack of information, we would like to model the thermodynamic behavior of the $Li(Mn_yFe_{1-y})PO_4$

cathode material mainly based on Yamada et al. [42] results assuming similar thermodynamic behavior of chemical and electrochemical (de)lithiation.

7.1.3 Existence of coherent phase transformations

Mn doping can improve electronic conductivity of $LiFePO_4$ because it could narrow the band gap according to the first principles investigation of Xu et al. [398]. However, having good electrochemical performances requires not only a high electronic conductivity but also fast-ionic transport, meaning a high Li^+ solid state diffusion coefficient. In olivine $Li_x(Mn_yFe_{1-y})PO_4$, Li^+ ions diffuse rapidly along the 1D channels and only a small fraction of Li^+ ions cross between channels [32]. The substitution of Mn for Fe, due to the larger ionic radius of Mn^{2+}, should facilitate a wider channel for Li^+ movement. The substitution of 10%Mn ($Li(Fe_{0.9}Mn_{0.1})PO_4$) enhances the Li^+ ionic transport, therefore, improves the electrochemical performance of the battery at higher rates [399]. No significant difference in the local structure of Mn^{3+} over the entire range of manganese substitution suggests no intrinsic obstacle for extracting Li^+ from $Li(Mn_yFe_{1-y})PO_4$ [386]. Although doping Mn in $LiFePO_4$ or doping Fe in $LiMnPO_4$ could improve electrical and ionic conductivity [19], the values of both conductivities of $Li(Mn_yFe_{1-y})PO_4$ are still much lower than those of $LiCoO_2$, the most common cathode material [19, 92, 176]. Low conductivities restrict the applications of this cathode material, especially for high-rate applications.

Notably, like other olivines, the crystal structure of $Li(Mn_yFe_{1-y})PO_4$ does not change via charging process, favoring the coherent phase transformation which should improve the battery charging/discharging rate and cyclability. The $LiFePO_4$ cathode material was shown to be likely to follow the (100) coherent phase transformation [232]. The coherent phase transformation explains the existence of the strains [127, 134-136], the favor interfacial planes [127, 135, 136, 141, 144], the observed metastable phase [148-151] and the formation of dislocations and cracks [142, 144-147] during charging/discharging of the battery with $LiFePO_4$ cathode. A consistent study concerning coherent phase transformations in $LiMnPO_4$ battery material has not been reported yet. Because of the important similarities between $LiFePO_4$ and $LiMnPO_4$, the coherent phase transformation should also be favorable in the $LiMnPO_4$-$MnPO_4$ system. So far, only Ravnsbæk et al. [152] proposed coherent phase transformations of $Li(Mn_{0.4}Fe_{0.6})PO_4$ cathode material via charging/discharging. Two voltage plateaus corresponding to two two-phase transformations during charging processes were identified. According to the authors, the intermediate phase $Li_x(Mn_{0.4}Fe_{0.6})PO_4$ breaks the phase transformation into two steps to reduce the misfit strain [152]. Consequently, for small particles, a coherent transformation model has been proposed. As suggested by Ravnsbæk et al. [152], in the Li-poor region, the charging/discharging process occurs through the first-order phase transformation where $Li_x(Mn_{0.4}Fe_{0.6})PO_4$ and $(Mn_{0.4}Fe_{0.6})PO_4$ are coherent. However, in the Li-rich region, the charging process and the discharging one are asymmetric. The coherent coexistence of $Li_x(Mn_{0.4}Fe_{0.6})PO_4$ and $Li(Mn_{0.4}Fe_{0.6})PO_4$ is present during lithium extraction while lithium insertion goes via a solid solution phase transformation [152]. Up to now, only one paper focusing on coherent phase transformation of $Li(Mn_yFe_{1-y})PO_4$ is not enough to understand and then utilize the cathode material for high-rate applications.

To sum up, in this study, we would like to develop thermodynamic models of the para-equilibrium $Li(Mn_yFe_{1-y})PO_4$-$(Mn_yFe_{1-y})PO_4$ cathode join which is necessary for describing the thermodynamic behavior of the cathode during battery operations. Moreover, the coherent phase transformation of the cathode, which favors the high charging/discharging rates and improves cyclability, will also be treated. Noticeably, since we are dealing with olivine $Li(Mn_yFe_{1-y})PO_4$ battery materials, the present study is only focusing on pure compounds and solid solutions with olivine structures. That is our thermodynamic models are not developed to predict the unstable region of olivine-$MnPO_4$ as a function of the substitution level and temperature.

7.2 Para-equilibrium in the $Li(Mn_yFe_{1-y})PO_4$-$(Mn_yFe_{1-y})PO_4$ cathode joins

Prior the development of thermodynamic models for describing the para-equilibrium of $Li(Mn_yFe_{1-y})PO_4$-$(Mn_yFe_{1-y})PO_4$ olivine join, knowing the Gibbs energy of pure $LiFePO_4$, $FePO_4$, $LiMnPO_4$, and $MnPO_4$ is essential. The Gibbs energy is estimated from entropy and enthalpy, which are calculated from the temperature dependent heat capacity of compounds. Our reinvestigation of the heat capacity of $LiFePO_4$ clarifies the role of the heat capacity produced by magnon-phonon interactions, $C_p^{pho-mag}$, the heat capacity induced from structure defects including anti-site defects and vacancies, C_{def}, and the anharmonic heat capacity induced by those crystal defects, C_{anhar}.

The antisite defects mentioned here are generated by the exchange of their lattice sites of Li and Fe atoms to form anti-site pairs Fe_{Li}-Li_{Fe} [216, 400-404]. Vacancies in this study is considered as the vacancy in Li sites [404]. The contribution of anti-sites and vacancies to heat capacity is quantified from the DFT calculated formation energy [216, 404] (Appendix J). Based on the reported heat capacity of $LiFePO_4$ [100], our calculated magnetic moment, entropy, enthalpy of formation and Gibbs energy at room temperature are in agreement with the reported values in other studies [25, 112, 113, 405-411] (Appendix K). However, unlike $LiFePO_4$, there is no reported experimental data on the heat capacity of olivine-$FePO_4$. The heat capacity measurement reported by Shi et al. [104] was done on berlinite-$FePO_4$ with the Neel temperature of $T_N = 25\ K$ [104-107] while olivine-$FePO_4$ shows a higher Neel temperature ($T_N \cong 125\ K$) [108-110]. As we assume the average magnetism heat capacity per atom of $FePO_4$ is the same as that of $LiFePO_4$ at their corresponding Neel temperatures, the calculated average magnetic moment of $FePO_4$ is comparable to the reported experimental values [109, 409]. Due to the vast similarities between olivine-$LiFePO_4$ and olivine-$FePO_4$ and the lack of knowledge on heterosite-$FePO_4$, its average entropy per atom is assumed to be the same as that of $LiFePO_4$ (Appendix K). Subsequently, our estimated Gibbs energy of $FePO_4$ at room temperature is similar to what was obtained by Xie et al. [25] (Appendix K). As a result, the expected voltage by delithiating $LiFePO_4$ is 3.48 V which is comparable to the ~3.5 V voltage plateau found in electrochemical experiments [16, 17, 19, 23, 27, 88, 127, 130, 136, 160, 180, 183, 189]. Because of the shortage of studies on thermodynamic properties of $LiMnPO_4$ and $MnPO_4$, the knowledge of their Gibbs energy is limited. According to our DFT simulations, which will be mentioned in the next section, our estimated enthalpy of formation of all the olivine compounds are comparable to those reported by Xie et al. [25] (Appendix K). Hence, we use their reported Gibbs energy of $LiMnPO_4$ and $MnPO_4$ in our thermodynamic models of the $Li(Mn_yFe_{1-y})PO_4$-$(Mn_yFe_{1-y})PO_4$ olivine join. Note that the difference of Gibbs energy of $LiMnPO_4$ and $MnPO_4$ results the average intercalation voltage of 4.03 V [25], which is close to the reported value of ~4.1 V [16, 78, 83, 86, 88, 91, 92, 97, 412, 413]. After having good Gibbs energy of formation of compounds, the enthalpy of mixing and the thermodynamic models of the sub-systems need to be accounted for.

7.2.1 Details on DFT simulations

To alleviate the lack of experimental data, the first principles Density Functional Theory (DFT) simulations have been performed to predict on one hand, the enthalpy of formation and the elastic constants of $LiFePO_4$, $LiMnPO_4$, $MnPO_4$ and $FePO_4$ compounds with orthorhombic structure (*pnma* space group) and on the other hand, the enthalpy of mixing of $LiFePO_4$-$FePO_4$, $LiMnPO_4$-$MnPO_4$, $MnPO_4$-$FePO_4$, $LiMnPO_4$-$LiFePO_4$ systems through the enthalpy of formation of the corresponding solid solution with olivine structure (*pnma* space group). Note that both the enthalpy of formation of compounds and the enthalpy of mixing of solid solutions are calculated at 0 K, i.e. neither the heat capacity nor the excess heat capacity were considered in the calculations.

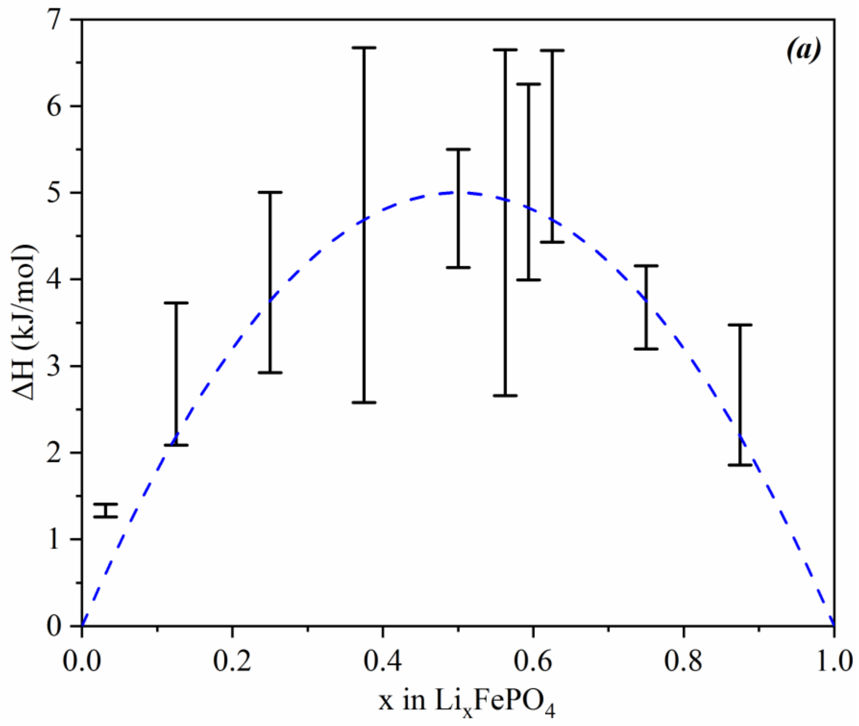

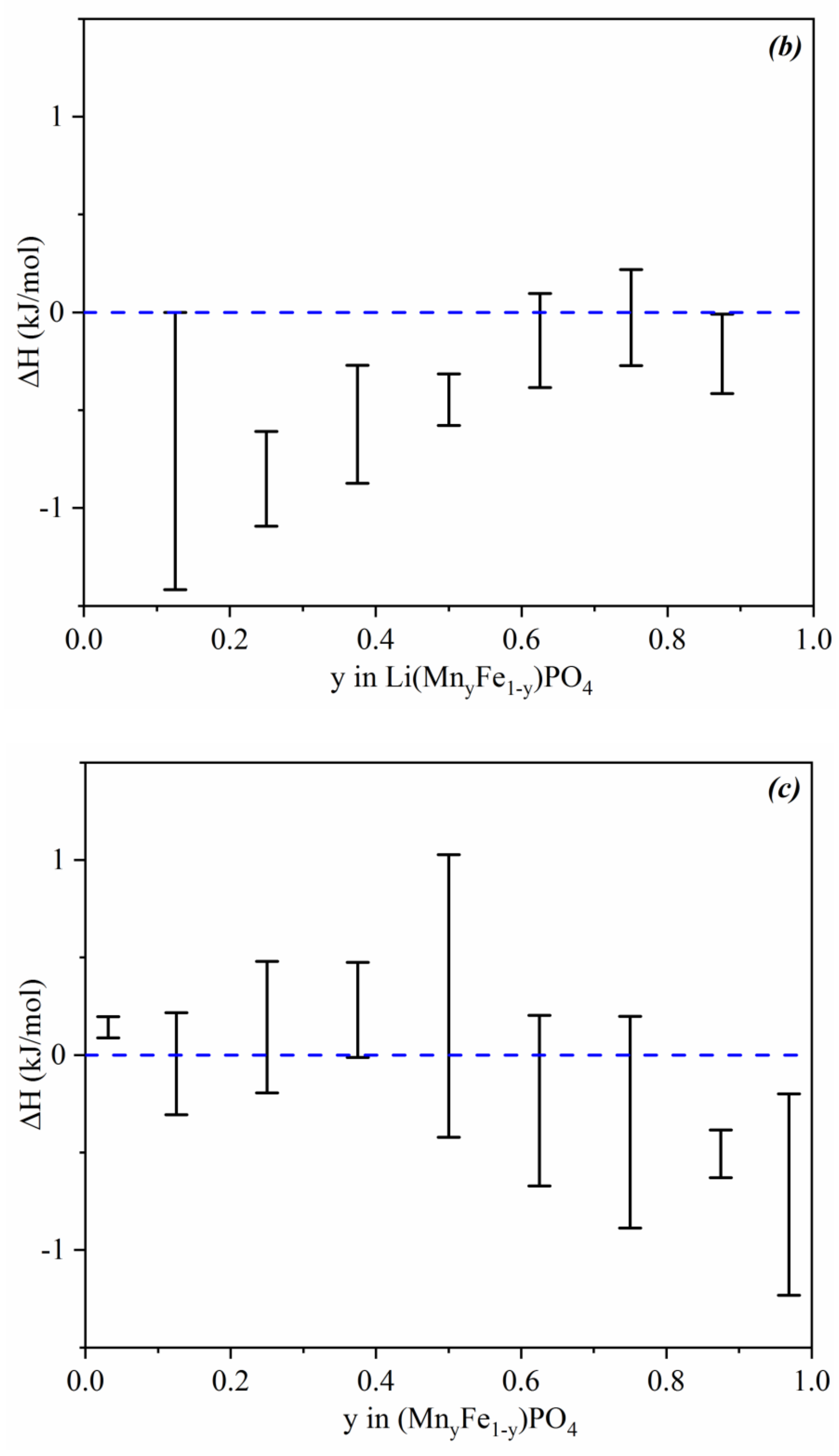
(b)
ΔH (kJ/mol)
1
0
-1
0.0
0.2
0.4
0.6
0.8
1.0
y in Li(Mn$_y$Fe$_{1-y}$)PO$_4$
(c)
ΔH (kJ/mol)
1
0
-1
0.0
0.2
0.4
0.6
0.8
1.0
y in (Mn$_y$Fe$_{1-y}$)PO$_4$

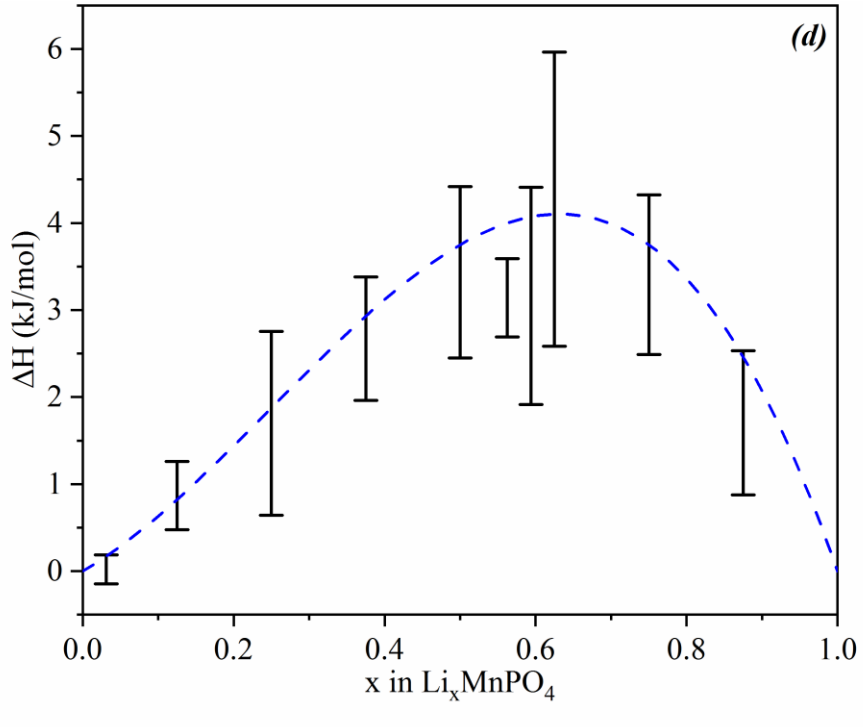

Figure 7.1: Calculated molar enthalpy of mixing (ΔH) using DFT for different Li contents (shown as vertical lines) and the modeled molar enthalpy of mixing (blue dashed line) for the a/ $LiFePO_4$-$FePO_4$ system, b/ $LiFePO_4$-$LiMnPO_4$ system, c/ $FePO_4$-$MnPO_4$ system, and d/ $LiMnPO_4$-$MnPO_4$ system.

The DFT calculations in periodic boundary conditions were based on plane-wave basis sets and were carried out using the Vienna Ab initio Simulation Package (VASP) [115-118]. The projector augmented wave (PAW) approach was employed to represent the core electrons [414, 415]. The generalized gradient approximation (GGA) as parameterized by Perdew, Burke and Ernzerhof (PBE) [416, 417] was used as the exchange-correlation function. In order to improve the accuracy of the predicted electronic ground state properties in our simulations, GGA+U [120] has been performed with an effective Hubbard-U parameter of 5.3 and 3.9 for Fe and Mn, respectively, as proposed by Wang et al. [418]. A plane-wave kinetic cut-off energy of 520 eV and a Monkhorst–Pack grid of dimension 1×2×2 for solutions to sample the Brillouin zone with a first-order Methfessel–Paxton smearing parameter of 0.02 eV were used to meet the force and energy convergence criteria of better than 0.02 eV/Å and 0.01 meV, respectively. To take into account the magnetism of Fe and Mn at 0 K, spin polarization has been included. We have considered supercells of 224 atoms for $LiFePO_4$, $LiMnPO_4$, and the $Li(Mn_yFe_{1-y})PO_4$ solid solution and supercells of 192 atoms for $MnPO_4$, $FePO_4$ and the $(Mn_yFe_{1-y})PO_4$ solid solution. For the $LiFePO_4$-$FePO_4$ and $LiMnPO_4$-$MnPO_4$ systems, the number of atoms of a supercell of the solid solution Li_xFePO_4 or Li_xMnPO_4 varies from 224 atoms to 192 atoms corresponding to different Li contents. To calculate the enthalpy of any solid solutions, for each composition, the ground state total energy has been calculated for 10 different configurations via either the delithiation of $LiFePO_4$ or $LiMnPO_4$ or random replacement of Fe in $FePO_4$/$LiFePO_4$ by Mn or random substitution of Mn in $MnPO_4$/$LiMnPO_4$ by Fe. The lattice positions of both P and O remained fixed. As the range of enthalpy of mixing of the binary systems at different compositions is obtained, we have modeled the enthalpy of mixing of each system to fit our DFT simulations (Figure 7.1a-d). In addition, the linear dependence of the lattice parameters on the lithium or manganese content of the solid solution in all sub-binary systems has been verified by our simulation.

Lastly, since the elastic constants of the solid solutions are necessary to calculate the coherent phase diagrams, we have determined the 9 elastic constants of the pure compounds. The procedure for calculating elastic constants of compounds is identical to the one employed in our previous study [102, 103, 419]. We calculated the energy difference between the equilibrium lattice and an expanded or compressed lattice, which is achieved by applying very small strains in each crystallographic direction while ensuring that the deformed lattice remains in the elastic domain. The elastic constants are then obtained by fitting the energy versus the strain curve by a second order polynomial (Table K.2). Our estimated elastic constants of $LiFePO_4$ and $FePO_4$ are similar to that reported by Xie et al. [25] which were used in our previous investigation of the coherent phase diagram $LiFePO_4$-$FePO_4$ [232]. Among a few studies reporting the elastic constants of $LiMnPO_4$ and $MnPO_4$ [25, 186, 420, 421], the results of Xie et al. [25] and Maxisch et al. [186] are comparable to our calculations. Due to computational resource limitations, we have assumed that the elastic constants of the $Li_x(Mn_yFe_{1-y})PO_4$ solid solutions vary linearly with its lithium and manganese compositions. This assumption is in agreement with the vast similarities of the crystal structure and physical properties of the solid solutions at various compositions and consistent with the observation of elastic constants for most solid solutions of oxides [422].

7.2.2 Calculated phase diagrams for the binary sub-systems

When studying the $Li(Mn_yFe_{1-y})PO_4$-$(Mn_yFe_{1-y})PO_4$ olivine join, the parameters of the thermodynamic models for four binary sub-systems including $LiFePO_4$-$FePO_4$, $LiFePO_4$-$LiMnPO_4$, $FePO_4$-$MnPO_4$, and $LiMnPO_4$-$MnPO_4$ must be optimized formerly. Among them, the $LiFePO_4$-$FePO_4$ join has been well investigated in our previous studies [133, 232]. Four compound energy formalism (CEF) models were proposed for describing the solid solutions Li_xFePO_4 [133]. Except M6 (the most complicated model), the other three models including ***M4*** (the simplest model), ***M5.L*** and ***M5.F*** (the most suitable models for describing the $LiFePO_4$-$FePO_4$ phase diagram) can be extended to include Mn in $Li(Mn_yFe_{1-y})PO_4$-$(Mn_yFe_{1-y})PO_4$ olivine join. Note that, our enthalpy of mixing of the $LiFePO_4$-$FePO_4$ system simulated by DFT (Figure 7.1a) is comparable with that calculated by using the reported ***M4***, ***M5.L*** and ***M5.F*** models [133]. Like the $LiFePO_4$-$FePO_4$ join, the other sub-systems are modeled by CEF.

7.2.2.1 $LiFePO_4$-$LiMnPO_4$

Olivine $LiMnPO_4$, similar to $LiFePO_4$, is stable at up to 683 K without showing any noticeable changes [75] due to its strong P-O covalent bonding [16, 75, 79, 82-84, 413]. First principles calculations revealed that olivine $Li(Mn_yFe_{1-y})PO_4$, is a stable complete solid solution in the $LiFePO_4$-$LiMnPO_4$ binary system (discharge state) because of the small lattice distortion brought by the small ionic radius difference between Fe^{2+} and Mn^{2+} [56]. This result is in good agreement with Molenda et al. [70], in which synthesized $Li(Mn_yFe_{1-y})PO_4$ was claimed to exhibit a single-phase olivine-type orthorhombic structure. The complete miscible $Li(Mn_yFe_{1-y})PO_4$ solid solution is stable above 120 K as predicted by Snydacker and Wolverton [71]. No information on the stability of this solid solution at higher temperatures has been found in the literature. However, due to the similarities between the crystal structure, the lattice parameters and the other physical properties of $LiFePO_4$ and $LiMnPO_4$, the solid solution $Li(Mn_yFe_{1-y})PO_4$ should be quite stable even at high temperatures. We assumed that the solid solution is stable at up to 623 K (the consolute temperature of the $LiFePO_4$-$FePO_4$ system). The stable olivine $Li(Mn_yFe_{1-y})PO_4$ phase is modeled easily as an ideal solid solution with random mixing of species in its sublattice using the sublattice model $(Li^{+})_1(Mn^{2+},Fe^{2+})_1(P^{5+})_1(O^{2-})_4$. Hence, the two pure compounds, $LiFePO_4$ and $LiMnPO_4$, are totally miscible in the olivine structure. The assumption of ideal solid solution is suitable with the ideal enthalpy of mixing expected from our first principles calculations (Figure 7.1b).

7.2.2.2 $FePO_4$-$MnPO_4$

Unlike olivine $FePO_4$ which is stable at up to 873 K without oxygen loss [75], olivine-$MnPO_4$ is unstable [75, 76]. $MnPO_4$ can decompose into $Mn_2P_2O_7$ and O_2 gas at a temperature as low as 483 K [76]. The large particle $MnPO_4$ decomposes into $Mn_2P_2O_7$ from 473 K to 523 K while $Mn_3(PO_4)_2$ forms as a product of the decomposition of small particles of $MnPO_4$ in the same temperature range [77]. Nevertheless, Choi et al. [78] showed that $MnPO_4$ starts to reduce into $Mn_2P_2O_7$ at 763 K and because of the Jahn-Teller effect, $MnPO_4$ undergoes amorphization above 453 K. Unstable $MnPO_4$ and the occurrence of an amorphous phase above 473 K are also later reported [72, 79]. However, Aurbach’s group found that $MnPO_4$ is as stable as $FePO_4$ [80]. Recently, Huang et al. [75] revealed the critical role of carbon coating in the stability of $MnPO_4$. Even a small amount of carbon can prevent the amorphization of the delithiated phase and keep it stable at up to 573 K [75]. In addition, $MnPO_4$ can absorb water easily and change its crystal structure [75]. In brief, even though there are discrepancies among studies on the stability of the olivine-$MnPO_4$, all of them agree that $MnPO_4$ remains stable below ~473 K. Therefore, our developed thermodynamic model for $FePO_4$-$MnPO_4$ should only be strictly valid at up to 473 K, above which only metastable states can be computed.

The single-phase solid solution $(Mn_yFe_{1-y})PO_4$ $(0 < y < 0.8)$ with an olivine-type structure was observed by Yamada et al. [56]. Unlike the $LiFePO_4$-$LiMnPO_4$ binary system, in which the solid solution is stable because of the small difference between the ionic radii of Fe^{2+} and Mn^{2+}, in $(Mn_yFe_{1-y})PO_4$, the electron $3d^4$ of the ion Mn^{3+}-lattice interaction induces large anisotropic distortion [56]. Moreover, the accumulation of elastic energy destabilizes the solid solution at large manganese contents $(y < 0.8)$ [56]. However, the solid solution seems to be more stable in the investigation of Kim et al. [72]. The fully delithiated phase, $(Mn_yFe_{1-y})PO_4$, is stable even at high manganese contents according to their reported phase stability map [72]. Nevertheless, the thermal decomposition temperature generally declines with an increase of manganese content [72]. Similarly, Huang et al. [73] reported the phase decomposition of the olivine $(Mn_{0.8}Fe_{0.2})PO_4$ to form sarcopside-$(Mn_{0.8}Fe_{0.2})_3(PO_4)_2$ from 523 K to 623 K. The solid solution $(Mn_yFe_{1-y})PO_4$ is reported to be stable at up to 673 K and $y < 0.9$ [74]. Since the two phases are completely miscible from 298 K to 473 K according to the $FePO_4$-$MnPO_4$ binary join reported by Kim et al. [72] and the first principles calculations [71], our chosen sublattice model is $(Mn^{2+}, Fe^{2+})_1(P^{5+})_1(O^{2-})_4$ with no excess parameter. This model agrees with the ideal enthalpy of mixing expected from our first principles calculations (Figure 7.1c). Note that because of the stability of the solid solution $(Mn_yFe_{1-y})PO_4$ and the $MnPO_4$ phase, this sublattice model is valid at up to 473 K.

7.2.2.3 $LiMnPO_4$-$MnPO_4$

$LiMnPO_4$, belonging to the olivine family, is used as a cathode material [81, 84-87, 91, 423, 424]. As lithium is extracted from $LiMnPO_4$, an electron is also removed from the Mn site nearby. When complete delithiation of the $LiMnPO_4$ cathode is reached, olivine-$MnPO_4$ is obtained. Delithiation of $LiMnPO_4$ is the only way to produce metastable $MnPO_4$ under ambient conditions [81]. In comparison with $LiFePO_4$, olivine-$LiMnPO_4$ can provide a higher energy density and a higher voltage plateau due to the higher Mn^{3+}/Mn^{2+} redox potential (~4.1 V versus Li/Li^+) with a similar theoretical capacity (170 mAh/g) [16, 56, 84, 86-90, 95, 388, 413, 425, 426]. The redox potential of ~4.1 V vs. Li/Li^+ is considered to be the maximum limit accessible to most common electrolytes [87, 388, 412]. However, the rate capability of $LiMnPO_4$ is significantly poorer [91] due to the poor Li^+ intercalation/deintercalation kinetics caused by the intrinsically low ionic and electrical conductivity of $LiMnPO_4$. $LiMnPO_4$ has an electronic conductivity of at least 4 orders of magnitude lower than that of $LiFePO_4$ [92, 93]. It is a result of the severe Jahn-Teller (JT) distortion and the mismatched interface of $MnPO_4/LiMnPO_4$ [88, 89, 95, 96]. As lithium is extracted from $LiMnPO_4$, Mn^{2+} changes into Mn^{3+} charge state [84]. As Mn^{3+} character increases, split of the Mn-O nearest-neighbor distances and distortion of the MnO_6 octahedra are found [84, 94]. The large effective mass of the polarons around the Mn^{3+} sites coupled with the large local lattice deformation cause the slow kinetics of Li^+ during charging/discharging processes [88].

Similarly to the case of $LiFePO_4$, Piper et al. [84] revealed a two-phase reaction upon delithiation, in agreement with other authors [85, 89, 97, 98, 388]. The two-phase reaction mechanism results in a flat two-phase region with OCV ~4.1 V [85, 86, 89, 97] and the voltage plateau exists even at 328 K [89]. Clearly, the voltage plateau due to the two-phase coexistence should be related to the phase diagram of $LiMnPO_4$-$MnPO_4$. However, there is very little information on this olivine join.

According to the phase stability reported by Kim et al. [76], two-phase regions are stable at up to 473 K. In addition, Chen & Richardson [98] showed that as lithium is chemically removed from crystalline $LiMnPO_4$, the two phases $LiMnPO_4$ and $Li_\alpha MnPO_4$ (α is small and $\alpha < 1$), not $MnPO_4$, coexist. The delithiated phase $Li_\alpha MnPO_4$ is claimed to be dependent on the extent of delithiation and on the crystalline domain size [98]. It is noted that the cell volume of the lithiated phase is dependent on the domain size while it is independent of the amount of lithium removal. The dependence of the cell volumes of both the delithiated and lithiated phases could be a result of the variation of lithium concentration in each phase. The lithium solubility of the two phases could reflect the miscibility gap shrinkage with the decrease of particle size, like it is in the case for the $LiFePO_4$-$FePO_4$ system [23, 27, 34, 35]. The change of solubility of the delithiated phase $Li_\alpha MnPO_4$ with the global Li content via electrochemical delithiation or lithiation is caused by the growth restriction of the lithiated phase $LiMnPO_4$, as a result of the accumulation of elastic energy [98]. From our perspective, the more sluggish Li^+ movement due to lower conductivity [19] and the higher elastic energy accumulation due to larger lattice parameter changes make the delithiation/lithiation of $LiMnPO_4$/$MnPO_4$ more difficult than that of $LiFePO_4$/$FePO_4$. Hence, only the reported result of Kim et al. [76], rather than that of Chen & Richardson [98], is used for verifying the equilibrium phase diagram.

To model the $LiMnPO_4$-$MnPO_4$ olivine join, the $(Li^+, Va)_1(Mn^{2+}, Mn^{3+})_1(P^{5+})_1(O^{2-})_4$ sublattice is chosen. This model is similar to the simplest model ***M4*** of the $LiFePO_4$-$FePO_4$ system [133]. The thermodynamic parameter $\Delta G^{\circ}_{MnPO_4^-}$ and $\Delta G^{\circ}_{LiMnPO_4^+}$ showing the corresponding molar energy gained by forming non-neutral end-members from the corresponding compounds (Equation 4.7) is optimized in order to reproduce the miscibility gaps reported by Kim et al. [76] (Figure 7.2):

$$\Delta G^{\circ}_{MnPO_4^-} = \Delta G^{\circ}_{LiMnPO_4^+} = 10000\ (J/mol) \tag{7.1}$$

Given that the solubility of Li in the two coexisting phases is very close to $LiMnPO_4$ and $MnPO_4$, the thermodynamic parameters (Equation 7.1) are chosen to ignore any significant solubility at room temperature (Figure 7.2). The model reproduces sufficiently well our enthalpy of mixing simulated by DFT (Figure 7.1d) while describing well the reported two-phase coexistence samples

[76]. Note that this model is valid at up to about 473 K because of the stability of $MnPO_4$ [72, 75, 76, 78, 79, 98].

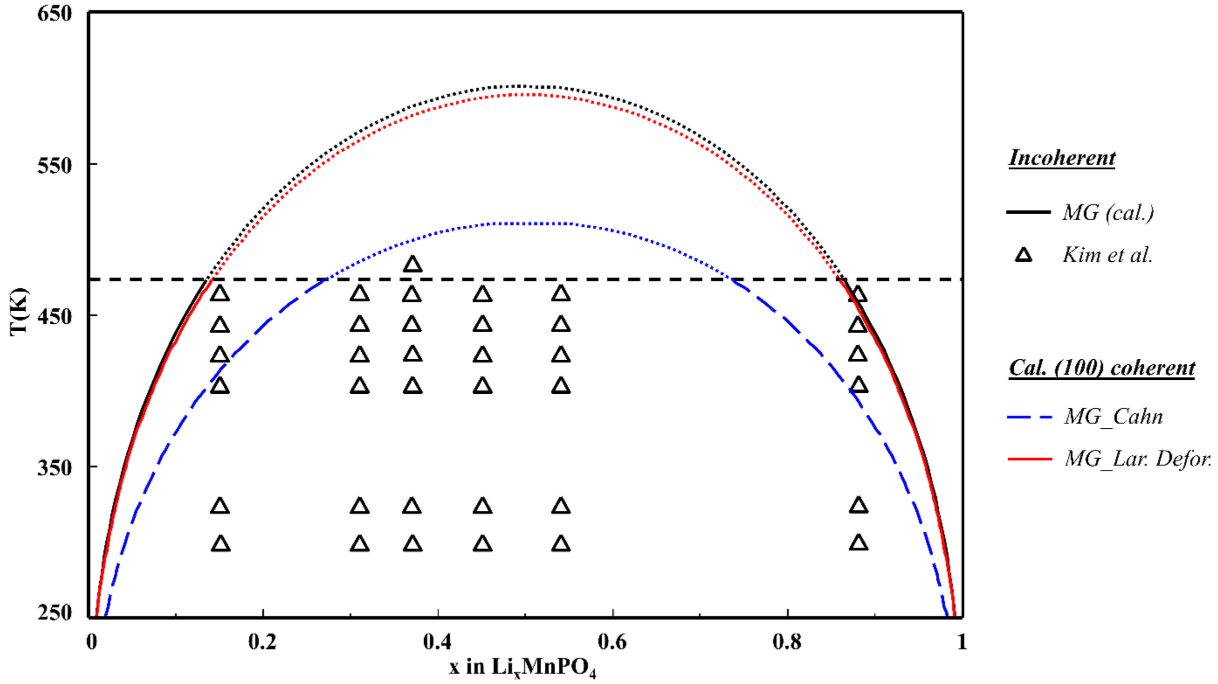

Figure 7.2: Calculated equilibrium and (100) coherent miscibility gaps of the LiMnPO4-MnPO4 join using Cahn's approach and our elastic Gibbs energy approach for a large deformation in comparison with the calculated incoherent miscibility gap and equilibrium two-phase coexistent samples reported by Kim et al. [76]. Above 473 K, the miscibility gaps are unstable and they are shown as dotted lines.

7.2.3 Models of Gibbs energy for $Li(Mn_yFe_{1-y})PO_4$-$(Mn_yFe_{1-y})PO_4$ battery joins

After finding the Gibbs energy of compounds and developing suitable thermodynamic models for all the four olivine sub-systems, we are able to develop thermodynamic models for the para-equilibrium $Li(Mn_yFe_{1-y})PO_4$-$(Mn_yFe_{1-y})PO_4$ battery join. In this section, we would like to list all the thermodynamic models that we have investigated, starting from the simplest one. Since $LiFePO_4$-$FePO_4$ is the most complicate binary join among the four binary sub-systems, our proposed thermodynamic models of $Li(Mn_yFe_{1-y})PO_4$-$(Mn_yFe_{1-y})PO_4$ are extended from the thermodynamic models of $LiFePO_4$-$FePO_4$ developed in our previous study [133]. In every thermodynamic model of the solid solution $Li_x(Mn_yFe_{1-y})PO_4$ describing the battery join, the manganese content (i.e. “y”) is prior fixed and the Gibbs energy minimization technique is used for calculating the equilibrium of the $Li(Mn_yFe_{1-y})PO_4$-$(Mn_yFe_{1-y})PO_4$ isoplethal section at a given value of y. This ensures that the Mn/Fe and Fe/P content ratios are kept constant, satisfying the condition of a para-equilibrium. Performing this constrained Gibbs energy minimization and collecting equilibrium isoplethal sections with various manganese contents allow us to present the para-equilibrium $Li(Mn_yFe_{1-y})PO_4$-$(Mn_yFe_{1-y})PO_4$ battery join which is critical when studying the thermodynamic behavior of the $Li(Mn_yFe_{1-y})PO_4$ cathode. We have investigated several thermodynamic models which are distinguished by how Fe^{2+}, Fe^{3+}, Mn^{2+}, Mn^{3+} cations are put in the olivine crystal structure at specific sites called sublattice sites (Table 7.1). Two standard CEF models (***M1*** and ***M2***) extended from the reported thermodynamic models of $LiFePO_4$-$FePO_4$ join [133] were tested before we develop new type of models.

Table 7.1: Thermodynamic models investigated for modeling $Li(Mn_yFe_{1-y})PO_4$-$(Mn_yFe_{1-y})PO_4$ battery join

Standard CEF models	***Hierarchical sublattice (HS) models***
M1 $(Li^{+}_{x}, Va_{1-x})_{1}(Mn^{2+}_{y\cdot z1}, Mn^{3+}_{y\cdot(1-z1)}, Fe^{2+}_{(1-y)\cdot z2}, Fe^{3+}_{(1-y)\cdot(1-z2)})_{1}(P^{5+})_{1}(O^{2-})_{4}$	***M1hs*** $(Li^{+}_{x}, Va_{1-x})_{1}([Mn^{2+}_{z1}, Mn^{3+}_{1-z1}]_{y}, [Fe^{2+}_{z2}, Fe^{3+}_{1-z2}]_{1-y})_{1}(P^{5+})_{1}(O^{2-})_{4}$
M2 $(Li^{+}_{x}, Va_{1-x})_{5}(Mn^{2+}_{z1\cdot y}, Mn^{3+}_{(1-z1)\cdot y}, Fe^{2+}_{z2\cdot(1-y)}, Fe^{3+}_{(1-z2)\cdot(1-y)})_{3}(Mn^{2+}_{z3\cdot y}, Mn^{3+}_{(1-z3)\cdot y}, Fe^{2+}_{z4\cdot(1-y)}, Fe^{3+}_{(1-z4)\cdot(1-y)})_{2}(P^{5+})_{5}(O^{2-})_{20}$	***M2hs*** $(Li^{+}_{x}, Va_{1-x})_{5}([Mn^{2+}_{z1}, Mn^{3+}_{1-z1}]_{y}, [Fe^{2+}_{z2}, Fe^{3+}_{1-z2}]_{1-y})_{3}([Mn^{2+}_{z3}, Mn^{3+}_{1-z3}]_{y}, [Fe^{2+}_{z4}, Fe^{3+}_{1-z4}]_{1-y})_{2}(P^{5+})_{5}(O^{2-})_{20}$
	M3hy

	$(Li^+_x, Va_{1-x})_5([Mn^{2+}_{z1}, Mn^{3+}_{1-z1}]_{5y},[(Fe^{2+}_{z2}, Fe^{3+}_{1-z2})_3(Fe^{2+}_{z3}, Fe^{3+}_{1-z3})_2]_{(1-y)})(P^{5+})_5(O^{2-})_{20}$

7.2.3.1 Standard CEF models

In the sublattice model ***M1***, manganese and iron occupy the second sublattice and y is the fraction of iron substituted by manganese. If $y = 0$, model ***M1*** becomes model ***M4*** for the $LiFePO_4$-$FePO_4$ join in our previous publication [133]. $LiFePO_4$-$FePO_4$ is a reciprocal system [133] which includes the mixing of two entities (Li^+, Va) with two cations (Fe^{2+}, Fe^{3+}). The exchange Gibbs energy which is obtained from the exchange reaction: $VaFe^{2+} + Li^+Fe^{3+} \rightarrow Li^+Fe^{2+} + VaFe^{3+}$ is an important parameter in the thermodynamic models for this reciprocal system [133]. A reciprocal thermodynamic model tends to have a miscibility gap (shown as the largest dashed ring in Figure 7.3) along the stable pair (the pair which has lower Gibbs energy), i.e, Li^+Fe^{2+}-$VaFe^{3+}$ [133], if the value of the exchange Gibbs energy deviates from 0 (a few kJ/mole at room temperature). According to experimental data [28, 29], above 500 K, the miscibility gap in the $LiFePO_4$-$FePO_4$ join should split into two smaller gaps showing as two smaller dashed rings (Figure 7.3). As stated by Dessureault & Pelton [164], the miscibility gap along the stable pair can split into two miscibility gaps when the exchange Gibbs energy is large enough. $LiMnPO_4$-$MnPO_4$ is a simpler reciprocal system where only one miscibility gap is found along the stable pair Li^+Mn^{2+}-$VaMn^{3+}$ (Figure 7.3). $Li(Mn_yFe_{1-y})PO_4$-$(Mn_yFe_{1-y})PO_4$ (illustrated as the red diagonal rectangle in Figure 7.3) is not a simple reciprocal system, in which two entities (Li^+, Va) mix with four cations (Mn^{2+}, Mn^{3+}, Fe^{2+}, Fe^{3+}). $FePO_4$-$LiMnPO_4$ should be the stable pair since Mn^{3+} is easier to reduce than Fe^{3+}. The standard CEF ***M1*** is likely to create a miscibility gap along the stable pair if a large enough exchange Gibbs energy is applied [164] (Figure 7.3). However, according to the experimental data reported by Yamada et al. [42], at room temperature, miscibility gaps are separated in relation to the redox pairs, Fe^{3+}/Fe^{2+} and Mn^{3+}/Mn^{2+}. The (de)lithiation of $Li_x(Mn_yFe_{1-y})PO_4$ also reveals the separation of voltage regions caused by the Fe^{3+}/Fe^{2+} and Mn^{3+}/Mn^{2+} redox pairs along the $x = y$ line [19, 37, 49, 50, 57, 61, 70, 383, 386, 427-432]. Therefore, miscibility gaps are expected to occur on the two sides of the stable pair $FePO_4$-$LiMnPO_4$ rather than along it. It means that optimizing this system through Gibbs exchange energy is challenging. Therefore, optimization of Gibbs energy model parameters for the end-members is not preferable. As a second trial, the excess Gibbs energy in the form of a Redlich-Kister polynomial [67] is introduced in model ***M1*** to reproduce the phase diagram. It is possible to create two miscibility gaps in the $Li(Mn_yFe_{1-y})PO_4$-$(Mn_yFe_{1-y})PO_4$ join at an average manganese composition $(0.3 \leq y \leq 0.5)$ using a Redlich-Kister expression of excess Gibbs energy. However, as the site fractions become small for the solid solution with rich Fe or rich Mn content, the excess terms become very small and their contribution in the total Gibbs energy is insignificant. A more complicated expression of the excess Gibbs energy should be involved in order to create two miscibility gaps on two sides of the $x = y$ line. The difficulties and complexity that we have encountered while dealing with the ***M1*** model are expected to be intensified if a more advanced model ***M2*** considering the long-range-ordering of Mn^{2+}, Mn^{3+} and Fe^{2+}, Fe^{3+} is developed. The troubles that we bump into while modelling the $Li(Mn_yFe_{1-y})PO_4$-$(Mn_yFe_{1-y})PO_4$ phase diagram using standard CEF models encourage us to develop a new approach for our thermodynamic models.

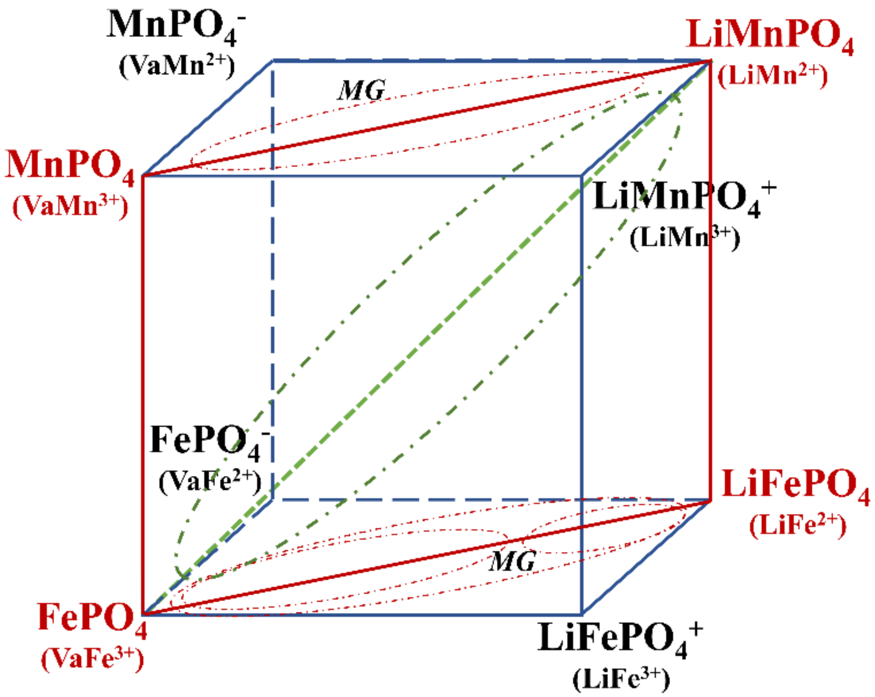

Figure 7.3: Schematic of the reciprocal system $Li(Mn_yFe_{1-y})PO_4$-$(Mn_yFe_{1-y})PO_4$.

7.2.3.2 Hierarchical sublattice (HS) models

*Model **M1hs**:*

Like in the standard CEF model ***M1***, in our newly developed hierarchical sublattice (HS) model ***M1hs***, the four species Mn^{2+}, Mn^{3+}, Fe^{2+}, and Fe^{3+} are in the same *primary sublattice* which represents the tetrahedral *4c* sites in the olivine structure. In this primary sublattice, we define 2 *secondary sublattices*: [Mn^{2+}, Mn^{3+}] and [Fe^{2+}, Fe^{3+}] with the flexible stoichiometry numbers ("y" and "$1-y$"). The molar Gibbs energy calculated by HS model ***M1hs*** is defined differently from that of model ***M1***. First, the molar Gibbs energy of end-members with secondary sublattice is defined through the molar Gibbs energy of end-members of primary sublattice. For example, for the fully lithiated end-member at a fraction of substituted Fe^{2+} by Mn^{2+} of "y", we have:

$$\begin{aligned} G_{LiMn_y^{2+}Fe_{1-y}^{2+}PO_4} &= G^{\circ}_{LiMn_y^{2+}Fe_{1-y}^{2+}PO_4} + G^{ex}_{LiMn_y^{2+}Fe_{1-y}^{2+}PO_4} \\ &= yG^{\circ}_{LMP} + (1-y)G^{\circ}_{LFP} + RT[y\ln(y) + (1-y)\ln(1-y)] \\ &\quad + G^{ex}_{LiMn_y^{2+}Fe_{1-y}^{2+}PO_4} \end{aligned} \tag{7.2}$$

Here the molar Gibbs energy of the $LiMn_y^{2+}Fe_{1-y}^{2+}PO_4$ end-member is defined as the solid solution of $LiMnPO_4$ and $LiFePO_4$ through the sublattice model Li(Mn^{2+}, Fe^{2+})PO_4. If the excess term $G^{ex}_{LiMn_y^{2+}Fe_{1-y}^{2+}PO_4} = 0$, the end-member is considered as an ideal solid solution ($G_{LiMn_y^{2+}Fe_{1-y}^{2+}PO_4} = G^{\circ}_{LiMn_y^{2+}Fe_{1-y}^{2+}PO_4}$). The other end-members are formulated similarly (Appendix L.1). The configuration entropy at a fixed value of "y" of this system is defined as follow:

$$\begin{aligned} \Delta S^{config}_{M1hs} &= -R\{[x\ln x + (1-x)\ln(1-x)] + y[z_1\ln(z_1) + (1-z_1)\ln(1-z_1)] \\ &\quad + (1-y)[z_2\ln(z_2) + (1-z_2)\ln(1-z_2)]\} \end{aligned} \tag{7.3}$$

The boundary conditions to ensure electrical neutrality in models ***M1*** and ***M1hs*** are the same:

$$x - (z_1 - z_2)y - z_2 = 0 \tag{7.4}$$

We have proven that model ***M1*** and model ***M1hs*** of an ideal solid solution are equivalent (Appendix L.1). In model ***M1hs***, excess energy can be introduced as excess Gibbs energy of end-members (e.g. $G^{ex}_{LiMn^{2+}_{y}Fe^{2+}_{1-y}PO_4}$) or global excess energy G^{ex}, like in ***M1***. By introducing molar excess Gibbs energy (like in Equation 7.2) for two end-members favoring the coexistence of Fe^{3+} and Mn^{2+} (Table L.3, Appendix L.2), two miscibility gaps separating at the $x = y$ line at room temperature are reproduced using the ***M1hs*** model (Figure 7.4a). The maximum magnitude of the excess energy is only around 1% of the magnitude of the Gibbs energy of the end-member (Appendix L.2). According to our calculation, at 298 K, as the Li content increases from 0 to $x = y$, Mn^{3+} is reduced to Mn^{2+}. When the Li content rises further, $x > y$, Fe^{3+} starts being reduced. The calculated results of our HS model show that the single solid solution region related to the Fe^{3+}/Fe^{2+} redox reaction is still too small in comparison with experimental data [42] (Figure 7.4a). Moreover, model ***M1hs*** does not show the long-range-order present in the $LiFePO_4$-$FePO_4$ binary system which is including the split of miscibility gaps above 500 K [133]. Therefore we would like to extend model ***M1hs*** to describe the long-range-order of Fe^{3+}-Fe^{2+} and properly reproduce the single solid solution region Fe^{3+}/Fe^{2+} redox reaction at room temperature [42].

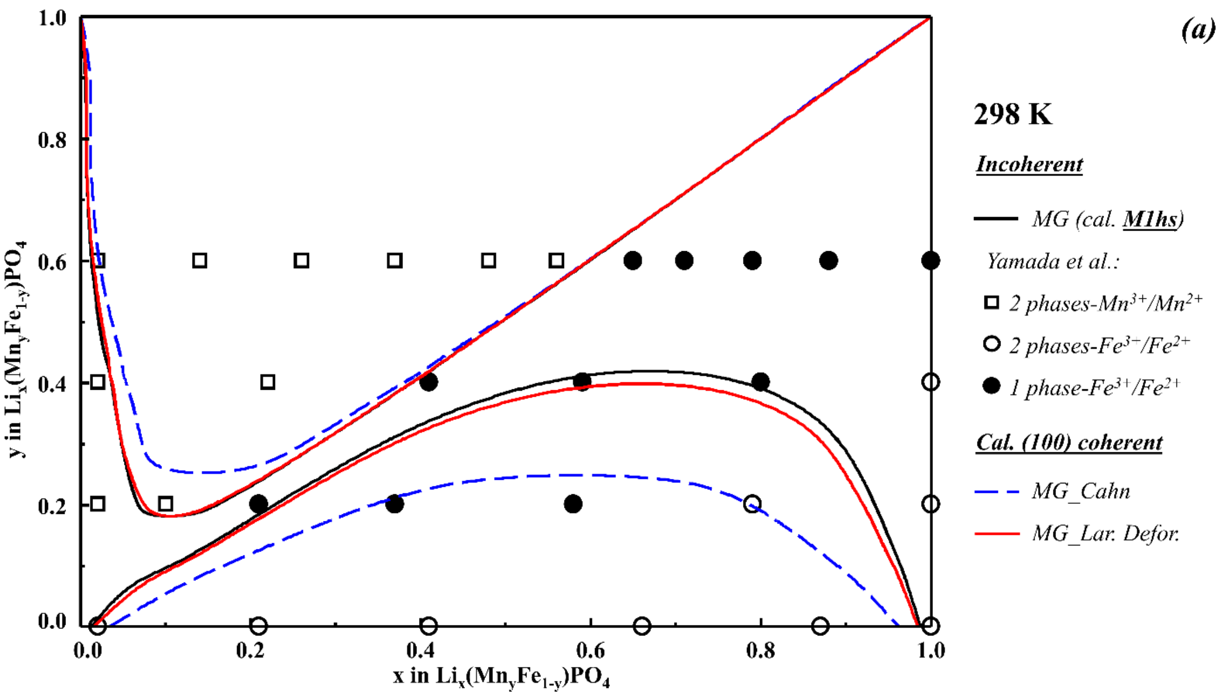

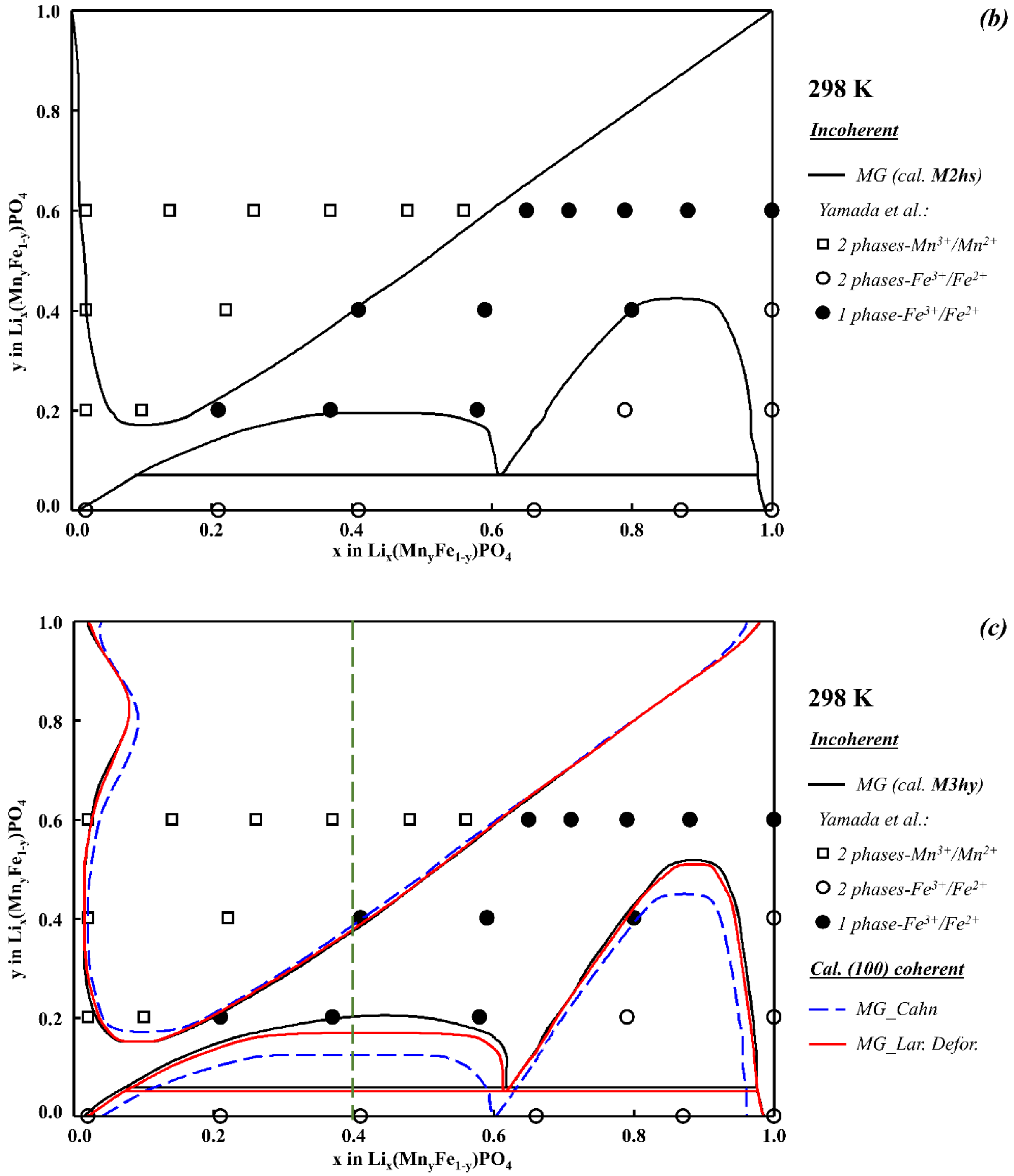

Figure 7.4: The para-equilibrium $Li(Mn_yFe_{1-y})PO_4$-$(Mn_yFe_{1-y})PO_4$ join at 298 K calculated using a/M1hs, b/M2hs and c/ M3hy thermodynamic models in comparison with the para-equilibrium experiment data (□ the two-phase coexisted by Mn^{3+}/Mn^{2+}; ○ the two-phase coexisted by Fe^{3+}/Fe^{2+}; ● the single solid solution phase by Fe^{3+}/Fe^{2+}) [42] and the corresponding (100) coherent

miscibility gaps calculated using Cahn's approach and our elastic Gibbs energy approach in the large deformation regime.

*Model **M2hs**:*

The standard CEF model ***M2*** and the newly developed HS model ***M2hs*** are considered as extended versions of our model ***M5.F*** for the $LiFePO_4$-$FePO_4$ olivine join in our previous publication [133]. Similar to the previous case, the two models, ***M2*** and ***M2hs***, are equivalent in describing the ideal behavior of the $Li(Mn_yFe_{1-y})PO_4$-$(Mn_yFe_{1-y})PO_4$ join. Model ***M2hs*** is, of course, more advantageous when describing experimental data [42] due to the flexible stoichiometry of the secondary sublattices. Note that the Mn content in the two primary sublattices is assumed to be the same as the global content of Mn for simplicity. By modifying the Gibbs energy of end-members (Table L.4, Appendix L.2), the experimental points of Yamada et al. [42] are described properly using our model ***M2hs*** (Figure 7.4b). Many variables are involved in the calculations which make the process of identifying the local and global minima more difficult. More severely, the numerical approach along with many variables make the calculated Gibbs energy curve rough (accuracy threshold). Post-treatment of the rough curves in the para-equilibrium phase diagram is necessary. Therefore, we developed a simpler thermodynamic model for describing this $Li(Mn_yFe_{1-y})PO_4$-$(Mn_yFe_{1-y})PO_4$ olivine join at room temperature.

*Model **M3hy**:*

Because model ***M1hs*** cannot describe the para-equilibrium experimental data [42] properly, and because model **M2hs** is numerically heavy, we have developed model ***M3hy***-a hybrid of model ***M1hs*** and model ***M2***. Model ***M3hy*** (*hy* stands for "*hybrid*") is expected to inherit the flexibility of ***M1hs*** and the long-range-order of Fe^{2+} and Fe^{3+} of the ***M2*** model. Model ***M3hy*** is unique as no standard CEF model is equivalent to it. In this model, Mn^{2+} and Mn^{3+} reside in a secondary sublattice and Fe^{2+} and Fe^{3+} are considered in two primary sublattices with site ratio 3:2. If there is no Mn doped, Fe^{2+} and Fe^{3+} coexist in the solid solution with a long-range-order manner. As Mn ions replace Fe ions, Mn^{2+} and Mn^{3+} take the lattice site of Fe^{2+} and Fe^{3+} but they do not inherit the long-range-order character of the Fe ions in the solid solution which is a weakness of the model but for low Mn content, it should have less impact. Within the tetrahedral $4c$ sites, Mn^{2+} and Mn^{3+} ions distribute randomly. As the Mn content increases, the Fe content becomes smaller and the long-range-ordering degree reduces. Consequently, the contribution of long-range-order in the rich-Mn side of the phase diagram is negligible.

Our sublattice model ***M3hy*** describes well the experimental data of Yamada et al. [42] at room temperature (Figure 7.4c). By separating Mn and Fe ions into different types of sublattice, we can separate the effect of the two redox pairs and the long-range-order of Fe^{2+} and Fe^{3+}. Like in model ***M2hs***, the miscibility gaps separated by the redox reactions are modeled by using the parameter d_{Li} and d_{Va} (Table L.4,5, Appendix L.2). In ***M3hy***, the thermodynamic parameter d_{FF3} signifies the affection of manganese content on the long-range-order of the Fe ions (Table L.5, Appendix L.2). Our model also represents well the fact that as Li content increases, Mn^{3+} is reduced first, and when all the Mn^{2+} ions are obtained, Fe^{3+} starts to be reduced. Vice versa, in delithiation of the $Li(Mn_yFe_{1-y})PO_4$ phase, as Li content decreases, Fe^{2+} is oxidized and as all Fe^{2+} becomes Fe^{3+}, the delithiation continues by oxidizing Mn^{2+}. Moreover, our calculated $Li_{0.4}(Mn_yFe_{1-y})PO_4$-$Li_{0.4}(Mn_yFe_{1-y})PO_4$ phase diagram at room temperature (green dashed line in Figure 7.4c) is comparable with experiments done by Kim et al. [72] Note that all thermodynamic models of the $Li(Mn_yFe_{1-y})PO_4$-$(Mn_yFe_{1-y})PO_4$ join developed in this study are valid at room temperature only. Due to the lack of knowledge on the Gibbs energy of pure compounds at high temperatures and no reliable experiments at elevated temperatures, it has not been possible to properly predict the thermodynamic behavior of the cathode at higher temperatures yet.

To sum up, by introducing the "secondary sublattice" in a HS sublattice model, the phase para-equilibria of the $Li(Mn_yFe_{1-y})PO_4$-$(Mn_yFe_{1-y})PO_4$ join at room temperature are successfully described. In common sense, primary sublattices describe different types of lattice sites in the crystal while secondary sublattices consider different entities occupying the same type of lattice sites in the crystal. In comparison to the standard CEF sublattice models (like ***M1***, ***M2***), formulation of the Gibbs energy of end-members in the newly developed HS models is more complicated. Our HS models (***M1hs***, ***M2hs***) introduce an additional way to implement the excess Gibbs energy and the excess terms are systematically separated. The hybrid model ***M3hy*** is unique since it possesses the characteristics of both the classic model ***M2*** and the newly developed model ***M1hs***. All the newly developed models (***M1hs***, ***M2hs***, and ***M3hy***) show the separation of miscibility gaps by two redox reactions (Figure 7.4). ***M3hy*** is the best for describing the experimental data of Yamada et al. [42] as ***M1hs*** does not describe well the experimental solid solution regions related to Fe^{2+}/Fe^{3+} redox reaction and ***M2hs*** is mathematically complicated. In this study, the minimization of Gibbs energy of the solid solution is only considered under fixed manganese contents and hence, para-equilibrium phase diagram is reproduced. Our HS models are still suitable for describing equilibrium phase diagram where global minimization of Gibbs energy is required since all the parameters belonging to a standard CEF model can be implemented in an equivalent HS model with secondary sublattice.

7.3 Coherent miscibility gaps along a $Li(Mn_yFe_{1-y})PO_4$-$(Mn_yFe_{1-y})PO_4$ join

Coherent miscibility gaps of the para-equilibrium $Li(Mn_yFe_{1-y})PO_4$-$(Mn_yFe_{1-y})PO_4$ joins can now be calculated, provided lattice parameters and elastic constants can be estimated. Based on our knowledge of the Cahn's approach for orthorhombic systems [232] and the Gibbs elastic energy approach for cubic systems [433], in this study, the elastic Gibbs energy approach is considered for orthorhombic systems for the first time. In the $LiFePO_4$-$FePO_4$ system, (100) is the most favorable habit plane because it avoids the largest lattice mismatch in (100) direction [232]. Similarly, (100) lattice mismatch is the largest lattice mismatch of the $LiMnPO_4$-$MnPO_4$ and $Li(Mn_yFe_{1-y})PO_4$-$(Mn_yFe_{1-y})PO_4$ systems and their (100) lattice misfits are even larger than that of the $LiFePO_4$-$FePO_4$ system. According to our calculation of the coherent consolute temperatures of the $LiMnPO_4$-$MnPO_4$ system for various habit planes by using extended Cahn's approach [232], (100) and (110) are the two habit planes which produce stable coherent miscibility gaps above room temperature with the coherent consolute temperature of 511.7 K and 382.3 K, respectively. Similar to $LiFePO_4$-$FePO_4$ and $LiMnPO_4$-$MnPO_4$ system, (100) should be the most favorable habit plane for $Li(Mn_yFe_{1-y})PO_4$-$(Mn_yFe_{1-y})PO_4$. Therefore, in the present study, only the (100) habit plane for an orthorhombic system is formulated by using the elastic Gibbs energy approach.

7.3.1 Elastic Gibbs energy for an orthorhombic system

Like the stress-strain relation developed for the (100) habit plane of cubic systems [433], the stress-strain relation for the (100) habit plane of an orthorhombic system, where only σ_2 and σ_3 are nonzero stress components, is proposed (Equation M.1). The boundary of the (100) coherent spinodal should obey the following condition:

$$\frac{\partial^2 G}{\partial x^2} + 2V_m Y_{(100)} {\eta_b}^2 = 0 \qquad (3.1)$$

Subsequently, the elastic Gibbs energy for (100) is considered as a double integration of elastic Gibbs energy density:

$$G_m^{el} = \iint_0^x V_m Y_{(100)} {\eta_b}^2 dx dx \qquad (3.2)$$

with the boundary conditions: $G_{LiFePO_4}^{el} = 0$ and $G_{FePO_4}^{el} = 0$. The formulation of $Y_{(100)}$ in both the small and large deformation regimes is shown in appendix M. Please note that in the small deformation regime, expressions of $Y_{(100)}$ and G_m^{el} are exactly as what we have developed for orthohombic systems using Cahn's approach [232]. The elastic energy is formulated in the large deformation regime using Almansi-Lagrange strain tensor and the second Piola-Kirchhoff stress tensor. We did not find the analytical expression of $Y_{(100)}$ in the large deformation regime because of the complexity of the f_{el}^l expression. Instead, $Y_{(100)}$ is considered as composition dependent $Y'_{(100)}$ which is the series of coefficients obtained by fitting f_{el}^l as a function of ${\varepsilon_2}^2$ at different Li contents (Appendix M). The fitting of f_{el}^l as a function of ${\varepsilon_2}^2$ is satisfactory (Figure M.1). We have chosen ε_2 because it is the larger strain. As shown from our calculation of elastic energy, when ε_2 is small, $f_{el}^l \approx f_{el}^s$. If ε_2 increases, the difference $\left(f_{el}^s - f_{el}^l\right)$ becomes significant (Figure M.1). Noticeably, for calculating (100) coherent miscibility gap, Cahn's approach eliminates the contribution of η_a while η_a is still considered in the calculation of the elastic Gibbs energy approach for a large deformation. Even though the elastic Gibbs energy in both the small and large deformation regimes show the ease of fitting the lattice parameters, b and c, of the two coherent phases on the (100) habit plane, only the approach in the large deformation regime treates the molar volume change (mainly due to η_a) which makes the coherent transformation slightly more difficult. (100) coherent miscibility gaps of the sub-systems and the $Li(Mn_yFe_{1-y})PO_4$-$(Mn_yFe_{1-y})PO_4$ join, in which the maximum lattice mismatchs go beyond 5%, are therefore estimated by using the elastic Gibbs energy approach for the large deformation regime.

7.3.2 Coherent phase diagram

7.3.2.1 $LiFePO_4$-$FePO_4$

Although the coherent miscibility gaps of $LiFePO_4$-$FePO_4$ were calculated in the small deformation regime in our previous work [232], they are recalculated by using formulae in the large deformation regime (Figure 7.5) because the maximum lattice mismatch of this system is 5.11% [232]. All the parameters needed for calculating coherent miscibility gaps are taken from Phan et al. [232] The calculated coherent miscibility gaps using the formulae of the large deformation regime are much larger than the ones calculated by Cahn's approach and they are just slightly smaller than the equilibrium ones. At room temperature, the coherent phase transformation along (100) habit plane is very likely to occur.

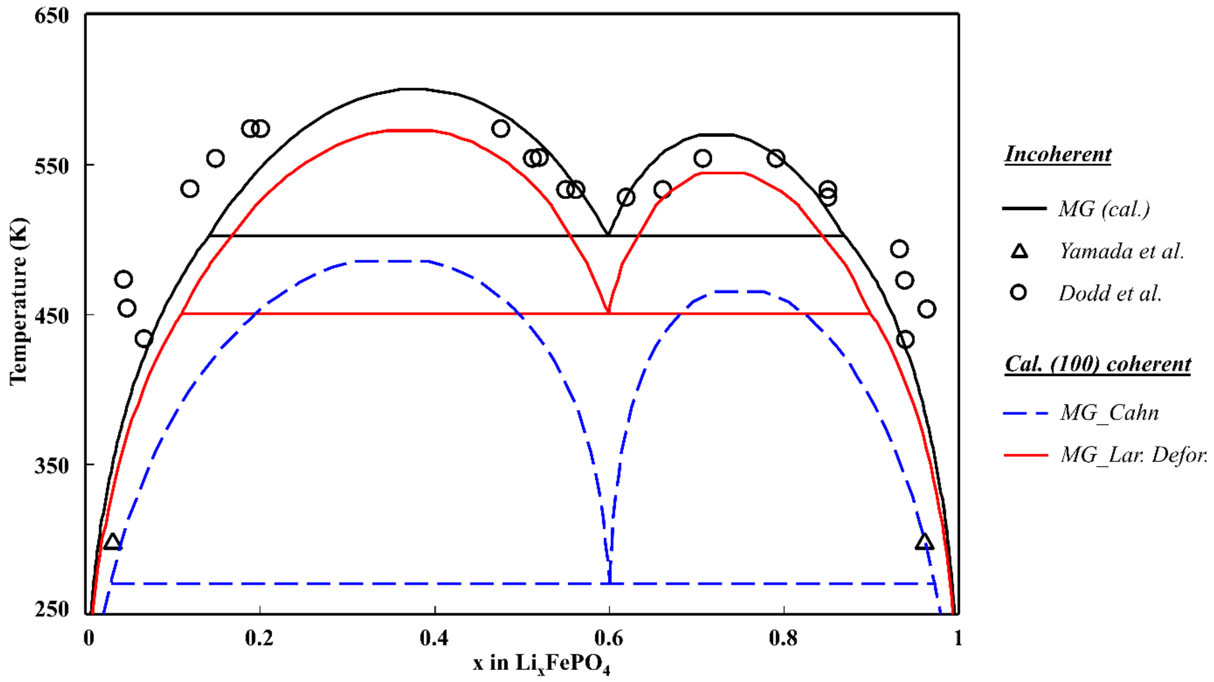

Figure 7.5: Calculated (100) coherent miscibility gaps for the $LiFePO_4$-$FePO_4$ join using Cahn's approach [232] and our elastic Gibbs energy approach for the large deformation regime in comparison with the calculation and the experimental data of the incoherent miscibility gap [26, 28, 133].

7.3.2.2 $LiMnPO_4$-$MnPO_4$

First principles calculations performed in this work (Section 7.2.1) and obtained by Nie et al. [94] reveal the linearity of the lattice constants of the solid solution Li_xMnPO_4 versus the Li content. Therefore, for the calculation of the coherent miscibility gap of the $LiMnPO_4$-$MnPO_4$ join, we consider a linear change of the lattice parameters and molar volume of the solid solution Li_xMnPO_4 versus its Li content. The three lattice mismatch terms of the $LiMnPO_4$-$MnPO_4$ system are calculated by our reported expression [433] and the experimental lattice parameters of pure compounds shown in Piper et al. [84] ($\eta_a = 0.0787$; $\eta_b = 0.0292$; and $\eta_c = -0.0089$). Since η_a is large, the calculation of coherent miscibility gap should be considered in the large deformation regime. In addition, elastic constants necessary for calculating coherent miscibility gap are taken from our DFT simulations. The calculated (100) coherent miscibility gap using the Gibbs energy approach for a large deformation is much larger than that estimated by Cahn's approach due to the large maximum lattice misfit of 7.8% (Figure 7.2). In addition, it is just slightly smaller than the equilibrium one (Figure 7.2).

Note that for both $LiFePO_4$-$FePO_4$ and $LiMnPO_4$-$MnPO_4$ systems, the calculation of (100) coherent miscibility gap in the large deformation regime mainly depends on the two lattice mismatch terms η_b and η_c while the largest lattice mismatch η_a does not play any significant role except its contribution to the molar volume change. For both joins, η_b and η_c are small. Moreover, they are of opposite signs meaning that if an extension occurs along the (010) direction, compression should occur along the (001) direction and vice versa. A simultaneous occurrence of both the local compression and local extension would therefore lower the overall elastic Gibbs energy. Consequently, both systems tend to experience the (100) coherent phase transformation. Lastly, at room temperature, when the miscibility is still wide, the coherent phase transformation is very likely since the coherent effect is not yet as significant as that at high temperatures. To sum up, the avoidance of the large lattice mismatch direction, the small elastic Gibbs energy due to the simultaneous existence of both compression and tension, and the low temperature consideration are the reasons why the (100) habit plane is favorable and the coherent phase transformation is likely to occur in the $LiFePO_4$-$FePO_4$ and $LiMnPO_4$-$MnPO_4$ battery joins.

7.3.2.3 Li(Mn_yFe_{1-y})PO_4-(Mn_yFe_{1-y})PO_4

In order to calculate the (100) coherent miscibility gap of the Li(Mn_yFe_{1-y})PO_4-(Mn_yFe_{1-y})PO_4 olivine join, the knowledge of its physical properties is critical. The lattice parameters of the solid solution Li(Mn_yFe_{1-y})PO_4 show a linear increase of lattice parameters with increased manganese content [16, 46, 49, 70, 389, 431, 434]. Our first principles calculations show a linear change of lattice parameters of (Mn_yFe_{1-y})PO_4 versus its manganese content. Due to the vast similarities among the crystal structure of the Li_x(Mn_yFe_{1-y})PO_4 solid solution with various lithium and manganese compositions, the lattice parameters are properly assumed to be linearly dependent on its lithium and manganese compositions. The molar volume is calculated from the estimated lattice parameters. The elastic constants of compounds are extracted from our DFT simulations and those of the solid solution are assumed to be linearly dependent on its lithium and manganese contents.

The estimation of the (100) coherent miscibility gaps at room temperature is done on the ***M1hs*** and ***M3hy*** thermodynamic models of the Li(Mn_yFe_{1-y})PO_4-(Mn_yFe_{1-y})PO_4 olivine join. Because of the complexity of the thermodynamic model ***M2hs*** and the accuracy threshold, the calculation of the (100) coherent miscibility gap was not performed. The (100) coherent miscibility gaps calculated by the elastic Gibbs energy approach for large deformations are sgnificantly larger than the ones calculated by Cahn's approach (Figure 7.4a, c). The differences of the coherent miscibility gaps estimated using two approaches are more pronounced at a higher temperature, 343 K (at which common LIB electrolytes are still functional [435]) (Figure 7.6a, b). The calculated coherent miscibility gaps on the Fe^{2+}/Fe^{3+} redox reaction side of the phase diagram is smaller and more sensitive to temperature change in comparison with those on the Mn^{2+}/Mn^{3+} side (Figure 7.6a, b). As shown from our calculation (Figure 7.4a, c and Figure 7.6a, b), the coherent miscibility gaps estimated by the elastic Gibbs energy approach are just slightly smaller than the incoherent miscibility gaps. Like in $LiFePO_4$-$FePO_4$ and $LiMnPO_4$-$MnPO_4$ joins, η_b and η_c being of opposite signs reduce the elastic Gibbs energy, consequently, make the coherent phase transformation more likely. Moreover, the elastic Gibbs energy seems to have a slightly larger effect on the miscibility gaps of the Fe^{3+}/Fe^{2+} redox region than that of the Mn^{3+}/Mn^{2+} redox side (Figure 7.4a, c and Figure 7.6a, b). There are three factors which should contribute to this phenomenon. Firstly, when considering the (100) habit plane, the value of η_a does not play a significant role and the magnitudes of η_b and η_c are more important. Therefore, even if $\eta_a^{LFP} < \eta_a^{LMP}$ (where LFP stands for the $LiFePO_4$-$FePO_4$ system and LMP stands for the $LiMnPO_4$-$MnPO_4$ system), since $\eta_b^{LFP} > \eta_b^{LMP}$ and $|\eta_c^{LFP}| > |\eta_c^{LMP}|$, the elastic Gibbs energy still have a smaller effect on the calculation of the (100) coherent miscibility gap in the $LiMnPO_4$-$MnPO_4$ system than that in $LiFePO_4$-$FePO_4$ system. Consequently, the (100) coherent phase transformation is more likely to occur on the Mn^{3+}/Mn^{2+} redox side. Secondly, the elastic constants of Li_xMnPO_4 are generally smaller than those of Li_xFePO_4 [25]. Finally, the asymmetry of the para-equilibrium $Li(Mn_yFe_{1-y})PO_4$-$(Mn_yFe_{1-y})PO_4$ could lead to the dissimilar contribution of elastic Gibbs energy on the Fe^{3+}/Fe^{2+} and Mn^{3+}/Mn^{2+} redox sides. In brief, coherent phase transformation is favorable during charging/discharging processes of the battery with $Li(Mn_yFe_{1-y})PO_4$ cathode. The lower magnitudes of η_b and η_c, lower elastic constants, and asymmetry are the reasons why the coherent phase transformation on the Mn^{3+}/Mn^{2+} redox side is a little more favorable than that on the Fe^{3+}/Fe^{2+} redox side.

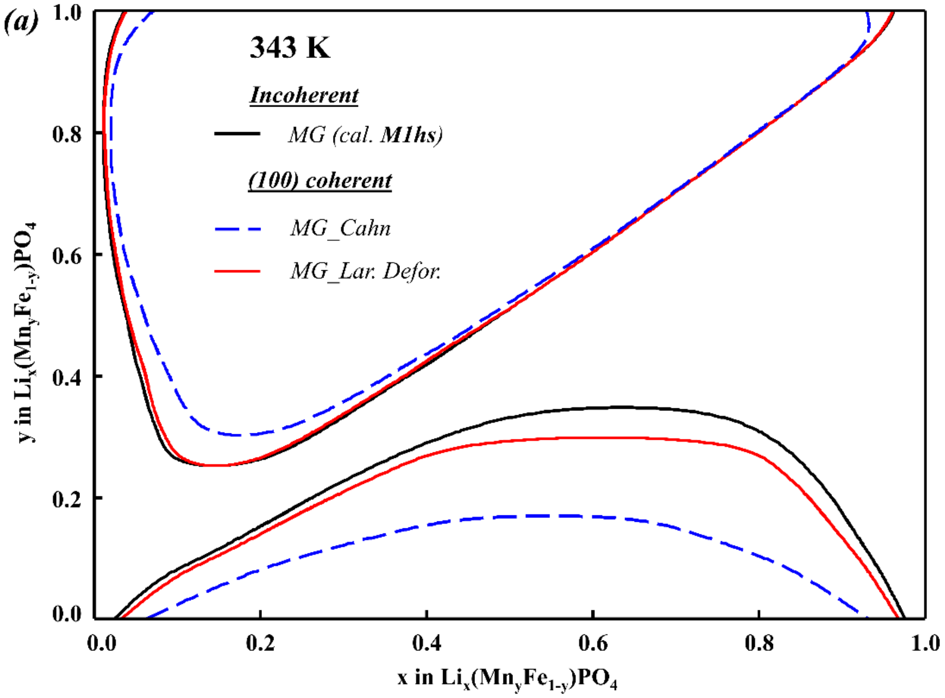

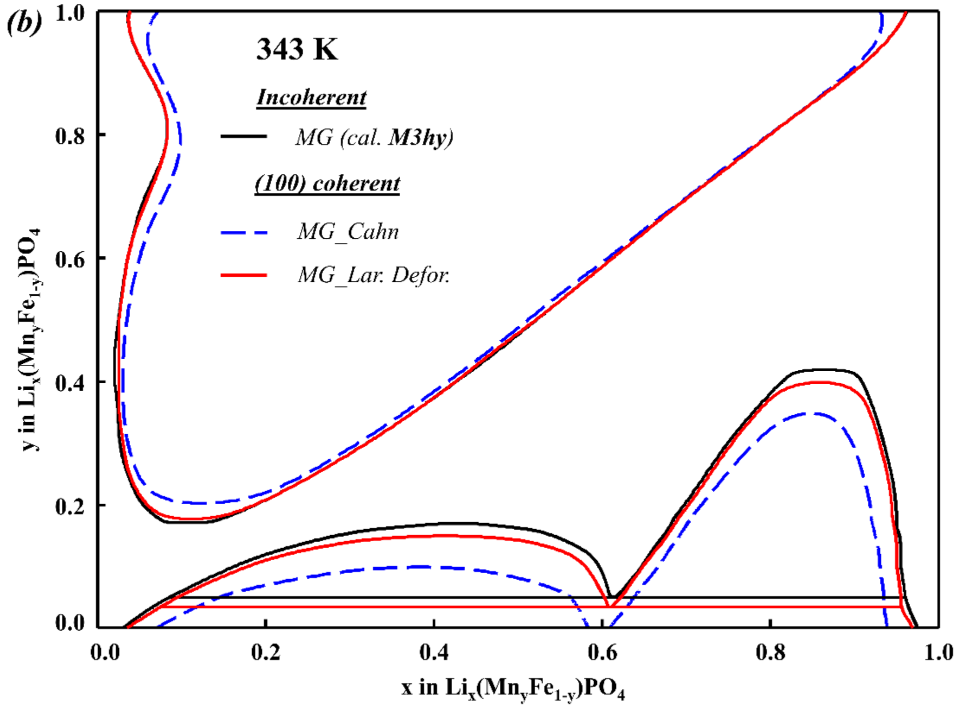

Figure 7.6: Calculated para-equilibrium $Li(Mn_yFe_{1-y})PO_4$-$(Mn_yFe_{1-y})PO_4$ join at 343 K calculated using a/M1hs, b/ M3hy thermodynamic models and the corresponding (100) coherent miscibility gaps calculated using Cahn's approach and our elastic Gibbs energy approach in the large deformation regime.

7.4 Electrochemical delithitation/lithiation

7.4.1 Electrochemically-driven phase transformation

It is well known that the behavior of the open circuit voltage (OCV) of the battery is closely related to the $Li(Mn_yFe_{1-y})PO_4$-$(Mn_yFe_{1-y})PO_4$ olivine join [18, 25, 42, 133, 232]. Therefore, the (100) coherent and para-equilibrium $Li(Mn_yFe_{1-y})PO_4$-$(Mn_yFe_{1-y})PO_4$ join can help us understand and later, predict the electrochemical behavior of the cathode material. First of all, our thermodynamic models allow the complete reversible change of Fe and Mn ions during charge/discharge processes as suggested experimentally [386, 436-438]. Contrary to the phase para-equilibrium of $Li(Mn_yFe_{1-y})PO_4$-$(Mn_yFe_{1-y})PO_4$ joins identified by chemical analyses [42], the electrochemical delithiation/lithiation of samples with high Mn contents ($y > 0.6$) is stable [49, 397, 427, 431, 432, 439]. The electrochemical performance of the $Li_x(Mn_yFe_{1-y})PO_4$ cathode ($y \geq 0.8$) is reported even better than that of $LiMnPO_4$ [439]. Despite the unstable Mn-rich cathode material synthesized chemically, our thermodynamic models of the $Li(Mn_yFe_{1-y})PO_4$-$(Mn_yFe_{1-y})PO_4$ join could still be valid at high Mn content when considering electrochemical applications.

So far, only Ravnbaek et al. [397] reported the electrochemically-driven phase transformation in $Li_x(Mn_yFe_{1-y})PO_4$. Our calculated miscibility gap on the Mn^{3+}/Mn^{2+} side (Figure 7.4) describes quite well the delithiated experimental data [397]. The Mn^{3+}/Mn^{2+} miscibility gap extends towards the Li-rich side and even goes beyond the $x = y$ line during lithiation [397]. In the Fe^{3+}/Fe^{2+} redox side, the reported solid solution regions are quite significant for both charge and discharge phase diagrams [397], in agreement with our para-equilibrium calculated by model ***M3hy*** (Figure 7.4c). The miscibility gaps related to the Fe^{3+}/Fe^{2+} redox reaction during both charge and discharge [397] are smaller than our calculation at low Mn contents. The charged Fe^{3+}/Fe^{2+} miscibility gap is larger than the discharged one and both of them are in the Li-rich regions [397] like the Fe^{3+}/Fe^{2+} miscibility gap showed in our ***M3hy*** phase diagram (Figure 7.4c). The distinct shape of the Fe^{3+}/Fe^{2+} two-phase regions during discharge [397] is in agreement with our calculated miscibility gaps using model ***M3hy*** (Figure 7.4c). The small two-phase region in the Fe^{3+}/Fe^{2+} redox side at low Mn content can be bypass and the solid solution phase transformation could occur instead because of the low Gibbs energy of mixing in this region. In general, our ***M1hs*** and ***M3hy*** thermodynamic models are able to reproduce some features yet all the characteristics of the reported electrochemical charge and discharge $Li(Mn_yFe_{1-y})PO_4$-$(Mn_yFe_{1-y})PO_4$ phase diagram [397]. Note that Ravnbaek et al. [397] defined their phase diagrams as the systematic screening of the electrochemical-driven phase transformations, rather than para-equilibrium or coherent ones. As differences exist between their charge and discharge phase diagrams, they should be close to but not exact para-equilibrium diagram.

7.4.2 Open circuit voltage (OCV)

In addition, the Gibbs energy of the solid solution taken from the thermodynamic models (***M1hs*** and ***M3hy***) provides us the OCV curves of the $Li_x(Mn_yFe_{1-y})PO_4$ battery corresponding to various Mn contents (Figure 7.7). At a certain manganese content, two regions related to two redox couples are identified, separated by the line $x = y$ (Figure 7.7). In the early research on olivine cathode materials [16], two voltage plateaus of almost equal width on both discharging and charging curves were revealed for Li($Mn_{0.5}Fe_{0.5}$)PO_4. The ~4.1 V plateau is associated with the Mn^{3+}/Mn^{2+} redox couple while the Fe^{3+}/Fe^{2+} redox couple is responsible for the plateau with the average voltage of ~3.5 V. In between the two plateaus, there is a single-phase transition region [16]. The separation of the voltage profile into two regions related to two redox couples and the relation of the width of voltage regions with Mn content have been reported in numerous studies [19, 37, 49, 50, 57, 61, 70, 383, 386, 427-432]. Such features are well described by our models (Figure 7.7). At a low Mn content ($y = 0.05$), the Fe^{3+}/Fe^{2+} voltage plateau is expected during delithitation/lithiation for both thermodynamic models. At high Mn content ($y = 0.6$), the voltage plateau related to the Mn^{3+}/Mn^{2+} redox reaction occurs, the solid solution phase transition on the Fe^{3+}/Fe^{2+} redox side is shown. For materials with an average Mn content ($y = 0.3$), two voltage plateaus related to Mn^{3+}/Mn^{2+} and Fe^{3+}/Fe^{2+} redox pairs are revealed using both thermodynamic models. A significant single solid solution phase exists on the Fe^{3+}/Fe^{2+} redox side when model ***M3hy*** is considered, while the single solid solution regions shown by considering model ***M1hs*** is the transition phase between the two two-phase transformations corresponding to two voltage plateaus (Figure 7.4, 7.7). Several phase transformation mechanisms during delithiation/lithiation directly associated with the phase diagram, have been considered among studies.

Two miscibility gaps:

Similar to the measurement reports done by Padhi et al. [16], electrochemical delithiation/lithiation reveals two voltage plateaus of ~3.5 V (Fe^{2+}/Fe^{3+}) and ~4.1 V (Mn^{2+}/Mn^{3+}) in a wide range of manganese content ($0.25 \leq y \leq 0.75$) [47, 50, 429, 431]. The delithiation of Li($Mn_{0.6}Fe_{0.4}$)PO_4 also revealed a solid solution domain in the intermediate state, $0.55 \leq x \leq 0.67$, where the Fe^{2+}/Fe^{3+} electrochemical reaction is replaced by Mn^{2+}/Mn^{3+} in between the two two-phase regions [429]. Meanwhile, the simultaneous redox reactions of Fe^{2+}/Fe^{3+} and Mn^{2+}/Mn^{3+} in the narrow single phase transformation was found in another study [430]. The OCV curves calculated by using model ***M1hs*** also reveal two voltage plateaus for the samples with low and average Mn contents (Figure 7.7). However, since model ***M1hs*** was developed based on experiments of Yamada et al.

[42], the calculated OCV for the delithiation of $Li(Mn_{0.6}Fe_{0.4})PO_4$ shows a voltage plateau related to Mn^{2+}/Mn^{3+} and a solid solution phase transformation on the Fe^{2+}/Fe^{3+} side rather than two voltage plateaus as reported by Bramnik et al. [429]. However, our calculated OCV curve is actually in agreement with the electrochemical delithiation of $Li(Mn_{0.6}Fe_{0.4})PO_4$ performed by Yamada et al. [57].

Mn^{3+}/Mn^{2+} miscibility gap and Fe^{3+}/Fe^{2+} solid solution:

Roberts et al. [432] stated that iron oxidation always begins by the two-phase mechanism with an approximately constant onset potential of ~3.5 V. However, with Mn substitution, the reduction $Fe^{3+} \rightarrow Fe^{2+}$ is increasingly pre-empted by the one-phase reaction. In the investigation of the electrochemical behavior of the $Li(Mn_yFe_{1-y})PO_4$ battery material with intermediate Mn contents, rather than two voltage plateaus [61, 429, 430], a single voltage plateau corresponding to the Mn^{3+}/Mn^{2+} redox pair and a solid solution transition related to the Fe^{3+}/Fe^{2+} redox pair have been found [57, 383, 427, 428, 432]. In agreement with Yamada et al. [42], the reported OCV of charging or discharging $Li_x(Mn_{0.6}Fe_{0.4})PO_4$ revealed two distinct regions [57]. The first region is a ~4.1 V voltage plateau which is based on the two-phase reaction between $(Mn_{0.6}^{3+}Fe_{0.4}^{3+})PO_4$ and $Li_{0.6}(Mn_{0.6}^{2+}Fe_{0.4}^{3+})PO_4$ with fixed lattice constants. The second region with an average voltage of ~3.5V shows an S-curved profile which is related to a single-phase solid solution $Li_x(Mn_{0.6}^{2+}Fe_{0.4}^{a+})PO_4$ (with $2 \leq a \leq 3$) with continuous lattice constants. In the second region, an iron ion changes its oxidation state among Fe^{2+} and Fe^{3+} [57]. This electrochemical behavior of $Li_x(Mn_{0.6}Fe_{0.4})PO_4$ is well described using both of our models (Figure 7.7). A similar electrochemical behavior of $Li(Mn_{0.7}Fe_{0.3})PO_4$ and $Li(Mn_{0.5}Fe_{0.5})PO_4$ were later reported [383, 427, 428]. In contrast to the para-equilibrium reported by Yamada et al. [42] and our calculation of cell voltage (Figure 7.7), in the charging/discharging of $Li(Mn_{0.5}Fe_{0.5})PO_4/(Mn_{0.5}Fe_{0.5})PO_4$, a single phase transformation with continuous changes of lattice parameters instead of a voltage plateau in the “iron side” is found [427, 428]. The intermediate range $(0.4 < x < 0.7)$ where simultaneous Fe^{2+}/Fe^{3+} and Mn^{2+}/Mn^{3+} redox reactions were included [428] is wider than that reported by Nam et al. [430]. According to the cyclic voltammograms reported by Hashambhoy and Whitacre [383], a distinct potential separation between Mn anodic and cathodic current peaks characterizes a two-phase regime with an increased degree of irreversibility and a slight overlap of Fe anodic and cathodic peaks represents a “more reversible” reaction associated with a single phase transition. The authors [383] proposed a mechanistic model. The domino-cascade model [129] is applied to the Mn redox regime. Assuming that half of the lithium ions are associated with the Fe^{2+}/Fe^{3+} sites and the other half are associated with the Mn^{2+}/Mn^{3+} sites, delithiation experiences a single phase transformation on the Fe^{2+}/Fe^{3+} sites until $x = 0.5$, then it continues with dual phase transformation on the Mn^{2+}/Mn^{3+} redox sites [383]. However, this model is insufficient since the solid solution transition region, where the redox reaction is changing among Fe^{2+}/Fe^{3+} and Mn^{2+}/Mn^{3+} [428, 430], is totally omitted. The operando ^{57}Fe Mossbauer and XRD investigation of $Li_x(Mn_{0.5}Fe_{0.5})PO_4$ done by Perea et al. [434] revealed a complex three steps mechanism during the charge. During delithiation, the material experiences a biphasic reaction ($0.7 \leq x < 0.95$), then a solid solution transformation ($0.5 \leq x \leq 0.7$) and finally a biphasic reaction until $x{\sim}0.1$ [434]. The existence of an intermediate solid solution and a miscibility gap on the Fe^{2+}/Fe^{3+} redox reaction side of the phase diagram at $y = 0.5$ [434] is consistent with our calculations using model ***M3hy*** (Figure 7.4, 7.7).

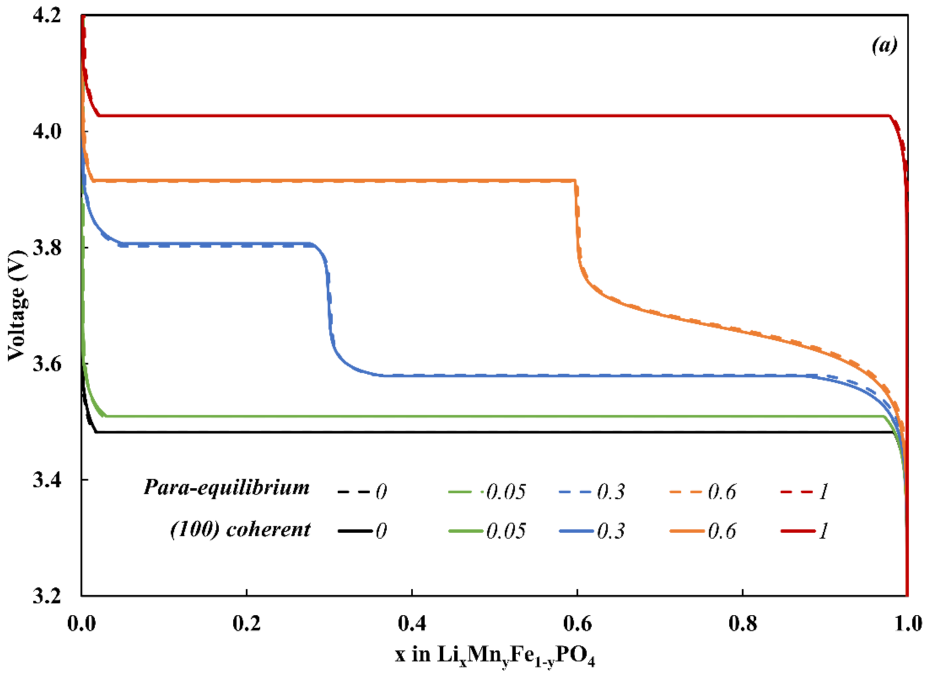

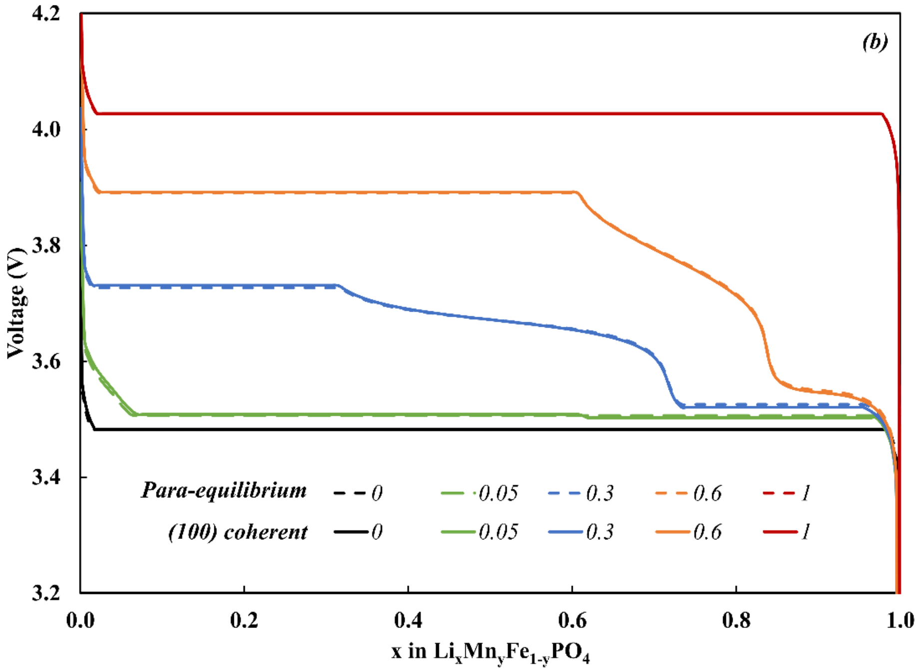

Figure 7.7: Calculated open circuit voltage (OCV) curves obtained by delithiating a $Li(Mn_yFe_{1-y})PO_4$ particle via equilibrium and (100) coherent phase transformation with various Mn contents ($y = 0; 0.05; 0.3; 0.6; 1$) by using either a/ M1hs or b/M3hy thermodynamic models. The (100) coherent OCV curves are obtained from the elastic Gibbs energy approach for the large deformation regime.

Solid solution (de)lithiation:

Alternatively, $Li(Mn_yFe_{1-y})PO_4$ samples could reveal a single-phase mechanism of deintercalation in the whole range of lithium concentration in contrary to the $LiFePO_4$ and $LiMnPO_4$ [70]. The low reversibility of the lithium extraction process in the high-voltage Mn^{2+}/Mn^{3+} range and high reversibility in the Fe^{2+}/Fe^{3+} range were characterized through voltammetric cycles [70]. Nevetherless, the charge/discharge curves were obtained under constant load of C/25 [70] which is much higher than the charge/discharge rate in the experiments of Bramnik et al. [429] or Hashambhoy & Whitacre. [383]. A high current provides a large driving force for the deintercalation/intercalation of lithium ions, which allows the samples to follow the single-phase solid solution transformation [133]. In addition, particle size has not been mentioned. As known, nanoparticles decrease the Li^+ movement path and relax strain energy at the particle surfaces, hence favor the solid solution phase transformation like in the case of $LiFePO_4$ [232].

In brief, there is discrepancy among studies of electrochemical behavior of the $Li(Mn_yFe_{1-y})PO_4$ cathode material with an average amount of manganese ($0.5 \leq y \leq 0.6$). For such material, the two-phase transformation related to the Mn^{2+}/Mn^{3+} redox reaction and the single-phase transformation where sequential or simultaneous redox reactions occur are identified. These two regions can be described using our models. However, the phase transformation in the iron side is unclear. Some studies [16, 61, 429-431] claim a two-phase transformation while the others [57, 383, 427, 428, 432] suggest a single-phase transformation corresponding to the Fe^{2+}/Fe^{3+} redox reaction. The similarities of the phases occurring during delithiation/lithiation are numerous, especially for the phases with different oxidation states of iron. The massive similarities between phases make the experimental analysis very difficult. For example, upon delithiation of $Li_x(Mn_{0.5}Fe_{0.5})PO_4$ at up to $x \approx 0.7$, only one phase was observed. Its lattice parameters insignificantly change: parameters a and b decrease by ~0.5% and ~0.1%, respectively and parameter c increases by ~0.4% [428]. However, the authors did not exclude the possibility of the coexistence of the two-phases with very close lattice parameters [428]. Although the delithiation of $Li_x(Mn_{0.6}Fe_{0.4})PO_4$ up to $x \approx 0.67$ is characterized by a two-phase transformation, the reported molar volume difference is only 1% [429]. In addition, numerous parameters affecting the phase transformation including the charge/discharge rate, particle size, the number of defects or the amount of carbon coating, etc., have not been stated clearly. Furthermore, our thermodynamic models of the $Li(Mn_yFe_{1-y})PO_4$-$(Mn_yFe_{1-y})PO_4$ join were developed based on chemical delithiation, which could not describe the electrochemical behavior precisely. Hence, more experimental evidence and systematic analysis on the electrochemical behavior of this cathode material, especially the one with an average amount of manganese, are necessary. Nevertheless, such controversy on the phase transformation mechanism is not found among studies considering low-Mn-doped-$LiFePO_4$.

7.4.3 Low Mn-doped-$LiFePO_4$

First principles investigation done by Xu et al. [398] showed that only a small amount of Mn^{2+} ion doping could narrow the band gap, and consequently improve $LiFePO_4$ electronic conductivity. Moreover, a high Li^+ solid state diffusion coefficient is required for good electrochemical performance. The substitution of 10%Mn enhances Li ionic transport, therefore, improves the electrochemical performance of the battery at a higher rate [399]. The diffusion of Li^+ increases significantly with Mn^{2+}-substitution degree for the $Li(Mn_yFe_{1-y})PO_4$ ($y \leq 0.2$) olivine compounds [46]. Therefore, low-Mn-doped-$LiFePO_4$ is promising for an effective improvement of the electrochemical properties of $LiFePO_4$.

Among the investigated $Li(Mn_yFe_{1-y})PO_4$ ($y = 0; 0.25; 0.5; 0.75$) materials, the one with low manganese content, $LiMn_{0.25}Fe_{0.75}PO_4$, reveals the highest capacity and the best cyclability [49]. As the manganese content increases ($y \geq 0.25$), both the capacity and cyclic performance decrease [49]. A noticeable capacity loss was observed as $y \geq 0.25$, mainly in the Mn^{2+}/Mn^{3+} range, due to the loss of electronic mobility [431]. Meanwhile $Li(Mn_{0.3}Fe_{0.7})PO_4$ shows a similar or worse charge/discharge capacity than that of $LiFePO_4$ [43, 60, 440], $LiMn_{0.1}Fe_{0.9}PO_4$ and $LiMn_{0.2}Fe_{0.8}PO_4$ reveal better conductivities, charge/discharge capacities, and cyclabilities [43, 60, 381]. The effective improvement of the electrochemical performance of olivine $LiFePO_4$ by only a small amount of Mn^{2+}-doping, especially at high charge/discharge rate, was also observed [44, 48, 381, 441, 442]. Manganese substitution widens the solid solution in Li-poor region and a two-phase transformation was still detected [44, 48, 61, 442]. Actually, our para-equilibrium thermodynamic models show either a solid solution or a two-phase phase transformation on the Mn redox side (Figure 7.4, 7.7). Even if a miscibility gap exists in the Mn^{2+}/Mn^{3+} redox side, at a low Mn content, the energy barrier for the solid solution transformation should be small since the two phases $\left(Mn_y^{3+}Fe_{1-y}^{3+}\right)PO_4$ and $Li_{\sim y}\left(Mn_y^{2+}Fe_{1-y}^{3+}\right)PO_4$ are very similar in terms of physical properties and the lattice mismatch is negligible.

7.4.4 Asymmetry of charging/discharging processes

Like $LiFePO_4$, an uneven charging/discharging performance of $Li(Mn_yFe_{1-y})PO_4$ was also reported. First of all, the phases are more favorable to experience a solid solution phase transformation on the Fe^{2+}/Fe^{3+} redox side rather than that on the Mn^{2+}/Mn^{3+} side [42, 62, 72, 397]. Our calculated para-equilibrium and (100) coherent phase diagrams (Figure 7.4) and the OCV curves (Figure 7.7) are able to demonstrate this asymmetry. Additionally, delithiation and lithiation are asymmetric. The compositional phase diagrams for $Li_x(Mn_yFe_{1-y})PO_4$ measured during charge and discharge are different [397]. Interestingly, even if $Li(Fe_{0.5}Mn_{0.5})PO_4$ experiences two two-phase transitions separated by a single solid solution region during both delithiation and lithiation, at discharge, a noticeable increase in the extent of the single-phase region is detected [61]. $LiMn_{0.25}Fe_{0.75}PO_4$ undergoes two two-phase transformations during delithiation, however, the phase transformation during lithiation is different, becoming a two-phase (Mn^{2+}/Mn^{3+}) reaction and single-phase (Fe^{2+}/Fe^{3+}) reaction [47]. If electrochemical (de)lithiation obeys the para-equilibrium phase diagram, the asymmetry of charging and discharging processes should not be present. No clear answer explaining why asymmetric phase transformations were observed for delithiation and lithiation of $Li(Mn_yFe_{1-y})PO_4$. Ravnsbæk et al. [152] suggested that the phenomenon would be due to the non-symmetric character of coherency strains. Drozhzhin et al. [61] proposed a more direct explanation. The asymmetric phase transformation in $Li_x(Mn_{0.5}Fe_{0.5})PO_4$ is caused by the no-association of the transformation upon changing lithium content with dramatic structural variation, the accompaniment of phase transformation with significant changes of unit cells, and the simultaneous reduction and oxidation of Fe and Mn due to the random distribution of Mn and Fe cations in the lattice of the intermediate solid solution $Li_xMn_{0.5}Fe_{0.5}PO_4$ $(0.4 < x < 0.6)$ [61].

7.4.5 Potential shift

Early work of Padhi et al. [16] revealed the destabilization of the redox potential of the Mn^{3+}/Mn^{2+} couple from over 4.3 to 4.1 V in the presence of Fe. The shift of redox potentials was later observed in many studies [37, 46, 49, 50, 58, 59, 62, 70, 431, 434, 443, 444]. As Mn content changes, linear shifts of the redox potentials (OCV) of the Fe^{2+}/Fe^{3+} and Mn^{2+}/Mn^{3+} couples in $Li(Mn_yFe_{1-y})PO_4$ were reported [37, 46, 62, 431, 434, 443, 444]. Our calculations of OCV curves using both the

M1hs and ***M3hy*** thermodynamic models are able to predict the shifts of the redox potentials. The redox potential of Mn^{2+}/Mn^{3+} decreases and that of Fe^{2+}/Fe^{3+} increases with the increase of Mn content of $Li(Mn_yFe_{1-y})PO_4$ (Figure 7.7) in compatible with experiments [37, 46, 49, 50, 58, 59, 62, 70, 431, 434, 443, 444]. Noticeably, the reported unchanged difference between the average redox voltages of Fe^{2+}/Fe^{3+} and Mn^{2+}/Mn^{3+} in the whole manganese concentration range [431] is observed clearly in the calculated ***M1hs*** OCV curves (Figure 7.7).

According to Malik et al. [62], because Li^+-Fe^{3+} and Li^+-Mn^{2+} interactions are unfavorable, Fe^{3+} and Mn^{2+} states in the solid solution have higher energy than in their pure $FePO_4$ or $LiMnPO_4$ phases. Consequently, higher and lower plateau voltages for Fe^{3+}/Fe^{2+} and Mn^{3+}/Mn^{2+} respectively are observed. On the other hand, Padhi et al. [16] explained the voltage shift phenomenon on the basis of the Fe^{3+}-O-Mn^{2+} super-exchange interaction. On the word of Kobayashi et al. [443] and Muraliganth & Manthiram [37], Mn substitution increases the molar volume, then increases the average Fe-O bond length, consequently, lowers the Fe^{2+}/Fe^{3+} redox energy and increases the voltage of Fe^{2+}/Fe^{3+} couple. Similarly, the shortening of the Mn-O bond due to the substitution of the smaller Fe increases the covalence of the Mn-O bond, raises the Mn^{2+}/Mn^{3+} redox energy and decreases the voltage of the Mn^{2+}/Mn^{3+} couple in $Li(Mn_yFe_{1-y})PO_4$ [37, 443]. The small voltage shift in a single cell would become significant in a large-scale battery containing a large number of series connected single cells [443].

7.4.6 Coherent phase transformation during charging/discharging processes

Since coherent miscibility gaps of $Li(Mn_yFe_{1-y})PO_4$-$(Mn_yFe_{1-y})PO_4$ olivine join are just slightly smaller than the corresponding para-equilibrium gaps, the OCV curves following the coherent phase transformation are almost identical to the para-equilibrium ones (Figure 7.7). The strain, which should be related to coherence, is found during the phase transformation of $Li(Mn_yFe_{1-y})PO_4$ [445]. The intermediate phase in the middle of the two voltage regions should help to reduce the misfit strain [152]. Ravnsbæk et al. [152] suggested a coherent phase transformation for small particles. As known previously, particle size is one factor affecting the miscibility gap of the $LiFePO_4$-$FePO_4$ olivine join [23, 27, 34, 35, 232]. Small $LiMnPO_4$ particles show better electrochemical performances [412, 446-448]. Although this effect has not been systematically investigated in $Li(Mn_yFe_{1-y})PO_4$-$(Mn_yFe_{1-y})PO_4$, the role of particle size is still recognized [152]. In electrochemical measurement of micrometer-sized particle $Li(Mn_yFe_{1-y})PO_4$, the two distinct peak potentials in cyclic voltammetry (CV) corresponding to the two redox pairs Fe^{3+}/Fe^{2+} and Mn^{3+}/Mn^{2+} were observed. On the other hand, a single broad peak was detected in CV from ~10nm-platelet $LiMn_{0.5}Fe_{0.5}PO_4$. In the nanoplatelets, Fe and Mn cations were homogeneously distributed causing a synergetic effect on the redox potentials [449]. Similar to $LiFePO_4$, for $Li(Mn_yFe_{1-y})PO_4$ cathode, the smaller the particle size is, the more favorable the coherent phase transformation is expected since the lattice mismatches are smaller and the elastic strain could easily be relaxed at the particle surfaces.

To sum up, even though some studies show electrochemical charging/discharging in agreement with the phase diagram of Yamada et al. [42], other studies showed two two-phase transformations of intermediate manganese cathode materials. It means that for electrochemical applications, the Fe^{3+}/Fe^{2+} miscibility gap can be larger than the reported chemical miscibility gaps [42] especially in the range of $0.4 \leq y \leq 0.6$. Up to now, model ***M3hy*** describes well the experimental data of Yamada et al. [42] and model ***M1hs*** describes the OCV two-voltage plateaus better. Our models could distinguish the voltage regions related to two redox reactions with the Mn/Fe content ratio. Noticeably, the massive resemblances of the phases which could occur during phase transitions make the voltage plateaus and solid solution curves more difficult to distinguish and the experimental phase analysis more challenging. Asymmetry and potential shift are properly described using both our models. As shown in our thermodynamic models, the (100) coherent phase transformation which allows Li ions to move in its favorite (010) channels [32, 399] is promising. Therefore, it is preferred to fabricate $Li(Mn_yFe_{1-y})PO_4$ cathodes as (100) wires or (100) plate-like nanoparticles, etc. in order to promote the (100) coherent phase transformation and improve the charge/discharge rates and cyclability of the cathode materials.

7.5 Conclusion

In summary, the thermodynamic behavior of the Mn-doped-$LiFePO_4$ cathode material was investigated by considering the para-equilibrium and (100) coherent $Li(Mn_yFe_{1-y})PO_4$-$(Mn_yFe_{1-y})PO_4$ battery join. It is the first time that:

- the phase diagrams of the $LiFePO_4$-$LiMnPO_4$, $FePO_4$-$MnPO_4$ and $LiMnPO_4$-$MnPO_4$ olivine joins were modeled at up to 473 K;
- the concept of secondary sublattice in a HS model is introduced to the compound energy formalism (CEF);
- the hybrid model ***M3hy*** is unique however it skips the possible LRO character of the Mn^{2+} and Mn^{3+} in the solid solution which has never been reported in any works up to now;
- the para-equilibrium $Li(Mn_yFe_{1-y})PO_4$-$(Mn_yFe_{1-y})PO_4$ olivine join at room temperature is successfully modeled, describing well the experimental data[42];
- the (100) coherent miscibility gap of an orthorhombic system is formulated using the elastic Gibbs energy approach in both the small and large deformation regimes;
- and the (100) coherent $Li(Mn_yFe_{1-y})PO_4$-$(Mn_yFe_{1-y})PO_4$ olivine join at room temperature is shown.

Using our thermodynamic models, the electrochemical properties of $Li(Mn_yFe_{1-y})PO_4$ including electrochemical phase transformation, OCV, potential shift, asymmetry and favorable (100) coherent phase transformation, are well described. Nevertheless, discrepancy still exists in electrochemical delithiation/lithiation experiments among studies. Therefore, more systematic investigations and electrochemical experiments along with advanced analysis techniques are required for verifying and improving our thermodynamic models of the $Li(Mn_yFe_{1-y})PO_4$-$(Mn_yFe_{1-y})PO_4$ olivine join. Another contribution worth to mention is that typical thermal behavior of $LiFePO_4$ was explained via second order phase transition induced by magnon-phonon interactions, the appearance of "antisite" defects and thermally activated vacancies, and anharmonic behaviors of the lattice vibrations.

7.6 Acknowledgments

The authors recognize the support of Natural Science, Engineering Research Council of Canada and the Canadian Foundation for Innovation through the Automotive Partnership Canada program and our industry partner Johnson-Matthey. Computations were made on the supercomputer Graham at University of Waterloo managed by Compute Ontario and Compute Canada and on the supercomputer Cedar at Simon Fraser University managed by WestGrid and Compute Canada.

CHAPTER 8 GENERAL DISCUSSION

In this chapter, the synthesis and the limitations of this research will be discussed. The synthesis of this work emphasizes the contribution to computational thermochemistry and electrochemistry. The discussion on the limitations of the present study gives the audience the scope of research to help them avoid any extrapolation beyond its fundamental limits.

8.1 Synthesis of the work

In this doctoral project, the thermodynamics of the $LiFePO_4$-$FePO_4$ and $Li(Mn_yFe_{1-y})PO_4$-$(Mn_yFe_{1-y})PO_4$ olivine cathode joins is investigated in order to understand the thermodynamic behavior of the $LiFePO_4$ and Mn-doped-$LiFePO_4$ cathode materials during charge/discharge processes. As the title of the thesis suggests, the thermodynamics of the cathode joins is examined by describing the corresponding solid solution with various amounts of lithium. The Gibbs free energy of the Li_xFePO_4 solid solution is modeled by CEF and the Gibbs energy minimization technique is utilized to describe the low-temperature miscibility gaps of the $LiFePO_4$-$FePO_4$ join. An extra order of long-range-order introduced in the thermodynamic models of Li_xFePO_4 helps us to describe the eutectoid reaction existing in the $LiFePO_4$-$FePO_4$ phase diagram. Using our thermodynamic models, the voltage plateau of OCV can be illustrated. Analysis of the spinodal decomposition during lithiation/delithiation reveals that the low-temperature miscibility gap is the blend of two sub-miscibility gaps (paper 1 presented in Chapter 4).

$LiFePO_4$ is said to be still suitable for high-rate applications since lithium ions can transfer without changing the olivine crystal structure. The unchanged crystal structure is achieved during lithiation/delithiation only when a coherent phase transformation is ensured. The extended Cahn's approach is used for calculating the coherent miscibility gaps of the $LiFePO_4$-$FePO_4$ join. (100) appears as the most stable habit plane for coherent phase transformation while (110) and (010) habit planes may also occur. The presence of a metastable phase, the existence of the preferred phase boundaries during lithiation/delithiation and the creation of cracks and dislocations are explainable by a coherent phase transformation. In addition, two scenarios of the contraction of miscibility gaps due to particle size effect are proposed. The combined coherency-size effect is calculated for the first time. Both coherence and particle size effects on the $LiFePO_4$-$FePO_4$ phase diagram are reported in our second paper (presented in chapter 5).

Further improvement of the electrochemical properties of the $LiFePO_4$ cathode can be achieved by Mn-doping. Similar to the previous chapters concerning thermodynamic modeling of equilibrium and coherent $LiFePO_4$-$FePO_4$ phase diagram, the para-equilibrium and coherent $Li(Mn_yFe_{1-y})PO_4$ - $(Mn_yFe_{1-y})PO_4$ olivine joins are described. Note that the maximum lattice mismatch of the $Li(Mn_yFe_{1-y})PO_4$ - $(Mn_yFe_{1-y})PO_4$ system is beyond 5%. Therefore, the extended Cahn's approach formulated in paper 2 (presented in chapter 5) is not applicable for this system. Hence, an alternative approach for describing the coherent phase diagram must be formerly developed. The elastic Gibbs energy approach describes the elastic energy stored in the coherent boundaries as an elastic contribution of the total Gibbs energy of the solid solution. This approach is firstly formulated for cubic systems based on the linear elasticity theory in both the small and the large deformation regimes. The formula of (100) elastic Gibbs energy developed by the elastic Gibbs energy for the small deformation is the same as that of Cahn's approach for cubic systems. A new stress-strain relationship, i.e. a new formula of elastic Gibbs energy for the (111) habit plane is reported. This elastic Gibbs energy approach is applied to various cubic systems, and it shows an appropriate predictive ability when calculating the coherent miscibility gaps (paper 3 presented in chapter 6).

Before describing the coherent $Li(Mn_yFe_{1-y})PO_4$ - $(Mn_yFe_{1-y})PO_4$ phase diagram, it is necessary to first, develop a thermodynamic model of the $Li(Mn_yFe_{1-y})PO_4$ - $(Mn_yFe_{1-y})PO_4$ phase para-equilibria and second, extend the elastic Gibbs energy approach for orthorhombic systems in the large deformation regime. As Li^+ ions diffuse much faster than metallic ions (Fe^{2+}, Fe^{3+}, Mn^{2+}, and Mn^{3+}) do in the olivine structure, the Fe/Mn content ratio is unchanged during lithiation/delithiation. Hence, not equilibrium, but the para-equilibrium $Li(Mn_yFe_{1-y})PO_4$ - $(Mn_yFe_{1-y})PO_4$ phase diagram is modeled. By introducing hierarchical sublattices, the miscibility gaps of this system are produced, illustrating well the experimental data. The miscibility gaps are not only separated by the redox reactions, Fe^{2+}/Fe^{3+} and Mn^{2+}/Mn^{3+}, but also by the Fe^{2+}/Fe^{3+} long-range-order. Our thermodynamic models can be used to explain the electrochemically driven phase diagrams, OCV, asymmetry of charge/discharge and potential shifts of this system. The calculation of the coherent $Li(Mn_yFe_{1-y})PO_4$ - $(Mn_yFe_{1-y})PO_4$ join by using the elastic Gibbs energy approach for orthorhombic systems reveals the likelihood of Mn-doped-$LiFePO_4$ cathodes to experience a (100) coherent phase transformation during charge/discharge (paper 4 presented in chapter 7).

8.2 Limitations of the work

Like other researches, this doctoral research has its own limitations. First, the thermodynamic behavior of cathodes was considered in comparison with electrochemical experiments in which the carbon coating of the particles always exists. The role of carbon coating is ignored in this study since carbon can improve the physical properties of the cathode material such as electric conductivity, tap density, etc. [178] rather than its thermodynamic behavior. Nano $LiFePO_4$ particles are highly stable during the carbon coating process with no secondary phase formed [179].

Secondly, our developed thermodynamic models are mainly based on chemical experiments. Consequently, our thermodynamic models might not describe well electrochemical behaviors of the cathode material precisely since electrons and ions exchange directly in chemical lithiation/delithiation while they transfer indirectly in electrochemical experiments.

Thirdly, this study concerns only the thermodynamic behavior, hence, kinetics related phenomena such as degradation of capacity and cyclability with high charge/discharge rates are out of scope.

Finally, the reported OCV curves obtained from thermodynamic models describing equilibrium, spinodal or coherent phase transformation during lithiation/delithiation are likely applied for one particle or simultaneous lithiation/delithiation of particles within the cathode. Our models have not been suitable for illustrating the consecutive lithiation/delithiation of particles yet.

CHAPTER 9 CONCLUSION

In summary, the main objective of the thesis to develop thermodynamic models describing (i) the coherent and particle size dependent phase equilibria of the $LiFePO_4$-$FePO_4$; and (ii) the coherent and para-equilibrium phase transformation of the Mn-doped-$LiFePO_4$ cathode material is successfully achieved. All the secondary objectives are attained in the four scientific papers related to this thesis. Some future perspectives are brought to demonstrate the potential of this work after the presentation of the originality of the thesis.

9.1 Originality of the thesis

The originality of the thesis is summarized as follows:

- In the context of the thesis, the combination of coherence-size is first ever calculated. The size-dependent coherent $LiFePO_4$-$FePO_4$ phase diagram is shown.
- In this thesis, for the first time, CEF models with secondary sublattices are introduced to describe the miscibility gaps separated by two redox reactions, Fe^{2+}/Fe^{3+} and Mn^{2+}/Mn^{3+}, in the $Li(Mn_yFe_{1-y})PO_4$-$(Mn_yFe_{1-y})PO_4$ system. Unlike the classical sublattice (primary sublattice) which describes the different types of lattice sites, the secondary sublattice designates different species on the same type of lattice site. Therefore, in the case of $Li(Mn_yFe_{1-y})PO_4$-$(Mn_yFe_{1-y})PO_4$ join, by using both primary and secondary sublattices, it is possible to simultaneously obtain the miscibility gaps which are separated by the two redox reactions and long-range-order of Fe^{2+}/Fe^{3+}.
- In addition, Cahn's approach for calculating the coherent miscibility gaps of orthorhombic systems is formulated and applied for the first time.
- Last but not least, in order to overcome the limitation of Cahn's approach, the elastic Gibbs energy approach is first ever developed for both cubic systems and orthorhombic systems in both small and large deformation regimes. So far, in the elastic Gibbs energy approach, only the (100) and (111) coherent habit planes are formulated for cubic systems and only the (100) habit plane is considered for orthorhombic systems.

9.2 Future development

This discussion of the future development will be limited to two main proposals of extension and improvement of my doctoral research: (1) development of the thermodynamic understandings of cathode materials and (2) development and applications of thermodynamic models with secondary sublattices and thermodynamic models of coherent elastic Gibbs energy. Firstly, for improving our knowledge of the thermodynamic behavior of $LiFePO_4$ and Mn-doped-$LiFePO_4$ cathode materials, electrochemical experiments and systematic analysis are necessary. Since all phases possibly occurring during charge/discharge have an olivine structure with similar lattice parameters, experimental techniques for analyzing the phases are important in order to distinguish them and their relations. In addition, according to our prediction, the (100) habit plane is the most stable one in both $LiFePO_4$-$FePO_4$ and $Li(Mn_yFe_{1-y})PO_4$-$(Mn_yFe_{1-y})PO_4$ joins. Therefore, cathodes consisting of particles with shapes encouraging a (100) coherent phase transformation such as (100) platelets, (100) wires, etc. should improve electrochemical properties of cathode materials such as high-rate performance, cyclability, etc. Moreover, the thermodynamic models reported in this work can be utilized in integrated computational materials engineering for $LiFePO_4$ and $Li(Mn_yFe_{1-y})PO_4$ cathode materials.

On the other hand, the hierarchical sublattice thermodynamic models with secondary sublattices can possibly be applied to other systems. For example, Co doping of $LiFePO_4$ also reveals two voltage plateau regions corresponding to two redox reactions, Co^{2+}/Co^{3+} and Fe^{2+}/Fe^{3+} [450]. Hence, a thermodynamic model with secondary sublattices might be useful when considering the $Li(Co_yFe_{1-y})PO_4$-$(Co_yFe_{1-y})PO_4$ join. The idea of secondary sublattice could also be applied in other olivine cathodes such as $Li(Ni_yFe_{1-y})PO_4$, $Li(Ni_yMn_{1-y})PO_4$, $Li(Ni_yCo_{1-y})PO_4$, $Li(Co_yMn_{1-y})PO_4$. Moreover, this idea should not be restricted within olivine solid solutions. It is suitable for any solid solutions where it is necessary to separate the effects of different types of species of the same kind of lattice. Besides, this study provides a new tool for estimating coherent miscibility gaps. The elastic Gibbs energy approach is applicable for predicting the coherent phase diagram of cubic systems and orthorhombic systems. This approach should be expanded to more habit planes.

Hopefully, this thesis has demonstrated that classical thermodynamics still have their roles in the range of tools available to scientists. Although this approach seems to be rudimental in comparison with other simulation techniques (DFT, molecular dynamics), traditional approaches like the one presented in this doctoral thesis should not lose their value in the modern literature. From my perspective, in the future, modeling should persist to incorporate the three big fundamental dimensions of science: phenomenology, numerical simulations and experimental analysis. Only with this triple dependence, researches on modeling are reliable and stand out with innovations.

REFERENCES

[1] U. N. F. C. o. C. C. (UNFCCC), "2015 United Nations Climate Change Conference (COP21 or CMP 11)," in *Conference of the Parties (COP)*, Paris, France, 2015.

[2] E. Commision, "White Paper: European Transport Policy for 2010: Time to Decide," European Commision, Luxemburg2001.

[3] G. Berckmans, M. Messagie, J. Smekens, N. Omar, L. Vanhaverbeke, and J. Van Mierlo, "Cost Projection of State of the Art Lithium-Ion Batteries for Electric Vehicles Up to 2030," *Energies*, vol. 10, 2017.

[4] P. Patel, T. Ellis, and J. Howes, "How green is your electric vehicle?," *MRS Bulletin*, vol. 42, pp. 416-417, 2017.

[5] S. Chen, T. He, Y. Lu, Y. Su, J. Tian, N. Li, *et al.*, "Renovation of LiCoO2 with outstanding cycling stability by thermal treatment with Li2CO3 from spent Li-ion batteries," *Journal of Energy Storage*, vol. 8, pp. 262-273, 2016/11/01/ 2016.

[6] M. Yoshio, R. J. Brodd, and A. Kozawa, *Lithium-Ion Batteries: Science and Technologies*: Springer New York, 2010.

[7] A. Ulvestad, "A Brief Review of Current Lithium Ion Battery Technology and Potential Solid State Battery Technologies," 03/12 2018.

[8] B. Nykvist and M. Nilsson, "Rapidly falling costs of battery packs for electric vehicles," *Nature Climate Change*, vol. 5, pp. 329-332, 2015/04/01 2015.

[9] M. Wentker, M. Greenwood, and J. Leker, "A Bottom-Up Approach to Lithium-Ion Battery Cost Modeling with a Focus on Cathode Active Materials," *Energies*, vol. 12, 2019.

[10] M. S. Whittingham, "Lithium Batteries and Cathode Materials," *Chemical Reviews*, vol. 104, pp. 4271-4302, 2004/10/01 2004.

[11] D. H. Doughty, *Vehicle Battery Safety Roadmap Guidance*: National Renewable Energy Laboratory, 2012.

[12] D. D. MacNeil and J. R. Dahn, "The Reaction of Charged Cathodes with Nonaqueous Solvents and Electrolytes: I. Li0.5CoO2," *Journal of The Electrochemical Society*, vol. 148, pp. A1205-A1210, November 1, 2001 2001.

[13] J. R. Dahn, E. W. Fuller, M. Obrovac, and U. von Sacken, "Thermal stability of LixCoO2, LixNiO2 and λ-MnO2 and consequences for the safety of Li-ion cells," *Solid State Ionics*, vol. 69, pp. 265-270, 1994/08/01/ 1994.

[14] J. Bozich, M. Hang, R. Hamers, and R. Klaper, "Core chemistry influences the toxicity of multicomponent metal oxide nanomaterials, lithium nickel manganese cobalt oxide, and lithium cobalt oxide to Daphnia magna," *Environmental Toxicology and Chemistry*, vol. 36, pp. 2493-2502, 2017/09/01 2017.

[15] L.-X. Yuan, Z.-H. Wang, W.-X. Zhang, X.-L. Hu, J.-T. Chen, Y.-H. Huang, *et al.*, "Development and challenges of LiFePO4 cathode material for lithium-ion batteries," *Energy & Environmental Science*, vol. 4, pp. 269-284, 2011.

[16] A. K. Padhi, K. S. Nanjundaswamy, and J. B. Goodenough, "Phospho-olivines as Positive-Electrode Materials for Rechargeable Lithium Batteries," *Journal of the Electrochemical Society,* vol. 144, pp. 1188-1194, April 1, 1997 1997.

[17] A. Yamada, S. C. Chung, and K. Hinokuma "Optimized LiFePO4 for Lithium Battery Cathodes," *Journal of The Electrochemical Society,* vol. 148, pp. A224-A229, March 1, 2001 2001.

[18] T. Ichitsubo, K. Tokuda, S. Yagi, M. Kawamori, T. Kawaguchi, T. Doi, *et al.*, "Elastically constrained phase-separation dynamics competing with the charge process in the LiFePO4/FePO4 system," *Journal of Materials Chemistry A,* vol. 1, pp. 2567-2577, 2013.

[19] J. Molenda, A. Kulka, A. Milewska, W. Zając, and K. Świerczek, "Structural, Transport and Electrochemical Properties of LiFePO4 Substituted in Lithium and Iron Sublattices (Al, Zr, W, Mn, Co and Ni)," *Materials,* vol. 6, p. 1656, 2013.

[20] R. Malik, A. Abdellahi, and G. Ceder, "A Critical Review of the Li Insertion Mechanisms in LiFePO4 Electrodes," *Journal of The Electrochemical Society,* vol. 160, pp. A3179-A3197, January 1, 2013 2013.

[21] K. Wang, M. Hou, S. Yuan, H. Yu, Y. Wang, C. Wang, *et al.*, "An additional discharge plateau of Mn3 + in LiFe0.5Mn0.5PO4 at high current rates," *Electrochemistry Communications,* vol. 55, pp. 6-9, 6// 2015.

[22] A. Yamada, H. Koizumi, S.-i. Nishimura, N. Sonoyama, R. Kanno, M. Yonemura, *et al.*, "Room-temperature miscibility gap in LixFePO4," *Nature Materials,* vol. 5, pp. 357-60, May 2006 2006.

[23] N. Meethong, H.-Y. S. Huang, W. C. Carter, and Y.-M. Chiang, "Size-Dependent Lithium Miscibility Gap in Nanoscale Li1 − x FePO4," *Electrochemical and Solid-State Letters,* vol. 10, pp. A134-A138, May 1, 2007 2007.

[24] S. H. Lee, "A study of ionic materials for the energy applications through first-principles calculations and calphad modeling," 3576127 Ph.D., The Pennsylvania State University, Ann Arbor, 2011.

[25] Y. Xie, H.-T. Yu, T.-F. Yi, and Y.-R. Zhu, "Understanding the Thermal and Mechanical Stabilities of Olivine-Type LiMPO4 (M = Fe, Mn) as Cathode Materials for Rechargeable Lithium Batteries from First Principles," *ACS Applied Materials & Interfaces,* vol. 6, pp. 4033-4042, 2014/03/26 2014.

[26] A. Yamada, H. Koizumi, N. Sonoyama, and R. Kanno, "Phase Change in LixFePO4," *Electrochemical and Solid-State Letters,* vol. 8, p. A409, 2005.

[27] G. Kobayashi, S.-i. Nishimura, M.-S. Park, R. Kanno, M. Yashima, T. Ida, *et al.*, "Isolation of Solid Solution Phases in Size-Controlled LixFePO4 at Room Temperature," *Advanced Functional Materials,* vol. 19, pp. 395-403, 2009.

[28] J. L. Dodd, R. Yazami, and B. Fultz, "Phase Diagram of LixFePO4," *Electrochemical and Solid-State Letters,* vol. 9, p. A151, 2006.

[29] C. Delacourt, P. Poizot, J.-M. Tarascon, and C. Masquelier, "The existence of a temperature-driven solid solution in LixFePO4 for $0 \leq x \leq 1$," *Nature Materials,* vol. 4, pp. 254-260, 2005.

[30] D. Li and H. Zhou, "Two-phase transition of Li-intercalation compounds in Li-ion batteries," *Materials Today,* vol. 17, pp. 451-463, 2014/11/01/ 2014.

[31] J. Molenda and M. Molenda, "Composite Cathode Material for Li-Ion Batteries Based on $LiFePO_4$ System," in *Metal, Ceramic and Polymeric Composites for Various Uses*, J. Cuppoletti, Ed., ed Rijeka: InTech, 2011, p. 30.

[32] D. Morgan, A. Van der Ven, and G. Ceder, "Li Conductivity in Li x MPO 4 (M =Mn , Fe , Co , Ni) Olivine Materials," *Electrochemical and Solid-State Letters,* vol. 7, pp. A30-A32, February 1, 2004 2004.

[33] M. S. Islam, D. J. Driscoll, C. A. J. Fisher, and P. R. Slater, "Atomic-Scale Investigation of Defects, Dopants, and Lithium Transport in the LiFePO4 Olivine-Type Battery Material," *Chemistry of Materials,* vol. 17, pp. 5085-5092, 2005/10/01 2005.

[34] M. Wagemaker, D. P. Singh, W. J. H. Borghols, U. Lafont, L. Haverkate, V. K. Peterson, *et al.*, "Dynamic Solubility Limits in Nanosized Olivine LiFePO4," *Journal of the American Chemical Society,* vol. 133, pp. 10222-10228, 2011/07/06 2011.

[35] S. Furutsuki, S.-C. Chung, S.-i. Nishimura, Y. Kudo, K. Yamashita, and A. Yamada, "Electrochromism of LixFePO4 Induced by Intervalence Charge Transfer Transition," *The Journal of Physical Chemistry C,* vol. 116, pp. 15259-15264, 2012/07/26 2012.

[36] S.-Y. Chung, J. T. Bloking, and Y.-M. Chiang, "Electronically conductive phospho-olivines as lithium storage electrodes," *Nat Mater,* vol. 1, pp. 123-128, 10//print 2002.

[37] T. Muraliganth and A. Manthiram, "Understanding the Shifts in the Redox Potentials of Olivine LiM1−yMyPO4 (M = Fe, Mn, Co, and Mg) Solid Solution Cathodes," *The Journal of Physical Chemistry C,* vol. 114, pp. 15530-15540, 2010/09/16 2010.

[38] N. Meethong, Y.-H. Kao, S. A. Speakman, and Y.-M. Chiang, "Aliovalent Substitutions in Olivine Lithium Iron Phosphate and Impact on Structure and Properties," *Advanced Functional Materials,* vol. 19, pp. 1060-1070, 2009.

[39] W. Zhang, Y. Hu, X. Tao, H. Huang, Y. Gan, and C. Wang, "Synthesis of spherical LiFePO4/C via Ni doping," *Journal of Physics and Chemistry of Solids,* vol. 71, pp. 1196-1200, 9// 2010.

[40] H. Gao, L. Jiao, J. Yang, Z. Qi, Y. Wang, and H. Yuan, "High rate capability of Co-doped LiFePO4/C," *Electrochimica Acta,* vol. 97, pp. 143-149, 2013/05/01/ 2013.

[41] B. Pei, Q. Wang, W. Zhang, Z. Yang, and M. Chen, "Enhanced performance of LiFePO4 through hydrothermal synthesis coupled with carbon coating and cupric ion doping," *Electrochimica Acta,* vol. 56, pp. 5667-5672, 2011/06/30/ 2011.

[42] A. Yamada, Y. Kudo, and K.-Y. Liu, "Phase Diagram of Li x (Mn y Fe1 −y) PO 4 (0 ⩽ x, y ⩽ 1)" *Journal of The Electrochemical Society,* vol. 148, pp. A1153-A1158, October 1, 2001 2001.

[43] J. Ding, Z. Su, and H. Tian, "Synthesis of high rate performance LiFe1−xMnxPO4/C composites for lithium-ion batteries," *Ceramics International,* vol. 42, pp. 12435-12440, 2016/08/01/ 2016.

[44] Y. Lin, B. Zeng, G. Zhao, T. Zhou, M. Chen, X. Mao, *et al.*, *An optimized Mn-doped LiFePO 4/C composite synthesized by carbonthermal reduction technique* vol. 6, 2011.

[45] J. Triwibowo, S. Priyono, R. I. Purawiardi, C. R. Ratri, and E. Suwandi, "Electrochemical performance of LiFe(1-x)MnxPO4 (x = 0, 0.10, 0.15, 0.2) synthesized by solid state process as cathode material for Li-ion battery," *AIP Conference Proceedings,* vol. 1712, p. 050015, 2016/02/24 2016.

[46] T. Nakamura, K. Sakumoto, S. Seki, Y. Kobayashi, M. Tabuchi, and Y. Yamada, "Apparent Diffusion Constant and Electrochemical Reaction in LiFe1 − x Mn x PO4 Olivine Cathodes," *Journal of The Electrochemical Society,* vol. 154, pp. A1118-A1123, December 1, 2007 2007.

[47] Y.-C. Chen, J.-M. Chen, C.-H. Hsu, J.-W. Yeh, H. C. Shih, Y.-S. Chang, *et al.*, "Structure studies on LiMn0.25Fe0.75PO4 by in-situ synchrotron X-ray diffraction analysis," *Journal of Power Sources,* vol. 189, pp. 790-793, 2009/04/01/ 2009.

[48] A. Naik, J. Zhou, C. Gao, G. Liu, and L. Wang, "Rapid and facile synthesis of Mn doped porous LiFePO4/C from iron carbonyl complex," *Journal of the Energy Institute,* vol. 89, pp. 21-29, 2// 2016.

[49] R.-R. Zhao, B.-Y. Lan, H.-Y. Chen, and G.-Z. Ma, "Hydrothermal synthesis and properties of manganese-doped LiFePO4," *Ionics,* vol. 18, pp. 873-879, 2012.

[50] A. Guéguen, L. Castro, R. Dedryvère, E. Dumont, J. Bréger, C. Tessier, *et al.*, "The Electrode/Electrolyte Reactivity of LiFe0.33Mn0.67PO4 Compared to LiFePO4," *Journal of The Electrochemical Society,* vol. 160, pp. A387-A393, January 1, 2013 2013.

[51] Y. Wang, D. Zhang, X. Yu, R. Cai, Z. Shao, X.-Z. Liao, *et al.*, "Mechanoactivation-assisted synthesis and electrochemical characterization of manganese lightly doped LiFePO4," *Journal of Alloys and Compounds,* vol. 492, pp. 675-680, 3/4/ 2010.

[52] C.-C. Yang and W.-H. Chen, "Microsphere LiFe0.5Mn0.5PO4/C composite as high rate and long-life cathode material for lithium-ion battery," *Materials Chemistry and Physics,* vol. 173, pp. 482-490, 2016/04/15/ 2016.

[53] S. Li, X. Meng, Q. Yi, J. A. Alonso, M. T. Fernández-Díaz, C. Sun, *et al.*, "Structural and electrochemical properties of LiMn0.6Fe0.4PO4 as a cathode material for flexible lithium-ion batteries and self-charging power pack," *Nano Energy,* vol. 52, pp. 510-516, 2018/10/01/ 2018.

[54] A. K. Budumuru, M. Viji, A. Jena, B. R. K. Nanda, and C. Sudakar, "Mn substitution controlled Li-diffusion in single crystalline nanotubular LiFePO4 high rate-capability cathodes: Experimental and theoretical studies," *Journal of Power Sources,* vol. 406, pp. 50-62, 2018/12/01/ 2018.

[55] D. Wang, C. Ouyang, T. Drézen, I. Exnar, A. Kay, N.-H. Kwon, *et al.*, "Improving the Electrochemical Activity of LiMnPO4 Via Mn-Site Substitution," *Journal of The Electrochemical Society,* vol. 157, pp. A225-A229, February 1, 2010 2010.

[56] A. Yamada and S.-C. Chung "Crystal Chemistry of the Olivine-Type Li (Mn y Fe1 − y) PO 4 and (Mn y Fe1 − y) PO 4 as Possible 4 V Cathode Materials for Lithium Batteries," *Journal of The Electrochemical Society,* vol. 148, pp. A960-A967, August 1, 2001 2001.

[57] A. Yamada, Y. Kudo, and K.-Y. Liu, "Reaction Mechanism of the Olivine-Type Li x (Mn0.6Fe0.4) PO 4 ($0 \leqslant x \leqslant 1$) " *Journal of The Electrochemical Society,* vol. 148, pp. A747-A754, July 1, 2001 2001.

[58] W. Ojczyk, "Transport and electrochemical properties of cathode materials from the group of transition metals phosphates with olivine structure.," PhD, AGH University of Science and Technology, Cracow, Poland,, 2011.

[59] A. Osnis, M. Kosa, D. Aurbach, and D. T. Major, "Systematic First-Principles Investigation of Mixed Transition Metal Olivine Phosphates LiM1-yM′yPO4 (M/M′ = Mn, Fe, and Co) as Cathode Materials," *The Journal of Physical Chemistry C,* vol. 117, pp. 17919-17926, 2013/09/05 2013.

[60] S. Novikova, S. Yaroslavtsev, V. Rusakov, A. Chekannikov, T. Kulova, A. Skundin, *et al.*, "Behavior of LiFe1−yMnyPO4/C cathode materials upon electrochemical lithium intercalation/deintercalation," *Journal of Power Sources,* vol. 300, pp. 444-452, 12/30/ 2015.

[61] O. A. Drozhzhin, V. D. Sumanov, O. M. Karakulina, A. M. Abakumov, J. Hadermann, A. N. Baranov, *et al.*, "Switching between solid solution and two-phase regimes in the Li1-xFe1-yMnyPO4 cathode materials during lithium (de)insertion: combined PITT, in situ XRPD and electron diffraction tomography study," *Electrochimica Acta,* vol. 191, pp. 149-157, 2/10/ 2016.

[62] R. Malik, F. Zhou, and G. Ceder, "Phase diagram and electrochemical properties of mixed olivines from first-principles calculations," *Physical Review B,* vol. 79, p. 214201, 06/04/ 2009.

[63] F. Zhou, T. Maxisch, and G. Ceder, "Configurational Electronic Entropy and the Phase Diagram of Mixed-Valence Oxides: The Case of Li_{x}FePO_{4}," *Physical Review Letters,* vol. 97, 2006.

[64] P. J. Spencer, "A brief history of CALPHAD," *Calphad,* vol. 32, pp. 1-8, 3// 2008.

[65] M. Hillert, "The compound energy formalism," *Journal of Alloys and Compounds,* vol. 320, pp. 161-176, 5/24/ 2001.

[66] K. Frisk and M. Selleby, "The compound energy formalism: applications," *Journal of Alloys and Compounds,* vol. 320, pp. 177-188, 5/24/ 2001.

[67] M. Hillert, "Partial Gibbs energies from Redlich-Kister polynomials," *Thermochimica Acta,* vol. 129, pp. 71-75, 1988/06/30/ 1988.

[68] T. Abe and T. Koyama, "Thermodynamic modeling of the LiCoO2–CoO2 pseudo-binary system," *Calphad,* vol. 35, pp. 209-218, 2011/06/01/ 2011.

[69] C. C. R. S. Rossi, L. Cardozo-Filho, and R. Guirardello, "Gibbs free energy minimization for the calculation of chemical and phase equilibrium using linear programming," *Fluid Phase Equilibria,* vol. 278, pp. 117-128, 2009/04/15/ 2009.

[70] J. Molenda, W. Ojczyk, and J. Marzec, "Electrical conductivity and reaction with lithium of LiFe1−yMnyPO4 olivine-type cathode materials," *Journal of Power Sources,* vol. 174, pp. 689-694, 2007/12/06/ 2007.

[71] D. H. Snydacker and C. Wolverton, "Transition-Metal Mixing and Redox Potentials in Lix(M1–yM′y)PO4 (M, M′ = Mn, Fe, Ni) Olivine Materials from First-Principles Calculations," *The Journal of Physical Chemistry C,* vol. 120, pp. 5932-5939, 2016/03/24 2016.

[72] J. Kim, K.-Y. Park, I. Park, J.-K. Yoo, J. Hong, and K. Kang, "Thermal stability of Fe-Mn binary olivine cathodes for Li rechargeable batteries," *Journal of Materials Chemistry,* vol. 22, pp. 11964-11970, 2012.

[73] Y. Huang, Y.-C. Lin, D. M. Jenkins, N. A. Chernova, Y. Chung, B. Radhakrishnan, *et al.*, "Thermal Stability and Reactivity of Cathode Materials for Li-Ion Batteries," *ACS Applied Materials & Interfaces,* vol. 8, pp. 7013-7021, 2016/03/23 2016.

[74] G. M. Nolis, F. Omenya, R. Zhang, B. Fang, S. Upreti, N. A. Chernova, *et al.*, "Structure, defects and thermal stability of delithiated olivine phosphates," *Journal of Materials Chemistry,* vol. 22, pp. 20482-20489, 2012.

[75] Y. Huang, J. Fang, F. Omenya, M. O'Shea, N. A. Chernova, R. Zhang, *et al.*, "Understanding the stability of MnPO4," *Journal of Materials Chemistry A,* vol. 2, pp. 12827-12834, 2014.

[76] S.-W. Kim, J. Kim, H. Gwon, and K. Kang, "Phase Stability Study of Li1 − x MnPO4 ($0 \leqslant x \leqslant 1$) Cathode for Li Rechargeable Battery," *Journal of The Electrochemical Society,* vol. 156, pp. A635-A638, August 1, 2009 2009.

[77] J. Kim, K.-Y. Park, I. Park, J.-K. Yoo, D.-H. Seo, S.-W. Kim, *et al.*, "The Effect of Particle Size on Phase Stability of the Delithiated LixMnPO4," *Journal of The Electrochemical Society,* vol. 159, pp. A55-A59, January 1, 2011 2011.

[78] D. Choi, J. Xiao, Y. J. Choi, J. S. Hardy, M. Vijayakumar, M. S. Bhuvaneswari, *et al.*, "Thermal stability and phase transformation of electrochemically charged/discharged LiMnPO4 cathode for Li-ion batteries," *Energy & Environmental Science,* vol. 4, pp. 4560-4566, 2011.

[79] J. Yoshida, S. Nakanishi, H. Iba, H. Abe, and M. Naito, "Thermal Behavior of Delithiated Li1−xMnPO4 ($0 \le x < 1$) Structure for Lithium-Ion Batteries," *International Journal of Applied Ceramic Technology,* vol. 10, pp. 764-772, 2013.

[80] S. K. Martha, O. Haik, E. Zinigrad, I. Exnar, T. Drezen, J. H. Miners, *et al.*, "On the Thermal Stability of Olivine Cathode Materials for Lithium-Ion Batteries," *Journal of The Electrochemical Society,* vol. 158, pp. A1115-A1122, October 1, 2011 2011.

[81] Y. Huang, N. A. Chernova, Q. Yin, Q. Wang, N. F. Quackenbush, M. Leskes, *et al.*, "What Happens to LiMnPO4 upon Chemical Delithiation?," *Inorganic Chemistry,* vol. 55, pp. 4335-4343, 2016/05/02 2016.

[82] A. Yamada, Y. Takei, H. Koizumi, N. Sonoyama, R. Kanno, K. Itoh, *et al.*, "Electrochemical, Magnetic, and Structural Investigation of the Lix(MnyFe1-y)PO4 Olivine Phases," *Chemistry of Materials,* vol. 18, pp. 804-813, 2006.

[83] J. Xiao, N. A. Chernova, S. Upreti, X. Chen, Z. Li, Z. Deng, *et al.*, "Electrochemical performances of LiMnPO4 synthesized from non-stoichiometric Li/Mn ratio," *Physical Chemistry Chemical Physics,* vol. 13, pp. 18099-18106, 2011.

[84] L. F. J. Piper, N. F. Quackenbush, S. Sallis, D. O. Scanlon, G. W. Watson, K. W. Nam, *et al.*, "Elucidating the Nature of Pseudo Jahn–Teller Distortions in LixMnPO4: Combining Density Functional Theory with Soft and Hard X-ray Spectroscopy," *The Journal of Physical Chemistry C,* vol. 117, pp. 10383-10396, 2013/05/23 2013.

[85] C. Delacourt, P. Poizot, M. Morcrette, J. M. Tarascon, and C. Masquelier, "One-Step Low-Temperature Route for the Preparation of Electrochemically Active LiMnPO4 Powders," *Chemistry of Materials,* vol. 16, pp. 93-99, 2004/01/01 2004.

[86] D. Di Lecce, T. Hu, and J. Hassoun, "Electrochemical features of LiMnPO4 olivine prepared by sol-gel pathway," *Journal of Alloys and Compounds,* vol. 693, pp. 730-737, 2017/02/05/ 2017.

[87] K. Zaghib, A. Mauger, and C. M. Julien, "Olivine-Based Cathode Materials," in *Rechargeable Batteries: Materials, Technologies and New Trends*, Z. Zhang and S. S. Zhang, Eds., ed Cham: Springer International Publishing, 2015, pp. 25-65.

[88] M. Yonemura, A. Yamada, Y. Takei, N. Sonoyama, and R. Kanno, "Comparative Kinetic Study of Olivine Li x MPO 4 (M = Fe , Mn)," *Journal of The Electrochemical Society,* vol. 151, pp. A1352-A1356, September 1, 2004 2004.

[89] H.-C. Dinh, S.-i. Mho, Y. Kang, and I.-H. Yeo, "Large discharge capacities at high current rates for carbon-coated LiMnPO4 nanocrystalline cathodes," *Journal of Power Sources,* vol. 244, pp. 189-195, 2013/12/15/ 2013.

[90] M. S. Whittingham, "Ultimate Limits to Intercalation Reactions for Lithium Batteries," *Chemical Reviews,* vol. 114, pp. 11414-11443, 2014/12/10 2014.

[91] M. Pivko, M. Bele, E. Tchernychova, N. Z. Logar, R. Dominko, and M. Gaberscek, "Synthesis of Nanometric LiMnPO4 via a Two-Step Technique," *Chemistry of Materials,* vol. 24, pp. 1041-1047, 2012/03/27 2012.

[92] C. Delacourt, L. Laffont, R. Bouchet, C. Wurm, J.-B. Leriche, M. Morcrette, *et al.*, "Toward Understanding of Electrical Limitations (Electronic, Ionic) in LiMPO4 (M = Fe , Mn) Electrode Materials," *Journal of The Electrochemical Society,* vol. 152, pp. A913-A921, May 1, 2005 2005.

[93] K. Rissouli, K. Benkhouja, J. R. Ramos-Barrado, and C. Julien, "Electrical conductivity in lithium orthophosphates," *Materials Science and Engineering: B,* vol. 98, pp. 185-189, 2003/04/15/ 2003.

[94] Z. X. Nie, C. Y. Ouyang, J. Z. Chen, Z. Y. Zhong, Y. L. Du, D. S. Liu, *et al.*, "First principles study of Jahn–Teller effects in LixMnPO4," *Solid State Communications,* vol. 150, pp. 40-44, 2010/01/01/ 2010.

[95] S.-M. Oh, S.-W. Oh, C.-S. Yoon, B. Scrosati, K. Amine, and Y.-K. Sun, "High-Performance Carbon-LiMnPO4 Nanocomposite Cathode for Lithium Batteries," *Advanced Functional Materials,* vol. 20, pp. 3260-3265, 2010.

[96] V. Aravindan, J. Gnanaraj, Y.-S. Lee, and S. Madhavi, "LiMnPO4 - A next generation cathode material for lithium-ion batteries," *Journal of Materials Chemistry A,* vol. 1, pp. 3518-3539, 2013.

[97] G. Li, H. Azuma, and M. Tohda "LiMnPO4 as the Cathode for Lithium Batteries," *Electrochemical and Solid-State Letters,* vol. 5, pp. A135-A137, June 1, 2002 2002.

[98] G. Chen and T. J. Richardson, "Solid Solution Phases in the Olivine-Type LiMnPO4 / MnPO4 System," *Journal of The Electrochemical Society,* vol. 156, pp. A756-A762, September 1, 2009 2009.

[99] J. Nanda, S. K. Martha, W. D. Porter, H. Wang, N. J. Dudney, M. D. Radin, *et al.*, "Thermophysical properties of LiFePO4 cathodes with carbonized pitch coatings and organic binders: Experiments and first-principles modeling," *Journal of Power Sources,* vol. 251, pp. 8-13, 2014/04/01/ 2014.

[100] S. Loos, D. Gruner, M. Abdel-Hafiez, J. Seidel, R. Hüttl, A. U. B. Wolter, *et al.*, "Heat capacity (Cp) and entropy of olivine-type LiFePO4 in the temperature range (2 to 773)K," *The Journal of Chemical Thermodynamics,* vol. 85, pp. 77-85, 2015/06/01/ 2015.

[101] A. Seifitokaldani, A. E. Gheribi, A. T. Phan, P. Chartrand, and M. Dollé, "Important Variation in Vibrational Properties of LiFePO4 and FePO4 Induced by Magnetism," *Scientific Reports,* vol. 6, p. 33033, 2016.

[102] A. E. Gheribi, A. Seifitokaldani, P. Wu, and P. Chartrand, "An ab initio method for the prediction of the lattice thermal transport properties of oxide systems: Case study of Li2O and K2O," *Journal of Applied Physics,* vol. 118, p. 145101, 2015/10/14 2015.

[103] A. Seifitokaldani, A. E. Gheribi, M. Dollé, and P. Chartrand, "Thermophysical properties of titanium and vanadium nitrides: Thermodynamically self-consistent approach coupled with density functional theory," *Journal of Alloys and Compounds,* vol. 662, pp. 240-251, 2016/03/25/ 2016.

[104] Q. Shi, L. Zhang, M. E. Schlesinger, J. Boerio-Goates, and B. F. Woodfield, "Low temperature heat capacity study of FePO4 and Fe3(P2O7)2," *The Journal of Chemical Thermodynamics,* vol. 62, pp. 35-42, 7// 2013.

[105] W. Bruckner, W. Fuchs, and G. Ritter, "Mössbauer effect in calcinated FePO4 below 26°K," *Physics Letters A,* vol. 26, pp. 32-33, 1967/12/04/ 1967.

[106] V. Beckmann, W. Bruckner, W. Fuchs, G. Ritter, and H. Wegener, "The Measurement of the Anisotropy Constant of Antiferromagnetic FePO4 by Means of the Mössbauer Effect," *physica status solidi (b),* vol. 29, pp. 781-791, 1968/01/01 1968.

[107] M. Thomas and K. George, "Characterisation and magnetic properties of nanocrystalline FePO 4," *Indian Journal of Pure and Applied Physics,* vol. 48, pp. 104-109, 02/01 2010.

[108] I. K. Lee, S. J. Moon, I. Shim, and C. S. Kim, "The Structural Transition and Magnetic Properties of Lithium Deintercalation in LiFePO4," *IEEE Transactions on Magnetics,* vol. 45, pp. 4268-4270, 2009.

[109] G. Rousse, J. Rodriguez-Carvajal, S. Patoux, and C. Masquelier, "Magnetic Structures of the Triphylite LiFePO4 and of Its Delithiated Form FePO4," *Chemistry of Materials,* vol. 15, pp. 4082-4090, 2003/10/01 2003.

[110] V. Palomares, A. Goñi, I. G. d. Muro, L. Lezama, I. d. Meatza, M. Bengoechea*, et al.*, "Near Heterosite Li0.1FePO4 Phase Formation as Atmospheric Aging Product of LiFePO4/C Composite. Electrochemical, Magnetic and EPR Study," *Journal of The Electrochemical Society,* vol. 158, pp. A1042-A1047, September 1, 2011 2011.

[111] R. G. Iyer, C. Delacourt, C. Masquelier, J.-M. Tarascon, and A. Navrotsky, "Energetics of LiFePO4 and Polymorphs of Its Delithiated Form, FePO4," *Electrochemical and Solid-State Letters,* vol. 9, pp. A46-A48, February 1, 2006 2006.

[112] L.-h. He, Z.-w. Zhao, X.-h. Liu, A.-l. Chen, and X.-f. Si, "Thermodynamics analysis of LiFePO4 pecipitation from Li–Fe(II)–P–H2O system at 298 K," *Transactions of Nonferrous Metals Society of China,* vol. 22, pp. 1766-1770, 7// 2012.

[113] A. V. Churikov, A. V. Ivanishchev, A. V. Ushakov, I. M. Gamayunova, and I. A. Leenson, "Thermodynamics of LiFePO4 Solid-Phase Synthesis Using Iron(II) Oxalate and Ammonium Dihydrophosphate as Precursors," *Journal of Chemical & Engineering Data,* vol. 58, pp. 1747-1759, 2013/06/13 2013.

[114] R. Stevens, J. L. Dodd, M. G. Kresch, R. Yazami, B. Fultz, B. Ellis*, et al.*, "Phonons and Thermodynamics of Unmixed and Disordered Li0.6FePO4," *The Journal of Physical Chemistry B,* vol. 110, pp. 22732-22735, 2006/11/01 2006.

[115] G. Kresse and J. Hafner, "Ab initio molecular dynamics for liquid metals," *Physical Review B,* vol. 47, pp. 558-561, 01/01/ 1993.

[116] G. Kresse and J. Hafner, "Ab initio molecular-dynamics simulation of the liquid-metal--amorphous-semiconductor transition in germanium," *Physical Review B,* vol. 49, pp. 14251-14269, 05/15/ 1994.

[117] G. Kresse and J. Furthmüller, "Efficiency of ab-initio total energy calculations for metals and semiconductors using a plane-wave basis set," *Computational Materials Science,* vol. 6, pp. 15-50, 1996/07/01/ 1996.

[118] G. Kresse and J. Furthmüller, "Efficient iterative schemes for ab initio total-energy calculations using a plane-wave basis set," *Physical Review B,* vol. 54, pp. 11169-11186, 10/15/ 1996.

[119] A. Berche, J. C. Tédenac, and P. Jund, "Ab-initio calculations and CALPHAD description of Cr–Ge–Mn and Cr–Ge–Si," *Calphad,* vol. 49, pp. 50-57, 2015/06/01/ 2015.

[120] A. Jain, G. Hautier, S. P. Ong, C. J. Moore, C. C. Fischer, K. A. Persson, *et al.*, "Formation enthalpies by mixing GGA and GGA+U calculations," *Physical Review B*, vol. 84, p. 045115, 07/12/ 2011.

[121] T. Ichitsubo, T. Doi, K. Tokuda, E. Matsubara, T. Kida, T. Kawaguchi, *et al.*, "What determines the critical size for phase separation in LiFePO4 in lithium ion batteries?," *Journal of Materials Chemistry A*, vol. 1, pp. 14532-14537, 2013.

[122] J. Park and J. Lee, "Phase diagram reassessment of Ag–Au system including size effect," *Calphad*, vol. 32, pp. 135-141, 3// 2008.

[123] J. Lee, T. Tanaka, J. Lee, and H. Mori, "Effect of substrates on the melting temperature of gold nanoparticles," *Calphad*, vol. 31, pp. 105-111, 3// 2007.

[124] J. Lee and K. J. Sim, "General equations of CALPHAD-type thermodynamic description for metallic nanoparticle systems," *Calphad*, vol. 44, pp. 129-132, 3// 2014.

[125] G. Garzel, J. Janczak-Rusch, and L. Zabdyr, "Reassessment of the Ag–Cu phase diagram for nanosystems including particle size and shape effect," *Calphad*, vol. 36, pp. 52-56, 3// 2012.

[126] M. Ghasemi, Z. Zanolli, M. Stankovski, and J. Johansson, "Size- and shape-dependent phase diagram of In-Sb nano-alloys," *Nanoscale*, vol. 7, 2015.

[127] N. Meethong, H. Y. S. Huang, S. A. Speakman, W. C. Carter, and Y. M. Chiang, "Strain Accommodation during Phase Transformations in Olivine-Based Cathodes as a Materials Selection Criterion for High-Power Rechargeable Batteries," *Advanced Functional Materials*, vol. 17, pp. 1115-1123, 2007.

[128] A. S. Andersson and J. O. Thomas, "The source of first-cycle capacity loss in LiFePO4," *Journal of Power Sources*, vol. 97–98, pp. 498-502, 7// 2001.

[129] C. Delmas, M. Maccario, L. Croguennec, F. Le Cras, and F. Weill, "Lithium deintercalation in LiFePO4 nanoparticles via a domino-cascade model," *Nat Mater*, vol. 7, pp. 665-671, 08//print 2008.

[130] G. Brunetti, D. Robert, P. Bayle-Guillemaud, J. L. Rouvière, E. F. Rauch, J. F. Martin, *et al.*, "Confirmation of the Domino-Cascade Model by LiFePO4/FePO4 Precession Electron Diffraction," *Chemistry of Materials*, vol. 23, pp. 4515-4524, 2011/10/25 2011.

[131] D. Burch and M. Z. Bazant, "Size-Dependent Spinodal and Miscibility Gaps for Intercalation in Nanoparticles," *Nano Letters*, vol. 9, pp. 3795-3800, 2009/11/11 2009.

[132] P. Bai, D. A. Cogswell, and M. Z. Bazant, "Suppression of Phase Separation in LiFePO4 Nanoparticles During Battery Discharge," *Nano Letters*, vol. 11, pp. 4890-4896, 2011/11/09 2011.

[133] A. T. Phan, A. E. Gheribi, and P. Chartrand, "Modelling of Phase Equilibria of LiFePO4-FePO4 Olivine Join for Cathode Material," *The Canadian Journal of Chemical Engineering*, vol. 0, 2018.

[134] G. Chen, X. Song, and T. J. Richardson, "Electron Microscopy Study of the LiFePO4 to FePO4 Phase Transition," *Electrochemical and Solid-State Letters,* vol. 9, pp. A295-A298, June 1, 2006 2006.

[135] L. Laffont, C. Delacourt, P. Gibot, M. Y. Wu, P. Kooyman, C. Masquelier*, et al.*, "Study of the LiFePO4/FePO4 Two-Phase System by High-Resolution Electron Energy Loss Spectroscopy," *Chemistry of Materials,* vol. 18, pp. 5520-5529, 2006/11/01 2006.

[136] C. V. Ramana, A. Mauger, F. Gendron, C. M. Julien, and K. Zaghib, "Study of the Li-insertion/extraction process in LiFePO4/FePO4," *Journal of Power Sources,* vol. 187, pp. 555-564, 2009.

[137] D. A. Porter, K. E. Easterling, and M. Sherif, *Phase Transformations in Metals and Alloys, Third Edition (Revised Reprint)*: CRC Press, 2009.

[138] H. I. Aaronson, M. Enomoto, and J. K. Lee, *Mechanisms of Diffusional Phase Transformations in Metals and Alloys*: CRC Press, 2010.

[139] D. R. Askeland and W. J. Wright, *The Science and Engineering of Materials*: Cengage Learning, 2016.

[140] J. B. Leriche, S. Hamelet, J. Shu, M. Morcrette, C. Masquelier, G. Ouvrard*, et al.*, "An Electrochemical Cell for Operando Study of Lithium Batteries Using Synchrotron Radiation," *Journal of The Electrochemical Society,* vol. 157, pp. A606-A610, May 1, 2010 2010.

[141] A. Van der Ven, K. Garikipati, S. Kim, and M. Wagemaker, "The Role of Coherency Strains on Phase Stability in Li x FePO4: Needle Crystallites Minimize Coherency Strain and Overpotential," *Journal of The Electrochemical Society,* vol. 156, pp. A949-A957, November 1, 2009 2009.

[142] J. Wang, Y. C. K. Chen Wiegart, and J. Wang, "In operando tracking phase transformation evolution of lithium iron phosphate with hard X-ray microscopy," *Nat Commun,* vol. 5, 08/04/online 2014.

[143] K. Weichert, W. Sigle, P. A. van Aken, J. Jamnik, C. Zhu, R. Amin*, et al.*, "Phase Boundary Propagation in Large LiFePO4 Single Crystals on Delithiation," *Journal of the American Chemical Society,* vol. 134, pp. 2988-2992, 2012/02/15 2012.

[144] D. A. Cogswell and M. Z. Bazant, "Coherency Strain and the Kinetics of Phase Separation in LiFePO4 Nanoparticles," *ACS Nano,* vol. 6, pp. 2215-2225, 2012/03/27 2012.

[145] D. Wang, X. Wu, Z. Wang, and L. Chen, "Cracking causing cyclic instability of LiFePO4 cathode material," *Journal of Power Sources,* vol. 140, pp. 125-128, 2005/01/10/ 2005.

[146] G. Sun, T. Sui, B. Song, H. Zheng, L. Lu, and A. M. Korsunsky, "On the fragmentation of active material secondary particles in lithium ion battery cathodes induced by charge cycling," *Extreme Mechanics Letters,* vol. 9, pp. 449-458, 2016/12/01/ 2016.

[147] Y. Hu, X. Zhao, and Z. Suo, "Averting cracks caused by Insertion reaction In lithium-ion batteries," *Journal of Materials Research,* vol. 25, pp. 1007-1010, Jun 2010 2010.

[148] M. Hess, T. Sasaki, C. Villevieille, and P. Novak, "Combined operando X-ray diffraction-electrochemical impedance spectroscopy detecting solid solution reactions of LiFePO4 in batteries," *Nat Commun,* vol. 6, 09/08/online 2015.

[149] X. Zhang, M. van Hulzen, D. P. Singh, A. Brownrigg, J. P. Wright, N. H. van Dijk, *et al.*, "Rate-Induced Solubility and Suppression of the First-Order Phase Transition in Olivine LiFePO4," *Nano Letters,* vol. 14, pp. 2279-2285, 2014/05/14 2014.

[150] Y. Orikasa, T. Maeda, Y. Koyama, H. Murayama, K. Fukuda, H. Tanida, *et al.*, "Direct Observation of a Metastable Crystal Phase of LixFePO4 under Electrochemical Phase Transition," *Journal of the American Chemical Society,* vol. 135, pp. 5497-5500, 2013/04/17 2013.

[151] S. Pongha, B. Seekoaon, W. Limphirat, P. Kidkhunthod, S. Srilomsak, Y.-M. Chiang, *et al.*, "XANES Investigation of Dynamic Phase Transition in Olivine Cathode for Li-Ion Batteries," *Advanced Energy Materials,* vol. 5, p. 1500663, 2015.

[152] D. B. Ravnsbæk, K. Xiang, W. Xing, O. J. Borkiewicz, K. M. Wiaderek, P. Gionet, *et al.*, "Extended Solid Solutions and Coherent Transformations in Nanoscale Olivine Cathodes," *Nano Letters,* vol. 14, pp. 1484-1491, 2014/03/12 2014.

[153] G. Thomas, R. M. Fulrath, and R. M. Fisher, *Electron Microscopy and Structure of Materials: Proceedings*: University of California Press, 1972.

[154] J. W. Cahn, "On spinodal decomposition in cubic crystals," *Acta Metallurgica,* vol. 10, pp. 179-183, 1962/03/01 1962.

[155] J. W. Cahn, "On spinodal decomposition," *Acta Metallurgica,* vol. 9, pp. 795-801, 9// 1961.

[156] J. W. Cahn, "Coherent fluctuations and nucleation in isotropic solids," *Acta Metallurgica,* vol. 10, pp. 907-913, 10// 1962.

[157] K. T. Wu and K. S. Mendelson, "Spinodal decomposition in the tetragonal system," *The Journal of Chemical Physics,* vol. 58, pp. 2929-2933, 1973.

[158] S. Nambu and M. Oiji, "Coherent Phase Diagram for Spinodal Decomposition in the Tetragonal Titanium Dioxide—Tin Oxide System," *Journal of the American Ceramic Society,* vol. 74, pp. 1910-1915, 1991.

[159] A. H. Schultz, W. R. Bitler, and V. S. Stubican, "Spinodal Decomposition in the Tetragonal System," *physica status solidi (b),* vol. 32, pp. K117-K119, 1969.

[160] A. S. Andersson, B. Kalska, L. Häggström, and J. O. Thomas, "Lithium extraction/insertion in LiFePO4: an X-ray diffraction and Mössbauer spectroscopy study," *Solid State Ionics,* vol. 130, pp. 41-52, 5/1/ 2000.

[161] O. Redlich and A. T. Kister, "Algebraic Representation of Thermodynamic Properties and the Classification of Solutions," *Industrial & Engineering Chemistry,* vol. 40, pp. 345-348, 1948/02/01 1948.

[162] M. Blander and J. Braunstein†, "A quasi-latice model of molten reciprocal salt systems," *Annals of the New York Academy of Sciences,* vol. 79, pp. 838-852, 1960.

[163] M. Blander and S. J. Yosim, "Conformal Ionic Mixtures," *The Journal of Chemical Physics*, vol. 39, pp. 2610-2616, 1963/11/15 1963.

[164] Y. Dessureault and A. D. Pelton, "Contribution to the quasichemical model of reciprocal modelt salt solutions," *Journal de Chimie Physique*, vol. 1991, pp. 1811-1830, 1991.

[165] C. W. Bale, P. Chartrand, S. A. Degterov, G. Eriksson, K. Hack, R. Ben Mahfoud, *et al.*, "FactSage thermochemical software and databases," *Calphad*, vol. 26, pp. 189-228, 6// 2002.

[166] C. W. Bale, E. Bélisle, P. Chartrand, S. A. Decterov, G. Eriksson, K. Hack, *et al.*, "FactSage thermochemical software and databases — recent developments," *Calphad*, vol. 33, pp. 295-311, 6// 2009.

[167] P. Papon, S. L. Schnur, J. Leblond, and P. H. E. Meijer, *The Physics of Phase Transitions: Concepts and Applications*: Springer Berlin Heidelberg, 2013.

[168] C. Reviews, *Condensed Matter Physics: Physics, Condensed matter physics*: Cram101, 2016.

[169] H. Liu, F. C. Strobridge, O. J. Borkiewicz, K. M. Wiaderek, K. W. Chapman, P. J. Chupas, *et al.*, "Capturing metastable structures during high-rate cycling of LiFePO4 nanoparticle electrodes," *Science*, vol. 344, p. 1252817, June 27, 2014 2014.

[170] R. Malik, F. Zhou, and G. Ceder, "Kinetics of non-equilibrium lithium incorporation in LiFePO4," *Nat Mater*, vol. 10, pp. 587-590, 08//print 2011.

[171] T. Sasaki, Y. Ukyo, and P. Novák, "Memory effect in a lithium-ion battery," *Nature Materials*, vol. 12, p. 569, 04/14/online 2013.

[172] K. Jalkanen and M. Karppinen, "Electrochemical Performance and Delithiation/Lithiation Characteristics of Mixed LiFe1-yMyPO4 (M = Co, Ni) Electrode Materials," *Journal of The Electrochemical Society*, vol. 162, pp. A2780-A2788, January 1, 2015 2015.

[173] J. B. Goodenough, "Electrochemical energy storage in a sustainable modern society," *Energy & Environmental Science*, vol. 7, pp. 14-18, 2014.

[174] L. Lu, X. Han, J. Li, J. Hua, and M. Ouyang, "A review on the key issues for lithium-ion battery management in electric vehicles," *Journal of Power Sources*, vol. 226, pp. 272-288, 2013/03/15/ 2013.

[175] A. Eftekhari, "Lithium-Ion Batteries with High Rate Capabilities," *ACS Sustainable Chemistry & Engineering*, vol. 5, pp. 2799-2816, 2017/04/03 2017.

[176] M. Park, X. Zhang, M. Chung, G. B. Less, and A. M. Sastry, "A review of conduction phenomena in Li-ion batteries," *Journal of Power Sources*, vol. 195, pp. 7904-7929, 2010/12/15/ 2010.

[177] A. Eftekhari, "LiFePO4/C nanocomposites for lithium-ion batteries," *Journal of Power Sources*, vol. 343, pp. 395-411, 2017/03/01/ 2017.

[178] J. Wang and X. Sun, "Understanding and recent development of carbon coating on LiFePO4 cathode materials for lithium-ion batteries," *Energy & Environmental Science*, vol. 5, pp. 5163-5185, 2012.

[179] J. Wang, J. Yang, Y. Tang, J. Liu, Y. Zhang, G. Liang, *et al.*, "Size-dependent surface phase change of lithium iron phosphate during carbon coating," *Nat Commun,* vol. 5, 03/05/online 2014.

[180] H. Huang, S.-C. Yin, and L. F. Nazar, "Approaching Theoretical Capacity of LiFePO4 at Room Temperature at High Rates," *Electrochemical and Solid-State Letters,* vol. 4, pp. A170-A172, October 1, 2001 2001.

[181] B. Orvananos, H.-C. Yu, A. Abdellahi, R. Malik, C. P. Grey, G. Ceder, *et al.*, "Kinetics of Nanoparticle Interactions in Battery Electrodes," *Journal of The Electrochemical Society,* vol. 162, pp. A965-A973, January 1, 2015 2015.

[182] W. Dreyer, J. Jamnik, C. Guhlke, R. Huth, J. Moskon, and M. Gaberscek, "The thermodynamic origin of hysteresis in insertion batteries," *Nat Mater,* vol. 9, pp. 448-453, 05//print 2010.

[183] M. R. Roberts, A. Madsen, C. Nicklin, J. Rawle, M. G. Palmer, J. R. Owen, *et al.*, "Direct Observation of Active Material Concentration Gradients and Crystallinity Breakdown in LiFePO4 Electrodes During Charge/Discharge Cycling of Lithium Batteries," *The Journal of Physical Chemistry C,* vol. 118, pp. 6548-6557, 2014/04/03 2014.

[184] X. Liu, D. Wang, G. Liu, V. Srinivasan, Z. Liu, Z. Hussain, *et al.*, "Distinct charge dynamics in battery electrodes revealed by in situ and operando soft X-ray spectroscopy," *Nat Commun,* vol. 4, 10/08/online 2013.

[185] V. Novikov, *Concise Dictionary of Materials Science: Structure and Characterization of Polycrystalline Materials*: CRC Press, 2002.

[186] T. Maxisch and G. Ceder, "Elastic properties of olivine LixFePO4 from first principles," *Physical Review B*, vol. 73, p. 174112, 05/15/ 2006.

[187] J. Jung, M. Cho, and M. Zhou, "Ab initio study of the fracture energy of LiFePO4/FePO4 interfaces," *Journal of Power Sources,* vol. 243, pp. 706-714, 2013.

[188] A. S. Andersson, J. O. Thomas, B. Kalska, and L. Häggström, "Thermal Stability of LiFePO4 - Based Cathodes," *Electrochemical and Solid-State Letters,* vol. 3, pp. 66-68, February 1, 2000 2000.

[189] P. Gibot, M. Casas-cabanas, L. Laffont, S. Levasseur, P. Carlach, S. Hamelet, *et al.*, "Room-temperature single-phase Li insertion/extraction in nanoscale LixFePO4," *Nature Materials,* vol. 7, pp. 741-7, Sep 2008 2008.

[190] G. Chen, X. Song, and T. J. Richardson, "Metastable Solid Solution Phases in the LiFePO4/FePO4 System," *Lawrence Berkeley National Laboratory,* 01-02-2006 2006.

[191] C. Delacourt, J. Rodríguez-Carvajal, B. Schmitt, J.-M. Tarascon, and C. Masquelier, "Crystal chemistry of the olivine-type LixFePO4 system ($0 \leq x \leq 1$) between 25 and 370 °C," *Solid State Sciences,* vol. 7, pp. 1506-1516, 12// 2005.

[192] S.-P. Badi, M. Wagemaker, B. L. Ellis, D. P. Singh, W. J. H. Borghols, W. H. Kan, *et al.*, "Direct synthesis of nanocrystalline Li0.90FePO4: observation of phase segregation of anti-site defects on delithiation," *Journal of Materials Chemistry,* vol. 21, pp. 10085-10093, 2011.

[193] N. Ohmer, B. Fenk, D. Samuelis, C.-C. Chen, J. Maier, M. Weigand, *et al.*, "Phase evolution in single-crystalline LiFePO4 followed by in situ scanning X-ray microscopy of a micrometre-sized battery," *Nat Commun,* vol. 6, 01/20/online 2015.

[194] !!! INVALID CITATION !!! [129, 140].

[195] J. Niu, A. Kushima, X. Qian, L. Qi, K. Xiang, Y.-M. Chiang, *et al.*, "In Situ Observation of Random Solid Solution Zone in LiFePO4 Electrode," *Nano Letters,* vol. 14, pp. 4005-4010, 2014/07/09 2014.

[196] X. N. Xu, G. W. Qin, Y. P. Ren, B. Shen, and W. L. Pei, "Experimental study of the miscibility gap and calculation of the spinodal curves of the Au–Pt system," *Scripta Materialia,* vol. 61, pp. 859-862, 11// 2009.

[197] F. Hofer and P. Warbichler, "Spinodal decomposition in the gold-nickel system," *International journal of materials research = Zeitschrift für Metallkunde,* vol. 76, pp. 11-15, 1985.

[198] S. Kogo and S. Hirosawa, "Thermodynamic assessment and determination of spinodal lines for Al-Zn binary system," presented at the 14th International Conference on Aluminium Alloys, ICAA 2014, Trondheim, Norway, 2014.

[199] T. Kozakai, S. Mizuno, M. Doi, and T. Miyazaki, "Spinodal Decomposition in Liquid-Quenched Co-Cu Alloys," *Journal of the Japan Institute of Metals,* vol. 48, pp. 1138-1143, 1984.

[200] J. B. Liu, L. Zhang, D. W. Yao, and L. Meng, "Microstructure evolution of Cu/Ag interface in the Cu–6wt.% Ag filamentary nanocomposite," *Acta Materialia,* vol. 59, pp. 1191-1197, 2011/02/01/ 2011.

[201] S. Chen, C. Li, Z. Du, C. Guo, and C. Niu, "Overall composition dependences of coherent equilibria," *Calphad,* vol. 37, pp. 65-71, 6// 2012.

[202] J. W. Cahn and F. Larché, "A simple model for coherent equilibrium," *Acta Metallurgica,* vol. 32, pp. 1915-1923, 11// 1984.

[203] Z.-K. Liu and J. Ågren, "On two-phase coherent equilibrium in binary alloys," *Acta Metallurgica et Materialia,* vol. 38, pp. 561-572, 4// 1990.

[204] J. K. Lee and W. Tao, "Coherent phase equilibria: Effect of composition-dependent elastic strain," *Acta Metallurgica et Materialia,* vol. 42, pp. 569-577, 2// 1994.

[205] J. F. Nye, "Elastic Behavior of Single Crystals: Anisotropy A2 - Buschow, K.H. Jürgen," in *Encyclopedia of Materials: Science and Technology (Second Edition)*, R. W. Cahn, M. C. Flemings, B. Ilschner, E. J. Kramer, S. Mahajan, and P. Veyssière, Eds., ed Oxford: Elsevier, 2001, pp. 2415-2422.

[206] Y.-H. Kao, M. Tang, N. Meethong, J. Bai, W. C. Carter, and Y.-M. Chiang, "Overpotential-Dependent Phase Transformation Pathways in Lithium Iron Phosphate Battery Electrodes," *Chemistry of Materials,* vol. 22, pp. 5845-5855, 2010/11/09 2010.

[207] V. Srinivasan and J. Newman, "Existence of Path-Dependence in the LiFePO4 Electrode," *Electrochemical and Solid-State Letters,* vol. 9, pp. A110-A114, March 1, 2006 2006.

[208] L. Gu, C. Zhu, H. Li, Y. Yu, C. Li, S. Tsukimoto, *et al.*, "Direct Observation of Lithium Staging in Partially Delithiated LiFePO4 at Atomic Resolution," *Journal of the American Chemical Society,* vol. 133, pp. 4661-4663, 2011/04/06 2011.

[209] L. Suo, W. Han, X. Lu, L. Gu, Y.-S. Hu, H. Li, *et al.*, "Highly ordered staging structural interface between LiFePO4 and FePO4," *Physical Chemistry Chemical Physics,* vol. 14, pp. 5363-5367, 2012.

[210] C. Zhu, L. Gu, L. Suo, J. Popovic, H. Li, Y. Ikuhara, *et al.*, "Size-Dependent Staging and Phase Transition in LiFePO4/FePO4," *Advanced Functional Materials,* vol. 24, pp. 312-318, 2014.

[211] A. Abdellahi, O. Akyildiz, R. Malik, K. Thornton, and G. Ceder, "The thermodynamic stability of intermediate solid solutions in LiFePO4 nanoparticles," *Journal of Materials Chemistry A,* vol. 4, pp. 5436-5447, 2016.

[212] L. Hong, L. Liang, S. Bhattacharyya, W. Xing, and L. Q. Chen, "Anisotropic Li intercalation in a LixFePO4 nano-particle: a spectral smoothed boundary phase-field model," *Physical Chemistry Chemical Physics,* vol. 18, pp. 9537-9543, 2016.

[213] Y. Honda, S. Muto, K. Tatsumi, H. Kondo, K. Horibuchi, T. Kobayashi, *et al.*, "Microscopic mechanism of path-dependence on charge–discharge history in lithium iron phosphate cathode analysis using scanning transmission electron microscopy and electron energy-loss spectroscopy spectral imaging," *Journal of Power Sources,* vol. 291, pp. 85-94, 9/30/ 2015.

[214] L. Wang, F. Zhou, Y. S. Meng, and G. Ceder, "First-principles study of surface properties of LiFePO4: Surface energy, structure, Wulff shape, and surface redox potential," *Physical Review B,* vol. 76, p. 165435, 10/26/ 2007.

[215] C. A. J. Fisher and M. S. Islam, "Surface structures and crystal morphologies of LiFePO4: relevance to electrochemical behaviour," *Journal of Materials Chemistry,* vol. 18, p. 1209, 2008.

[216] R. Malik, D. Burch, M. Bazant, and G. Ceder, "Particle Size Dependence of the Ionic Diffusivity," *Nano Letters,* vol. 10, pp. 4123-4127, 2010/10/13 2010.

[217] A. Abdellahi, O. Akyildiz, R. Malik, K. Thornton, and G. Ceder, "Particle-size and morphology dependence of the preferred interface orientation in LiFePO4 nano-particles," *Journal of Materials Chemistry A,* vol. 2, pp. 15437-15447, 2014.

[218] S. B. Park, C. K. Park, J. T. Hwang, W. I. Cho, and H. Jang, "Anisotropic lithium ion migration in LiFePO4," *Metals and Materials International,* vol. 17, pp. 1017-1020, 2011/12/01 2011.

[219] Y. Zhu, J. W. Wang, Y. Liu, X. Liu, A. Kushima, Y. Liu, *et al.*, "In Situ Atomic-Scale Imaging of Phase Boundary Migration in FePO4 Microparticles During Electrochemical Lithiation," *Advanced Materials,* vol. 25, pp. 5461-5466, 2013.

[220] H. Gabrisch, J. Wilcox, and M. M. Doeff, "TEM Study of Fracturing in Spherical and Plate-like LiFePO4 Particles," *Electrochemical and Solid-State Letters,* vol. 11, pp. A25-A29, March 1, 2008 2008.

[221] R. Amin, J. Maier, P. Balaya, D. P. Chen, and C. T. Lin, "Ionic and electronic transport in single crystalline LiFePO4 grown by optical floating zone technique," *Solid State Ionics*, vol. 179, pp. 1683-1687, 9/30/ 2008.

[222] Z. Li, Z. Peng, H. Zhang, T. Hu, M. Hu, K. Zhu, *et al.*, "[100]-Oriented LiFePO4 Nanoflakes toward High Rate Li-Ion Battery Cathode," *Nano Letters*, vol. 16, pp. 795-799, 2016/01/13 2016.

[223] S. Kim, V. P. Dravid, and K. He, "In Situ Observation of Structural Change in Single-Crystalline LiFePO4 Nanoflakes during Electrochemical Cycling," *Microscopy and Microanalysis*, vol. 23, pp. 1988-1989, 2017.

[224] Y. Sun, X. Lu, R. Xiao, H. Li, and X. Huang, "Kinetically Controlled Lithium-Staging in Delithiated LiFePO4 Driven by the Fe Center Mediated Interlayer Li–Li Interactions," *Chemistry of Materials*, vol. 24, pp. 4693-4703, 2012/12/21 2012.

[225] K. K. Chawla, *Composite Materials: Science and Engineering*: Springer, 1998.

[226] I. Egry, "The Surface Tension of Binary Alloys: Simple Models for Complex Phenomena," *International Journal of Thermophysics*, vol. 26, pp. 931-939, July 01 2005.

[227] J. A. V. Butler, "The thermodynamics of the surfaces of solutions," *Proceedings of the Royal Society of London. Series A*, vol. 135, pp. 348-375, 1932.

[228] K. T. Ramesh, "Mechanical Properties: Density and Elasticity," in *Nanomaterials: Mechanics and Mechanisms*, K. T. Ramesh, Ed., ed Boston, MA: Springer US, 2009, pp. 95-119.

[229] H. L. Duan, J. Wang, Z. P. Huang, and B. L. Karihaloo, "Size-dependent effective elastic constants of solids containing nano-inhomogeneities with interface stress," *Journal of the Mechanics and Physics of Solids*, vol. 53, pp. 1574-1596, 2005/07/01/ 2005.

[230] H. J. Tan, J. L. Dodd, and B. Fultz, "Thermodynamic and Kinetic Stability of the Solid Solution Phase in Nanocrystalline LixFePO4," *Journal of Physical Chemistry C*, vol. 113, pp. 20527-20530, 2009/12/03 2009.

[231] J. W. Cahn, "A correction to spinodal decomposition in cubic crystals," *Acta Metallurgica*, vol. 12, p. 1457, 12// 1964.

[232] A. T. Phan, A. E. Gheribi, and P. Chartrand, "Modeling of coherent phase transformation and particle size effect in LiFePO4 cathode material and application to the charging/discharging process," *Electrochimica Acta*, vol. 295, pp. 632-644, 2019/02/01/ 2019.

[233] G. Abadias, A. Marty, and B. Gilles, "Influence of epitaxial stress on spinodal decomposition in binary alloys with large size effects: application to the Au–Ni system," *Acta Materialia*, vol. 46, pp. 6403-6419, 1998/11/01/ 1998.

[234] W. B. White, S. M. Johnson, and G. B. Dantzig, "Chemical Equilibrium in Complex Mixtures," *The Journal of Chemical Physics*, vol. 28, pp. 751-755, 1958/05/01 1958.

[235] G. Eriksson, "Thermodynamic Studies of High Temperature Equilibria. III. SOLGAS, a Computer Program for Calculating the Composition and Heat Condition of an Equilibrium Mixture," *Acta Chemica Scandinavica,* vol. 25, pp. 2651-2658, 1971.

[236] G. Eriksson, "Thermodynamic studies of high temperature equilibria. XII. SOLGASMIX, A computer program for calculation of equilibrium compositions in multiphase systems," *Chemica scripta,* vol. 8, pp. 100-103, 1975.

[237] G. Eriksson and W. T. Thompson, "A procedure to estimate equilibrium concentrations in multicomponent systems amd related applications," *Calphad,* vol. 13, pp. 389-400, 1989/10/01/ 1989.

[238] A. E. Gheribi, J. Rogez, and J. C. Mathieu, "Formulation of the integral Gibbs energy of crystalline elements versus temperature and mechanical stress," *Calphad,* vol. 32, pp. 315-319, 6// 2008.

[239] H. Lukas, S. G. Fries, and B. Sundman, *Computational Thermodynamics: The Calphad Method*. Cambridge: Cambridge University Press, 2007.

[240] L. J. van Der Toorn, "Precipitation in gold-platinum alloys—II," *Acta Metallurgica,* vol. 8, pp. 715-727, 1960/10/01 1960.

[241] R. W. Carpenter, "Growth of modulated structure in gold-platinum alloys," *Acta Metallurgica,* vol. 15, pp. 1567-1572, 1967/10/01 1967.

[242] X.-n. Xu, Y.-p. Ren, C.-f. Li, S. Li, and G.-w. Qin, "Thermodynamic assessment of Au–Pt system," *Transactions of Nonferrous Metals Society of China,* vol. 22, pp. 1432-1436, 6// 2012.

[243] V. A. Lubarda, "On the effective lattice parameter of binary alloys," *Mechanics of Materials,* vol. 35, pp. 53-68, 2003/01/01/ 2003.

[244] J. W. Arblaster, "Crystallographic Properties of Platinum," *Platinum Metals Review,* vol. 41, p. 12, 1997.

[245] *AIP Physics Desk Reference,* 3 ed.: Springer-Verlag New York, 2003.

[246] F. Cverna and A. S. M. I. M. P. D. Committee, *ASM Ready Reference: Thermal properties of metals*: ASM International, 2002.

[247] T. Çağın, G. Dereli, M. Uludoğan, and M. Tomak, "Thermal and mechanical properties of some fcc transition metals," *Physical Review B,* vol. 59, pp. 3468-3473, 02/01/ 1999.

[248] S. M. Collard and R. B. McLellan, "High-temperature elastic constants of gold single-crystals," *Acta Metallurgica et Materialia,* vol. 39, pp. 3143-3151, 1991/12/01/ 1991.

[249] Y. A. Chang and L. Himmel, "Temperature Dependence of the Elastic Constants of Cu, Ag, and Au above Room Temperature," *Journal of Applied Physics,* vol. 37, pp. 3567-3572, 1966/08/01 1966.

[250] K. Yun, Y.-H. Cho, P.-R. Cha, J. Lee, H.-S. Nam, J. S. Oh, *et al.*, "Monte Carlo simulations of the structure of Pt-based bimetallic nanoparticles," *Acta Materialia,* vol. 60, pp. 4908-4916, 2012/07/01/ 2012.

[251] R. O. Williams, *Elastic energy and metastable phase equilibria for coherent mixtures in cubic systems*. Oak Ridge, Tenn. :: Dept. of Energy, [Office of Energy Technology], Oak Ridge National Laboratory ;, 1979.

[252] C. M. F. Jantzen and H. Herman, "III - Spinodal Decomposition—Phase Diagram Representation and Occurrence," in *Phase Diagrams: Material Science and Technology, Volume 5*, A. M. Alper, Ed., ed: Academic Press, 1978, pp. 127-184.

[253] J. Nishii, A. Ohtomo, M. Ikeda, Y. Yamada, K. Ohtani, H. Ohno, *et al.*, "High-throughput synthesis and characterization of Mg1−xCaxO films as a lattice and valence-matched gate dielectric for ZnO based field effect transistors," *Applied Surface Science*, vol. 252, pp. 2507-2511, 2006/01/31/ 2006.

[254] M. J. Iedema, N. Kizhakevariam, and J. P. Cowin, "Mixed Oxide Surfaces: Ultrathin Films of CaxMg(1-x)O," *The Journal of Physical Chemistry B*, vol. 102, pp. 693-700, 1998/01/01 1998.

[255] G. Spinolo and U. Anselmi-Tamburini, "Nonequilibrium calcium oxide-magnesium oxide solid solutions produced by chemical decomposition," *The Journal of Physical Chemistry*, vol. 93, pp. 6837-6843, 1989/09/01 1989.

[256] H. D. Li, X. N. Zhang, Z. Zhang, Z. X. Mei, X. L. Du, and Q. K. Xue, "Structure stability of epitaxial MgO-CaO solid-solution films: effect of diffusion," *Journal of Applied Physics*, vol. 101, p. 106102, 2007.

[257] P. Wu, G. Eriksson, and A. D. Pelton, "Critical Evaluation and Optimization of the Thermodynamic Properties and Phase Diagrams of the CaO–FeO, CaO–MgO, CaO–MnO, FeO–MgO, FeO–MnO, and MgO–MnO Systems," *Journal of the American Ceramic Society*, vol. 76, pp. 2065-2075, 1993.

[258] G. Fiquet, P. Richet, and G. Montagnac, "High-temperature thermal expansion of lime, periclase, corundum and spinel," *Physics and Chemistry of Minerals*, vol. 27, pp. 103-111, 1999.

[259] E. S. Hellman and E. H. Hartford, "Epitaxial Solid-Solution Films of Immiscible MgO and CaO," *MRS Online Proceedings Library Archive*, vol. 341, p. 127 (5 pages), 1994.

[260] Q. Fan, C. Chai, Q. Wei, Y. Yang, L. Qiao, Y. Zhao, *et al.*, "Mechanical and electronic properties of Ca1−xMgxO alloys," *Materials Science in Semiconductor Processing*, vol. 40, pp. 676-684, 2015/12/01/ 2015.

[261] A. S. M. Rao and K. Narender, "Studies on Thermophysical Properties of CaO and MgO by -Ray Attenuation," *Journal of Thermodynamics*, vol. 2014, p. 8, 2014.

[262] Y. Sumino, O. L. Anderson, and I. Suzuki, "Temperature coefficients of elastic constants of single crystal MgO between 80 and 1,300 K," *Physics and Chemistry of Minerals*, vol. 9, pp. 38-47, 1983.

[263] D. G. Isaak, O. L. Anderson, and T. Goto, "Measured elastic moduli of single-crystal MgO up to 1800 K," *Physics and Chemistry of Minerals*, vol. 16, pp. 704-713, 1989.

[264] H. Oda, O. L. Anderson, D. G. Isaak, and I. Suzuki, "Measurement of elastic properties of single-crystal CaO up to 1200 K," *Physics and Chemistry of Minerals,* vol. 19, pp. 96-105, 1992.

[265] K. Marklund and S. A. Mahmoud, "Elastic Constants of Magnesium Oxide," *Physica Scripta,* vol. 3, p. 75, 1971.

[266] M. A. Durand, "The Temperature Variation of the Elastic Moduli of NaCl, KCl and MgO," *Physical Review,* vol. 50, pp. 449-455, 09/01/ 1936.

[267] Z.-H. Fang, "Temperature dependence of elastic moduli for MgO and CaO minerals," *Solid State Sciences,* vol. 10, pp. 950-954, 2008/07/01/ 2008.

[268] X. Wu, L. Liu, W. Li, R. Wang, and Q. Liu, "Effect of temperature on elastic constants, generalized stacking fault energy and dislocation cores in MgO and CaO," *Computational Condensed Matter,* vol. 1, pp. 38-44, 12// 2014.

[269] A. Alper, *Phase Diagrams 6-V: Materials Science and Technology*: Elsevier Science, 2012.

[270] G. Rao, J. M. Howe, and P. Wynblatt, "Analysis of the interfacial structure of a twinned variant of Ag precipitate in Cu□Ag alloys," *Scripta Metallurgica et Materialia,* vol. 30, pp. 731-736, 1994/03/15/ 1994.

[271] C. Watanabe, R. Monzen, H. Nagayoshi, and S. Onaka, "Elastic state of rod-shaped Ag precipitates in a Cu−5.7 wt% Ag single crystal," *Philosophical Magazine Letters,* vol. 86, pp. 65-73, 2006/02/01 2006.

[272] E. Shizuya and T. J. Konno, "A Study on Age Hardening in Cu-Ag Alloys by Transmission Electron Microscopy," in *Frontiers in Materials Research,* Y. Fujikawa, K. Nakajima, and T. Sakurai, Eds., ed Berlin, Heidelberg: Springer Berlin Heidelberg, 2008, pp. 217-226.

[273] R. Monzen, K. Murase, H. Nagayoshi, and C. Watanabe, "Discontinuous precipitation in {100} planes in a Cu–5.7 wt% Ag alloy single crystal," *Philosophical Magazine Letters,* vol. 84, pp. 349-358, 2004/06/01 2004.

[274] J. B. Liu and L. Meng, "Phase orientation, interface structure, and properties of aged Cu-6 wt.% Ag," *Journal of Materials Science,* vol. 43, pp. 2006-2011, 2008/03/01 2008.

[275] K. Han, A. A. Vasquez, Y. Xin, and P. N. Kalu, "Microstructure and tensile properties of nanostructured Cu-25wt%Ag," *Acta Materialia,* vol. 51, pp. 767-780, 2003/02/07/ 2003.

[276] K. W. Moon, W. J. Boettinger, U. R. Kattner, F. S. Biancaniello, and C. A. Handwerker, "Experimental and thermodynamic assessment of Sn-Ag-Cu solder alloys," *Journal of Electronic Materials,* vol. 29, pp. 1122-1136, 2000/10/01 2000.

[277] P. R. Subramanian and J. H. Perepezko, "The ag-cu (silver-copper) system," *Journal of Phase Equilibria,* vol. 14, pp. 62-75, 1993/02/01 1993.

[278] A. Wolfenden and M. R. Harmouche, "Elastic constants of silver as a function of temperature," *Journal of Materials Science,* vol. 28, pp. 1015-1018, 1993/01/01 1993.

[279] H. M. Ledbetter and E. R. Naimon, "Elastic Properties of Metals and Alloys. II. Copper," *Journal of Physical and Chemical Reference Data,* vol. 3, pp. 897-935, 1974/10/01 1974.

[280] J. L. Murray, "The Al–Zn (Aluminum-Zinc) system," *Bulletin of Alloy Phase Diagrams*, vol. 4, pp. 55-73, 1983.

[281] J. Lašek, "Resistometrische Untersuchungen über kohärente Phasengleichgewichte in der Mischungslücke von Al-Zn-Legierungen," *physica status solidi (b)*, vol. 5, pp. K117-K120, 1964/01/01 1964.

[282] M. Ohta, F. Hashimoto, and H. Maeda, "Initial Aging of Al–Zn Binary Alloys," *Nippon Kinzoku Gakkaishi*, vol. 32, pp. 1097–1103, 1968.

[283] V. Gerold and W. Merz, "On the decomposition of an aluminum-zinc alloy," *Scripta Metallurgica*, vol. 1, pp. 33-35, 1967/10/01/ 1967.

[284] A. J. Ardell, K. Nuttall, and R. B. Nicholson, "The Decomposition of Concentrated Aluminium-(28–59 pct) Zinc Alloys," in *Inst. Met. Proc. Internat. Symp. on The Mechanism of Phase Transformations in Crystalline Solids*, Manchester, 1968, pp. 22–26.

[285] T. Niklewski, P. Spiegelberg, and K. Sunbulli, "The Solvus Curve for Guinier–Preston Zones in Al–Zn Alloys: A Diffuse X-Ray Study," *Metal Science Journal*, vol. 3, pp. 23-25, 1969/01/01 1969.

[286] M. Murakami, O. Kawano, and Y. Murakami, "On the Determination of the Solvus Temperature for Guinier-Preston Zones in an Al-6.8 at.% Zn Alloy," *Journal of the institute of metals*, vol. 99, pp. 160-163, 1971.

[287] G. Rivaud, J. Guillot, and J. Grilhé, "Determination de la lacune de miscibilite par mesures de resistivite - cas de Al□Zn," *Scripta Metallurgica*, vol. 6, pp. 411-415, 1972/05/01 1972.

[288] M. H. Jacobs, "The Morphology and Crystal Structure of a New Precipitate in Rapidly Quenched Aluminium–Zinc Alloys," *Metal Science Journal*, vol. 6, pp. 143-148, 1972/01/01 1972.

[289] J. M. Pelletier, J. Merlin, and R. Borrelly, "Etude de l'evolution des solutions solides Al□Zn par mesures de pouvoir thermoélectrique," *Materials Science and Engineering*, vol. 33, pp. 95-100, 1978/04/01 1978.

[290] D. Schwahn and W. Schmatz, "Neutron small angle scattering from the alloy Al-Zn above the critical point," *Acta Metallurgica*, vol. 26, pp. 1571-1578, 1978/10/01 1978.

[291] A. Junqua, J. Mimault, and J. Delafond, "Etude des differents domaines de formation des zones G.P. dans le diagramme d'equilibre Al-Zn," *Acta Metallurgica*, vol. 24, pp. 779-787, 1976/08/01/ 1976.

[292] M. Simerská, V. Syneček, and V. Šíma, "Solvus line of the metastable rhombohedral phase in the Al-Zn system for Al-rich alloys," *Czechoslovak Journal of Physics B*, vol. 24, pp. 543-552, 1974.

[293] M. Simerská, V. Šíma, and P. Bartuška, "The formation of rhombohedral phase during the slow cooling of the Al-Zn solid solutions," *Czechoslovak Journal of Physics B*, vol. 24, pp. 654-659, 1974/06/01 1974.

[294] R. Ciach, H. Löffler, J. Salawa, and G. Wendrock, "Modulated structures and position of the coherent spinodal curve in Al–Zn(22 at%)–Cu(x) alloys," *physica status solidi (a),* vol. 53, pp. 441-446, 1979.

[295] R. Kroggel, H. Löffler, and O. Kabisch, "On the position of the coherency spinodal curve in an Al□Zn (18 at.%) alloy," *Kristall und Technik*, vol. 12, pp. 737-742, 1977.

[296] H. Kroggel, H. LÖFfler, and O. Kabisch, "Experimental investigations on the position of the coherency spinodal curve in Al-Zn (15, 16, and 18 at%) Alloys," *physica status solidi (a),* vol. 40, pp. K163-K164, 1977.

[297] W. Truszkowski and J. Dutkiewicz, "Spinodal Decomposition and Discontinuous Precipitation in the Aging of Aluminium-Zinc Alloys Within the Range of Miscibility Gap," *Bull. Acad. Pol. Sci. Ser. Tech.*, vol. 21, pp. 19-24, 1973.

[298] M. Simerská and V. Syneček, "The mechanism of structure transformations in supersaturated Al-Zn alloys," *Acta Metallurgica,* vol. 15, pp. 223-230, 1967/02/01/ 1967.

[299] S. a. Mey, *Zeitschrift für Metallkunde,* vol. 84 pp. 451–455, 1993.

[300] C. Kittel, *Introduction to solid state physics*: Wiley, 1976.

[301] S. Müller, L. W. Wang, A. Zunger, and C. Wolverton, "Coherent phase stability in Al-Zn and Al-Cu fcc alloys: The role of the instability of fcc Zn," *Physical Review B,* vol. 60, pp. 16448-16462, 12/15/ 1999.

[302] P. M. Sutton, "The Variation of the Elastic Constants of Crystalline Aluminum with Temperature between 63\ifmmode^\circ\else\textdegree\fi{}K and 773\ifmmode^\circ\else\textdegree\fi{}K," *Physical Review,* vol. 91, pp. 816-821, 08/15/ 1953.

[303] J. Vallin, M. Mongy, K. Salama, and O. Beckman, "Elastic Constants of Aluminum," *Journal of Applied Physics,* vol. 35, pp. 1825-1826, 1964.

[304] G. N. Kamm and G. A. Alers, "Low-Temperature Elastic Moduli of Aluminum," *Journal of Applied Physics,* vol. 35, pp. 327-330, 1964.

[305] D. Gerlich and E. S. Fisher, "The high temperature elastic moduli of aluminum," *Journal of Physics and Chemistry of Solids,* vol. 30, pp. 1197-1205, 1969/05/01/ 1969.

[306] J. L. Tallon and A. Wolfenden, "Temperature dependence of the elastic constants of aluminum," *Journal of Physics and Chemistry of Solids,* vol. 40, pp. 831-837, 1979/01/01/ 1979.

[307] H. H. Pham, M. E. Williams, P. Mahaffey, M. Radovic, R. Arroyave, and T. Cagin, "Finite-temperature elasticity of fcc Al: Atomistic simulations and ultrasonic measurements," *Physical Review B,* vol. 84, p. 064101, 08/08/ 2011.

[308] B. Magyari-Köpe, G. Grimvall, and L. Vitos, "Elastic anomalies in Ag-Zn alloys," *Physical Review B,* vol. 66, p. 064210, 08/23/ 2002.

[309] J. Nuss, U. Wedig, A. Kirfel, and M. Jansen, "The Structural Anomaly of Zinc: Evolution of Lattice Constants and Parameters of Thermal Motion in the Temperature Range of 40 to 500 K " *Zeitschrift für anorganische und allgemeine Chemie,* vol. 636, pp. 309-313, 2010.

[310] W. D. Callister and D. G. Rethwisch, *Materials Science and Engineering: An Introduction*: Wiley, 2013.

[311] J. Lašek, "über den einfluss der Durchschnittlichen Zusammensetzung auf die Lage der Kohärenten Mischungslücke von Al-Zn Legierungen," *Czechoslovak Journal of Physics*, vol. 15, pp. 848-857, 1965/11/01 1965.

[312] G. A. Andreev and L. G. Buritskova, "Coherent spinodal decomposition of equimolar mixed crystals of NaCl-KCl," *Crystal Research and Technology,* vol. 19, pp. 1085-1092, 1984.

[313] G. A. Andreev and L. G. Buritskova, "Linear growth of two-phase regions during unmixing of NaCl-KCl crystals," *Crystal Research and Technology,* vol. 19, pp. 155-163, 1984.

[314] A. D. Pelton, A. Gabriel, and J. Sangster, "Liquidus measurements and coupled thermodynamic-phase-diagram analysis of the NaCl-KCl system," *Journal of the Chemical Society, Faraday Transactions 1: Physical Chemistry in Condensed Phases,* vol. 81, pp. 1167-1172, 1985.

[315] W. T. Barrett and W. E. Wallace, "Studies of NaCl-KCl Solid Solutions. I. Heats of Formation, Lattice Spacings, Densities, Schottky Defects and Mutual Solubilities1,2," *Journal of the American Chemical Society,* vol. 76, pp. 366-369, 1954/01/01 1954.

[316] P. D. Pathak and N. G. Vasavada, "Thermal expansion of NaCl, KCl and CsBr by X-ray diffraction and the law of corresponding states," *Acta Crystallographica Section A: Foundations of Crystallography,* vol. 26, pp. 655-658, 1970.

[317] O. D. Slagle and H. A. McKinstry, "Temperature Dependence of the Elastic Constants of the Alkali Halides. I. NaCl, KCl, and KBr," *Journal of Applied Physics,* vol. 38, pp. 437-446, 1967/02/01 1967.

[318] J. T. Lewis, A. Lehoczky, and C. V. Briscoe, "Elastic Constants of the Alkali Halides at 4.2 K," *Physical Review,* vol. 161, pp. 877-887, 09/15/ 1967.

[319] A. A. Botaki, I. N. Gyrbu, M. S. Ivankina, É. V. Pozdeeva, and A. V. Sharko, "Temperature dependence of the elastic constants of a KCl-NaCl solid solution," *Soviet Physics Journal,* vol. 16, pp. 1441-1443, 1973/10/01 1973.

[320] W. C. Overton and R. T. Swim, "The Adiabatic Elastic Constants of Rock Salt," *Physical Review,* vol. 84, pp. 758-762, 11/15/ 1951.

[321] F. C. Rose, "The Variation of the Adiabatic Elastic Moduli of Rocksalt with Temperature Between 80K and 270K," *Physical Review,* vol. 49, pp. 50-54, 01/01/ 1936.

[322] L. Hunter, "The Variation with Temperature of the Principal Elastic Moduli of NaCl near the Melting Point," *Physical Review,* vol. 61, pp. 84-90, 01/01/ 1942.

[323] S. Yamamoto, I. Ohno, and O. L. Anderson, "High temperature elasticity of sodium chloride," *Journal of Physics and Chemistry of Solids,* vol. 48, pp. 143-151, 1987/01/01/ 1987.

[324] S. Yamamoto and O. L. Anderson, "Elasticity and anharmonicity of potassium chloride at high temperature," *Physics and Chemistry of Minerals,* vol. 14, pp. 332-340, May 01 1987.

[325] L. Benckert and G. Bäckström, "Elastic Constants of KCl and NaCl from Brillouin Scattering," *Physica Scripta,* vol. 11, p. 43, 1975.

[326] V. S. Urusov, T. G. Petrova, E. V. Leonenko, and N. N. Eremin, "A computer simulation of halite-sylvite (NaCl-KCl) solid solution local structure, properties, and stability," *Moscow University Geology Bulletin,* vol. 62, pp. 117-122, 2007/04/01 2007.

[327] O. L. Anderson and D. G. Isaak, "Elastic Constants of Mantle Minerals at High Temperature," in *Mineral Physics & Crystallography: A Handbook of Physical Constants,* ed: American Geophysical Union, 2013, pp. 64-97.

[328] A. Vijay and T. S. Verma, "Analysis of temperature dependence of elastic constants and bulk modulus for ionic solids," *Physica B: Condensed Matter,* vol. 291, pp. 373-378, 2000/09/01/ 2000.

[329] L. M. Thomas and J. Shanker, "Temperature dependence of elastic constants and thermal expansion coefficient for NaCl crystals," *physica status solidi (b),* vol. 195, pp. 361-366, 1996.

[330] S.-C. Kim and T. H. Kwon, "Temperature variation of elastic constants of NaCl," *Physical Review B,* vol. 45, pp. 2105-2112, 02/01/ 1992.

[331] S. K. Srivastava and S. K. Sharma, "Elastic constants for NaCl and KCl solids at high temperatures," *Journal of Physics and Chemistry of Solids,* vol. 68, pp. 1648-1651, 2007/09/01/ 2007.

[332] R. G. Wolfson, W. Kobes, and M. E. Fine, "Precipitation in NaCl-KCl Mixed Crystals," *Journal of Applied Physics,* vol. 37, pp. 704-712, 1966.

[333] Y. Fukano, "Study on Precipitation Phenomena in Thin Films of Supersaturated Gold-Nickel Alloy," *Journal of the Physical Society of Japan,* vol. 16, pp. 1195-1204, 1961/06/15 1961.

[334] J. E. Woodilla and B. L. Averbach, "Modulated structures in Au□Ni alloys," *Acta Metallurgica,* vol. 16, pp. 255-263, 1968/02/01/ 1968.

[335] R. Sinclair, R. Gronsky, and G. Thomas, "Optical diffraction from lattice images of alloys," *Acta Metallurgica,* vol. 24, pp. 789-796, 1976/09/01/ 1976.

[336] R. Gronsky and G. Thomas, "Electron microscopy of spinodal structures at high resolution," *AIP Conference Proceedings,* vol. 53, pp. 266-268, 1979/07/01 1979.

[337] D. J. H. Cockayne and R. Gronsky, "Lattice fringe imaging of modulated structures," *Philosophical Magazine A,* vol. 44, pp. 159-175, 1981/07/01 1981.

[338] C. K. Wu, "Lattice Imaging of One-Dimensional Spinodal Decomposition in Au-Ni Alloys," *Transactions of the Japan Institute of Metals,* vol. 25, pp. 663-671, 1984.

[339] J.-C. Zhao and M. R. Notis, "Ordering transformation and spinodal decomposition in Au-Ni alloys," *Metallurgical and Materials Transactions A,* vol. 30, pp. 707-716, 1999/03/01 1999.

[340] B. Golding and S. C. Moss, "A re-calculation of the gold-nickel spinodal," *Acta Metallurgica,* vol. 15, pp. 1239-1241, 1967/07/01/ 1967.

[341] J. Wang, X.-G. Lu, B. Sundman, and X. Su, "Thermodynamic assessment of the Au–Ni system," *Calphad,* vol. 29, pp. 263-268, 12// 2005.

[342] A. E. Gheribi, J. Rogez, and J. C. Mathieu, "Magnetic contribution to the Gibbs energy of elements versus temperature and pressure," *Journal of Physics and Chemistry of Solids,* vol. 67, pp. 1719-1723, 2006/08/01/ 2006.

[343] J. R. Neighbours, F. W. Bratten, and C. S. Smith, "The Elastic Constants of Nickel," *Journal of Applied Physics,* vol. 23, pp. 389-393, 1952.

[344] M. Yamamoto, "The Elastic Constants of Nickel Single Crystals," *Journal of the Japan Institute of Metals,* vol. 6, pp. 331-338, 1942.

[345] G. A. Alers, J. R. Neighbours, and H. Sato, "Temperature dependent magnetic contributions to the high field elastic constants of nickel and an Fe-Ni alloy," *Journal of Physics and Chemistry of Solids,* vol. 13, pp. 40-55, 1960/05/01/ 1960.

[346] T. Çagin and B. M. Pettitt, "Elastic constants of nickel: Variations with respect to temperature and pressure," *Physical Review B,* vol. 39, pp. 12484-12491, 06/15/ 1989.

[347] F. Luo, X.-R. Chen, L.-C. Cai, and Q. Wu, "Thermoelastic properties of nickel from molecular dynamic simulations," *Journal of Atomic and Molecular Sciences,* vol. 2, pp. 10-19, 2011.

[348] B. Golding, S. C. Moss, and B. L. Averbach, "Composition and Pressure Dependence of the Elastic Constants of Gold-Nickel Alloys," *Physical Review,* vol. 158, pp. 637-646, 06/15/ 1967.

[349] J. R. Clinton, E. H. Tyler, and H. L. Luo, "Electrical and magnetic properties of Au-Ni alloys," *Journal of Physics F: Metal Physics,* vol. 4, p. 1162, 1974.

[350] A. F. Crawley and D. J. Fabian, *Journal of the Institute of Metals,* vol. 94, pp. 39-40, 1966.

[351] J. M. Leger, C. Loriers-Susse, and B. Vodar, "Pressure Effect on the Curie Temperatures of Transition Metals and Alloys," *Physical Review B,* vol. 6, pp. 4250-4261, 12/01/ 1972.

[352] Y. Shoaib Mohammed, Y. Yan, H. Wang, K. Li, and X. Du, "Stability of Ferromagnetism in Fe, Co, and Ni Metals under High Pressure with GGA and GGA+U," *Journal of Magnetism and Magnetic Materials,* vol. 322, pp. 653-657, 2010/03/01/ 2010.

[353] W. M. C. Yang, PhD, Northwestern University, Evanston, Illinois, 1971.

[354] E. Du Trémolet de Lacheisserie, U. J. Fourier, D. Gignoux, and M. Schlenker, *Magnetism*: Springer, 2005.

[355] R. Asai, S. Ota, T. Namazu, T. Takenobu, T. Koyama, and D. Chiba, "Stress-induced large anisotropy field modulation in Ni films deposited on a flexible substrate," *Journal of Applied Physics,* vol. 120, p. 083906, 2016.

[356] D. Sander, "The correlation between mechanical stress and magnetic anisotropy in ultrathin films," *Reports on Progress in Physics,* vol. 62, pp. 809-858, 1999/01/01 1999.

[357] J.-H. Shim, H.-J. L. Voigt, and B. D. Wirth, "Temperature dependent dislocation bypass mechanism for coherent precipitates in Cu–Co alloys," *Acta Materialia*, vol. 110, pp. 276-282, 2016/05/15/ 2016.

[358] D. Watanabe, C. Watanabe, and R. Monzen, "Coarsening Behavior of Co Precipitates in Cu-Co Alloys," *Metallurgical and Materials Transactions A*, vol. 39, pp. 725-732, 2008/04/01 2008.

[359] V. A. Phillips, "Electron microscope observations on moiré fringes and interfacial dislocations at cobalt precipitates in copper," *Acta Metallurgica*, vol. 14, pp. 271-278, 1966/03/01/ 1966.

[360] Z. C. Li, H. Abe, M. Ishikawa, and N. Sekimura, "Effects of Ion Irradiation on Coherency of Precipitates in Cu-Co Alloy," *MATERIALS TRANSACTIONS*, vol. 46, pp. 1783-1785, 2005.

[361] M. Takeda, K. Inukai, N. Suzuki, G. Shinohara, and H. Hashimoto, "Precipitation Behaviour of Cu□Co Alloys," *physica status solidi (a)*, vol. 158, pp. 39-46, 1996.

[362] M. Takeda, N. Suzuki, G. Shinohara, T. Endo, and J. v. Landuyt, "TEM Study on Precipitation Behavior in Cu–Co Alloys," *physica status solidi (a)*, vol. 168, pp. 27-35, 1998.

[363] H. P. Degischer, "Diffraction contrast from coherent precipitates in elastically-anisotropic materials," *The Philosophical Magazine: A Journal of Theoretical Experimental and Applied Physics*, vol. 26, pp. 1137-1151, 1972/11/01 1972.

[364] Y. Tomokiyo, S. Matsumuras, and M. Toyohara, "Strain Contrast of Coherent Precipitates in Cu-Co Alloys under Excitation of High Order Reflections," *Journal of Electron Microscopy*, vol. 34, pp. 338-346, 1985.

[365] S. Matsumura, Y. Seno, Y. Tomokiyo, K. Oki, and T. Eguchi, "Precipitation Behavior in a Cu-4.5 wt%Co Alloy," *Japanese Journal of Applied Physics*, vol. 20, p. L605, 1981.

[366] T. Nishizawa and K. Ishida, "The Co−Cu (Cobalt-Copper) system," *Bulletin of Alloy Phase Diagrams*, vol. 5, pp. 161-165, 1984/04/01 1984.

[367] C. P. Wang, X. J. Liu, I. Ohnuma, R. Kainuma, and K. Ishida, "Thermodynamic assessments of the Cu–Mn–X (X: Fe, Co) systems," *Journal of Alloys and Compounds*, vol. 438, pp. 129-141, 2007/07/12/ 2007.

[368] J. R. Cerda, P. L. d. Andres, A. Cebollada, R. Miranda, E. Navas, P. Schuster, *et al.*, "Epitaxial growth of cobalt films on Cu(100): a crystallographic LEED determination," *Journal of Physics: Condensed Matter*, vol. 5, p. 2055, 1993.

[369] B. Strauss, F. Frey, W. Petry, J. Trampenau, K. Nicolaus, S. M. Shapiro, *et al.*, "Martensitic phase transformation and lattice dynamics of fcc cobalt," *Physical Review B*, vol. 54, pp. 6035-6038, 09/01/ 1996.

[370] J. Gump, H. Xia, M. Chirita, R. Sooryakumar, M. A. Tomaz, and G. R. Harp, "Elastic constants of face-centered-cubic cobalt," *Journal of Applied Physics*, vol. 86, pp. 6005-6009, 1999/12/01 1999.

[371] B. W. Bennett and G. W. Shannette, "Single crystal elastic constants of cobalt-aluminum face centered cubic alloys," *Acoustics Letters,* vol. 4, pp. 99-104, 1980.

[372] G. Grimvall, *Thermophysical Properties of Materials*: Elsevier Science, 1999.

[373] X. Y. Lu, C. D. Cao, M. Kolbe, B. Wei, and D. M. Herlach, "Microstructure analysis of Co–Cu alloys undercooled prior to solidification," *Materials Science and Engineering: A,* vol. 375-377, pp. 1101-1104, 2004/07/01/ 2004.

[374] C. D. Cao, T. Letzig, G. P. Görler, and D. M. Herlach, "Liquid phase separation in undercooled Co–Cu alloys processed by electromagnetic levitation and differential thermal analysis," *Journal of Alloys and Compounds,* vol. 325, pp. 113-117, 2001/07/26/ 2001.

[375] C. D. Cao, G. P. Görler, D. M. Herlach, and B. Wei, "Liquid–liquid phase separation in undercooled Co–Cu alloys," *Materials Science and Engineering: A,* vol. 325, pp. 503-510, 2002/02/28/ 2002.

[376] A. Munitz, A. Venkert, P. Landau, M. J. Kaufman, and R. Abbaschian, "Microstructure and phase selection in supercooled copper alloys exhibiting metastable liquid miscibility gaps," *Journal of Materials Science,* vol. 47, pp. 7955-7970, 2012/12/01 2012.

[377] M. Minakshi, P. Singh, D. Appadoo, and D. E. Martin, "Synthesis and characterization of olivine LiNiPO4 for aqueous rechargeable battery," *Electrochimica Acta,* vol. 56, pp. 4356-4360, 2011.

[378] O. L. Bacq, A. Pasturel, and O. Bengone, "Impact on electronic correlations on the structural stability, magnetism, and voltage of LiCoPO4 battery," *Physical Review B,* vol. 69, p. 245107, 06/17/ 2004.

[379] J. Molenda, W. Ojczyk, K. Świerczek, W. Zając, F. Krok, J. Dygas, *et al.*, "Diffusional mechanism of deintercalation in LiFe1-yMnyPO4 cathode material," *Solid State Ionics,* vol. 177, pp. 2617-2624, 10/31/ 2006.

[380] R. Gupta, S. Saha, M. Tomar, V. K. Sachdev, and V. Gupta, "Effect of manganese doping on conduction in olivine LiFePO4," *Journal of Materials Science: Materials in Electronics,* vol. 28, pp. 5192-5199, 2017/04/01 2017.

[381] C. Li, N. Hua, C. Wang, X. Kang, W. Tuerdi, and Y. Han, "Effect of Mn2+-doping in LiFePO4 and the low temperature electrochemical performances," *Journal of Alloys and Compounds,* vol. 509, pp. 1897-1900, 2/3/ 2011.

[382] P. F. Xiao, B. Ding, M. O. Lai, and L. Lu, "High Performance LiMn1−xFexPO4 (0 ≤ x ≤ 1) Synthesized via a Facile Polymer-Assisted Mechanical Activation," *Journal of The Electrochemical Society,* vol. 160, pp. A918-A926, January 1, 2013 2013.

[383] A. M. Hashambhoy and J. F. Whitacre, "Li Diffusivity and Phase Change in LiFe0.5Mn0.5PO4: AComparative Study using Galvanostatic Intermittent Titrationand Cyclic Voltammetry," *Journal of The Electrochemical Society,* vol. 158, pp. A390-A395, April 1, 2011 2011.

[384] G. Li, H. Azuma, and M. Tohda "Optimized LiMn y Fe1 − y PO 4 as the Cathode for Lithium Batteries," *Journal of The Electrochemical Society,* vol. 149, pp. A743-A747, June 1, 2002 2002.

[385] R. Amisse, S. Hamelet, D. Hanzel, M. Courty, R. Dominko, and C. Masquelier, "Nonstochiometry in LiFe0.5Mn0.5PO4: Structural and Electrochemical Properties," *Journal of The Electrochemical Society,* vol. 160, pp. A1446-A1450, January 1, 2013 2013.

[386] G. Li, Y. Kudo, K.-Y. Liu, H. Azuma, and M. Tohda, "X-Ray Absorption Study of Li x Mn y Fe1 − y PO 4 (0 ⩽ x ⩽ 1 , 0 < y ⩽ 1) " *Journal of The Electrochemical Society,* vol. 149, pp. A1414-A1418, November 1, 2002 2002.

[387] T. Nakamura, Y. Miwa, M. Tabuchi, and Y. Yamada, "Structural and Surface Modifications of LiFePO4 Olivine Particles and Their Electrochemical Properties," *Journal of The Electrochemical Society,* vol. 153, pp. A1108-A1114, June 1, 2006 2006.

[388] L. Esmezjan, D. Mikhailova, M. Etter, J. Cabana, C. P. Grey, S. Indris, *et al.*, "Electrochemical Lithium Extraction and Insertion Process of Sol-Gel Synthesized LiMnPO4 via Two-Phase Mechanism," *Journal of The Electrochemical Society,* vol. 166, pp. A1257-A1265, January 1, 2019 2019.

[389] X. Y. Li, B. Zhang, Z. G. Zhang, L. H. He, H. Li, X. J. Huang, *et al.*, "Crystallographic structure of LiFe1−x Mn x PO4 solid solutions studied by neutron powder diffraction," *Powder Diffraction,* vol. 29, pp. 248-253, 2014.

[390] R. J. Clément, A. J. Pell, D. S. Middlemiss, F. C. Strobridge, J. K. Miller, M. S. Whittingham, *et al.*, "Spin-Transfer Pathways in Paramagnetic Lithium Transition-Metal Phosphates from Combined Broadband Isotropic Solid-State MAS NMR Spectroscopy and DFT Calculations," *Journal of the American Chemical Society,* vol. 134, pp. 17178-17185, 2012/10/17 2012.

[391] M. Bini, M. C. Mozzati, P. Galinetto, D. Capsoni, S. Ferrari, M. S. Grandi, *et al.*, "Structural, spectroscopic and magnetic investigation of the LiFe1−xMnxPO4 (x=0–0.18) solid solution," *Journal of Solid State Chemistry,* vol. 182, pp. 1972-1981, 2009/07/01/ 2009.

[392] G. R. Gardiner and M. S. Islam, "Anti-Site Defects and Ion Migration in the LiFe0.5Mn0.5PO4 Mixed-Metal Cathode Material," *Chemistry of Materials,* vol. 22, pp. 1242-1248, 2010/02/09 2010.

[393] M. Hillert and J. Ågren, "On the definitions of paraequilibrium and orthoequilibrium," *Scripta Materialia,* vol. 50, pp. 697-699, 2004/03/01/ 2004.

[394] M. Hillert and J. Ågren, "Reply to comments on “On the definition of paraequilibrium and orthoequilibrium”," *Scripta Materialia,* vol. 52, pp. 87-88, 2005/01/01/ 2005.

[395] A. D. Pelton, "9 - Paraequilibrium Phase Diagrams and Minimum Gibbs Energy Diagrams," in *Phase Diagrams and Thermodynamic Modeling of Solutions,* A. D. Pelton, Ed., ed Amsterdam: Elsevier, 2019, pp. 149-158.

[396] G. M. Michal, F. Ernst, and A. H. Heuer, "Carbon paraequilibrium in austenitic stainless steel," *Metallurgical and Materials Transactions A,* vol. 37, pp. 1819-1824, 2006/06/01 2006.

[397] D. B. Ravnsbaek, K. Xiang, W. Xing, O. J. Borkiewicz, K. Wiaderek, P. J. Chupas, *et al.*, "In-Situ Study of Electrochemically-Driven Phase Transitions in LiMnyFe1-YPO4," *Meeting Abstracts,* vol. MA2013-02, p. 255, October 27, 2013 2013.

[398] N. Hua, C. Wang, X. Kang, T. Wumair, and Y. Han, "Studies of V doping for the LiFePO4-based Li Ion batteries," *Journal of Alloys and Compounds,* vol. 503, pp. 204-208, 7/30/ 2010.

[399] K. T. Lee and K. S. Lee, "Electrochemical properties of LiFe0.9Mn0.1PO4/Fe2P cathode material by mechanical alloying," *Journal of Power Sources,* vol. 189, pp. 435-439, 4/1/ 2009.

[400] S.-Y. Chung, S.-Y. Choi, T. Yamamoto, and Y. Ikuhara, "Atomic-Scale Visualization of Antisite Defects in LiFePO4," *Physical Review Letters,* vol. 100, p. 125502, 03/26/ 2008.

[401] S.-Y. Chung, S.-Y. Choi, T. Yamamoto, and Y. Ikuhara, "Orientation-Dependent Arrangement of Antisite Defects in Lithium Iron(II) Phosphate Crystals," *Angewandte Chemie International Edition,* vol. 48, pp. 543-546, 2009/01/05 2009.

[402] K.-Y. Park, I. Park, H. Kim, H.-d. Lim, J. Hong, J. Kim, *et al.*, "Anti-Site Reordering in LiFePO4: Defect Annihilation on Charge Carrier Injection," *Chemistry of Materials,* vol. 26, pp. 5345-5351, 2014/09/23 2014.

[403] J. Chen and J. Graetz, "Study of Antisite Defects in Hydrothermally Prepared LiFePO4 by in Situ X-ray Diffraction," *ACS Applied Materials & Interfaces,* vol. 3, pp. 1380-1384, 2011/05/25 2011.

[404] K. Hoang and M. Johannes, "Tailoring Native Defects in LiFePO4: Insights from First-Principles Calculations," *Chemistry of Materials,* vol. 23, pp. 3003-3013, 2011/06/14 2011.

[405] G. Liang, K. Park, J. Li, R. E. Benson, D. Vaknin, J. T. Markert, *et al.*, "Anisotropy in magnetic properties and electronic structure of single-crystal $\mathrm{Li}\mathrm{Fe}\mathrm{P}{\mathrm{O}}_{4}$," *Physical Review B,* vol. 77, p. 064414, 02/12/ 2008.

[406] R. P. Santoro and R. E. Newnham, "Antiferromagnetism in LiFePO4," *Acta Crystallographica,* vol. 22, pp. 344-347, 1967.

[407] J. G. Creer and G. J. Troup, "The magnetic susceptibility of LiFePO4 and LiCoPO4," *Physics Letters A,* vol. 32, pp. 439-440, 1970/08/24/ 1970.

[408] C. M. Julien, K. Zaghib, A. Mauger, and H. Groult, "Enhanced Electrochemical Properties of LiFePO4 as Positive Electrode of Li-Ion Batteries for HEV Application," *Advances in Chemical Engineering and Science*, vol. 2, pp. 321-329, 2012.

[409] T. Gallien, H. Krenn, R. Fischer, S. Lauterbach, B. Schweighofer, and H. Wegleiter, "Magnetism Versus LiFePO4 Battery's State of Charge: A Feasibility Study for Magnetic-Based Charge Monitoring," *IEEE Transactions on Instrumentation and Measurement,* vol. 64, pp. 2959-2964, 2015.

[410] P. Tang and N. Holzwarth, "Electronic structure of FePO4, LiFePO4, and related materials," *Physical Review B,* vol. 68, 2003.

[411] P. Jozwiak, J. Garbarczyk, F. Gendron, A. Mauger, and C. M. Julien, "Disorder in LixFePO4: From glasses to nanocrystallites," *Journal of Non-Crystalline Solids,* vol. 354, pp. 1915-1925, 4/1/ 2008.

[412] N.-H. Kwon, T. Drezen, I. Exnar, I. Teerlinck, M. Isono, and M. Graetzel, "Enhanced Electrochemical Performance of Mesoparticulate LiMnPO4 for Lithium Ion Batteries," *Electrochemical and Solid-State Letters,* vol. 9, pp. A277-A280, June 1, 2006 2006.

[413] S. K. Martha, B. Markovsky, J. Grinblat, Y. Gofer, O. Haik, E. Zinigrad, *et al.*, "LiMnPO4 as an Advanced Cathode Material for Rechargeable Lithium Batteries," *Journal of The Electrochemical Society,* vol. 156, pp. A541-A552, July 1, 2009 2009.

[414] P. E. Blöchl, "Projector augmented-wave method," *Physical Review B,* vol. 50, pp. 17953-17979, 12/15/ 1994.

[415] G. Kresse and D. Joubert, "From ultrasoft pseudopotentials to the projector augmented-wave method," *Physical Review B,* vol. 59, pp. 1758-1775, 01/15/ 1999.

[416] J. P. Perdew, K. Burke, and M. Ernzerhof, "Generalized Gradient Approximation Made Simple," *Physical Review Letters,* vol. 77, pp. 3865-3868, 10/28/ 1996.

[417] J. P. Perdew, K. Burke, and M. Ernzerhof, "Generalized Gradient Approximation Made Simple [Phys. Rev. Lett. 77, 3865 (1996)]," *Physical Review Letters,* vol. 78, pp. 1396-1396, 02/17/ 1997.

[418] L. Wang, T. Maxisch, and G. Ceder, "Oxidation energies of transition metal oxides within the GGA+U framework," *Physical Review B,* vol. 73, p. 195107, 05/04/ 2006.

[419] A. E. Gheribi and P. Chartrand, "Thermal Conductivity of Compounds Present in the Side Ledge in Aluminium Electrolysis Cells," *JOM,* vol. 69, pp. 2412-2417, 2017/11/01 2017.

[420] L. Lethole, H. Chauke, and P. Ngoepe, *Structural, electronic and mechanical stability of olivine LiMPO4 (M: Mn, Fe,Co)*, 2013.

[421] N. L. Lethole, "Computer Modelling Studies of MPO4, LiMPO4 and NaMPO4 (M: Fe, Co, Mn) Polymorphs," Doctor of Philosophy (PhD) in Physics, Faculty of Science and Agriculture _ School of Physical and Mineral Sciences, University of Limpopo, 2016.

[422] A. G. Every and A. K. McCurdy, "Second and Higher Order Elastic Constants · 84K1 - 90Z1: Datasheet from Landolt-Börnstein - Group III Condensed Matter · Volume 29A: "Second and Higher Order Elastic Constants" in SpringerMaterials (https://doi.org/10.1007/10046537_86)," D. F. Nelson, Ed., ed: Springer-Verlag Berlin Heidelberg.

[423] D. S. Middlemiss, A. J. Ilott, R. J. Clément, F. C. Strobridge, and C. P. Grey, "Density Functional Theory-Based Bond Pathway Decompositions of Hyperfine Shifts: Equipping Solid-State NMR to Characterize Atomic Environments in Paramagnetic Materials," *Chemistry of Materials,* vol. 25, pp. 1723-1734, 2013/05/14 2013.

[424] J. Chen, M. J. Vacchio, S. Wang, N. Chernova, P. Y. Zavalij, and M. S. Whittingham, "The hydrothermal synthesis and characterization of olivines and related compounds for electrochemical applications," *Solid State Ionics,* vol. 178, pp. 1676-1693, 2008/01/15/ 2008.

[425] A. Yamada, M. Hosoya, S.-C. Chung, Y. Kudo, K. Hinokuma, K.-Y. Liu, *et al.*, "Olivine-type cathodes: Achievements and problems," *Journal of Power Sources*, vol. 119-121, pp. 232-238, 2003/06/01/ 2003.

[426] T.-F. Yi, Z.-K. Fang, Y. Xie, Y.-R. Zhu, and C. Dai, "Band structure analysis on olivine LiMPO4 and delithiated MPO4 (M=Fe, Mn) cathode materials," *Journal of Alloys and Compounds*, vol. 617, pp. 716-721, 12/25/ 2014.

[427] N. D. Trinh, Z. W. Ai, G. Liang, and S. B. Schougaard, "Structural changes in electrochemically cycled LiMn0.7Fe0.3PO4," *Solid State Ionics*, vol. 324, pp. 33-39, 2018/10/15/ 2018.

[428] N. V. Kosova, E. T. Devyatkina, A. I. Ancharov, A. V. Markov, D. D. Karnaushenko, and V. K. Makukha, "Structural studies of nanosized LiFe0.5Mn0.5PO4 under cycling by in situ synchrotron diffraction," *Solid State Ionics*, vol. 225, pp. 564-569, 2012/10/04/ 2012.

[429] N. N. Bramnik, K. G. Bramnik, K. Nikolowski, M. Hinterstein, C. Baehtz, and H. Ehrenberg, "Synchrotron Diffraction Study of Lithium Extraction from LiMn0.6Fe0.4PO4," *Electrochemical and Solid-State Letters*, vol. 8, pp. A379-A381, August 1, 2005 2005.

[430] K.-W. Nam, W.-S. Yoon, K. Zaghib, K. Yoon Chung, and X.-Q. Yang, "The phase transition behaviors of Li1−xMn0.5Fe0.5PO4 during lithium extraction studied by in situ X-ray absorption and diffraction techniques," *Electrochemistry Communications*, vol. 11, pp. 2023-2026, 2009/10/01/ 2009.

[431] N. V. Kosova, E. T. Devyatkina, A. B. Slobodyuk, and S. A. Petrov, "Submicron LiFe1−yMnyPO4 solid solutions prepared by mechanochemically assisted carbothermal reduction: The structure and properties," *Electrochimica Acta*, vol. 59, pp. 404-411, 1/1/ 2012.

[432] M. R. Roberts, G. Vitins, G. Denuault, and J. R. Owen, "High Throughput Electrochemical Observation of Structural Phase Changes in LiFe1 − x Mn x PO4 during Charge and Discharge," *Journal of The Electrochemical Society*, vol. 157, pp. A381-A386, April 1, 2010 2010.

[433] A. T. Phan, A. E. Gheribi, and P. Chartrand, "Coherent phase equilibria of systems under large elastic deformations," *Physical Chemistry Chemical Physics*, pp. 10808-10822, 2019.

[434] A. Perea, M. T. Sougrati, C. M. Ionica-Bousquet, B. Fraisse, C. Tessier, L. Aldon, *et al.*, "Operando 57Fe Mössbauer and XRD investigation of LixMnyFe1-yPO4/C composites (y = 0.50; 0.75)," *RSC Advances*, vol. 2, pp. 9517-9524, 2012.

[435] S. Ma, M. Jiang, P. Tao, C. Song, J. Wu, J. Wang, *et al.*, "Temperature effect and thermal impact in lithium-ion batteries: A review," *Progress in Natural Science: Materials International*, vol. 28, pp. 653-666, 2018/12/01/ 2018.

[436] C. M. Burba and R. Frech, "Local structure in the Li-ion battery cathode material Lix(MnyFe1−y)PO4 for 0<x≤1 and y=0.0, 0.5 and 1.0," *Journal of Power Sources*, vol. 172, pp. 870-876, 2007/10/25/ 2007.

[437] T. Nedoseykina, M. G. Kim, S.-A. Park, H.-S. Kim, S.-B. Kim, J. Cho, *et al.*, "In situ X-ray absorption spectroscopic study for the electrochemical delithiation of a cathode LiFe0.4Mn0.6PO4 material," *Electrochimica Acta,* vol. 55, pp. 8876-8882, 2010/12/01/ 2010.

[438] M. Kope¢, A. Yamada, G. Kobayashi, S. Nishimura, R. Kanno, A. Mauger, *et al.*, "Structural and magnetic properties of Lix(MnyFe1−y)PO4 electrode materials for Li-ion batteries," *Journal of Power Sources,* vol. 189, pp. 1154-1163, 2009/04/15/ 2009.

[439] J. Hong, F. Wang, X. Wang, and J. Graetz, "LiFexMn1−xPO4: A cathode for lithium-ion batteries," *Journal of Power Sources,* vol. 196, pp. 3659-3663, 4/1/ 2011.

[440] N. A. Hamid, S. Wennig, A. Heinzel, C. Schulz, and H. Wiggers, "Influence of carbon content, particle size, and partial manganese substitution on the electrochemical performance of LiFexMn1-xPO4/carbon composites," *Ionics,* vol. 21, pp. 1857-1866, 2015.

[441] Y. Lin, B. Zeng, Y. Lin, X. Li, G. Zhao, T. Zhou, *et al.*, "Electrochemical properties of carbon-coated LiFePO4 and LiFe0.98Mn0.02PO4 cathode materials synthesized by solid-state reaction," *Rare Metals,* vol. 31, pp. 145-149, 2012.

[442] Y. Mi, C. Yang, Z. Zuo, L. Qi, C. Tang, W. Zhang, *et al.*, "Positive Effect of Minor Manganese Doping on the Electrochemical Performance of LiFePO4/C under Extreme Conditions," *Electrochimica Acta,* vol. 176, pp. 642-648, 9/10/ 2015.

[443] G. Kobayashi, A. Yamada, S.-i. Nishimura, R. Kanno, Y. Kobayashi, S. Seki, *et al.*, "Shift of redox potential and kinetics in Lix(MnyFe1−y)PO4," *Journal of Power Sources,* vol. 189, pp. 397-401, 4/1/ 2009.

[444] S. Loftager, S. B. Schougaard, T. Vegge, and J. M. García-Lastra, "Density Functional Theory Study of Redox Potential Shifts in LixMnyFe1–yPO4 Battery Electrodes," *The Journal of Physical Chemistry C,* vol. 123, pp. 102-109, 2019/01/10 2019.

[445] D. B. Ravnsbæk, K. Xiang, W. Xing, O. J. Borkiewicz, K. M. Wiaderek, P. Gionet, *et al.*, "Engineering the Transformation Strain in LiMnyFe1–yPO4 Olivines for Ultrahigh Rate Battery Cathodes," *Nano Letters,* 2016/03/01 2016.

[446] T. Drezen, N.-H. Kwon, P. Bowen, I. Teerlinck, M. Isono, and I. Exnar, "Effect of particle size on LiMnPO4 cathodes," *Journal of Power Sources,* vol. 174, pp. 949-953, 2007/12/06/ 2007.

[447] J. Yoshida, M. Stark, J. Holzbock, N. Hüsing, S. Nakanishi, H. Iba, *et al.*, "Analysis of the size effect of LiMnPO4 particles on the battery properties by using STEM-EELS," *Journal of Power Sources,* vol. 226, pp. 122-126, 2013/03/15/ 2013.

[448] D. Rangappa, K. Sone, Y. Zhou, T. Kudo, and I. Honma, "Size and shape controlled LiMnPO4 nanocrystals by a supercritical ethanol process and their electrochemical properties," *Journal of Materials Chemistry,* vol. 21, pp. 15813-15818, 2011.

[449] A. Paolella, G. Bertoni, E. Dilena, S. Marras, A. Ansaldo, L. Manna, *et al.*, "Redox Centers Evolution in Phospho-Olivine Type (LiFe0.5Mn0.5 PO4) Nanoplatelets with Uniform Cation Distribution," *Nano Letters,* vol. 14, pp. 1477-1483, 2014/03/12 2014.

[450] R.-r. Zhao, I. M. Hung, Y.-T. Li, H.-y. Chen, and C.-P. Lin, "Synthesis and properties of Co-doped LiFePO4 as cathode material via a hydrothermal route for lithium-ion batteries," *Journal of Alloys and Compounds,* vol. 513, pp. 282-288, 2012/02/05/ 2012.

[451] L. D. Landau, E. M. Lifshitz, A. M. Kosevich, and L. P. Pitaevskiĭ, *Theory of Elasticity*: Butterworth-Heinemann, 1986.

[452] C.-K. ChiuHuang and H.-Y. S. Huang, "Critical lithiation for C-rate dependent mechanical stresses in LiFePO4," *Journal of Solid State Electrochemistry,* vol. 19, pp. 2245-2253, 2015.

[453] I. M. Daniel and O. Ishai, *Engineering Mechanics of Composite Materials*: Oxford University Press, 1994.

[454] D. L. Fancher and G. R. Barsch, "Lattice theory of alkali halide solid solutions—III. Pressure dependence of solid solubility and spinodal decomposition," *Journal of Physics and Chemistry of Solids,* vol. 32, pp. 1303-1313, // 1971.

[455] P. Ravindran, L. Fast, P. A. Korzhavyi, B. Johansson, J. Wills, and O. Eriksson, "Density functional theory for calculation of elastic properties of orthorhombic crystals: Application to TiSi2," *Journal of Applied Physics,* vol. 84, pp. 4891-4904, 1998/11/01 1998.

[456] Z. Sun, S. Li, R. Ahuja, and J. M. Schneider, "Calculated elastic properties of M2AlC (M=Ti, V, Cr, Nb and Ta)," *Solid State Communications,* vol. 129, pp. 589-592, 2004/03/01/ 2004.

[457] O. L. Anderson, "A simplified method for calculating the debye temperature from elastic constants," *Journal of Physics and Chemistry of Solids,* vol. 24, pp. 909-917, 1963/07/01/ 1963.

[458] J. Serp, M. Allibert, O. Beneš, S. Delpech, O. Feynberg, V. Ghetta*, et al.*, "The molten salt reactor (MSR) in generation IV: Overview and perspectives," *Progress in Nuclear Energy,* vol. 77, pp. 308-319, 11// 2014.

[459] D. P. Chen, X. Wang, Y. S. Hu, C. T. Lin, S. X. Dou, and R. Nigam, "Magnetic anisotropy in doped and undoped LiFePO4 single crystals," *Journal of Applied Physics,* vol. 101, p. 09N512, 2007/05/01 2007.

[460] J. Yao, K. Konstantinov, G. X. Wang, and H. K. Liu, "Electrochemical and magnetic characterization of LiFePO4 and Li0.95Mg0.05FePO4 cathode materials," *Journal of Solid State Electrochemistry,* vol. 11, pp. 177-185, 2007/02/01 2007.

[461] N. Akutsu and H. Ikeda, "Specific Heat Capacities of CoF2, MnF2 and KMnF3 near the Néel Temperatures," *Journal of The Physical Society of Japan - J PHYS SOC JPN,* vol. 50, pp. 2865-2871, 09/15 1981.

[462] R. P. Rao, M. V. Reddy, S. Adams, and B. V. R. Chowdari, "Preparation, temperature dependent structural, molecular dynamics simulations studies and electrochemical properties of LiFePO4," *Materials Research Bulletin,* vol. 66, pp. 71-75, 2015/06/01/ 2015.

[463] L. Vočadlo, J. P. Poirer, and G. D. Price, "Grüneisen parameters and isothermal equations of state," in *American Mineralogist* vol. 85, ed, 2000, p. 390.

[464] S. L. Shang, Y. Wang, Z. G. Mei, X. D. Hui, and Z. K. Liu, "Lattice dynamics, thermodynamics, and bonding strength of lithium-ion battery materials LiMPO4 (M = Mn, Fe, Co, and Ni): a comparative first-principles study," *Journal of Materials Chemistry,* vol. 22, pp. 1142-1149, 2012.

[465] R. A. Swalin, *Thermodynamics of Solids*: Wiley, 1972.

[466] C. A. J. Fisher, V. M. Hart Prieto, and M. S. Islam, "Lithium Battery Materials LiMPO4 (M = Mn, Fe, Co, and Ni): Insights into Defect Association, Transport Mechanisms, and Doping Behavior," *Chemistry of Materials,* vol. 20, pp. 5907-5915, 2008/09/23 2008.

[467] B. Hu and G. Tao, "Molecular dynamics simulations on lithium diffusion in LiFePO4: the effect of anti-site defects," *Journal of Materials Chemistry A,* vol. 3, pp. 20399-20407, 2015.

[468] M. Bini, S. Ferrari, D. Capsoni, P. Mustarelli, G. Spina, F. D. Giallo, *et al.*, "Pair distribution function analysis and Mössbauer study of defects in microwave-hydrothermal LiFePO4," *RSC Advances,* vol. 2, pp. 250-258, 2012.

[469] H. Raj, S. Rani, and A. Sil, "Antisite Defects in Sol-Gel-Synthesized LiFePO4 at Higher Temperature: Effect on Lithium-Ion Diffusion," *ChemElectroChem,* vol. 5, pp. 3525-3532, 2018/11/13 2018.

APPENDIX A ELASTIC ENERGY FOR ORTHORHOMBIC SYSTEMS

An extension of Cahn's approach for calculating the coherent phase diagram of a tetragonal system was previously reported [157, 158]. However, no one has derived the expression of elastic Gibbs energy of an orthorhombic system using this approach yet. The general expression of the elastic energy density f_{el} of a crystal belonging to an orthorhombic system is known [451]:

$$\begin{aligned} f_{el} = \frac{1}{2}C_{11}{\varepsilon_{11}}^2 + \frac{1}{2}C_{22}{\varepsilon_{22}}^2 + \frac{1}{2}C_{33}{\varepsilon_{33}}^2 + C_{12}\varepsilon_{11}\varepsilon_{22} + C_{13}\varepsilon_{11}\varepsilon_{33} \\ + C_{23}\varepsilon_{22}\varepsilon_{33} + 2C_{44}{\varepsilon_{23}}^2 + 2C_{55}{\varepsilon_{13}}^2 + 2C_{66}{\varepsilon_{12}}^2 \end{aligned} \tag{A.1}$$

where ε_{ij} is the strain on the corresponding direction (1 stands for *x*-, 2 stands for *y*-, and 3 stands for *z*-direction); and C_{ij} is the elastic constant. Similar to Cahn, let us consider *x*, *y*, and *z* to be a coordinate system aligned along the axes of an orthogonal crystal, where *x*-, *y*-, and *z*- are the *a*-, *b*- and *c*- axis respectively. Let *x'*, *y'*, *z'* be a coordinate system where the *z'* axis is parallel to the fluctuation in concentration and let ε_{ij}' be the strain in this coordinate system. Then, the only non-vanishing strain component is ε_{33}'. The strain tensor is then expressed as a function of the stress tensor [159, 452, 453]:

$$\begin{bmatrix} \varepsilon_{11} \\ \varepsilon_{22} \\ \varepsilon_{33} \\ \varepsilon_{23} \\ \varepsilon_{13} \\ \varepsilon_{12} \end{bmatrix} = T * \begin{bmatrix} 0 \\ 0 \\ \varepsilon_{33}' \\ 0 \\ 0 \\ 0 \end{bmatrix} - \begin{bmatrix} \varepsilon_a \\ \varepsilon_b \\ \varepsilon_c \\ 0 \\ 0 \\ 0 \end{bmatrix} \tag{A.2}$$

where ε_a, ε_b, and ε_c are elastic strain corresponding to *a*-, *b*- and *c*- axis after deformation on and stress tensor $T = \begin{bmatrix} 0 & 0 & l^2 & 0 & 0 & 0 \\ 0 & 0 & m^2 & 0 & 0 & 0 \\ 0 & 0 & n^2 & 0 & 0 & 0 \\ 0 & 0 & mn & 0 & 0 & 0 \\ 0 & 0 & ln & 0 & 0 & 0 \\ 0 & 0 & lm & 0 & 0 & 0 \end{bmatrix}$. Hence, it is possible to obtain the elastic free energy density of an orthorhombic structure under Cahn's assumption. The elastic free energy density is then given by:

$$\begin{aligned} f_{el} = \frac{1}{2}C_{11}\left[l^4{\varepsilon'_{33}}^2 - 2l^2\varepsilon_a\varepsilon'_{33} + {\varepsilon_a}^2\right] \\ + \frac{1}{2}C_{22}\left[m^4{\varepsilon'_{33}}^2 - 2m^2\varepsilon_b\varepsilon'_{33} + {\varepsilon_b}^2\right] \\ + \frac{1}{2}C_{33}\left[n^4{\varepsilon'_{33}}^2 - 2n^2\varepsilon_c\varepsilon'_{33} + {\varepsilon_c}^2\right] \\ + C_{12}\left[l^2m^2{\varepsilon'_{33}}^2 - (l^2\varepsilon_b + m^2\varepsilon_a)\varepsilon'_{33} + \varepsilon_a\varepsilon_b\right] \\ + C_{13}\left[l^2n^2{\varepsilon'_{33}}^2 - (l^2\varepsilon_c + n^2\varepsilon_a)\varepsilon'_{33} + \varepsilon_a\varepsilon_c\right] \\ + C_{23}\left[m^2n^2{\varepsilon'_{33}}^2 - (m^2\varepsilon_c + n^2\varepsilon_b)\varepsilon'_{33} + \varepsilon_b\varepsilon_c\right] \\ + 2C_{44}m^2n^2{\varepsilon'_{33}}^2 + 2C_{55}l^2n^2{\varepsilon'_{33}}^2 + 2C_{66}l^2m^2{\varepsilon'_{33}}^2 \end{aligned} \tag{A.3}$$

where *l*, *m* and *n* are the direction cosines of the z' axis with the *x*-, *y*- and *z*-axis, respectively, and ε_a, ε_b and ε_c are the stress-free strains along the *a*-, *b*- and *c*-axis, respectively. The value of ε'_{33}, which could minimize the elastic energy density in Equation A.3, is given by:

$$\varepsilon'_{33} = \frac{[(\mathrm{C}_{11}\mathrm{l}^2 + \mathrm{C}_{12}\mathrm{m}^2 + \mathrm{C}_{13}\mathrm{n}^2)\varepsilon_a + (\mathrm{C}_{22}\mathrm{m}^2 + \mathrm{C}_{12}\mathrm{l}^2 + \mathrm{C}_{23}\mathrm{n}^2)\varepsilon_b + (\mathrm{C}_{33}\mathrm{n}^2 + \mathrm{C}_{23}\mathrm{m}^2 + \mathrm{C}_{13}\mathrm{l}^2)\varepsilon_c]}{[\mathrm{C}_{11}\mathrm{l}^4 + \mathrm{C}_{22}\mathrm{m}^4 + \mathrm{C}_{33}\mathrm{n}^4 + (2\mathrm{C}_{12} + 4\mathrm{C}_{66})\mathrm{l}^2\mathrm{m}^2 + (2\mathrm{C}_{13} + 4\mathrm{C}_{55})\mathrm{l}^2\mathrm{n}^2 + (2\mathrm{C}_{23} + 4\mathrm{C}_{44})\mathrm{m}^2\mathrm{n}^2]} \tag{A.4}$$

The minimum elastic free energy density in the crystal system is calculated by substituting Equation A.4 into Equation A.3. Similar to Cahn [154-156], we consider a concentration fluctuation in the form of a sinusoidal plane wave and compute the total free energy of a certain volume V of the solid solution, then the coherent spinodal is given by:

$$\frac{\partial^2 G_m^{chem}}{\partial x^2} + E_{elastic} = \frac{\partial^2 G_m^{chem}}{\partial x^2} + H^{[lmn]} \cdot V_m = 0 \tag{A.5}$$

where *H* is the stored strain energy $E_{elastic}$ per unit volume and the expression of *H* corresponding to various $[lmn]$ crystallographic directions is shown in Table A.1. The obtained results are consistent with the reported formulae for both cubic and tetragonal crystals.

Table A.1 Expressions of H corresponding to various crystallographic directions of an orthorhombic system

Direction	**Expression of H**
[100]	$H^{[100]} = C_{22}\eta_b{}^2 + C_{33}\eta_c{}^2 + 2C_{23}\eta_b\eta_c - \frac{(C_{12}\eta_b + C_{13}\eta_c)^2}{C_{11}}$
[010]	$H^{[010]} = C_{11}\eta_a{}^2 + C_{33}\eta_c{}^2 + 2C_{13}\eta_a\eta_c - \frac{(C_{12}\eta_a + C_{23}\eta_c)^2}{C_{22}}$
[001]	$H^{[001]} = C_{11}\eta_a{}^2 + C_{22}\eta_b{}^2 + 2C_{12}\eta_a\eta_b - \frac{(C_{13}\eta_a + C_{23}\eta_b)^2}{C_{33}}$
[110]	$\eta_{33}{}' = \frac{[(C_{11} + C_{12})\eta_a + (C_{22} + C_{12})\eta_b + (C_{23} + C_{13})\eta_c]}{[C_{11} + C_{22} + (2C_{12} + 4C_{66})]}$ $H^{[110]} = C_{11}(\eta'_{33} - \eta_a)^2 + C_{22}(\eta'_{33} - \eta_b)^2 + C_{33}\eta_c{}^2 + 2C_{12}(\eta'_{33} - \eta_a)(\eta'_{33} - \eta_b)$ $- 2C_{13}\eta_c(\eta'_{33} - \eta_a) - 2C_{23}\eta_c(\eta'_{33} - \eta_b) + 4C_{66}\eta'_{33}{}^2$
[101]	$\eta_{33}{}' = \frac{[(C_{11} + C_{13})\eta_a + (C_{12} + C_{23})\eta_b + (C_{33} + C_{13})\eta_c]}{[C_{11} + C_{33} + (2C_{13} + 4C_{55})]}$ $H^{[101]} = C_{11}(\eta'_{33} - \eta_a)^2 + C_{22}\eta_b{}^2 + C_{33}(\eta'_{33} - \eta_c)^2 - 2C_{12}\eta_b(\eta'_{33} - \eta_a)$ $+ 2C_{13}(\eta'_{33} - \eta_a)(\eta'_{33} - \eta_c) - 2C_{23}\eta_b(\eta'_{33} - \eta_c) + 4C_{55}\eta'_{33}{}^2$
[011]	$\eta_{33}{}' = \frac{[(C_{12} + C_{13})\eta_a + (C_{22} + C_{23})\eta_b + (C_{33} + C_{23})\eta_c]}{[C_{22} + C_{33} + (2C_{23} + 4C_{44})]}$ $H^{[011]} = C_{11}\eta_a{}^2 + C_{22}(\eta'_{33} - \eta_b)^2 + C_{33}(\eta'_{33} - \eta_c)^2 - 2C_{12}\eta_a(\eta'_{33} - \eta_b)$ $- 2C_{13}\eta_a(\eta'_{33} - \eta_c) + 2C_{23}(\eta'_{33} - \eta_b)(\eta'_{33} - \eta_c) + 4C_{44}\eta'_{33}{}^2$
[111]	$\eta_{33}{}' = \frac{[(C_{11} + C_{12} + C_{13})\eta_a + (C_{22} + C_{12} + C_{23})\eta_b + (C_{33} + C_{23} + C_{13})\eta_c]}{[C_{11} + C_{22} + C_{33} + (2C_{12} + 4C_{66}) + (2C_{13} + 4C_{55}) + (2C_{23} + 4C_{44})]}$ $H^{[111]} = C_{11}(\eta'_{33} - \eta_a)^2 + C_{22}(\eta'_{33} - \eta_b)^2 + C_{33}(\eta'_{33} - \eta_c)^2$ $+ 2C_{12}(\eta'_{33} - \eta_a)(\eta'_{33} - \eta_b) + 2C_{13}(\eta'_{33} - \eta_a)(\eta'_{33} - \eta_c)$ $+ 2C_{23}(\eta'_{33} - \eta_b)(\eta'_{33} - \eta_c) + 4C_{44}\eta'_{33}{}^2 + 4C_{55}\eta'_{33}{}^2 + 4C_{66}\eta'_{33}{}^2$

APPENDIX B THERMO-PHYSICAL PROPERTIES OF Li_xFePO_4 SOLID SOLUTION AS A FUNCTION OF COMPOSITION (x) AND TEMPERATURE (T)

In the literature, there are various experimental and *an initio* data of lattice parameters and molar volumes of $LiFePO_4$ and $FePO_4$ [25, 29, 88, 160, 186-192]. The solid solution Li_xFePO_4 obeys to Vegard's rule [29, 189, 191]. The changes of the lattice constants versus composition of the solid solution are considered as η_a, η_b, η_c. It is worth noticing that the selection of the η_a, η_b, η_c values influences our coherent calculation significantly. In fact, it is well noticed that first principle calculations slightly overestimate the molar volumes of both $LiFePO_4$ and $FePO_4$ [25, 187]. Obviously, the overestimation of the molar volume of $FePO_4$ is significantly larger than that of $LiFePO_4$. As a result, η_i obtained from reported calculations is not reliable. It can be due to the stronger magnetism effect on $FePO_4$ compared to $LiFePO_4$. Clearly, η_i is temperature dependent. However, in this work, those parameters are considered as constants and taken from Andersson et al. [160] since the thermal expansion coefficients of $FePO_4$ and $LiFePO_4$ are very similar.

The molar volume of the solid solution Li_xFePO_4 is also assumed to be linearly dependent on the composition of the two substances [29, 189, 191]:

$$V_m = V_m^{LiFePO_4} \cdot x + V_m^{FePO_4} \cdot (1-x) \tag{B.1}$$

with $V_m^{LiFePO4} = 43.821 \cdot 10^{-6}\ (m^3 mol^{-1})$ and $V_m^{FePO4} = 40.911 \cdot 10^{-6}\ (m^3 mol^{-1})$ [160]. Moreover, the molar volume of $LiFePO_4$ and $FePO_4$ is temperature dependent. The temperature dependent molar volume of $LiFePO_4$ and $FePO_4$ is estimated despite the fact that the estimation for $FePO_4$ is larger than the experimental data reported by Anderson et al. [160] and Padhi et al. [16] The molar volume is assumed to be linearly dependent on temperature. The following expressions are derived by fitting the data of our estimated molar volume in the temperature range of 270K to 650K [101], covering the miscibility gap of $LiFePO_4$ - $FePO_4$:

$$\begin{aligned} V_m^{LiFePO_4} &= (43.413 + 0.0025 \cdot T) \cdot 10^{-6}\ (m^3 mol^{-1}) \\ V_m^{FePO_4} &= (42.692 + 0.0024 \cdot T) \cdot 10^{-6}\ (m^3 mol^{-1}) \end{aligned} \tag{B.2}$$

The elastic constants of $LiFePO_4$ and $FePO_4$ are estimated [25, 186]. In this work, the most recent elastic constants of pure compounds reported by Xie et al. [25] are used. Each elastic constant of solid solution is assumed to be linearly dependent on the composition of the two substances:

$$C_{ij} = C_{ij}^{LiFePO_4} \cdot x + C_{ij}^{FePO_4} \cdot (1 - x) \tag{B.3}$$

The temperature dependent term is used to represent the influence of temperature on thermophysical properties then on $E_{elastic}$ value. The temperature dependent term of each compound $LiFePO_4$ and $FePO_4$ is calculated as follow:

$$t^i = \frac{E^i(T) \big/ \left(1 - \vartheta^i(T)\right)}{E^i(0K) \big/ \left(1 - \vartheta^i(0K)\right)} \tag{B.4}$$

where i is either $LiFePO_4$ or $FePO_4$. The temperature dependent term, which is obtained from our estimation of Young's modulus and Poison's ratio in the range 270K - 650K [101], is given as: $t^{LiFePO_4} = (104.5236 - 0.0207 \cdot T) \cdot 10^{-2}$ and $t^{LiFePO_4} = (105.4905 - 0.0272 \cdot T) \cdot 10^{-2}$. Again, the temperature dependence of the solid solution is assumed to be linearly dependent on that of the two compounds:

$$t(x, T) = t^{LiFePO_4} \cdot x + t^{FePO_4} \cdot (1 - x) \tag{B.5}$$

The coherent spinodal is given by Equation A.5 with

$$H^{[lmn]}(T) = t \cdot H^{[lmn]}(0K) \tag{B.6}$$

When studying the temperature effect, both temperature dependent terms (B.5) and temperature dependent molar volumes (B.2) should be considered together. When ignoring the temperature effect, the molar volumes should be taken from the experimental values [160] in order to avoid the overestimation of the molar volume of $FePO_4$ and $LiFePO_4$. The linear dependence of the physical properties of the solid solution on the composition and temperature is generally a good assumption for many ionic systems.

APPENDIX C MOLAR SURFACE ENERGY OF THE ISOTROPIC SOLID SOLUTION Li_xFePO_4

Molar surface energy is utilized to calculate the size-dependent phase equilibria of $LiFePO_4$-$FePO_4$ system. The average molar surface energy $\langle\gamma\rangle$ of the isotropic solid solution Li_xFePO_4 is given in Equation 5.8.

$$\langle\gamma\rangle = \langle\gamma\rangle_{FePO_4}\cdot(1-x^s)+\langle\gamma\rangle_{LiFePO_4}\cdot x^s+\langle\gamma\rangle^{ex} \tag{C.1}$$

where x^s is the surface composition of the component $LiFePO_4$ which is independent on the excess surface energy $\langle\gamma\rangle^{ex}$ and the surface compositions of $FePO_4$ and $LiFePO_4$ are estimated from the ideal solution model [226]:

$$x^s_{LiFePO_4} = x^s = \frac{x^b}{x^b+(1-x^b)\cdot S_0} \tag{C.2}$$

$$x^s_{FePO_4} = 1-x^s = \frac{1-x^b}{(1-x^b)+\frac{x^b}{S_0}}$$

where $x^b = x$ is the bulk composition of component $LiFePO_4$; S_0 is the surface segregation factor which is given by $S_0 = e^{\frac{A_m\cdot(\langle\gamma\rangle_{LiFePO_4}-\langle\gamma\rangle_{FePO_4})}{RT}} = e^{\frac{A_m\cdot\Delta\langle\gamma\rangle}{RT}}$; R is the gas constant, and T is the temperature; $A_m = 1.09\cdot V_m^{\frac{2}{3}}\cdot N_A^{\frac{1}{3}}$ is the average molar surface area; and N_A is Avogadro's constant.

The excess surface energy of the solid solution is considered as a function of composition

$$\langle\gamma\rangle^{ex} = \omega\cdot x^s\cdot(1-x^s) \tag{C.3}$$

With the excess term ω:

$$\omega = \sum \omega_{ij}\cdot(x^s)^i\cdot(1-x^s)^j \tag{C.4}$$

APPENDIX D METHOD OF CALCULATION OF SPINODAL DECOMPOSITION AS A FUNCTION OF PARTICLE SIZE

The differential equation governing spinodal decomposition is given by:

$$\frac{\partial^2 G_m^{tot}}{(\partial x^b)^2} = 0 \tag{D.1}$$

i.e.

$$\frac{\partial^2 \left(G_m^{ref} + G_m^s\right)}{(\partial x^b)^2} = 0 \tag{D.2}$$

Then,

$$\frac{\partial^2 G_m^{ref}}{(\partial x^b)^2} + \frac{\partial^2 \left(\frac{4C \cdot \langle\gamma\rangle \cdot V_m}{D}\right)}{(\partial x^b)^2} = 0 \tag{D.3}$$

Later,

$$\frac{\partial^2 G_m^{ref}}{(\partial x^b)^2} + \frac{4C}{D} \cdot \left(\langle\gamma\rangle \cdot \frac{\partial^2 V_m}{(\partial x^b)^2} + 2 \cdot \frac{\partial V_m}{\partial x^b} \cdot \frac{\partial \langle\gamma\rangle}{\partial x^b} + V_m \cdot \frac{\partial^2 \langle\gamma\rangle}{(\partial x^b)^2}\right) = 0 \tag{D.4}$$

When the solid solution obeys Vegard's law (as Li_xFePO_4 does [23, 27, 189]), Equation D.4 becomes:

$$\frac{\partial^2 G_m^{ref}}{(\partial x^b)^2} + \frac{4C}{D} \cdot \left(2 \cdot \Delta V_m \cdot \frac{\partial \langle\gamma\rangle}{\partial x^b} + V_m \cdot \frac{\partial^2 \langle\gamma\rangle}{(\partial x^b)^2}\right) = 0 \tag{D.5}$$

Finally,

$$\frac{\partial^2 G_m^{ref}}{\left(\partial x^b\right)^2} + \frac{4C}{D} \cdot \left[2 \cdot \Delta V_m \cdot \left(\Delta\langle\gamma\rangle \cdot \frac{\partial x^s}{\partial x^b} + \frac{\partial \langle\gamma\rangle^{ex}}{\partial x^b}\right) + V_m \cdot \left(\Delta\langle\gamma\rangle \cdot \frac{\partial^2 x^s}{\left(\partial x^b\right)^2} + \frac{\partial^2 \langle\gamma\rangle^{ex}}{\left(\partial x^b\right)^2}\right)\right] = 0 \tag{D.6}$$

The difference between the surface energies of the two compounds $\Delta\langle\gamma\rangle = \langle\gamma\rangle_{LiFePO_4} - \langle\gamma\rangle_{FePO_4}$ are important to calculate the spinodal compositions since it exist in the final equation and it is the only parameter which affects the surface concentration.

APPENDIX E MODEL PARAMETERS OF CALCULATION OF SPINODAL DECOMPOSITION AS A FUNCTION OF PARTICLE SIZE

Table E.1 The parameters used for calculating molar surface energy of the isotropic solid solution Li_xFePO_4:

Parameter	**$LiFePO_4$**	**$FePO_4$**	**Equilibrium phase diagram**	**[100] coherent phase diagram**
$\langle\gamma\rangle$ [J/m^2]	0.6	0.6015	-	-
ω [J/m^2]	-	-	-1.546	-1.05
$\omega(x^s)$[J/m^2]	-	-	$-0.75 - 1.7 \cdot (x^s)^2 - 2.1 \cdot (1 - x^s)^2$	$-0.5 - 0.95 \cdot (x^s)^2 - 1.1 \cdot (1 - x^s)^2$

APPENDIX F FORMULATION OF THE ELASTIC GIBBS ENERGY FOR A CUBIC SYSTEM

1. Small deformation regime

a. The [100] habit plane

According to the assumption stated by Cahn [154-156, 231], two elastic strains related to the difference of the lattice parameter (a') of the solid solution with the fluctuated composition (x) and that (a_0) with the overall composition (x_0) are $\varepsilon_2 = \varepsilon_3 = \varepsilon = \frac{a'-a_0}{a_0}$, and the corresponding stresses are $\sigma_2 = \sigma_3 = \sigma$:

$$\begin{bmatrix} \varepsilon_1 \\ \varepsilon \\ \varepsilon \\ 0 \\ 0 \\ 0 \end{bmatrix} = \begin{bmatrix} S_{11} & S_{12} & S_{12} & 0 & 0 & 0 \\ S_{12} & S_{22} & S_{12} & 0 & 0 & 0 \\ S_{12} & S_{12} & S_{33} & 0 & 0 & 0 \\ 0 & 0 & 0 & S_{44} & 0 & 0 \\ 0 & 0 & 0 & 0 & S_{44} & 0 \\ 0 & 0 & 0 & 0 & 0 & S_{44} \end{bmatrix} \cdot \begin{bmatrix} 0 \\ \sigma \\ \sigma \\ 0 \\ 0 \\ 0 \end{bmatrix} \tag{F.1}$$

where S_{ij} are the elastic compliance of the cubic material and where i and j are Voigt notations. Solving Equation F.1, we obtain:

$$\sigma = \frac{\varepsilon}{(S_{11} + S_{12})} = \frac{\varepsilon_1}{2S_{12}} \tag{F.2}$$

The elastic energy stored in the crystal in the small deformation regime is estimated as follows:

$$f_{el}^{s} = \frac{1}{2} \sum S_{ij} \sigma_i \sigma_j \tag{F.3}$$

Substituting Equation F.2 into Equation F.3, the elastic energy stored becomes:

$$f_{el}^{s} = Y_{100}^{s} \cdot \varepsilon^2 \tag{F.4}$$

with:

$$Y_{100}^{s} = \frac{1}{(S_{11} + S_{12})} = \frac{(C_{11} - C_{12}) \cdot (C_{11} + 2C_{12})}{C_{11}} \tag{F.5}$$

where C_{ij} are the elastic constants of the cubic material. Note that the expression of Y_{100}^{s} in Equation F.5 is exactly what was reported by Cahn [154-156, 231].

b. The [111] habit plane

In order to reproduce the elastic Gibbs energy of [111] plane reported by Cahn [154-156, 231], we will consider a general stress-strain relation in an isotropic material:

$$\begin{bmatrix} \varepsilon \\ \varepsilon_2 \\ \varepsilon_3 \\ \varepsilon_4 \\ \varepsilon_5 \\ \varepsilon_6 \end{bmatrix} = \begin{bmatrix} S_{11} & S_{12} & S_{12} & 0 & 0 & 0 \\ S_{12} & S_{22} & S_{12} & 0 & 0 & 0 \\ S_{12} & S_{12} & S_{33} & 0 & 0 & 0 \\ 0 & 0 & 0 & S_{44} & 0 & 0 \\ 0 & 0 & 0 & 0 & S_{44} & 0 \\ 0 & 0 & 0 & 0 & 0 & S_{44} \end{bmatrix} \cdot \begin{bmatrix} \sigma_1 \\ k_2\sigma_1 \\ k_3\sigma_1 \\ \sigma_4 \\ k_5\sigma_4 \\ k_6\sigma_4 \end{bmatrix} \tag{F.6}$$

where k_2, k_3, k_4, k_5 are real numbers.

So, the elastic energy stored in the crystal within the small deformation regime is estimated as follow:

$$\begin{aligned} f_{el}^{s} &= \frac{1}{2}\sum S_{ij}\sigma_i\sigma_j \\ &= \frac{1}{2}\left\{S_{11}{\sigma_1}^2\left(1 + {k_2}^2 + {k_3}^2\right)\right. \\ &\quad \left. + 2S_{12}{\sigma_1}^2(k_2 + k_3 + k_2k_3) + S_{44}{\sigma_4}^2\left(1 + {k_5}^2 + {k_6}^2\right)\right\} \end{aligned} \tag{F.7}$$

Substitute $\sigma_1 = \frac{\varepsilon}{(S_{11}+k_2S_{12}+k_3S_{12})}$ derived from Equation F.6 and $\sigma_4 = m\sigma_1$ (where m is a real number) into Equation F.7, we obtain:

$$\begin{aligned} f_{el}^{s} &= \frac{1}{2}\frac{\varepsilon^2}{(S_{11} + k_2S_{12} + k_3S_{12})^2}\left\{S_{11}\left(1 + {k_2}^2 + {k_3}^2\right)\right. \\ &\quad \left. + 2S_{12}(k_2 + k_3 + k_2k_3) + m^2S_{44}\left(1 + {k_5}^2 + {k_6}^2\right)\right\} \\ &= Y_{111}^{s} \cdot \varepsilon^2 \end{aligned} \tag{F.8}$$

i.e.,

$$Y_{111}^{s} = \frac{\{S_{11}(1+{k_2}^2+{k_3}^2)+2S_{12}(k_2+k_3+k_2k_3)+m^2S_{44}(1+{k_5}^2+{k_6}^2)\}}{2(S_{11}+k_2S_{12}+k_3S_{12})^2} \quad \text{(F.9)}$$

If the expression of Y_{111}^{s} in Equation F.9 is equivalent to Y_{111}^{s} obtained from Cahn's approach [154-156, 231], we should have:

$$\frac{\{S_{11}(1+{k_2}^2+{k_3}^2)+2S_{12}(k_2+k_3+k_2k_3)+m^2S_{44}(1+{k_5}^2+{k_6}^2)\}}{2(S_{11}+k_2S_{12}+k_3S_{12})^2} = \frac{6}{4(S_{11}+2S_{12})+S_{44}} \quad \text{(F.10)}$$

If there exists an exact stress-strain relation for the calculation of the elastic energy corresponding to the [111] habit plane, there exist values of k_2, k_3, k_5, k_6 satisfying Equation F.10 for every S_{11}, S_{12}, and S_{44}. However, since no set of k_2, k_3, k_5, and k_6 satisfying Equation F.10 is found, it is impossible to find a suitable stress-strain relation which could reproduce the elastic Gibbs energy of Cahn's approach for the [111] habit plane [154-156, 231]. In order to estimate the elastic Gibbs energy stored in the [111] habit plane, in this study, we propose another stress-strain relation for calculating the coherent miscibility gap as follows:

$$\begin{bmatrix} \varepsilon \\ \varepsilon_2 \\ \varepsilon_2 \\ \varepsilon \\ 0 \\ 0 \end{bmatrix} = \begin{bmatrix} S_{11} & S_{12} & S_{12} & 0 & 0 & 0 \\ S_{12} & S_{11} & S_{12} & 0 & 0 & 0 \\ S_{12} & S_{12} & S_{11} & 0 & 0 & 0 \\ 0 & 0 & 0 & S_{44} & 0 & 0 \\ 0 & 0 & 0 & 0 & S_{44} & 0 \\ 0 & 0 & 0 & 0 & 0 & S_{44} \end{bmatrix} \cdot \begin{bmatrix} \sigma_1 \\ 0 \\ 0 \\ \sigma_4 \\ 0 \\ 0 \end{bmatrix} \quad \text{(F.11)}$$

This stress-strain relation is proposed to reproduce the experimental data of the [111] coherent miscibility gap in our case studies (shown in part 3). Like the [100] habit plane, the elastic energy stored in the crystal for small deformation is estimated as follows:

$$f_{el}^{s} = Y_{111}^{s} \cdot \varepsilon^2 \quad \text{(F.12)}$$

with:

$$Y_{111}^{s} = \frac{1}{2}\left[\frac{1}{S_{11}} + \frac{1}{S_{44}}\right] = \frac{1}{2}\left[\frac{(C_{11} - C_{12}) \cdot (C_{11} + 2C_{12})}{C_{11} + C_{12}} + C_{44}\right] \qquad \text{(F.13)}$$

After obtaining the formulae of Y depending on the elastic constants C_{ij} corresponding to the [100] or [111] habit plane, in a similar way to Cahn's approach [154-156, 231], we consider a sinusoïdal plane wave fluctuation of the composition, then the elastic strain can be written as:

$$\varepsilon = \eta(x - x_0) = \eta A cos(\boldsymbol{\beta} \cdot \boldsymbol{r}) \qquad \text{(F.14)}$$

where x_0 is the overall composition and x is the local composition of the solid solution and the composition fluctuates as $x - x_0 = A cos(\boldsymbol{\beta} \cdot \boldsymbol{r})$; $\eta = \frac{1}{a}\frac{\partial a}{\partial x}$ is the rate of change of the lattice constants with composition. If $\frac{\partial a}{\partial x}$ is a constant, it is called Vegard's coefficient. According to Cahn [154-156, 231], the total free energy of volume V of an isotropic solid solution free from imperfections in which the molar volume is independent of both composition and pressure is:

$$F = \int_V \{f'(x) + Y^s\eta^2(x - x_0)^2 + \kappa(\nabla x)^2\} dV \qquad \text{(F.15)}$$

where $f'(x)$ is the Helmholtz free energy of a unit volume of homogeneous materials of composition x and $\kappa(\nabla x)^2$ is the first term of an expansion representing the increase in free energy due to the introduction of a gradient of composition. Expanding $f'(x)$ in a Taylor's series with $x - x_0 = A cos(\boldsymbol{\beta} \cdot \boldsymbol{r})$ and integrating the above equation, we obtain the change in free energy per unit volume between the initial homogeneous solution of concentration x_0 and the inhomogeneous solution of concentration x:

$$\frac{\Delta F}{V} = \frac{1}{4}A^2\left\{\frac{\partial^2 f'}{\partial x^2} + 2Y^s\eta^2 + 2\kappa\beta^2\right\} \qquad \text{(F.16)}$$

If the free energy change $\frac{\Delta F}{V}$ is negative for some wave vectors $\boldsymbol{\beta}$, then the solution is unstable to infinitesimal fluctuations with those wave vectors. Otherwise, the solution is stable to all infinitesimal fluctuations. The spinodal curve for a particular direction of the wave vector is given by the condition that the solution just be unstable to fluctuations of infinite wavelength but stable to fluctuations of finite wavelength in that directions, that is, the spinodal is given by:

$$\frac{\partial^2 f'}{\partial x^2} + 2Y^s\eta^2 = 0 \tag{F.17}$$

Equation F.17 is applied for a volume unit of the solid solution. Hence, for a molar volume of an isotropic material under coherent spinodal decomposition:

$$\frac{\partial^2 F}{\partial x^2} + 2V_m Y^s\eta^2 = 0 \tag{F.18}$$

where F is the molar Helmholtz free energy. In fact, the molar Gibbs energy $G = F - PV$. Since the second derivative of PV versus x is neglected, Equation F.18 becomes:

$$\frac{\partial^2 G}{\partial x^2} + 2V_m Y^s\eta^2 = 0 \tag{F.19}$$

2. Large deformation regime

a. The [100] habit plane

Corresponding to the stress-strain relation developed for calculating the elastic Gibbs energy of [100] coherence in the small deformation regime in Equation F.1, the Cauchy stress tensor is $\begin{bmatrix} 0 & 0 & 0 \\ 0 & \sigma & 0 \\ 0 & 0 & \sigma \end{bmatrix}$ and the strain tensor is $\begin{bmatrix} \varepsilon_1 & 0 & 0 \\ 0 & \varepsilon & 0 \\ 0 & 0 & \varepsilon \end{bmatrix}$. The elastic energy stored in the crystal is estimated from the Almansi strain and the second Poila-Kirchhoff stress. The deformation matrix is:

$$[\boldsymbol{F}] = \begin{bmatrix} \varepsilon_1 + 1 & 0 & 0 \\ 0 & \varepsilon + 1 & 0 \\ 0 & 0 & \varepsilon + 1 \end{bmatrix} = \begin{bmatrix} k\varepsilon + 1 & 0 & 0 \\ 0 & \varepsilon + 1 & 0 \\ 0 & 0 & \varepsilon + 1 \end{bmatrix} \tag{F.19}$$

Where $\varepsilon_1 = k\varepsilon$ with $k = \frac{2S_{12}}{(S_{11}+S_{12})}$ is a real number. Hence,

$$\boldsymbol{J} = |\det \boldsymbol{F}| = (k\varepsilon + 1) \cdot (\varepsilon + 1)^2 \tag{F.20}$$

The right Cauchy-Green deformation tensor

$$[\boldsymbol{C}] = [\boldsymbol{F}]^{\boldsymbol{T}} \cdot [\boldsymbol{F}] = \begin{bmatrix} (k\varepsilon + 1)^2 & 0 & 0 \\ 0 & (\varepsilon + 1)^2 & 0 \\ 0 & 0 & (\varepsilon + 1)^2 \end{bmatrix} \tag{F.21}$$

The Almansi-Lagrange strain tensor:

$$[\boldsymbol{e}] = \frac{1}{2}([\boldsymbol{I}] - [\boldsymbol{C}^{-1}])$$

$$= \frac{1}{2}\begin{bmatrix} 1 - \frac{1}{(k\varepsilon + 1)^2} & 0 & 0 \\ 0 & 1 - \frac{1}{(\varepsilon + 1)^2} & 0 \\ 0 & 0 & 1 - \frac{1}{(\varepsilon + 1)^2} \end{bmatrix} \tag{F.22}$$

The second Piola-Kirchhoff stress tensor:

$$[\widetilde{\boldsymbol{T}}] = [\boldsymbol{F}^{-1}] \cdot \boldsymbol{J} \cdot [\boldsymbol{T}] \cdot [\boldsymbol{F}^{-1}]^{\boldsymbol{T}} = (k\varepsilon + 1) \cdot \sigma \cdot \begin{bmatrix} 0 & 0 & 0 \\ 0 & 1 & 0 \\ 0 & 0 & 1 \end{bmatrix} \tag{F.23}$$

Similarly, the elastic energy stored in the crystal is estimated as follow:

$$f_{el}^{l} = \frac{1}{2}\sum e_{ij} \cdot \tilde{T}_{ij} = \frac{1}{2} \cdot (k\varepsilon + 1)\sigma \left[1 - \frac{1}{(\varepsilon + 1)^2}\right] \tag{F.24}$$

Substituting Equation F.2 into Equation F.24, we obtain the expression for the stored elastic energy in the crystal in large deformation regime:

$$f_{el}^{l} = Y_{100}^{l} \cdot \varepsilon^2 \tag{F.25}$$

with:

$$Y_{100}^{l} = \frac{1}{(S_{11} + S_{12})} \cdot \left[\frac{S_{12}}{(S_{11} + S_{12})} + \frac{S_{11}}{(S_{11} + S_{12})(\varepsilon + 1)^2} + \frac{\varepsilon}{2(\varepsilon + 1)^2}\right] \tag{F.26}$$

b. The [111] habit plane

Similarly, using the Cauchy stress tensor $[\boldsymbol{T}] = \begin{bmatrix} \sigma & 0 & 0 \\ 0 & 0 & k\sigma \\ 0 & k\sigma & 0 \end{bmatrix}$ and strain tensor $\begin{bmatrix} \varepsilon & 0 & 0 \\ 0 & \varepsilon_2 & \varepsilon/2 \\ 0 & \varepsilon/2 & \varepsilon_2 \end{bmatrix}$ in Equation F.6, where $\sigma_4 = k\sigma_1 = k\sigma = \varepsilon/S_{44}$ with $k = \frac{S_{11}}{S_{44}}$ is a real number, the deformation matrix is:

$$[\boldsymbol{F}] = \begin{bmatrix} \varepsilon + 1 & 0 & 0 \\ 0 & \varepsilon_2 + 1 & \varepsilon/2 \\ 0 & \varepsilon/2 & \varepsilon_2 + 1 \end{bmatrix} \tag{F.27}$$

Hence,

$$\boldsymbol{J} = |\det \boldsymbol{F}| = (\varepsilon + 1) \cdot [(\varepsilon_2 + 1)^2 - \varepsilon^2/4] \tag{F.28}$$

The right Cauchy-Green deformation tensor

$$[\boldsymbol{C}] = [\boldsymbol{F}]^{\boldsymbol{T}} \cdot [\boldsymbol{F}] = \begin{bmatrix} (\varepsilon + 1)^2 & 0 & 0 \\ 0 & (\varepsilon_2 + 1)^2 + \varepsilon^2/4 & \varepsilon(\varepsilon_2 + 1) \\ 0 & \varepsilon(\varepsilon_2 + 1) & (\varepsilon_2 + 1)^2 + \varepsilon^2/4 \end{bmatrix} \tag{F.29}$$

Then, the Almansi-Lagrange strain tensor:

$$\begin{aligned} [\boldsymbol{e}] &= \frac{1}{2}([\boldsymbol{I}] - [\boldsymbol{C}^{-1}]) \\ &= \frac{1}{2} \begin{bmatrix} 1 - \dfrac{1}{(\varepsilon + 1)^2} & 0 & 0 \\ 0 & 1 - \dfrac{(\varepsilon_2 + 1)^2 + \varepsilon^2/4}{D^2} & \dfrac{\varepsilon(\varepsilon_2 + 1)}{D^2} \\ 0 & \dfrac{\varepsilon(\varepsilon_2 + 1)}{D^2} & 1 - \dfrac{(\varepsilon_2 + 1)^2 + \varepsilon^2/4}{D^2} \end{bmatrix} \end{aligned} \tag{F.30}$$

With $D = (\varepsilon_2 + 1)^2 - \varepsilon^2/4$.

And the second Poila-Kirchhoff strain tensor:

$$[\widetilde{\boldsymbol{T}}] = \boldsymbol{J} \cdot [\boldsymbol{F^{-1}}] \cdot [\boldsymbol{T}] \cdot [\boldsymbol{F^{-1}}]^{\boldsymbol{T}}$$
$$= (\varepsilon + 1)\sigma \cdot D \cdot \begin{bmatrix} \frac{1}{(\varepsilon+1)^2} & 0 & 0 \\ 0 & \frac{-k\varepsilon(\varepsilon_2+1)}{D^2} & \frac{k((\varepsilon_2+1)^2+\varepsilon^2/4)}{D^2} \\ 0 & \frac{k((\varepsilon_2+1)^2+\varepsilon^2/4)}{D^2} & \frac{-k\varepsilon(\varepsilon_2+1)}{D^2} \end{bmatrix} \quad \text{(F.31)}$$

Then the stored elastic energy in the crystal is estimated as follow:

$$f_{el}^{l} = Y_{111}^{l} \cdot \varepsilon^2 \quad \text{(F.32)}$$

with:

$$Y_{111}^{l} = \frac{1}{4}\frac{\varepsilon^2}{S_{11}} \cdot \frac{(\varepsilon+2)D}{(\varepsilon+1)^3} + \frac{1}{2}\frac{\varepsilon^2}{S_{44}}\frac{(\varepsilon+1)(\varepsilon_2+1)}{D}\left[\left(\frac{2(\varepsilon_2+1)^2+\varepsilon^2/2}{D^2} - 1\right)\right] \quad \text{(F.33)}$$

APPENDIX G CALCULATION PREFERENCES

1. Calculation of η

As mentioned earlier (Equation F.14), $\eta = \frac{1}{a}\frac{\partial a}{\partial x}$ is the rate of change of the lattice constants with composition. If $\frac{\partial a}{\partial x}$ is a constant over the entire composition range, it is called Vegard's coefficient. From the definition, it is easy to see that η is not a constant. Actually, in studies [155, 201, 454], η is defined to be equal to $\eta = \frac{1}{a_0} * \frac{\partial a}{\partial x}$ with a_0 is the lattice constant of the interested solid solution. The definition of η makes it become flexible by changing the unit of composition and the reference value a_0. However, in many studies reporting the calculation of coherent miscibility gap using Cahn's approach, η is considered as a constant. The unclear explaination of the calculation procedures of η value makes us confused. Because η is an important parameter in the calculation of coherent miscibility gap, in this study, we would like to first, consider η as a paramenter represent the lattice misfit between two lattices and second, explain how η alters with changing reference value a_0. The variation of η corresponding to the reference a_0 of either two pure compounds is not significant, e.g. ~6% in Al-Zn system. However, in order to avoid any consfusion in the calculation of η value, we consider two kind of η:

Constant η should be suitable for the solid solution which obeys Vegard's rule or slightly deviates from Vegard's rule:

$$\eta = \frac{1}{a_0} * \frac{\partial a}{\partial x} = \left| \frac{1}{a_{A_{0.5}B}} * \frac{a_A - a_{A_{0.5}B}}{0.5} \right| = 2\left| \frac{a_A - a_B}{a_A + a_B} \right| \qquad \text{(G.1)}$$

where A and B are two pure which form the solid solution A_xB. The absolute value sign is used since only the magnitude of η is important.

Composition-dependent η is appropriate for the solid solution which significantly deviates from Vegard's rule:

$$\eta(x) = \frac{1}{a(x)} * \frac{\partial a}{\partial x} \qquad \text{(G.2)}$$

2. Temperature dependence of physical properties

For calculating the coherent miscibility gap and spinodal, we need to use some physical properties such as lattice parameters, molar volumes, elastic constants, etc. Clearly, they are temperature dependent. In this study, for showing the effect of temperature dependence of physical properties in our calculation of coherent miscibility gap of various system, two kinds of calculation namely calculation of coherent miscibility gap with or without temperature effect are performed:

For calculation without temperature effect, all physical properties are taken from available data at or near room temperature.

For calculation with temperature effect, all physical properties need to be calculated at different temperatures. The elastic constants are considered as functions of temperature by fitting available data of elastic constants with temperature. If there are available data of lattice parameters with temperature, we could do the fitting process to obtain a temperature dependent function of lattice parameters. If no data is available, the lattice parameters are considered as a function of thermal expansion as follow:

$$a = a^{*} \cdot \left(1 + \alpha \cdot (T - T^{*})\right) \tag{G.3}$$

with a and a^{*} are the lattice constants at temeprature T and T^{*}, respectively; α is the thermal expansion coefficient. Then, η, V_m, etc. are calculated correspondingly.

3. Physical properties of the solid solution

The experimental data of elastic constants, lattice parameters of the solid solution are not always available in all systems. If experimental or modeled data are available, it is easy to fit the elastic constants, lattice parameters of the solid solution as a function of its compositions. For many cases, the function is linear. In our following case study, we would do the fitting of the reported physical properties with the composition of the solid solution. However, if there is no reported data available, we assume that elastic constants, lattice parameters of the solid solution are linearly dependent on its compositions.

APPENDIX H ELASTIC PROPERTIES OF CUBIC MATERIALS

In this study, the values of elastic constants near room temperature are used in the calculation without temperature effect of elastic properties. The expression of elastic constants as a function of temperature is resulted from fitting the reported elastic constants at various temperatures.

Notice that in order to estimate the elastic constants of the FCC Al-Zn solid solution, we first calculated the elastic constants of the metastable FCC Zinc as no experimental data are reported in literature. The elastic constants were calculated *Ab initio* via Density Functional Theory (DFT). In the present study, DFT are based on the Plane-Wave basis sets and are done using the *Vienna Ab initio Simulation Package* (VASP) [115-118] using periodic boundary conditions. The Projected Augmented Wave (PAW) approach is employed to represent the core electrons [414, 415]. Generalized Gradient Approximation (GGA) parameterized by Perdew, Burke and Ernzerhof (PBE) [416, 417] was used as the exchange-correlation functional. Plane-Wave kinetic cut-of energy of 520 eV and Monkhorst Pack grid of 13×13×13 dimension to sample the Brillouin zone with a first order Methfessel-Paxton smearing parameter σ of 0.02 eV are used to ensure the force and energy convergence criterion are better than 0.02 eV/Å and 0.01 meV, respectively. The procedure to determine the elastic constants C_{ij} is well established and is detailed in our prior publications [102, 103]. Basically, it consists in calculating the energy difference between the equilibrium lattice $\boldsymbol{R}$ and distorted lattice $\boldsymbol{R}'$, by applying very small strains (ε) in each crystallographic direction, in order to make sure we stay within the elastic domain. The relation between the equilibrium and distorted lattice is linear and defined as: $\boldsymbol{R}' = \boldsymbol{R}\boldsymbol{D}(\varepsilon)$ where $\boldsymbol{D}$ is the distortion matrix. For the FCC structure, there are 3 independent elastic constants and many distortions matrices can be found in Ravindran et al. [455] C_{ij} are obtained by fitting the 3 energy curves $El(\varepsilon)$ by a second order polynomial.

Table H.1 List of elastic properties collected from the literature

Material/ Structure	**T [K]**	**Elastic constants**			**Reference**
		C_{11} [GPa]	**C_{12} [GPa]**	**C_{44} [GPa]**	
Al	293	106.49	60.39	28.28	Gerlich & Fisher [305]

	0-925	$117.6243 - 0.0392 \cdot T$	$63.0013 - 0.0094 \cdot T$	$32.5909 - 0.0151 \cdot T$	Kamm & Alers [304] and Gerlich & Fisher [305]
Ag	300	124	94	46.5	Chang & Himmel [249]
	300-800	$134.6136 - 0.0350 \cdot T$	$99.6409 - 0.0192 \cdot T$	$52.2209 + 0.0191 \cdot T$	Chang & Himmel [249]
Au	300	158.24	131.56	34.92	Cagin et al. [247]
	300-1000	$185.92 - 0.088 \cdot T$	$151.97 - 0.0648 \cdot T$	$42.881 - 0.0257 \cdot T$	Cagin et al. [247]
Co (FCC)	710	223	186	110	Strausse et al. [369]
Cu	300	170.0	122.5	75.8	Chang & Himmel [249]
	300-800	$181.7955 - 0.0405 \cdot T$	$128.5000 - 0.0200 \cdot T$	$83.9645 - 0.0271 \cdot T$	Chang & Himmel [249]
Ni	300	250.80	150.00	123.50	Alers et al. [345]
	280-760	$270.1 - 0.0625 \cdot T$	$152.52 - 0.0075 \cdot T$	$135.38 - 0.0392 \cdot T$	
Pt	300	289.63	239.55	65.07	Cagin et al. [247]
	300-1500	$319.2 - 0.0926 \cdot T$	$261.43 - 0.0686 \cdot T$	$73.223 - 0.0271 \cdot T$	Cagin et al. [247]
Zn (FCC)	0	106	70	11	Our first priciple calculation
CaO	300	220.53	57.67	80.3	Oda et al. [264]
	300-1200	$234.39 - 0.0471 \cdot T$	$57.4884 + 0.0015 \cdot T$	$82.4079 - 0.0075 \cdot T$	Oda et al. [264]
MgO	273	298.96	96.42	157.13	Isaak et al. [263]

	300-1800	$314.7003 - 0.0597 \cdot T$	$96.5851 - 0.0008 \cdot T$	$161.0125 - 0.0151 \cdot T$	Sumino et al. [262] and Isaak et al. [263]
KCl	298	40.69	7.11	6.31	Slagle & McKinstry [317]
	298-1073	$41.54 - 31.88 \cdot 10^{-3} \cdot (T - 273.15) + 3.47 \cdot 10^{-6} \cdot (T - 273.15)^2$	$6.96 + 4.36 \cdot 10^{-3} \cdot (T - 273.15) - 4.23 \cdot 10^{-6} \cdot (T - 273.15)^2$	$6.34 - 1.2 \cdot 10^{-3} \cdot (T - 273.15) - 0.88 \cdot 10^{-6} \cdot (T - 273.15)^2$	Slagle & McKinstry [317]
NaCl	298	49.47	12.88	12.87	Slagle & McKinstry [317]
	298-1073	$50.39 - 37 \cdot 10^{-3} \cdot (T - 273.15) + 4.36 \cdot 10^{-6} \cdot (T - 273.15)^2$	$12.69 + 12.78 \cdot 10^{-3} \cdot (T - 273.15) + 12.92 \cdot 10^{-6} \cdot (T - 273.15)^2$	$12.86 - 3.08 \cdot 10^{-3} \cdot (T - 273.15) - 1.58 \cdot 10^{-6} \cdot (T - 273.15)^2$	Slagle & McKinstry [317]
$Na_{1-x}K_xCl$	298	$C_{11}^{NaCl}(1 - x) + C_{11}^{KCl}x - 25x(1 - x)$	$C_{12}^{NaCl}(1 - x) + C_{12}^{KCl}x - 11x(1 - x)$	$C_{44}^{NaCl}(1 - x) + C_{44}^{KCl}x - 10x(1 - x)$	Botaki et al. [319]
	298-1073	$C_{11}^{NaCl}(1 - x) + C_{11}^{KCl}x - 25x(1 - x)$	$C_{12}^{NaCl}(1 - x) + C_{12}^{KCl}x - 13x(1 - x)$	$C_{44}^{NaCl}(1 - x) + C_{44}^{KCl}x - (14.394 - 0.0147 \cdot T)x(1 - x)$	Botaki et al. [319]

APPENDIX I LATTICE PARAMETERS, MOLAR VOLUME AND THERMAL EXPANSION COEFFICIENTS

Table I.1 List of lattice parameters and molar volume used in this study

Material/ Structure	**Lattice parameter [m]**	**Molar volume [m^3/mol]**	**Reference**
Al	$403 \cdot 10^{-12}$	$9.78189 \cdot 10^{-6}$	Kittel [300]
Ag	$408.57 \cdot 10^{-12}$	$10.2696 \cdot 10^{-6}$	Subramania & Perepezko [277]
Au	$407.84 \cdot 10^{-12}$	$1.0215 \cdot 10^{-5}$	Lubarda [243]
Co	$354.8 \cdot 10^{-12}$	$6.7252 \cdot 10^{-6}$	Cerda et al. [368]
Cu	$361.46 \cdot 10^{-12}$	$7.111 \cdot 10^{-6}$	Subramania & Perepezko [277]
Ni	$352.4 \cdot 10^{-12}$	$6.5888 \cdot 10^{-6}$	Lubarda [243]
Pt	$392.38 \cdot 10^{-12}$	$9.0951 \cdot 10^{-6}$	Arblaster [244]
Zn (FCC)	$3.79 \cdot 10^{-10}$	$8.65149 \cdot 10^{-6}$	Muller et al. [301]
CaO	$4.811 \cdot 10^{-10}$	$16.764 \cdot 10^{-6}$	Fiquet et al. [258]
	$(4.7866 + 7.6 \cdot 10^{-5} \cdot T) \cdot 10^{-10}$		Fiquet et al. [258]
MgO	$4.210 \cdot 10^{-10}$	$11.228 \cdot 10^{-6}$	Fiquet et al. [258]
	$(4.180459 + 7.3 \cdot 10^{-5} \cdot T) \cdot 10^{-10}$		Fiquet et al. [258]
KCl	$6.2916 \cdot 10^{-10}$	$37.5004 \cdot 10^{-6}$	Barrett & Wallace [315]
NaCl	$5.64 \cdot 10^{-10}$	$27.0141 \cdot 10^{-6}$	Barrett & Wallace [315]

Table I.2 Thermal expansion coefficient of substances

Material/ Structure	**Linear thermal expansion coefficient**	**Reference**

	[10^{-6}/K]	
Al	23.1	Cohen et al. [245]
Ag	18.9	Cohen et al. [245]
Au	14.2	Cohen et al. [245]
Co (HCP)	13	Cohen et al. [245]
Cu	16.5	Cohen et al. [245]
Ni	13.4	Cohen et al. [245]
Pt	8.8	Cohen et al. [245]
Zn (HCP)	30.2	Cohen et al. [245]
KCl	36.2	Pathak & Vasavada [316]
NaCl	39.8	Pathak & Vasavada [316]

APPENDIX J HEAT CAPACITY OF $LiFePO_4$

The Debye temperature is a fundamental parameter used to describe the vibrations of atoms within a crystal, its isochoric heat capacity C_v and isobaric heat capacity C_p. The Debye temperature can be estimated from the physical properties of the crystal [372, 456, 457]. The estimated Debye temperature of $LiFePO_4$ is about 550 K using the reported formulae [456] and elastic constants [25]. According to our previous study [101], unlike most of the crystal substances, only one Debye temperature is not sufficient to describe the experimental data of isobaric heat capacity C_p of $LiFePO_4$ reported by Loos et al. [100]. A significant contribution of vibrations induced by magnetism was claimed [101]. According to the authors [101], beyond a critical temperature, the Debye temperature would reach a plateau. However, as the temperature continues to increase, a decrease of Debye temperature is found in our analysis. Hence, a more suitable analysis of heat capacity of $LiFePO_4$ is necessary.

1. Magnetism heat capacity

In the isobaric heat capacity of $LiFePO_4$ measured by Loos et al. [100], the peak of heat capacity observed at a low temperature should be considered as the Neel peak which is related to the second phase transition from the antiferromagnetic phase into the paramagnetic phase. The Neel temperature of $LiFePO_4$ is reported at 50±2 K [108, 406, 458-460] which is accepted in this study. It is possible to approximate the peak of the specific heat that the phase transition of $LiFePO_4$ with a power law like other compounds [461]:

$$C_p^{mag} = a_{\pm}|t|^{\alpha} + b \tag{J.1}$$

with

$$t = \frac{T - T_N}{T_N} \tag{J.2}$$

where $a_{\pm}$; b; and α are optimized parameters and ($a_+ = -33$ for $T > T_N$; $a_- = -80$ for $T < T_N$; $\alpha = 0.4$; $b = 25$). For simplicity, we considered C_p^{mag} which is significant in the vicinity of the Neel temperature ($25\,K \leq T \leq 52.5\,K$) and in other temperature range, it is negligible (Figure J.1). Obviously, here the short-range-ordering of electron spins is negligible.

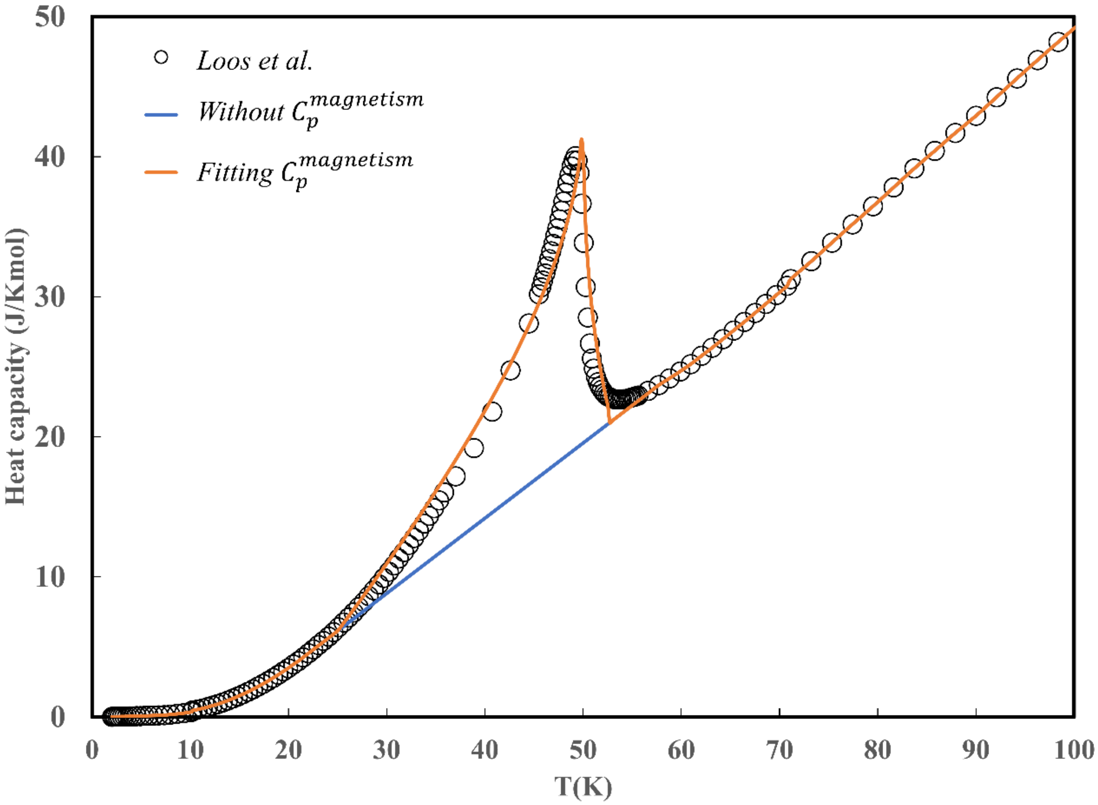

Figure J.1: Magnetic heat capacity of $LiFePO_4$ extracted from experimental data of Loos et al. [100] in comparison with the optimized magnetic heat capacity according to Equation J.1.

2. Debye model

The magnetic heat capacity is used for describing the additional contribution on total specific heat capacity by phase transition in the vicinity of Neel temperature only. The Debye model is used for describing the heat capacity of a crystal substance in a wide temperature range excluding the magnetic heat capacity contribution. However, we have found that the Debye model fails to fit experimental heat capacity of olivine $LiFePO_4$ [100] with temperature. First, the Debye temperature θ_D° is estimated as follow [372, 456, 457]:

$$\theta_D^{\circ,LiFePO_4} = \frac{h}{k_B}\left[\frac{3n}{4\pi}\frac{N_A\rho}{M}\right]^{\frac{1}{3}} v_m \qquad (J.3)$$

where h is the Plack's constant; k_B is Boltzmann's constant; N_A is Avogadro's number; ρ is the density; M is the molecular weight of the compound; and n is the number of moles of atoms per mole of chemical formulation; and v_m, which corresponds to the average sound velocity in the polycrystalline material, is approximately given by:

$$v_m = \left(\frac{1}{3}\left[\frac{2}{{v_s}^3} + \frac{1}{{v_l}^3}\right]\right)^{-\frac{1}{3}} \tag{J.4}$$

with,

$$v_s = \sqrt{\frac{G}{\rho}}$$
$$v_l = \sqrt{\frac{B + \frac{4}{3}G}{\rho}} \tag{J.5}$$

where G is the shear modulus and B is the bulk modulus. Using the reported elastic constants of LiFePO4 [25] and the formulae for calculating B and G [456], the bulk modulus B and the shear modulus G are considered as the average of the corresponding Voight and Reuss moduli (Table J.1). The molar volume is taken from the experimental work of Andersson et al. [160] and the density is calculated as $\rho = \frac{M}{V_m}$ (Table J.1). The Debye temperature estimated by Equation J.3 is $\theta_D^{\circ,LiFePO_4} = \mathbf{548}$ K. Please notice that the physical properties are considered as average values at room temperature. The isochoric heat capacity C_v is then calculated using Debye's model:

$$C_v = 9N_A k_B \left(\frac{T}{\theta_D^{\circ}}\right)^3 \int_0^{\frac{\theta_D^{\circ,LiFePO_4}}{T}} \frac{x^4 e^x}{(e^x - 1)^2} dx \tag{J.6}$$

According to Debye model, the isobaric heat capacity of LiFePO4 should be described as:

$$\mathrm{C}_p^{\circ} = C_v + \alpha^2 B V_m T \tag{J.7}$$

The term $\alpha^2 B V_m T$ in Equation J.7 corresponds to the difference in specific heat capacities at constant volume and constant pressure. All three parameter α, B and V_m are temperature dependent.

The consideration of average value or temperature-dependent value of α, B and V_m would affect the calculated C_p°. For simplicity, at first, only temperature-independent physical properties are considered (Table J.1). The thermal expansion α is considered at room temperature using the reported molar volume change $V_m(T)$ of $LiFePO_4$ upon temperature [462]. However, C_p° calculated from Equation J.7 could not describe the reported experimental data of Loos et al. [100] (Figure J.2). Considering the temperature effect on physical properties, the molar volume is fitted linearly with temperature using experimental data of Rao et al. [462]:

$$V_m(T) = (0.002 \cdot \mathrm{T(K)} + 43.285) \cdot 1\mathrm{E}-06 \left(\frac{\mathrm{m}^3}{\mathrm{mol}}\right) \tag{J.8}$$

Then the thermal expansion coefficient is calculated as follow:

$$\alpha(T) = \frac{1}{V_m(T)}\left(\frac{\partial V_m(T)}{\partial T}\right)_P \tag{J.9}$$

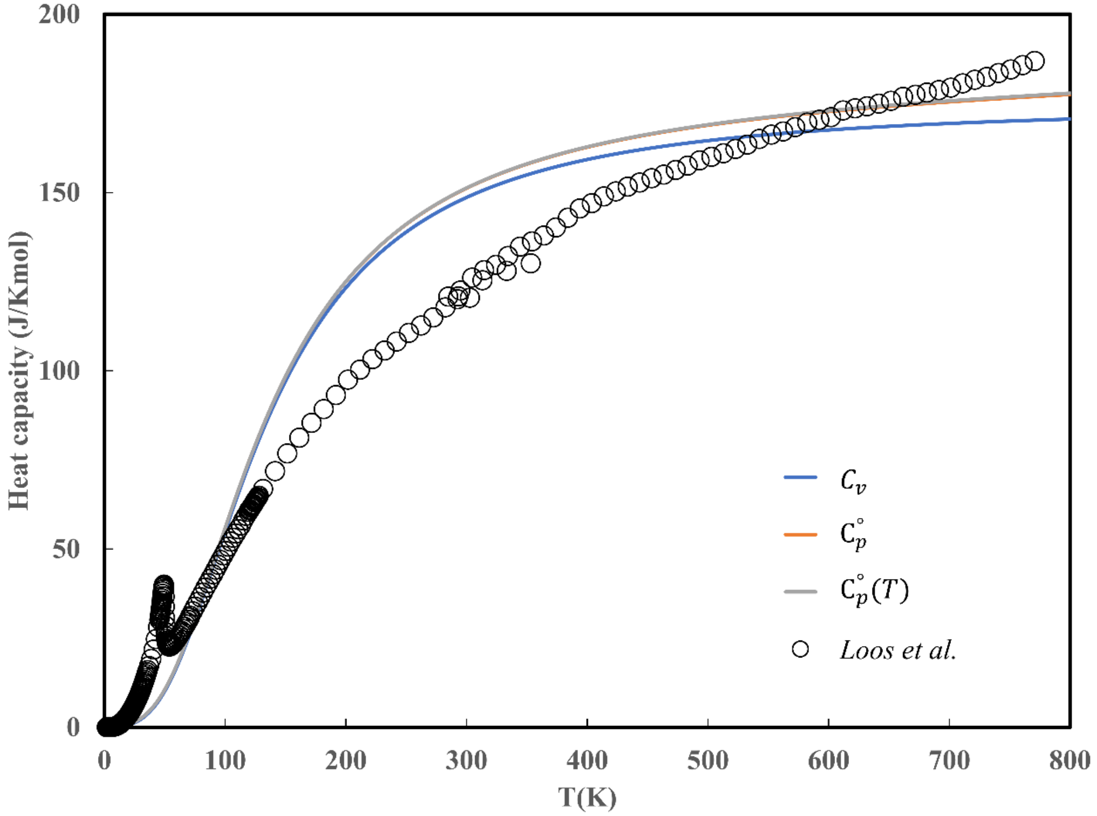

Figure J.2: Calculation of isochoric heat capacity C_v using the Debye model and the isobaric heat capacity with ($C_p^\circ(T)$) and without (C_p°) considering the temperature effect on physical properties.

The elastic Grüneisen parameter, in this case, is considered as the Dugdale and Macdonald one: $\gamma = \frac{1}{2}B' - \frac{1}{2} = \frac{1}{2}\left(\frac{\partial B}{\partial P}\right)_T - \frac{1}{2}$ [463] where $B' = 4.3$ [101, 464]. Hence, the temperature dependent $B(T)$ is calculated as follow [465]:

$$B(T) = B(0\ K) + \frac{2\gamma^2}{V_m(0\ K)}\int_0^T C_p dT \tag{J.10}$$

Even if temperature dependent terms $\alpha(T)$, $B(T)$ and $V_m(T)$ are considered, the calculated $C_p^\circ(T)$ is still insufficient in describing the isobaric heat capacity of $LiFePO_4$ (Figure J.2). Moreover, considering temperature-dependent terms $\alpha(T)$, $B(T)$ and $V_m(T)$ does not have significant impact on calculation of C_p°. So far, unlike most crystal substances, C_p° calculated from Equation J.7 could not describe the reported experimental data of Loos et al. [100].

Table J.1 Physical properties of $LiFePO_4$ and $FePO_4$ used in our calculation

Parameter	**$LiFePO_4$**		**$FePO_4$**	
	Value	**Reference**	**Value**	**Reference**
$\boldsymbol{M}$	0.157755 kg/mol	-	0.150815 kg/mol	-
$\boldsymbol{\rho}$	3601 kg/m^3	-	3687 kg/m^3	-
$\boldsymbol{B}$	95 GPa	use $C_{ij}^{LiFePO_4}$[25]	68 GPa	use $C_{ij}^{FePO_4}$[25]
$\boldsymbol{G}$	47 GPa	use $C_{ij}^{LiFePO_4}$[25]	45 GPa	use $C_{ij}^{FePO_4}$[25]
$\boldsymbol{\theta_D^\circ}$	548 K	-	512 K	-
$\boldsymbol{V_m}$	4.381E-05 m^3/mol	Andersson et al. [160]	4.091E-05 m^3/mol	Andersson et al. [160]
$\boldsymbol{\alpha}$	4.557E-05	Rao et al. [462]	4.557E-05	-

$\boldsymbol{B'}$	4.3	Shang et al. [464] and Seifitokaldani et al. [101]	4.2	Seifitokaldani et al. [101]
$\boldsymbol{\gamma}$	1.65	-	1.6	-

3. Extended Debye model

As observed from Figure J.2, the Debye model is not sufficient in describing the heat capacity of $LiFePO_4$. There should exist other contribution to its heat capacity. We have shown that one Debye temperature is not enough to cover the heat capacity values over a wide temperature range [101]. The Debye temperatures from which the predicted heat capacity values fit the experimental data for $LiFePO_4$ [99, 100] (exclude the magnetic heat capacity C_p^{mag} contribution mentioned in part J.1) have been recalculated (Figure J.3). As we know, phonons are waves that make the molecule oscillate while magnons are what controls the movement of spins. According to our previous paper [101], the phonon-magnon interactions, which caused the vibrations induced by magnetism, represented as $C_p^{pho-mag}$ should be responsible to the change of Debye temperature. As we consider the change of Debye temperature θ_D with temperature T, a noticeable peak is also observed in Neel temperature range (Figure J.4). It means that the change of Debye temperature θ_D should be related to magnetic properties of $LiFePO_4$. Therefore, our prediction of the contribution of $C_p^{pho-mag}$ should make sense. For simplicity, we would like to model the change of Debye temperature with temperature and this Debye temperature should correspond to the sum of $C_v + C_p^{pho-mag}$ where C_v is heat capacity contribution of phonon vibrations and $C_p^{pho-mag}$ is heat capacity contribution of phonon-magnon interaction. The phonon-magnon coupling effect should be saturated at some point meaning that the Debye temperature $\theta_D^{LiFePO_4}$ should reach a critical value at a certain temperature. The Debye temperature $\theta_D^{LiFePO_4}$ of $LiFePO_4$ is described by a critical function of t where t is defined in Equation J.2:

$$\begin{cases} \theta_D^{LiFePO_4} = 880 - 440e^{-0.4t} \text{ if } T > T_N \\ \theta_D^{LiFePO_4} = 440 + 230t \text{ if } T < T_N \end{cases} \tag{J.11}$$

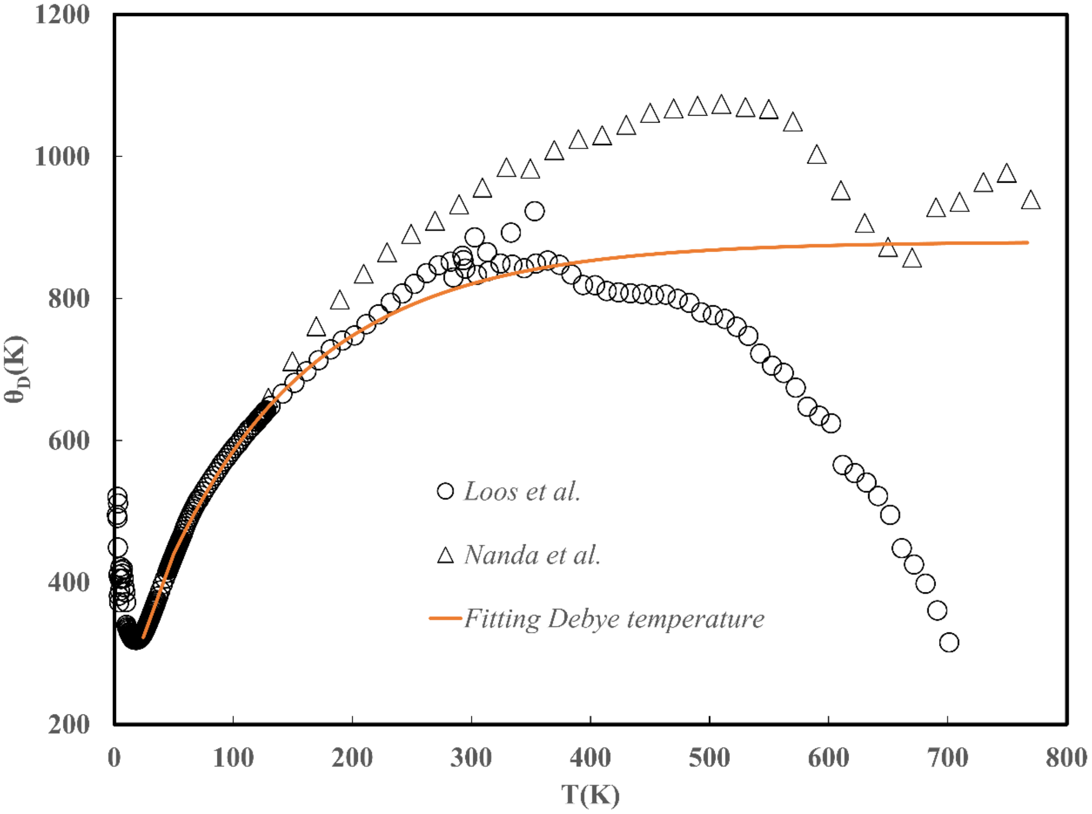

Figure J.3: Calculated Debye temperature function aimed at reproducing the experimental heat capacity values[99, 100] excluding the magnetic heat capacity contribution C_p^{mag}.

At low temperature ($T < T_N$), the calculation of Debye temperature is very sensitive to the accuracies of heat capacity. It means that a small change of heat capacity could cause a significant change of Debye temperature. Therefore, for a small temperature range, $T < T_N$, for simplicity, it is reasonable to consider Debye temperature as a linear function of temperature. The modeled Debye temperature is then used to calculate the sum of $C_v + C_p^{pho-mag}$ using Equation J.6. Using the Equation J.11 to calculate the Debye temperature, we would find the heat capacity contribution $C_p^* = C_v + C_p^{pho-mag} + \alpha^2 B V_m T$ (Figure J.5). The heat capacity contribution C_p^* could reasonably reproduce heat capacity up to 370 K. However, the increase rate of experimental heat capacity is much higher than the calculated one when $T > 370\ K$.

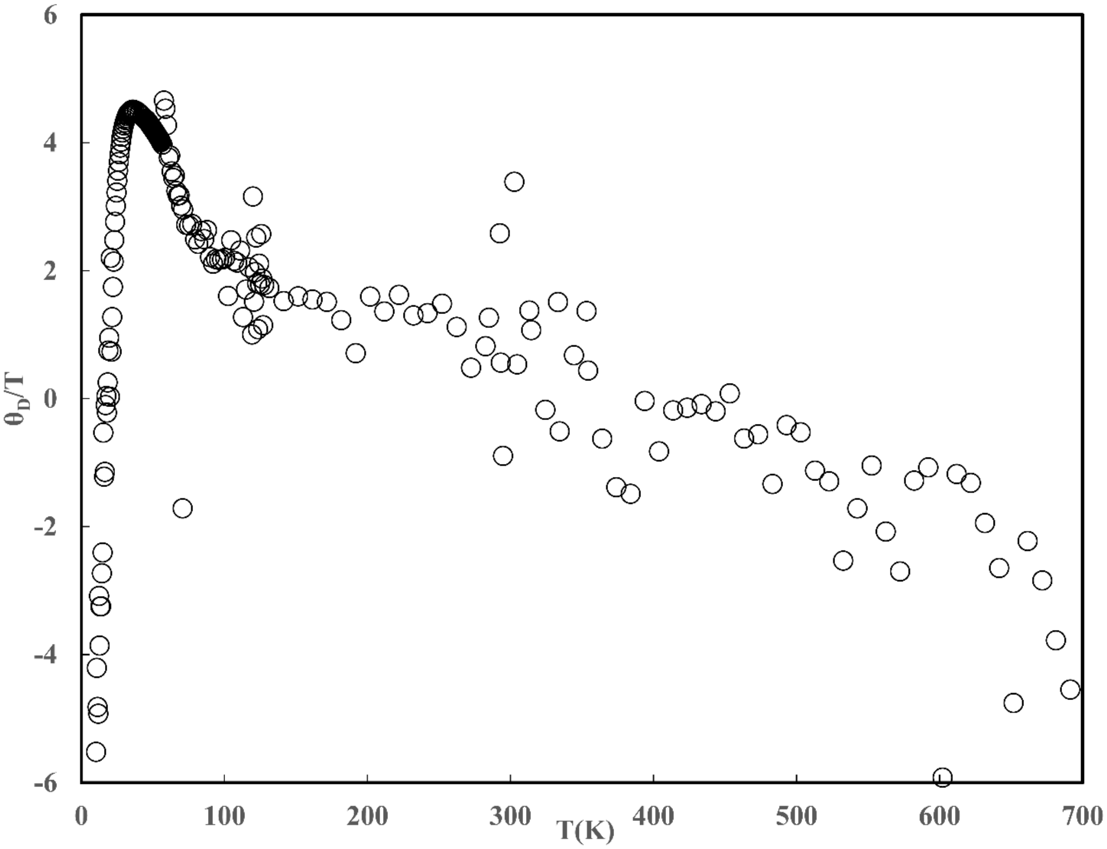

Figure J.4: Ratio of the calculated Debye temperature to temperature versus temperature. The calculated Debye temperature is taken from Figure J.3 which aimed at reproducing the experimental heat capacity values [100] excluding the magnetic heat capacity contribution C_p^{mag}.

Noticeably, unlike the typical reported behavior [101], instead of reaching a plateau, the Debye temperature decreases for temperature higher than the critical temperature. Similar behavior is found with the reported experimental heat capacities of Nanda et al. [99] (Figure J.3). Although the reported heat capacity values of Nanda et al. [99] are considering a $LiFePO_4$-3wt%C mixture, the study confirms the tendency of a decrease of the Debye temperature at high temperature for the olivine-$LiFePO_4$. It means that even with magnon-phonon interaction, the heat capacity values are predicted insufficiently at high temperatures (Figure J.5). Structure defects, which normally significant at high temperature, should be another contribution to heat capacity. The most common intrinsic defects found in $LiFePO_4$ crystals are anti-site defects, in which Fe atoms stay in Li sites while Li atoms occupy Fe sites [33, 466, 467]. Depending on experimental conditions, the anti-site defects range from 1-10% [403, 424, 468, 469]. However, it is noticeable that uncertainties exist in the quantitative measurement of the concentration of anti-site defects. The simulated high-angle annular dark-field (HAADF)-STEM images shows up to 15% of anti-site defects while the high resolution neutron diffraction measurements reveals 1% anti-site defects on the same sample [400]. The discrepancy could be explained by the non-homogeneous distribution of anti-sites through the whole lattice [400, 401]. In fact, the concentration of anti-site defects increase slightly with temperature and the anti-site defects are abruptly eliminated almost completely when the post-heat treatment temperature reaches about 700 K [403]. For the $LiFePO_4$ samples synthesized with solid state reaction, the higher annealed temperature, the lower the concentration of anti-site defects [400]. The anti-site defects could also reduce at room temperature via an electrochemical annealing process [402]. Loos et al. [100] prepared $LiFePO_4$ samples by a solvothermal method. The samples were heat treated at 773 K for 2h in an argon gas flow for minimizing lattice defects and especially, avoiding anti-site defects. The author did not perform any experiments to estimate the anti-site concentration and the anti-site effect was neglected in the measurement of heat capacity. From our perspectives, even the synthesized $LiFePO_4$ was free from anti-site defects before heat capacity measurements, the anti-site could be created during DSC measurements and those anti-site defects should be responsible for the increase of heat capacity at high temperatures.

Theorical calculation reveals the formation energy of the Li-Fe interchanged anti-site pairs Fe_{Li}-Li_{Fe} of 0.74eV [33]. Lower defect formation energy,~0.51÷0.55eV, has been found by ab initio DFT calculations [216, 404]. The molar heat capacity contribution of anti-site defects, C_{def}, are estimated thought the formation energy, E_{def}, and the entropy of defects, S_{def} [372]:

$$C_{def} \approx nRe^{(S_{def}/k_B)}\left(\frac{E_{def}}{k_BT}\right)^2 e^{(-E_{def}/k_BT)} \tag{J.12}$$

where n is the number of atoms per formula, R is gas constant, k_B is Boltzmann's constant. In Equation J.12, $\frac{S_{def}}{k_B}$ is hard to estimate. For close pack structure like metals, $\frac{S_{def}}{k_B} = 3$ for Cu and $\frac{S_{def}}{k_B} = 2.4$ for Al [372]. For $LiFePO_4$, $\frac{S_{def}}{k_B}$ should be smaller than that for metals and the value is put as 2 in the present study. With those parameters, the concentration of anti-sites which is negligible at room temperature ($c_{anti-site} = 2 \cdot 10^{-8}$), become significant at high temperatures ($c_{anti-site} = 0.0045$ at 800 K). In addition, there are other intrinsic defects in $LiFePO_4$ crystals. The average formation energy of vacancy in Li sites is 0.91 eV [404], which is relatively high in comparison with anti-sites defects and makes the vacancy defects less likely in the crystal. The contribution of vacancy in heat capacity can be also estimated by Equation J.12. Other possible defects mentioned in the work of Hoang & Johannes [404] is out of our interests since they should be corresponding to any charge related processes rather than a pure compound. According to our calculation, the contribution of heat capacity caused by defect is significant at high temperatures ($T > 370\ K$) (Figure J.6). Since structure defects like anti-sites and vacancies exist in the crystal, an anharmonic vibrations induced by those defects should further increase the heat capacity value at high temperatures. The anharmonic contribution is only significant at high temperature when there are nonnegligible number of defects:

$$C_{anhar} = \begin{cases} 0 & for\ T \leq 370\ K \\ 0.3 \cdot (T-370)^{0.5} & for\ T > 370\ K \end{cases} \tag{J.13}$$

The anharmonic heat capacity, C_{anhar}, function was chosen to reproduce the experimental data [100]. Then $C_p^{total} = C_p^* + \sum C_{def} + C_{anhar}$ could reasonably reproduce the heat capacity of $LiFePO_4$ up to 770 K. To sum up, the isobaric heat capacity C_p of $LiFePO_4$ could be calculated as the quasi-harmonic approximation (QHA) combined with the Debye model as follow:

$$C_p^{total} = C_p^{mag} + C_v + C_p^{pho-mag} + \alpha^2 B V_m T + \sum C_{def} + C_{anhar} \tag{J.14}$$

where C_p^{mag} is the heat capacity contributed by magnetism; C_v is the isochoric heat capacity induced by phonon; $C_p^{pho-mag}$ is the heat capacity induced by the phono-magnon interaction; and C_{def} is the heat capacity induced from structure defects including anti-site defects and vacancies and C_{anhar} is the heat capacity contribution of anharmonic vibrations caused by the imperfect crystal structure.

From the knowledge of the heat capacity, we could estimate the change of the enthalpy of formation upon temperatures. Moreover, the entropy contribution, then the Gibbs energy of mixing could be found. For calculating the molar Gibbs energy of $LiFePO_4$, the heat capacity experimental data of

Loos et al. [100] without magnetism contribution of $LiFePO_4$ is fitted as a function of temperature (Appendix K). Consequently, its entropy at room temperature is estimated as follow:

$$S_{LiFePO_4}^{298.15} = \int_0^{298.15} \frac{C_p^{LiFePO_4}}{T} dT + S_{LiFePO_4}^{mag} \tag{J.15}$$

where $S_{LiFePO_4}^{298.15}$ is the molar entropy of $LiFePO_4$ at room temperature, and $S_{LiFePO_4}^{mag}$ is the molar magnetic entropy calculated from the magnetism heat capacity:

$$S_{LiFePO_4}^{mag} = \int_0^{\infty} \frac{C_p^{mag}}{T} dT = R\ln(1+\beta) \tag{J.16}$$

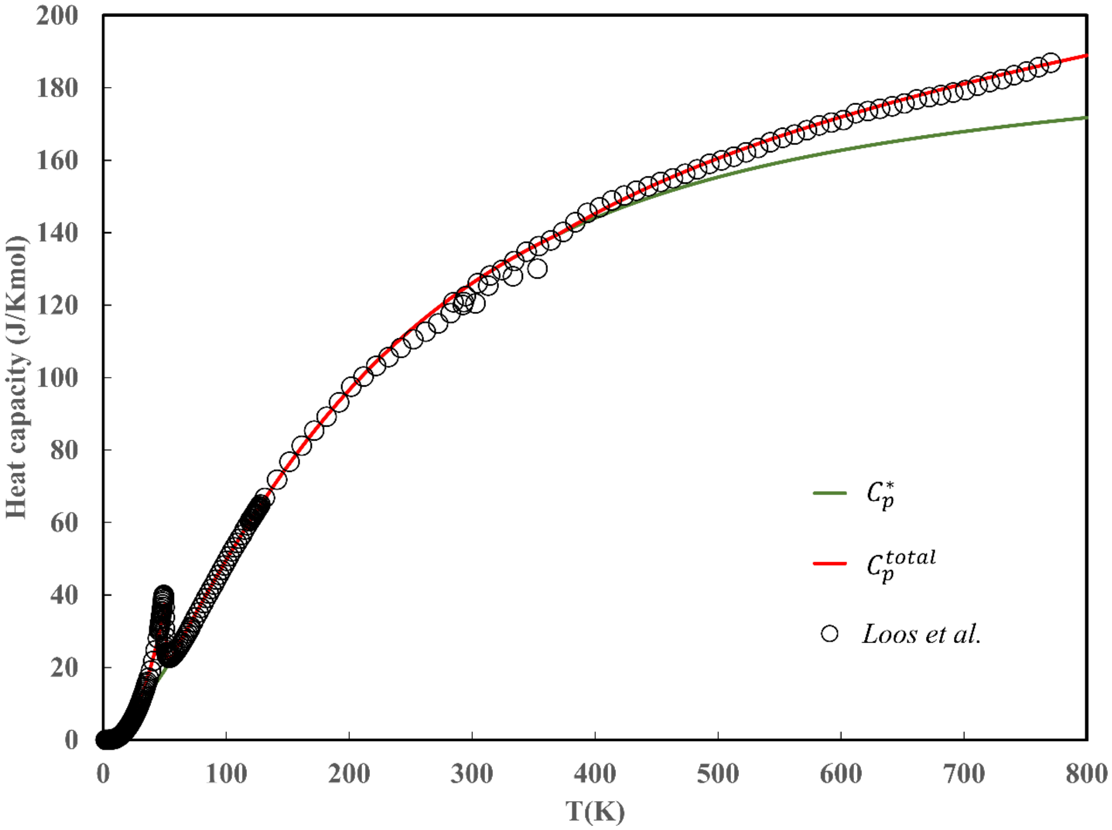

Figure J.5: Calculation of heat capacity $C_p^* = C_v + C_p^{pho-mag} + \alpha^2 B V_m T$ and C_p^{total} in comparison with experimental data [100].

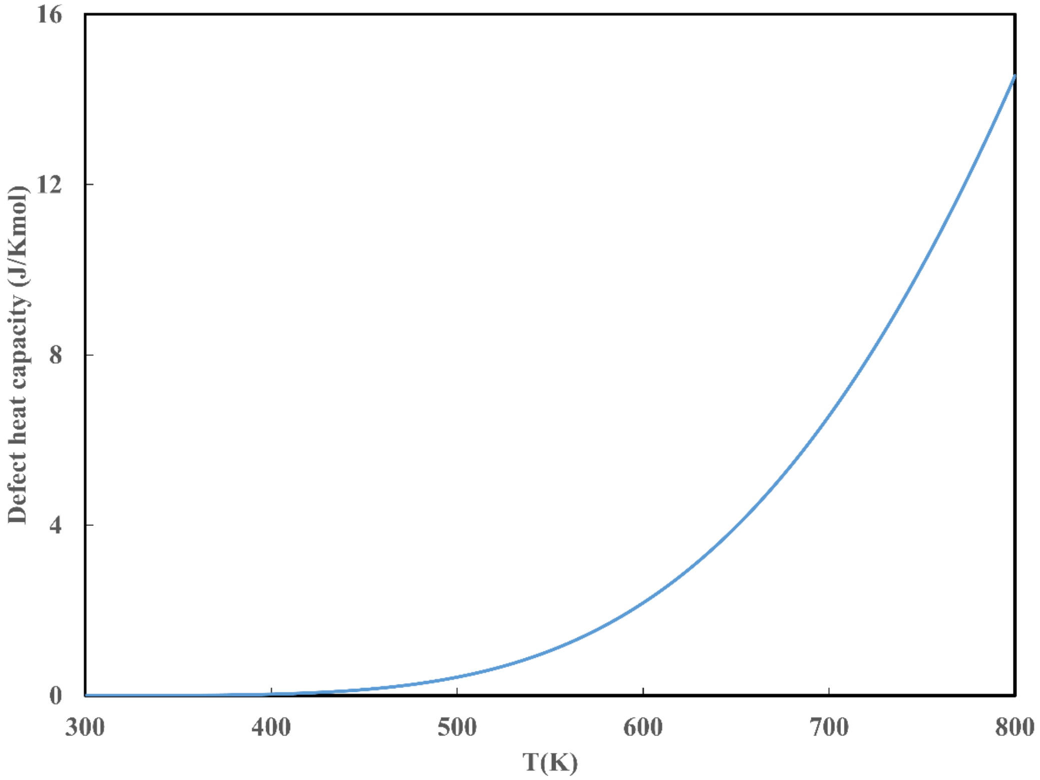

Figure J.6: Calculation of heat capacity caused by defects (anti-sites and vacancy) according to Equation J.12.

APPENDIX K GIBBS ENERGY AND ELASTIC CONSTANTS OF OLIVINE COMPOUNDS

For modeling the para-equilibria of the $Li(Mn_yFe_{1-y})PO_4$-$(Mn_yFe_{1-y})PO_4$ battery join, first, Gibbs energy of pure $LiFePO_4$, $FePO_4$, $LiMnPO_4$, and $MnPO_4$ are necessary. Their Gibbs energies are calculated from the enthalpy and entropy at room temperature and the change of the Gibbs energy versus temperature is estimated through the heat capacity of the substances.

1. $LiFePO_4$

Among the olivine substances, $LiFePO_4$ draws the most attention. The heat capacity of olivine $LiFePO_4$ is well reported by Loos et al. [100] and the vibration induced by magnetism is investigated [101]. We have shown that beyond the normal contribution of isobaric heat capacity including C_v, $\alpha^2 B V_m T$ and C_p^{mag}, the heat capacity contribution induced by phonon-magnon interaction $C_p^{pho-mag}$, the heat capacity induced from anti-site defects and thermally activated vacancies C_{def}, and heat capacity contribution of anharmonic vibrations caused by those defects C_{anhar} are significant for olivine – $LiFePO_4$ (Appendix J). The heat capacity of $LiFePO_4$ is presented as a function of temperature by fitting the experimental data of Loos et al. [100] with temperature:

$$\begin{aligned} C_p^{LiFePO_4}(J.mol^{-1}.K^{-1}) &= -2.08612524E03 - 1.06550805 \cdot T \\ &+ 4.67344530E06 \cdot T^{-2} + 4.08265171E-04 \cdot T^2 \\ &+ 4.27762581E02 \cdot \log T \end{aligned}$$

$$\text{with } 292\ K \leq T \leq 800\ K \qquad \text{(K.1)}$$

$$\begin{aligned} C_p^{LiFePO_4}(J.mol^{-1}.K^{-1}) &= 2.26443429 - 1.02819746 \cdot T - 2.51384702E \\ &- 03 \cdot T^2 - 2.22335032E - 06 \cdot T^3 + 7.31991238E \\ &- 09 \cdot T^4 + 3.83157327E - 01 \cdot T \cdot \log T + C_p^{mag} \end{aligned}$$

$$\text{with } 0\ K \leq T \leq 292\ K$$

From the values of heat capacity, the molar magnetic entropy of $LiFePO_4$ is $S_{LiFePO_4}^{mag} = 4.646\ (J.mol^{-1}.K^{-1})$ and our calculated absolute entropy value $S_{LiFePO_4}^{298.15} = 131.09(J.mol^{-1}.K^{-1})$ is about the reported values in Churikov et al. [113] (Table K.1). Moreover, the average magnetic moment per atom estimated from Equation J.16 is $\beta = 0.7485$. It means that the average magnetic moment of $LiFePO_4$ is 5.24 Bohr magneton in agreement with other studies [405-411]. Additionally, the enthalpy of formation of $LiFePO_4$ estimated from our DFT simulation is similar to that of Xie et al. [25]. However, even taking into account the integration of heat capacity, the calculated enthalpy of formations at room temperature are still more negative than the one estimated through the high-temperature melt solution calorimetry [111]. Furthermore, our estimated Gibbs energy of formation of $LiFePO_4$ is similar to the reported value of Xie et al. [25]. Nevertheless, both values are slightly more negative than Gibbs energy of formation of $LiFePO_4$ shown in He et al. [112] (Table K.1).

2. $FePO_4$

For $FePO_4$, only one experimental set of isobaric heat capacity is measured by Shi et al. [104]. In fact, α-$FePO_4$ or berlinite-$FePO_4$ with the Neel temperature of $T_N = 25\ K$ [104-107] which belongs to the trigonal group, is used in Shi et al. [104]. The olivine-$FePO_4$ shows a higher Neel temperature ($T_N \cong 125\ K$) [108-110]. Due to the lack of experimental data of heat capacity of orthorhombic-$FePO_4$, it is very difficult for us to formulate the molar Gibbs energy of olivine-$FePO_4$. Since the vibration induced by phonon-magnon interaction is significant in triphylite-$LiFePO_4$ and berlinite-$FePO_4$ [101], the phonon-magnon interaction should also be considered in heterosite-$FePO_4$. The Debye temperature of olivine $FePO_4$ calculated by Equation J.3 is $\theta_D^{\circ,FePO_4} = 512$ K (Table J.1), similar to that of $LiFePO_4$. Because of massive similarity between orthorhombic $LiFePO_4$ and orthorhombic $FePO_4$, we assume that the average heat capacity per atom and entropy per atom are the same. i.e $\int_0^{298.15} C_p^{FePO_4} dT = \frac{6}{7}\int_0^{298.15} C_p^{LiFePO_4} dT$ and $S_{FePO_4}^{298.15} = \frac{6}{7} S_{LiFePO_4}^{298.15}$. This assumed value of entropy at room temperature is comparable to that estimated from the data for the crystal hydrate $FePO_4.2H_2O$ [113] (Table K.1). Noticeably, if we assume the magnetism heat capacity per atom of $FePO_4$ is the same as that of $LiFePO_4$ at their corresponding Neel temperatures, the calculated average magnetic moment of $FePO_4$ will be 3.7 Bohr magneton which is in agreement with the reported experimental values [109, 409]. Like in the case of $LiFePO_4$, our estimated enthalpy of formation and Gibbs energy of orthorhombic-$FePO_4$ is similar to those of Xie et al. [25] (Table K.1). Iyer et al. [111] reported a less negative value of enthalpy of formation. From our calculated Gibbs energy of both $LiFePO_4$ and $FePO_4$ at room temperature, the expected voltage by delithiating $LiFePO_4$ is 3.48 V which is analogous to the ~3.5 V voltage plateau found in electrochemical experiments [16, 17, 19, 23, 27, 88, 127, 130, 136, 160, 180, 183, 189].

3. Gibbs energy of compounds

Table K.1 Thermodynamic properties of compounds

Compound	**Thermodynamic properties**	**Reference**
$LiFePO_4$	$C_p^{LiFePO_4}(J.mol^{-1}.K^{-1}) = -2.08612524E+03 - 1.06550805 \cdot T + 4.67344530E+06 \cdot T^{-2} + 4.08265171E-04 \cdot T^2 + 4.27762581E+02 \cdot \ln T$ with $292\ K \leq T \leq 800\ K$ $C_p^{LiFePO_4}(J.mol^{-1}.K^{-1}) = 2.26443429 - 1.02819746 \cdot T - 2.51384702E-03 \cdot T^2 - 2.22335032E-06 \cdot T^3 + 7.31991238E-09 \cdot T^4 + 3.83157327E-01 \cdot T \cdot \ln T + C_p^{magnetism}$ with $0\ K \leq T \leq 292\ K$ $\int_0^{298.15} C_p^{LiFePO_4} dT = 20537.4050349274(J.mol^{-1})$	Present study - by fitting experimental data of Loos et al. [100]
	$S_{LiFePO_4}^{298.15} = 136.75\ (J.mol^{-1}.K^{-1})$	Churikov et al. [113]
	$S_{LiFePO_4}^{mag} = 4.646\ (J.mol^{-1}.K^{-1})$	Present study

	$S^{298.15}_{LiFePO_4} = \int_0^{298.15} \frac{C_p^{LiFePO_4}}{T} dT + S^{mag}_{LiFePO_4}$ $= 131.09\ (J.mol^{-1}.K^{-1})$ $\Delta S^{298}_{LiFePO_4} = -376.427\ \ (J.mol^{-1}.K^{-1})$	
	$\Delta H^{298}_{LiFePO_4} = -1616.02\ \pm\ 2.1\ (kJmol^{-1})$	Iyer et al. [111]
	$\Delta H^{0}_{LiFePO_4} = -1682.36\ (kJmol^{-1})$	Xie et al. [25]
	$\Delta H^{0}_{LiFePO_4} = -1702 \pm 16.9\ (kJmol^{-1})$ $\rightarrow \Delta H^{298.15}_{LiFePO_4} = H^{0}_{LiFePO_4} + \int_0^{298.15} C_p^{LiFePO_4} dT =$ $-1702 + 20.5374 = -1681.4626\ (kJmol^{-1})$	Present study
	$G^{298}_{LiFePO_4} = -1517.7\ (kJmol^{-1})$	He et al. [112]
	$G^{0}_{LiFePO_4} = -1569.47\ (kJmol^{-1})$	Xie et al. [25]
	$\boldsymbol{G^{\circ,298.15}_{LiFePO_4}} = \Delta H^{298.15}_{LiFePO_4} - T \cdot S^{298.15}_{LiFePO_4}$ $= -1681.4626 - 298.15$ $\cdot -0.376427$ $= -1569.23088995\ \ (kJmol^{-1})$	Present study
FePO₄	$S^{298.15}_{FePO_4} = 108.51\ (J.mol^{-1}.K^{-1})$	Churikov et al. [113]
	$S^{mag}_{FePO_4} = S^{mag}_{LiFePO_4} = 3.9823\ (J.mol^{-1}.K^{-1})$ $S^{298.15}_{FePO_4} = \frac{6}{7} S^{298.15}_{LiFePO_4} = 112.3629\ (J.mol^{-1}.K^{-1})$ $\Delta S^{298}_{FePO_4} = -366.069\ (J.mol^{-1}.K^{-1})$	Present study
	$\Delta H^{298}_{FePO_4} = -1267.56\ \pm\ 1.44\ (kJmol^{-1})$	Iyer et al. [111]
	$\Delta H^{0}_{FePO_4} = -1343.13\ (kJmol^{-1})$	Xie et al. [25]
	$\Delta H^{0}_{FePO_4} = -1360 \pm 14.5\ (kJmol^{-1})$ $\rightarrow \Delta H^{298.15}_{FePO_4} = \Delta H^{0}_{FePO_4} + \int_0^{298.15} C_p^{FePO_4} dT =$ $-1360 + \frac{6}{7} \cdot 20.5374 =$ $-1342.39651428571\ (kJmol^{-1})$	Present study
	$G^{0}_{FePO_4} = -1230.24\ (kJmol^{-1})$	Xie et al. [25]

	$\boldsymbol{G^{\circ,298.15}_{FePO_4}} = \Delta H^{298.15}_{FePO_4} - T \cdot \Delta S^{298.15}_{FePO_4}$ $= -1342.39651428571 - 298.15$ $\cdot -0.366069$ $= -1233.25304193571\,(kJmol^{-1})$	Present study
$LiMnPO_4$	$\Delta H^{0}_{LiMnPO_4} = -1835.11\ (kJmol^{-1})$	Xie et al. [25]
	$\Delta H^{0}_{LiMnPO_4} = -1810 \pm 16.9\ (kJmol^{-1})$	Present study
	$G^{0}_{LiMnPO_4} = -1722.21\ (kJmol^{-1})$	Xie et al. [25]
$MnPO_4$	$\Delta H^{0}_{MnPO_4} = -1446.58\ (kJmol^{-1})$	Xie et al. [25]
	$\Delta H^{0}_{MnPO_4} = -1435 \pm 14.5\ (kJmol^{-1})$	Present study
	$G^{0}_{MnPO_4} = -1333.69\ (kJmol^{-1})$	Xie et al. [25]

4. Elastic constants of compounds

Table K.2 Elastic constants of compounds

Compound	**CC_{11}**	**C_{12}**	**C_{13}**	**C_{22}**	**C_{23}**	**C_{33}**	**C_{44}**	**C_{55}**	**C_{66}**	**Reference**
$LiFePO_4$	140.22	69.87	58.84	187.40	49.76	174.16	39.04	45.70	44.99	Xie et al. [25]
	138.90	72.80	52.50	198.00	45.80	173.00	36.80	50.60	47.60	Maxisch et al. [186]
	140	65	49	185	53	173	43	40	42	Present study
$FePO_4$	182.38	27.62	66.65	115.53	13.34	131.60	31.49	48.26	44.15	Xie et al. [25]
	175.90	29.60	54.00	153.60	19.60	135.00	38.80	47.50	55.60	Maxisch et al. [186]

	177	27	52	124	20.3	135	42	46	51	Present study
$LiMnPO_4$	127.49	68.87	48.24	156.73	42.60	151.16	32.82	37.24	39.52	Xie et al. [25]
	131	66	47	173	49	163	39	38	41	Present study
$MnPO_4$	99.62	-36.09	21.19	166.07	−10.60	73.57	16.96	48.71	17.93	Xie et al. [25]
	104	12	19	153	-4	98	23	41	29	Present study

APPENDIX L THERMODYNAMIC MODELS OF $Li_x(Mn_yFe_{1-y})PO_4$

First, since our thermodynamic models are quite complicated, for simplicity, we would use our abbreviations for expressing end - members and other thermodynamic parameters more conveniently (Table L.1). Using table L.1, the excess Gibbs energy of the end - member $LiMn^{2+}Fe^{2+}PO_4$ is expressed as G_{LMFP}^{ex} is or the ideal Gibbs energy of the end - member $VaMn^{2+}Fe^{2+}PO_4$ is considered under the term G_{MFP}°.

Table L.1 Abbreviations of entities and thermodynamic parameters

Li^+	L
Va	-
Mn^{2+}	M
Mn^{3+}	M3
Fe^{2+}	F
Fe^{3+}	F3
PO_4	P
$G_i = G_i^{\circ} + G_i^{ex}$	G_i : Gibbs energy of the end - member *i* G_i° : ideal Gibbs energy of the end - member *i* G_i^{ex}: excess Gibbs energy of the end - member *i*
S_m	Global configuration entropy of mixing of model *m*
G_m°	Ideal Gibbs energy of the solid solution calculated by model *m*

1. *M1* and *M1hs* are equivalent for describing an ideal solid solution $Li_x(Mn_yFe_{1-y})PO_4$

Model *M1*: $(Li^+_x,Va_{1-x})_1(Mn^{2+}_{y\cdot z1},Mn^{3+}_{y\cdot(1-z1)},Fe^{2+}_{(1-y)\cdot z2},Fe^{3+}_{(1-y)\cdot(1-z2)})_1(P^{5+})_1(O^{2-})_4$

Note that the parameter x, y, z_1 and z_2 used for describing the site fractions of ions should satisfy the constraint of electric neutrality (Equation 7.4). The molar configurational entropy and ideal

Gibbs energy of the solid solution $Li_x(Mn_yFe_{1-y})PO_4$ defined from the model ***M1*** are expressed as follow::

$$\begin{aligned}\Delta S_{M1} = -R\big\{&[x\ln x + (1-x)\ln(1-x)] \\ &+ \big[z_1 y\ln(z_1 y) + (1-z_1)y\ln\big((1-z_1)y\big) \\ &+ z_2(1-y)\ln\big(z_2(1-y)\big) \\ &+ (1-z_2)(1-y)\ln\big((1-z_2)(1-y)\big)\big]\big\} \\ = -R\{&[x\ln x + (1-x)\ln(1-x)] \\ &+ y[z_1\ln(z_1) + (1-z_1)\ln(1-z_1)] \\ &+ (1-y)[z_2\ln(z_2) + (1-z_2)\ln(1-z_2)] \\ &+ [y\ln(y) + (1-y)\ln(1-y)]\}\end{aligned} \tag{L.1}$$

$$\begin{aligned}\Delta G^{\circ}_{M1} = {} & xz_1y\cdot G^{\circ}_{LMP} + x(1-z_1)y\cdot G^{\circ}_{LM3P} + (1-x)z_1y\cdot G^{\circ}_{MP} \\ & + (1-x)(1-z_1)y\cdot G^{\circ}_{M3P} + xz_2(1-y)\cdot G^{\circ}_{LFP} + x(1-z_2)(1-y) \\ & \cdot G^{\circ}_{LF3P} + (1-x)z_2(1-y)\cdot G^{\circ}_{FP} + (1-x)(1-z_2)(1-y)\cdot G^{\circ}_{F3P} \\ & - T\Delta S_{M1}\end{aligned} \tag{L.2}$$

Model *M1hs*: $(Li^{+}_{x}, Va_{1-x})_1([Mn^{2+}_{z1}, Mn^{3+}_{1-z1}]_y, [Fe^{2+}_{z2}, Fe^{3+}_{1-z2}]_{1-y})_1(P^{5+})_1(O^{2-})_4$

The molar configurational entropy the solid solution $Li_x(Mn_yFe_{1-y})PO_4$ defined from the model ***M1hs*** is expressed as follow:

$$\begin{aligned}\Delta S_{M1hs} = -R\{&[x\ln x + (1-x)\ln(1-x)] + y[z_1\ln(z_1) + (1-z_1)\ln(1-z_1)] \\ &+ (1-y)[z_2\ln(z_2) + (1-z_2)\ln(1-z_2)]\} \\ = {} & \Delta S_{M1} + R[y\ln(y) + (1-y)\ln(1-y)]\end{aligned} \tag{L.3}$$

The ideal energy of end-members are defined as follows:

$$\left\{\begin{aligned} G_1 &= G^{\circ}_{LMFP} = yG^{\circ}_{LMP} + (1-y)G^{\circ}_{LFP} + RT[y\ln(y) + (1-y)\ln(1-y)] \\ G_2 &= G^{\circ}_{LMF3P} = yG^{\circ}_{LMP} + (1-y)G^{\circ}_{LF3P} + RT[y\ln(y) + (1-y)\ln(1-y)] \\ G_3 &= G^{\circ}_{LM3FP} = yG^{\circ}_{LM3P} + (1-y)G^{\circ}_{LFP} + RT[y\ln(y) + (1-y)\ln(1-y)] \\ G_4 &= G^{\circ}_{LM3F3P} = yG^{\circ}_{LM3P} + (1-y)G^{\circ}_{LF3P} + RT[y\ln(y) + (1-y)\ln(1-y)] \\ G_5 &= G^{\circ}_{MFP} = yG^{\circ}_{MP} + (1-y)G^{\circ}_{FP} + RT[y\ln(y) + (1-y)\ln(1-y)] \\ G_6 &= G^{\circ}_{MF3P} = yG^{\circ}_{MP} + (1-y)G^{\circ}_{F3P} + RT[y\ln(y) + (1-y)\ln(1-y)] \\ G_7 &= G^{\circ}_{M3FP} = yG^{\circ}_{M3P} + (1-y)G^{\circ}_{FP} + RT[y\ln(y) + (1-y)\ln(1-y)] \\ G_8 &= G^{\circ}_{M3F3P} = yG^{\circ}_{M3P} + (1-y)G^{\circ}_{F3P} + RT[y\ln(y) + (1-y)\ln(1-y)] \end{aligned}\right. \tag{L.4}$$

Then, the ideal molar Gibbs energy the solid solution $Li_x(Mn_yFe_{1-y})PO_4$ defined from the model ***M1hs*** is calculated:

$$\begin{aligned} G^{\circ}_{M1hs} = {} & xz_1z_2 \cdot G^{\circ}_{LMFP} + x(1-z_1)z_2 \cdot G^{\circ}_{LM3FP} + xz_1(1-z_2) \cdot G^{\circ}_{LMF3P} \\ & + x(1-z_1)(1-z_2) \cdot G^{\circ}_{LM3F3P} + (1-x)z_1z_2 \cdot G^{\circ}_{MFP} \\ & + (1-x)(1-z_1)z_2 \cdot G^{\circ}_{M3FP} + (1-x)z_1(1-z_2) \cdot G^{\circ}_{MF3P} \\ & + (1-x)(1-z_1)(1-z_2) \cdot G^{\circ}_{M3F3P} + RT\Delta S_{M3n} \\ & = xz_1y \cdot G^{\circ}_{LMP} + x(1-z_1)y \cdot G^{\circ}_{LM3P} + (1-x)z_1y \cdot G^{\circ}_{MP} \\ & + (1-x)(1-z_1)y \cdot G^{\circ}_{M3P} + xz_2(1-y) \cdot G^{\circ}_{LFP} + x(1-z_2)(1-y) \\ & \cdot G^{\circ}_{LF3P} + (1-x)z_2(1-y) \cdot G^{\circ}_{FP} + (1-x)(1-z_2)(1-y) \cdot G^{\circ}_{F3P} \\ & + RT[y\ln(y) + (1-y)\ln(1-y)] - T\Delta S_{M1hs} \end{aligned} \tag{L.5}$$

Compare the Equation L.2 and Equation L.5, we obtain:

$$G^{\circ}_{M1} = G^{\circ}_{M1hs} \tag{L.6}$$

2. Parameters of thermodynamic models

All the thermodynamic models of the $Li(Mn_yFe_{1-y})PO_4$-$(Mn_yFe_{1-y})PO_4$ battery join containing secondary sublattices in this study are considered with the Gibbs energy of endmembers of primary sublattice taken from our models of subsystems (Table L.2). All the thermodynamic parameters used in model ***M1hs***, ***M2hs*** and ***M3hy*** are listed on table L.3-5 (here, the unit of Gibbs energy is J/mol).

Table L.2 Gibbs energy of endmembers of primary sublattice

Primary endmember (J/mol)	**Reference**
$G^{\circ}_{LF3P} = G^{\circ}_{LFP} + 11000$	(Model M4) Phan et al. [133] (use for model ***M1hs***)
$G^{\circ}_{FP} = G^{\circ}_{F3P} + 11000$	
$G^{\circ}_{LM3P} = G^{\circ}_{LMP} + 10000$	Present study (used for model ***M1hs*** and ***M3hy***)
$G^{\circ}_{MP} = G^{\circ}_{M3P} + 10000$	
$\Delta G_{LFP} = 15000$	(Model M5.F) Phan et al. [133] (used for model ***M3hy*** and ***M2hs***)
$G^{\circ}_{LFF} = 5 \cdot G^{\circ}_{LFP}$	
$G^{\circ}_{F3F3} = 5 \cdot G^{\circ}_{F3P}$	
$G^{\circ}_{LF3F3} = 5 \cdot G^{\circ}_{LFP} + 5 \cdot \Delta G_{LFP}$	
$G^{\circ}_{FF} = 5 \cdot G^{\circ}_{F3P} + 5 \cdot \Delta G_{LFP}$	
$G^{\circ}_{F3F} = 5 \cdot G^{\circ}_{F3P} + 2 \cdot \Delta G_{LFP}$	
$G^{\circ}_{LF3F} = 5 \cdot G^{\circ}_{LF3P} + 3 \cdot \Delta G_{LFP}$	
$G^{\circ}_{FF3} = 5 \cdot G^{\circ}_{F3P} + 1.05 \cdot \Delta G_{LFP}$	
$G^{\circ}_{LFF3} = 5 \cdot G^{\circ}_{F3P} + 0.7 \cdot \Delta G_{LFP}$	
$\Delta G_{LMP} = 10000$	Present study (used for model ***M2hs***)
$G^{\circ}_{LMM} = 5 \cdot G^{\circ}_{LMP}$	
$G^{\circ}_{M3M3} = 5 \cdot G^{\circ}_{M3P}$	
$G^{\circ}_{LM3M3} = 5 \cdot G^{\circ}_{LMP} + 5 \cdot \Delta G_{LMP}$	
$G^{\circ}_{MM} = 5 \cdot G^{\circ}_{M3P} + 5 \cdot \Delta G_{LMP}$	
$G^{\circ}_{M3M} = 5 \cdot G^{\circ}_{M3P} + 2 \cdot \Delta G_{LMP}$	
$G^{\circ}_{LM3M} = 5 \cdot G^{\circ}_{LM3P} + 3 \cdot \Delta G_{LMP}$	
$G^{\circ}_{MM3} = 5 \cdot G^{\circ}_{M3P} + 3 \cdot \Delta G_{LMP}$	
$G^{\circ}_{LMM3} = 5 \cdot G^{\circ}_{F3P} + 2 \cdot \Delta G_{LMP}$	

$G^{\circ}_{LMF} = 3 \cdot G^{\circ}_{LMP} + 2 \cdot G^{\circ}_{LFP}$	
$G^{\circ}_{LMF3} = 3 \cdot G^{\circ}_{LMP} + 2 \cdot G^{\circ}_{LFP} + 2 \cdot \Delta G_{LFP}$	
$G^{\circ}_{LM3F} = 3 \cdot G^{\circ}_{LMP} + 3 \cdot \Delta G_{LMP} + 2 \cdot G^{\circ}_{LFP}$	
$G^{\circ}_{LM3F3} = 3 \cdot G^{\circ}_{LMP} + 3 \cdot \Delta G_{LMP} + 2 \cdot G^{\circ}_{LFP} + 2 \cdot \Delta G_{LFP}$	
$G^{\circ}_{LFM} = 3 \cdot G^{\circ}_{LFP} + 2 \cdot G^{\circ}_{LMP}$	
$G^{\circ}_{LFM3} = 3 \cdot G^{\circ}_{LFP} + 2 \cdot G^{\circ}_{LMP} + 2 \cdot \Delta G_{LMP}$	
$G^{\circ}_{LF3M} = 3 \cdot G^{\circ}_{LFP} + 3 \cdot \Delta G_{LFP} + 2 \cdot G^{\circ}_{LMP}$	
$G^{\circ}_{LF3M3} = 3 \cdot G^{\circ}_{LFP} + 3 \cdot \Delta G_{LFP} + 2 \cdot G^{\circ}_{LMP} + 2 \cdot \Delta G_{LMP}$	
$G^{\circ}_{MF} = 3 \cdot G^{\circ}_{M3P} + 3 \cdot \Delta G_{LMP} + 2 \cdot G^{\circ}_{F3P} + 2 \cdot \Delta G_{LFP}$	
$G^{\circ}_{MF3} = 3 \cdot G^{\circ}_{M3P} + 3 \cdot \Delta G_{LMP} + 2 \cdot G^{\circ}_{F3P}$	
$G^{\circ}_{M3F} = 3 \cdot G^{\circ}_{M3P} + 2 \cdot G^{\circ}_{F3P} + 2 \cdot \Delta G_{LFP}$	
$G^{\circ}_{M3F3} = 3 \cdot G^{\circ}_{M3P} + 2 \cdot G^{\circ}_{F3P}$	
$G^{\circ}_{FM} = 3 \cdot G^{\circ}_{F3P} + 3 \cdot \Delta G_{LFP} + 2 \cdot G^{\circ}_{M3P} + 2 \cdot \Delta G_{LMP}$	
$G^{\circ}_{FM3} = 3 \cdot G^{\circ}_{F3P} + 3 \cdot \Delta G_{LFP} + 2 \cdot G^{\circ}_{M3P}$	
$G^{\circ}_{F3M} = 3 \cdot G^{\circ}_{F3P} + 2 \cdot G^{\circ}_{M3P} + 2 \cdot \Delta G_{LMP}$	
$G^{\circ}_{F3M3} = 3 \cdot G^{\circ}_{F3P} + 2 \cdot G^{\circ}_{M3P}$	

Model *M1hs*: $(\mathrm{Li}^{+}_{x}, \mathrm{Va}_{1\text{-}x})_1([\mathrm{Mn}^{2+}_{z1}, \mathrm{Mn}^{3+}_{1\text{-}z1}]_y, [\mathrm{Fe}^{2+}_{z2}, \mathrm{Fe}^{3+}_{1\text{-}z2}]_{1\text{-}y})_1(\mathrm{P}^{5+})_1(\mathrm{O}^{2-})_4$

Table L.3 Thermodynamic parameters of model ***M1hs*** *(J/mol)*

$d_{Li} = 50000$	$d_{Va} = 200000 \cdot y(y - 0.8)$
$G_1 = G_{LMFP} = G^{\circ}_{LMFP}$	$G_5 = G_{MFP} = G^{\circ}_{MFP}$
$\boldsymbol{G_2 = G_{LMF3P} = G^{\circ}_{LMF3P} - d_{Li} \cdot y(1 - y)}$	$\boldsymbol{G_6 = G_{MF3P} = G^{\circ}_{MF3P} - d_{Va} \cdot y(1 - y)}$
$G_3 = G_{LM3FP} = G^{\circ}_{LM3FP}$	$G_7 = G_{M3FP} = G^{\circ}_{M3FP}$
$G_4 = G_{LM3F3P} = G^{\circ}_{LM3F3P}$	$G_8 = G_{M3F3P} = G^{\circ}_{M3F3P}$

Model *M2hs*: $(\mathrm{Li}^{+}_{x},\ \mathrm{Va}_{1-x})_5([\mathrm{Mn}^{2+}_{z1},\ \mathrm{Mn}^{3+}_{1-z1}]_y,\ [\mathrm{Fe}^{2+}_{z2},\ \mathrm{Fe}^{3+}_{1-z2}]_{1-y})_3([\mathrm{Mn}^{2+}_{z3},\ \mathrm{Mn}^{3+}_{1-z3}]_y,\ [\mathrm{Fe}^{2+}_{z4},\ \mathrm{Fe}^{3+}_{1-z4}]_{1-y})_2(\mathrm{P}^{5+})_5(\mathrm{O}^{2-})_{20}$

Table L.4 Thermodynamic parameters of model ***M2hs*** *(J/mol)*

$d_{Li} = 50000$	$d_{Va} = 20000$
$d_{FF3} = 120000$	
$G_1 = G^{\circ}_{LMFMFP}$	$G_{17} = G^{\circ}_{MFMFP}$
$G_2 = G^{\circ}_{LMFMF3P} - 2 \cdot d_{Li} \cdot y(1-y)$	**$G_{18} = G^{\circ}_{MFMF3P} - 2 \cdot d_{Va} \cdot y(1-y) - d_{FF3} \cdot y(1-y)^2$**
$G_3 = G^{\circ}_{LMFM3FP}$	$G_{19} = G^{\circ}_{MFM3FP}$
$G_4 = G^{\circ}_{LMFM3F3P}$	**$G_{20} = G^{\circ}_{MFM3F3P} - d_{FF3} \cdot y(1-y)^2$**
$G_5 = G^{\circ}_{LMF3MFP} - 3 \cdot d_{Li} \cdot y(1-y)$	**$G_{21} = G^{\circ}_{MF3MFP} - 3 \cdot d_{Va} \cdot y(1-y)$**
$G_6 = G^{\circ}_{LMF3MF3P} - 5 \cdot d_{Li} \cdot y(1-y)$	**$G_{22} = G^{\circ}_{MF3MF3P} - 5 \cdot d_{Va} \cdot y(1-y)$**
$G_7 = G^{\circ}_{LMF3M3FP} - 3 \cdot d_{Li} \cdot y(1-y)$	**$G_{23} = G^{\circ}_{MF3M3FP} - 3 \cdot d_{Va} \cdot y(1-y)$**
$G_8 = G^{\circ}_{LMF3M3F3P} - 3 \cdot d_{Li} \cdot y(1-y)$	**$G_{24} = G^{\circ}_{MF3M3F3P} - 3 \cdot d_{Va} \cdot y(1-y)$**
$G_9 = G^{\circ}_{LM3FMFP}$	$G_{25} = G^{\circ}_{M3FMFP}$
$G_{10} = G^{\circ}_{LM3FMF3P} - 2 \cdot d_{Li} \cdot y(1-y)$	**$G_{26} = G^{\circ}_{M3FMF3P} - 2 \cdot d_{Va} \cdot y(1-y) - d_{FF3} \cdot y(1-y)^2$**
$G_{11} = G^{\circ}_{LM3FM3FP}$	$G_{27} = G^{\circ}_{M3FM3FP}$
$G_{12} = G^{\circ}_{LM3FM3F3P}$	**$G_{28} = G^{\circ}_{M3FM3F3P} - d_{FF3} \cdot y(1-y)^2$**
$G_{13} = G^{\circ}_{LM3F3MFP}$	$G_{29} = G^{\circ}_{M3F3MFP}$
$G_{14} = G^{\circ}_{LM3F3MF3P} - 2 \cdot d_{Li} \cdot y(1-y)$	**$G_{30} = G^{\circ}_{M3F3MF3P} - 2 \cdot d_{Va} \cdot y(1-y)$**
$G_{15} = G^{\circ}_{LM3F3M3FP}$	$G_{31} = G^{\circ}_{M3F3M3FP}$
$G_{16} = G^{\circ}_{LM3F3M3F3P}$	$G_{32} = G^{\circ}_{M3F3M3F3P}$

Model *M3hy*: $(\mathrm{Li}^{+}_{x},\ \mathrm{Va}_{1-x})_5([\mathrm{Mn}^{2+}_{z1},\ \mathrm{Mn}^{3+}_{1-z1}]_{5y},[(\mathrm{Fe}^{2+}_{z2},\ \mathrm{Fe}^{3+}_{1-z2})_3(\mathrm{Fe}^{2+}_{z3},\ \mathrm{Fe}^{3+}_{1-z3})_2]_{(1-y)})(\mathrm{P}^{5+})_5(\mathrm{O}^{2-})_{20}$

In the hybrid model ***M3hy***, even secondary sublattice is shown slightly different in compassion with that in other models (***M1hs*** and ***M2hs***), the Gibbs energy of endmembers is still considered from the Gibbs energy of primary sublattices. For example,

$$G^{\circ}_{Li_5Mn^{3+}_{5y}Fe^{2+}_{3(1-y)}Fe^{3+}_{2(1-y)}P_5O_{20}} = G^{\circ}_{LM3FF3P} = yG^{\circ}_{LM3P} + (1-y)G^{\circ}_{LFF3P} \qquad \text{(L.7)}$$

Note that because our proposed thermodynamic models ***M3hy*** consider 5 formula units, therefore, G°_{LM3P} and G°_{MP} are 5 times the value reported in table L.2 and for adjust the solubility of lithium in the Li-poor end, one of the primary end-member is modified:

$$\begin{gathered} G^{\circ}_{LM3P}\,(J/mol) = 5\left(G^{\circ}_{LMP} + 10000\right) + 200000 \cdot y \cdot (1-y) \\ G^{\circ}_{MP}(J/mol) = 5\left(G^{\circ}_{M3P} + 10000\right) \end{gathered} \qquad \text{(L.8)}$$

Table L.5 Thermodynamic parameters of model ***M3hy*** *(J/mol)*

$d_{Li} = 50000$	$d_{Va} = 20000$
$d_{FF3} = 78000$	
$G_1 = G^{\circ}_{LMFFP}$	$G_9 = G^{\circ}_{MFFP}$
$\boldsymbol{G_2 = G^{\circ}_{LMFF3P} - 2 \cdot d_{Li} \cdot y(1-y)}$	$\boldsymbol{G_{10} = G^{\circ}_{MFF3P} - 2 \cdot d_{Va} \cdot y(1-y) - d_{FF3} \cdot y(1-y)}$
$\boldsymbol{G_3 = G^{\circ}_{LMF3FP} - 3 \cdot d_{Li} \cdot y(1-y)}$	$\boldsymbol{G_{11} = G^{\circ}_{MF3FP} - 3 \cdot d_{Va} \cdot y(1-y)}$
$\boldsymbol{G_4 = G^{\circ}_{LMF3F3P} - 5 \cdot d_{Li} \cdot y(1-y)}$	$\boldsymbol{G_{12} = G^{\circ}_{MF3F3P} - 5 \cdot d_{Va} \cdot y(1-y)}$
$G_5 = G^{\circ}_{LM3FFP}$	$G_{13} = G^{\circ}_{M3FFP}$
$G_6 = G^{\circ}_{LM3FF3P}$	$\boldsymbol{G_{14} = G^{\circ}_{M3FF3P} - d_{FF3} \cdot y(1-y)}$
$G_7 = G^{\circ}_{LM3F3FP}$	$G_{15} = G^{\circ}_{M3F3FP}$
$G_8 = G^{\circ}_{LM3F3F3P}$	$G_{16} = G^{\circ}_{M3F3F3P}$

APPENDIX M GIBBS ELASTIC ENERGY APPROACH FOR AN ORTHOGONAL SYSTEM

1. In the small deformation regime

For orthohombic systems, the stress - strain relation for (100) habit plane should be formulated similar to that of cubic systems [433]:

$$\begin{bmatrix} 0 \\ \sigma_2 \\ \sigma_3 \\ 0 \\ 0 \\ 0 \end{bmatrix} = \begin{bmatrix} C_{11} & C_{12} & C_{13} & 0 & 0 & 0 \\ C_{12} & C_{22} & C_{23} & 0 & 0 & 0 \\ C_{13} & C_{23} & C_{33} & 0 & 0 & 0 \\ 0 & 0 & 0 & C_{44} & 0 & 0 \\ 0 & 0 & 0 & 0 & C_{55} & 0 \\ 0 & 0 & 0 & 0 & 0 & C_{66} \end{bmatrix} \cdot \begin{bmatrix} \varepsilon_1 \\ \varepsilon_2 \\ \varepsilon_3 \\ 0 \\ 0 \\ 0 \end{bmatrix} \tag{M.1}$$

Solving Equation M.1, we got:

$$\begin{cases} \sigma_2 = \left(C_{22} - \dfrac{{C_{12}}^2}{C_{11}}\right)\varepsilon_2 + \left(C_{23} - \dfrac{C_{12}C_{13}}{C_{11}}\right)\varepsilon_3 \\ \\ \sigma_3 = \left(C_{23} - \dfrac{C_{12}C_{13}}{C_{11}}\right)\varepsilon_2 + \left(C_{33} - \dfrac{{C_{13}}^2}{C_{11}}\right)\varepsilon_3 \end{cases} \tag{M.2}$$

The elastic energy stored in the crystal in small deformation regime is estimated as summation of the products of stress and strain:

$$f_{el}^{s} = \frac{1}{2}\sum \varepsilon_i \sigma_i = \frac{1}{2}(\varepsilon_2\sigma_2 + \varepsilon_3\sigma_3) \tag{M.3}$$

Substitute Equation M.2 into Equation M.3, then

$$f_{el}^{s} = \frac{1}{2}\left[\left(C_{22} - \frac{{C_{12}}^2}{C_{11}}\right){\varepsilon_2}^2 + 2\left(C_{23} - \frac{C_{12}C_{13}}{C_{11}}\right)\varepsilon_3\varepsilon_2 + \left(C_{33} - \frac{{C_{13}}^2}{C_{11}}\right){\varepsilon_3}^2\right] \tag{M.4}$$

Consider a sinusoidal plane wave fluctuation of the composition, then the elastic strain should be expressed as:

$$\begin{cases} \varepsilon_2 = \eta_b(x - x_0) = \eta_b A cos(\boldsymbol{\beta} \cdot \boldsymbol{r}) \\ \varepsilon_3 = \eta_c(x - x_0) = \eta_c A cos(\boldsymbol{\beta} \cdot \boldsymbol{r}) \end{cases} \tag{M.5}$$

where x_0 is the overall composition and x is the local composition of the solid solution and the composition fluctuates as $x - x_0 = Acos(\boldsymbol{\beta} \cdot \boldsymbol{r})$. According to Cahn [154-156, 231], the total free energy of volume V of an isotropic solid solution free from imperfections in which the molar volume is independent of both composition and pressure is:

$$\begin{aligned} F = \int_V \Bigg\{ f'(x) + \frac{1}{2}\Bigg[\left(C_{22} - \frac{{C_{12}}^2}{C_{11}} \right) {\eta_b}^2 + 2\left(C_{23} - \frac{C_{12}C_{13}}{C_{11}} \right) \eta_b \eta_c \\ + \left(C_{33} - \frac{{C_{13}}^2}{C_{11}} \right) {\eta_c}^2 \Bigg] (x - x_0)^2 + \kappa(\nabla x)^2 \Bigg\} dV \end{aligned} \tag{M.6}$$

where $f'(x)$ is the Helmholtz free energy of a unit volume of homogeneous materials of composition x and $\kappa(\nabla x)^2$ is the first term of an expansion representing the increase in free energy due to introducing a gradient of composition. Expanding $f'(x)$ in Taylor's series with $x - x_0 = Acos(\boldsymbol{\beta} \cdot \boldsymbol{r})$ and integrating the above equation, we obtain the change in free energy per unit volume between the initial homogeneous solution of concentration x_0 and the inhomogeneous solution of concentration x:

$$\begin{aligned} \frac{\Delta F}{V} = \frac{1}{4} A^2 \Bigg\{ \frac{\partial^2 f'}{\partial x^2} \\ + \Bigg[\left(C_{22} - \frac{{C_{12}}^2}{C_{11}} \right) {\eta_b}^2 + 2\left(C_{23} - \frac{C_{12}C_{13}}{C_{11}} \right) \eta_b \eta_c \\ + \left(C_{33} - \frac{{C_{13}}^2}{C_{11}} \right) {\eta_c}^2 \Bigg] + 2\kappa\beta^2 \Bigg\} \end{aligned} \tag{M.7}$$

If the free energy change $\frac{\Delta F}{V}$ is negative for some wave vectors $\boldsymbol{\beta}$, then the solution is unstable to infinitesimal fluctuations with those wave vectors. Otherwise, the solution is stable for all infinitesimal fluctuations. The spinodal curve for a particular direction of the wave vector is given by the condition that the solution is just unstable to fluctuations infinite wavelength but stable to fluctuations of finite wavelength in that directions, that is, the spinodal is given by:

$$\frac{\partial^2 f'}{\partial x^2} + \left[\left(C_{22} - \frac{{C_{12}}^2}{C_{11}}\right){\eta_b}^2 + 2\left(C_{23} - \frac{C_{12}C_{13}}{C_{11}}\right)\eta_b\eta_c + \left(C_{33} - \frac{{C_{13}}^2}{C_{11}}\right){\eta_c}^2\right] = 0 \qquad \text{(M.8)}$$

Equation M.8 is applied for a volume unit of the solid solution. Hence, for a molar volume of an isotropic material under coherent spinodal decomposition:

$$\frac{\partial^2 F}{\partial x^2} + 2V_m Y^s_{(100)}{\eta_b}^2 = 0 \qquad \text{(M.9)}$$

where F is the molar Helmholtz free energy. In fact, the molar Gibbs energy $G = F - PV$. Since the second derivative of PV versus x is neglected, Equation M.9 becomes:

$$\frac{\partial^2 G}{\partial x^2} + 2V_m Y^s_{(100)}{\eta_b}^2 = 0 \qquad \text{(M.10)}$$

i.e.

$$E_{elastic} = V_m Y^s_{(100)}{\eta_b}^2 \qquad \text{(M.11)}$$

with

$$Y^s_{(100)} = \frac{1}{2}C_{22} + \frac{1}{2}C_{33}\left(\frac{\eta_c}{\eta_b}\right)^2 + C_{23}\frac{\eta_c}{\eta_b} - \frac{\left(C_{12} + C_{13}\frac{\eta_c}{\eta_b}\right)^2}{C_{11}} \qquad \text{(M.12)}$$

Consequently, the molar elastic energy is estimated through a double integration:

$$G^{el}_m = \iint_0^x V_m\left[C_{22}{\eta_b}^2 + C_{33}{\eta_c}^2 + 2C_{23}\eta_b\eta_c - \frac{(C_{12}\eta_b + C_{13}\eta_c)^2}{C_{11}}\right]dx^2 \qquad \text{(M.13)}$$

with the boundary conditions: $G^{el}_{LiFePO_4} = 0$ and $G^{el}_{FePO_4} = 0$. The expression of G^{el}_m in Equation M.13 is exactly like Cahn's approach for orthohombic system [232].

2. In the large deformation regime

Corresponding to the stress - strain relation developed for calculating the elastic Gibbs energy of (100) coherence in the small deformation regime in Equation M.1, the Cauchy stress tensor is $\begin{bmatrix}0 & 0 & 0\\ 0 & \sigma_2 & 0\\ 0 & 0 & \sigma_3\end{bmatrix}$ and the strain tensor is $\begin{bmatrix}\varepsilon_1 & 0 & 0\\ 0 & \varepsilon_2 & 0\\ 0 & 0 & \varepsilon_3\end{bmatrix}$. The elastic energy stored in the crystal is estimated from the Almansi strain and the second Poila - Kirchhoff stress. The deformation matrix is:

$$[\boldsymbol{F}] = \begin{bmatrix}\varepsilon_1 + 1 & 0 & 0\\ 0 & \varepsilon_2 + 1 & 0\\ 0 & 0 & \varepsilon_2 + 1\end{bmatrix} \tag{M.14}$$

Then,

$$\boldsymbol{J} = |\det \boldsymbol{F}| = (\varepsilon_1 + 1)\cdot(\varepsilon_2 + 1)\cdot(\varepsilon_3 + 1) \tag{M.15}$$

The right Cauchy - Green deformation tensor is expressed as follow:

$$[\boldsymbol{C}] = [\boldsymbol{F}]^{\boldsymbol{T}} \cdot [\boldsymbol{F}] = \begin{bmatrix}(\varepsilon_1 + 1)^2 & 0 & 0\\ 0 & (\varepsilon_2 + 1)^2 & 0\\ 0 & 0 & (\varepsilon_3 + 1)^2\end{bmatrix} \tag{M.16}$$

Consequently, the Almansi - Lagrange strain tensor is obtained:

$$\begin{aligned}[\boldsymbol{e}] &= \frac{1}{2}([\boldsymbol{I}] - [\boldsymbol{C^{-1}}])\\ &= \frac{1}{2}\begin{bmatrix}1 - \frac{1}{(\varepsilon_1 + 1)^2} & 0 & 0\\ 0 & 1 - \frac{1}{(\varepsilon_2 + 1)^2} & 0\\ 0 & 0 & 1 - \frac{1}{(\varepsilon_3 + 1)^2}\end{bmatrix}\end{aligned} \tag{M.17}$$

Next, we find the second Piola - Kirchhoff stress tensor:

$$[\widetilde{\boldsymbol{T}}] = [\boldsymbol{F}^{-1}] \cdot \boldsymbol{J} \cdot [\boldsymbol{T}] \cdot [\boldsymbol{F}^{-1}]^{\boldsymbol{T}} = (\varepsilon_1 + 1) \cdot (\varepsilon_2 + 1) \cdot (\varepsilon_3 + 1) \cdot \begin{bmatrix} 0 & 0 & 0 \\ 0 & \dfrac{\sigma_2}{(\varepsilon_2 + 1)^2} & 0 \\ 0 & 0 & \dfrac{\sigma_3}{(\varepsilon_3 + 1)^2} \end{bmatrix} \quad \text{(M.18)}$$

Hence, the elastic energy stored in the crystal is estimated as follow:

$$f_{el}^{l} = \frac{1}{2}\sum e_{ij} \cdot \tilde{T}_{ij} = \frac{1}{4} \cdot (\varepsilon_1 + 1) \cdot (\varepsilon_2 + 1) \cdot (\varepsilon_3 + 1) \cdot \left[\frac{(\varepsilon_2 + 2)\varepsilon_2\sigma_2}{(\varepsilon_2 + 1)^4} + \frac{(\varepsilon_3 + 1)\varepsilon_3\sigma_3}{(\varepsilon_3 + 1)^4}\right] \quad \text{(M.19)}$$

For small deformation, $(\varepsilon_1 + 1) \approx 1; (\varepsilon_2 + 1) \approx 1; \ (\varepsilon_3 + 1) \approx 1; \ (\varepsilon_2 + 2) \approx 2; \ (\varepsilon_3 + 2) \approx 2$, then:

$$f_{el}^{l} = \frac{1}{2} \cdot [\varepsilon_2\sigma_2 + \varepsilon_3\sigma_3] = f_{el}^{s} \quad \text{(M.20)}$$

Since $\frac{\varepsilon_2}{\varepsilon_3} = \frac{\eta_b}{\eta_c}$, f_{el}^{l} can be expressed as a function of ${\varepsilon_2}^2$:

$$f_{el}^{l} = Y_{[100]}^{l}{\varepsilon_2}^2 \quad \text{(M.21)}$$

with

$$Y_{[100]}^{l} = \frac{1}{4} \cdot (\varepsilon_1 + 1) \cdot (\varepsilon_2 + 1) \cdot (\varepsilon_3 + 1) \cdot \left[\frac{(\varepsilon_2 + 2)\varepsilon_2\sigma_2}{{\varepsilon_2}^2(\varepsilon_2 + 1)^4} + \frac{(\varepsilon_3 + 1)\varepsilon_3\sigma_3}{{\varepsilon_2}^2(\varepsilon_3 + 1)^4}\right] \quad \text{(M.22)}$$

As discussed previously in our paper on the calculation of coherent miscibility gap for cubic systems [433], as $Y_{[100]}^{l}$ is a function of composition, it is very difficult to take integration and calculated the elastic Gibbs energy G_m^{el}. Therefore, similar to what we have done for cubic systems

[433], for a specific composition, the f_{el}^{l} is fitted as a function of ${\varepsilon_2}^2$ with a scalar coefficient $Y'_{[100]}$. It means that $Y'_{[100]}$ is a serie of scalars and it is composition dependent. The fitting of f_{el}^{l} as a function of ${\varepsilon_2}^2$ is satisfactory especially in the range of $0.0 \leq \varepsilon_2 \leq 0.05$ (the range covers the lattice mismatch in the (010) direction of Li(Mn$_y$Fe$_{1-y}$)PO$_4$-(Mn$_y$Fe$_{1-y}$)PO$_4$ system) (Figure D.1). We have chosen ε_2 because $|\varepsilon_2| > |\varepsilon_3|$ for LiFePO$_4$-FePO$_4$, LiMnPO$_4$-MnPO$_4$, and Li(Mn$_y$Fe$_{1-y}$)PO$_4$-(Mn$_y$Fe$_{1-y}$)PO$_4$ battery joins. As shown from our calculation of elastic energy for Li$_{0.5}$FePO$_4$, $f_{el}^{l} < f_{el}^{s}$. The difference $(f_{el}^{s} - f_{el}^{l})$ become more significant when ε_2 is large (Figure D.1). When $\varepsilon_2 = 0.05$, $f_{el}^{l} \approx 0.9048 f_{el}^{s}$ and when $\varepsilon_2 = 0.15$, $f_{el}^{l} \approx 0.7773 f_{el}^{s}$. Hence, the elastic Gibbs energy should be expressed through the fitting parameter $Y'_{[100]}$:

$$G_m^{el} = \iint_0^x V_m Y'_{[100]} {\eta_b}^2 dx^2 \tag{M.23}$$

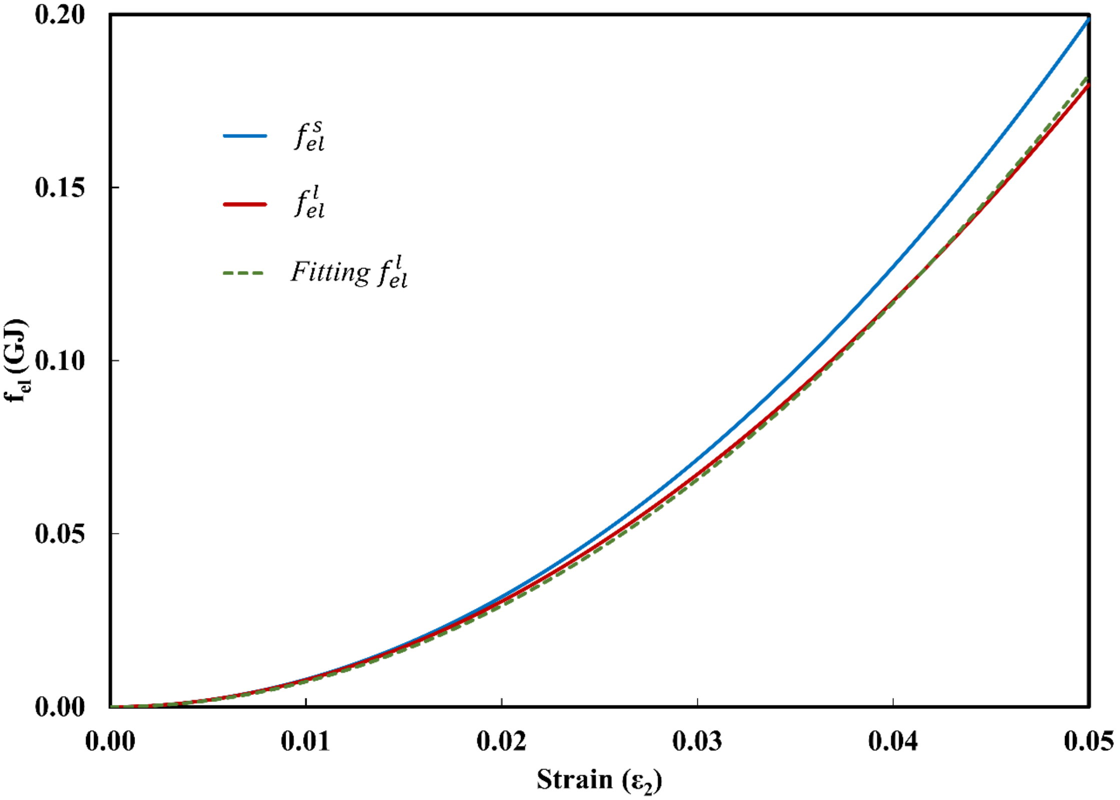

Figure M.1: Comparison of the calculated elastic energy f_{el} stored in the crystal structure of $Li_{0.5}FePO_4$ at room temperature for small deformation and large deformation. The fitting large deformation curve is used for estimating $Y'_{(100)}$.